

UiO : **University of Oslo**

Marianne Etzelmüller Bathen

Point defects in silicon carbide for quantum technologies: Identification, tuning and control

Thesis submitted for the degree of Philosophiae Doctor

Department of Physics

The Faculty of Mathematics and Natural Sciences



2020

© Marianne Etzelmüller Bathen, 2020

*Series of dissertations submitted to the
Faculty of Mathematics and Natural Sciences, University of Oslo
No. 2329*

ISSN 1501-7710

All rights reserved. No part of this publication may be
reproduced or transmitted, in any form or by any means, without permission.

Cover: Hanne Baadsgaard Utigard.
Print production: Reprosentralen, University of Oslo.

It's the job that's never started as takes longest to finish.
— J. R. R. Tolkien

Preface

This thesis is submitted in partial fulfillment of the requirements for the degree of *Philosophiae Doctor* at the University of Oslo. The research presented herein was conducted at the University of Oslo and at the University of Aveiro, under the supervision of Professor Lasse Vines, Dr. Augustinas Galeckas, Dr. José Coutinho and Professor Bengt G. Svensson.

Financial support was kindly provided by the Research Council of Norway and the University of Oslo through the frontier research project FUNDAMeNT (no. 251131, FriPro ToppForsk-program). The Research Council of Norway is also acknowledged for the support to the Norwegian Micro- and Nano-Fabrication Facility, NorFab, project number 245963. Some of the computations were performed on resources provided by UNINETT Sigma2 - the National Infrastructure for High Performance Computing and Data Storage in Norway.

The thesis is a collection of ten papers, presented to convey a comprehensive story. The common theme is understanding, utilizing and controlling point defects in silicon carbide, with particular emphasis being placed on the silicon and carbon vacancies. The papers are preceded by seven introductory chapters that are devoted to providing an overview over semiconductors for quantum technologies, silicon carbide material properties, the theoretical and experimental methods employed herein, and finally summarizing the results of the present work.

Acknowledgments

To write a PhD thesis, you have to rely on the help and support of a great deal of people, and I am eternally grateful to everyone who lent a hand along the way. This thesis would not have existed without the late Professor Bengt Svensson, my first main supervisor, who tragically passed away halfway through my PhD. He always had a remarkable level of insight, and took the time to provide invaluable guidance on issues both large and small. However, equal amounts of appreciation go to my second main supervisor, Professor Lasse Vines, who took me on in a turbulent time and helped me assemble the pieces. Your experience, insight, knowledge, passion for science and support have been paramount for completing this work, and I appreciate all your help. Furthermore, I would like to thank Dr. José Coutinho for guidance in how to conduct defect calculations, and Dr. Augustinas Galeckas for performing PL measurements and teaching me many things about luminescence. Thank you both for always taking the time for discussions both scientific and otherwise, and a special thanks to José for being so kind as to host me in Aveiro twice.

Several people have contributed significantly to the scientific work of this thesis. Hussein, I greatly appreciate you taking the time to share your insights into the world of silicon carbide, enthusiasm for science, and for helping me learn DLTS. Thank you to Ymir for all the help with my calculations and answering my endless questions, and for being such a great office mate (the new office is a lot better than the broom closet). Robert, thanks for all the fun discussions about what on earth the defects in silicon carbide are doing. Moreover, thank you to Lasse, Augustinas, José, Ymir and Robert for proof-reading parts of my thesis. My acknowledgments also go to Calliope and Cristian for performing TEM and CL measurements, and to Jon for the help with polishing. I am grateful to all the people at ETH; Judith and Thomas for the muon beamline experiments, Johanna for the device calculations, and Ulrike for both of those and for your advice and encouragement. Thank you also to Andrej, for your ever-present enthusiasm and overall positive attitude to my work. Jawad, I appreciate the help with samples, and I am deeply grateful to Margareta for all her insight, positivity and for conducting the SIMS measurements. I enjoyed the FUNDAMeNT meetings, and would like to thank all the participants for the interesting discussions. Thanks to Vilde and Torbjørn for being my first summer/masters students, and to Oliver, Marius and Gard for carrying on the torch. Thank you especially to Viktor, for performing all my implantations, and also to Halvor, Christoph and Ilia for keeping the cleanroom and E-lab running and helping me whenever I was stuck or had a question. Appreciation is also in order for the administrative staff (Marit, Heine and Kristin) — without you, the LENS group would probably collapse.

Acknowledgments

All my colleagues at LENS deserve a huge thank you for making the work-environment so pleasant, which always helped me get to the office in the morning. I am truly grateful, and deeply appreciate the laughs, discussions, scientific insight and encouragement in tough times. Thank you all for the great cabin trips, after-work beers and lunch table conversations. Special thanks go to the coffee gang for helping me spend my time wisely before starting work in the morning. Thank you especially to Johanna, Kristin, Mads, Sigbjørn, Torunn and Vegard for dinners, coffee breaks, forest runs, hiking trips, shared beers, cabin trips — you made these four years truly great.

Finally, I would like to thank my amazing friends and family for cheering me on, and making my life outside work so enjoyable — it would not be the same without you guys. And of course, my parents Trine and Bernd, and my brother Martin, deserve my eternal gratitude. Mom and dad, you have been my greatest inspiration, always supporting me and believing in me. Martin, you are the best brother anyone could have; you support me in everything, and have perfected making fun of me into an art. Finally, to Matias. Your unshakable belief that I can do anything helps me believe in myself even when nothing seems to work or make sense. I love you.

Thank you all!

• **Marianne Etzelmüller Bathen**

Oslo, November 2020

Abstract

Point defects strongly affect the electrical and optical properties of semiconductors, and are therefore of vast importance for device performance. Over recent years, however, point defects have been shown to possess properties that are highly suitable for applications related to quantum computing, sensing and communication. Single-photon emission and coherent spin manipulation at room temperature have been established for several systems, with the nitrogen-vacancy center in diamond counting among the first solid-state and semiconductor-based quantum platforms.

Despite the long coherence times and established entanglement protocols of diamond-based qubit systems, diamond is only marginally compatible with advanced device fabrication methodology, and methods for integration of quantum emitters with electrically and optically controlled devices remain immature. For this reason, silicon carbide (SiC) has gained the attention of the quantum community, having a wide band gap, low spin-orbit coupling, mature device fabrication, and playing host to several promising quantum emitters of both extrinsic and intrinsic type.

In this work, electrically and optically active point defects in silicon carbide have been studied using a combination of theoretical and experimental methods, with the aim of elucidating the role of different defects in power electronics and quantum technology devices. Hybrid density functional theory (DFT) calculations were employed to establish defect formation energies and charge-state transition levels, explore defect migration, and develop a new framework for studying the effect of electric fields on defect quantum emission. The calculations are correlated to experimental findings, where deep level transient spectroscopy (DLTS) and photo/cathodoluminescence (PL/CL) measurements reveal electrical and optical defect properties, respectively.

The thesis places a particular emphasis on the silicon vacancy (V_{Si}) in SiC, a room temperature single-photon source and qubit candidate exhibiting long spin coherence times. By monitoring V_{Si} emission and comparing to DLTS spectra of proton-irradiated 4H-SiC samples, the $V_{\text{Si}}(-/2-)$ and $V_{\text{Si}}(2-/3-)$ charge-state transitions are assigned to the S-center, enabling electrical control over the V_{Si} charge state. Depositing Schottky barrier diodes (SBDs) on the 4H-SiC sample surface enhances V_{Si} emission by almost an order of magnitude, and sequential biasing of the SBD results in V_{Si} charge-state switching, as detected by monitoring the V1 and V1' zero-phonon lines attributed to the negatively charged V_{Si} at a hexagonal lattice site. The framework of bulk 4H-SiC epitaxial layers is compared to that of a microparticle matrix of predominantly the 6H polytype, with the former ensuring a homogeneous environment for the qubit defect and the latter enabling self-assembly, flexibility and ease of addressability.

Importantly, both external and internal perturbations to the solid-state matrix wherein the V_{Si} is embedded are shown to influence the emitted photon energies, as evidenced by an electric field-induced Stark effect and strain tuning in SiC microparticles. Furthermore, a set of emitters observed in the vicinity of the $V1/V1'$ lines and having consistent subset spacings of 1.45 meV and 1.59 meV are tentatively attributed to vibronic replicas of the V_{Si} emission.

The V_{Si} is unstable at elevated temperatures, and this thesis addresses the topics of V_{Si} conversion and defect migration in p-type, intrinsic and n-type 4H-SiC material at 400 °C and above. Indeed, we find that hydrogen and V_{Si} are likely to form complexes in the case that both species are present and in close proximity. In the absence of H, the V_{Si} may convert to the carbon antisite-vacancy (CAV) pair in p-type material, however, temperatures above 1000 °C are needed in n-type 4H-SiC, where both recombination with interstitials and divacancy formations prove to be more favorable annealing pathways for the V_{Si} . The carbon vacancy (V_{C}) is far more stable than V_{Si} , and by comparing the two defect species using muon spin rotation (μSR) spectroscopy, we establish the μSR technique as a powerful tool for distinguishing different defect relaxation mechanisms and probing near-surface semiconductor defects in a non-destructive and depth-resolved manner. Annealing temperatures above 1200 °C are shown to be needed to induce V_{C} migration, which is further demonstrated to be anisotropic in 4H-SiC, with the V_{C} favoring in-plane atomic hops over the axial migration path. Finally, above temperatures of 2300 °C the lattice atoms themselves become mobile, and secondary ion mass spectrometry (SIMS) is employed to investigate the influence of a carbon cap covering the surface during annealing on self-diffusion of Si and C in 4H-SiC.

List of included papers

Paper I

M. E. Bathen, A. Galeckas, J. Müting, H. M. Ayedh, U. Grossner, J. Coutinho, Y. K. Frodason and L. Vines, “Electrical charge state identification and control for the silicon vacancy in 4H-SiC”, *npj Quantum Information* **5**, 111 (2019). DOI: 10.1038/s41534-019-0227-y.

Paper II

M. E. Bathen, L. Vines and J. Coutinho, “First-principles calculations of Stark shifts of electronic transitions for defects in semiconductors: The Si vacancy in 4H-SiC”. Accepted in *Journal of Physics: Condensed Matter* (2020). DOI: 10.1088/1361-648X/abc804.

Paper III

C. G. Vásquez, M. E. Bathen, A. Galeckas, C. Bazioti, K. M. Johansen, D. Maestre, A. Cremades, Ø. Prytz, A. M. Moe, A. Yu. Kuznetsov and L. Vines, “Strain modulation of Si vacancy quantum emission from SiC micro- and nanoparticles”. Accepted in *Nano Letters* (2020).

Paper IV

M. E. Bathen, A. Galeckas, R. Karsthof, A. Yu. Kuznetsov and L. Vines, “Near-IR emitters related to the silicon vacancy in n-type 4H-SiC”. *In manuscript* (2020).

Paper V

M. E. Bathen, A. Galeckas, J. Coutinho and L. Vines, “Influence of hydrogen implantation on emission from the silicon vacancy in 4H-SiC”, *Journal of Applied Physics Special Topic on Defects in Semiconductors*, **127**, 085701 (2019). DOI: 10.1063/1.5140659.

Paper VI

R. Karsthof, M. E. Bathen, A. Galeckas and L. Vines, “Conversion pathways of primary defects by annealing in proton-irradiated n-type 4H-SiC”. Accepted in

Physical Review B (2020).

Paper VII

J. Woerle, M. E. Bathen, T. Prokscha, A. Galeckas, H. M. Ayedh, L. Vines and U. Grossner, “Muon interaction with negative- U and high spin state defects: Differentiating the C and Si vacancy in 4H-SiC”. Accepted in *Physical Review Applied* (2020).

Paper VIII

M. E. Bathen, H. M. Ayedh, L. Vines, I. Farkas, E. Janzén and B. G. Svensson, “Diffusion of the Carbon Vacancy in a-Cut and c-Cut n-Type 4H-SiC”, *Materials Science Forum* **924**, pp. 200–203 (2018).
DOI: 10.4028/www.scientific.net/MSF.924.200.

Paper IX

M. E. Bathen, J. Coutinho, H. M. Ayedh, J. Ul Hassan, I. Farkas, S. Öberg, Y. K. Frodason, B. G. Svensson and L. Vines, “Anisotropic and plane-selective migration of the carbon vacancy in SiC: Theory and experiment”, *Physical Review B* **100**, 014103 (2019).
DOI: 10.1103/PhysRevB.100.014103.

Paper X

M. E. Bathen, M. Linnarsson, M. Ghezellou, J. Ul Hassan and L. Vines, “Influence of Carbon Cap on Self-Diffusion in Silicon Carbide”, *Crystals* Special Issue on Development and Investigation of SiC and SiC-based devices, **10**, 752 (2020).
DOI: 10.3390/cryst10090752.

Author contributions to appended papers

- Paper I: Contributing to idea, planning of work, DFT calculations, sample preparation, PL measurements, DLTS measurements, analyzing results, discussions, writing manuscript with input from co-authors.
- Paper II: Contributing to idea, planning of work, DFT calculations, analyzing results, discussions, writing manuscript with input from co-authors.
- Paper III: Contributing to idea, planning of work, sample preparation, discussions, contributing to manuscript writing and proof reading.
- Paper IV: Contributing to idea, planning of work, sample preparation, PL measurements, analyzing results, discussions, writing manuscript with input from co-authors.
- Paper V: Contributing to idea, planning of work, DFT calculations, sample preparation, analyzing results, discussions, writing manuscript with input from co-authors.
- Paper VI: Contributing to idea, planning of work, sample preparation, analyzing results, discussions, contributing to manuscript writing and proof reading.
- Paper VII: Contributing to idea, planning of work, sample preparation, partaking in the muon experiments, PL measurements, DLTS measurements, DFT calculations, analyzing results, discussions, contributing to manuscript writing and proof reading.
- Paper VIII: Sample preparation and heat treatments, DLTS measurements, analyzing results, discussions, writing manuscript with input from co-authors.
- Paper IX: Planning of work, DFT calculations, sample preparation and heat treatments, DLTS measurements, analyzing results, discussions, writing manuscript with input from co-authors.
- Paper X: Analyzing results, theory literature review, discussions, writing manuscript with input from co-authors.

Related publications not included in this thesis

1. J. Linder and M. E. Bathen, “Spin caloritronics with superconductors: Enhanced thermoelectric effects, generalized Onsager response-matrix, and thermal spin currents”, *Physical Review B* **93**, 224509 (2016).
2. M. E. Bathen and J. Linder, “Spin Seebeck effect and thermoelectric phenomena in superconducting hybrids with magnetic textures or spin-orbit coupling”, *Scientific Reports* **7**, 41409 (2017).
3. Y. K. Frodason, M. E. Bathen, A. J. Hupfer, L. Vines and C. Persson, “Hydrogen clustering at cation vacancies in covalent semiconductors: Stabilization by self-passivation”. *In manuscript* (2020).
4. V. M. Reinertsen, P. M. Weiser, Y. K. Frodason, M. E. Bathen, L. Vines and K. M. Johansen, “Anisotropic and trap-limited diffusion of hydrogen/deuterium in monoclinic gallium oxide single crystals”. Submitted to *Applied Physics Letters* Special Topic on Ultrawide Bandgap Semiconductors (2020).

Contents

Preface	iii
Acknowledgments	v
Abstract	vii
List of included papers	ix
Related publications not included in this thesis	xiii
Contents	xv
1 Introduction	1
2 Semiconductors as a quantum platform	5
2.1 Quantum technology	6
2.2 Electronic band structure of semiconductors	14
2.3 Defects in semiconductors	16
2.4 Point defects in semiconductors for quantum technology	24
3 Silicon carbide	27
3.1 Growth and crystal structure	27
3.2 Application	28
3.3 Point defects in SiC	29
4 Modeling of point defects in SiC	39
4.1 Introduction to density functional theory	39
4.2 Physical principles of the DFT	41
4.3 Practicalities	44
4.4 Defect calculations	48
4.5 Computational details	56
5 Point defect generation and characterization	61
5.1 Ion implantation	61
5.2 Electrical characterization	63
5.3 Optical characterization	73
5.4 Muon spin rotation spectroscopy	77
6 Summary of results	79
6.1 Experimental details	80
	xv

6.2	Identification and control of the silicon vacancy	81
6.3	Emission tuning	84
6.4	Point defect migration and controlled qubit formation . . .	90
6.5	Probing physics and migration of Si and C vacancies . . .	95
7	Concluding remarks	103
7.1	Suggestions for further work	104
7.2	Outlook	104
	Bibliography	107
	Papers	118
I	Electrical charge state identification and control for the silicon vacancy in 4H-SiC	119
II	First-principles calculations of Stark shifts of electronic transitions for defects in semiconductors: The Si vacancy in 4H-SiC	147
III	Strain modulation of Si vacancy quantum emission from SiC micro- and nanoparticles	157
IV	Near-IR emitters related to the silicon vacancy in n-type 4H-SiC	181
V	Influence of hydrogen implantation on emission from the silicon vacancy in 4H-SiC	193
VI	Conversion pathways of primary defects by annealing in proton-irradiated <i>n</i>-type 4H-SiC	207
VII	Muon interaction with negative-<i>U</i> and high spin state defects: Differentiating the C and Si vacancy in 4H-SiC	223
VIII	Diffusion of the Carbon Vacancy in a-Cut and c-Cut n-Type 4H-SiC	233
IX	Anisotropic and plane-selective migration of the carbon vacancy in SiC: Theory and experiment	239
X	Influence of Carbon Cap on Self-Diffusion in Silicon Carbide	257

Chapter 1

Introduction

As computers dominate more and more aspects of our lives, demands for computing power continue to escalate. Hitherto, computer capability has increased because the number of building blocks (known as transistors) in computers has approximately doubled every two years, following the prediction of Gordon Moore [1]. However, this development is starting to stagnate, as continued transistor size reduction (having been the driving force behind the transistor count increase until now) is no longer viable. Several alternative technologies are being investigated, and a promising avenue to pursue is the field of quantum technology (QT), which aims to capitalize on the captivating properties arising on the nanoscale. Quantum technologies can be roughly grouped into three sub-fields: quantum sensing, communication and computing. Recent years have seen a drastic increase in interest on QT topics, with more than 3000 papers published in the Nature and Science family of journals related to “Quantum”, and close to 4000 in Phys. Rev. Lett. alone. Moreover, the industrial and societal impacts are breathtaking, where the estimated industry value for quantum computing is \$15 billion by 2029. Nevertheless, an improved understanding of the building blocks needed for QT applications is important for the success of such advancements.

Until the birth of quantum physics in the early 20th century, nature was thought to be pre-determined. By knowing all initial variables, you could predict the outcome of any interaction. Fortunately, several revolutionizing breakthroughs revealed the world to be much more complex, uncertain and fascinating. If you restrict your focus to the smallest length scales, and consider the behavior of molecules, atoms and electrons, the predictable Newtonian physics that dominate our everyday lives no longer apply. On the nanoscale, we no longer know exactly where or in what state a particle will be at a certain time, and must instead predict the *probability* for a possible outcome. Quantum technology aims to exploit the principles of quantum physics to fabricate devices with novel capabilities and ways of functioning. Quantum computers, for instance, consist of quantum bits, popularly referred to as qubits. Whereas the classical bit, the transistor, behaves much like a switch and is either ON or OFF, the qubit can be both ON and OFF *at the same time*. We can initialize the qubit to either the ON or OFF state if necessary, but it will usually be found in a *superposition* of the two states (ON and OFF). Moreover, two or more qubits can be *entangled* with one another, meaning that they are described by the same total wavefunction and must be considered as one quantum object. As a result, the combination of quantum superposition and entanglement enables drastically enhanced computing power, and completely novel capabilities, compared to the classical scheme.

Currently, most quantum computers are rather small, comprising of only around 50 qubits, and are fabricated using superconducting materials. The computers are challenging to fabricate and require millikelvin temperatures to operate, foreshadowing challenges in scaling up the technology to a mass-production level. Alternative platforms include trapped ions, quantum dots and point defects in semiconductors [2], where the focus of this thesis will be devoted to the latter technology. Semiconductors are materials with intermediate electrical conductivity, in between that of metals and insulators. They are characterized by a fundamental band gap of energies that are forbidden to the charge carriers, a feature which governs much of the material properties and enables the use of semiconductors for vital technologies such as transistors and solar cells.

By removing an atom from its position in the crystalline semiconductor lattice, placing an atom in between lattice sites, or putting an alien atom at a specific site, we create a *point defect*. Point defects may alter the optical and electrical properties of semiconducting materials, and it is these alterations that we wish to exploit for quantum technology applications. Importantly, quantum computing is not the only feasible application area for such point defect systems, as they can likely be utilized within the fields of quantum communication, cryptography, imaging and sensing as well. The hallmark qubit defect system, with demonstrated single-photon emission, millisecond spin coherence times at room temperature and even defect spin entanglement, is the nitrogen-vacancy (NV) center in diamond [3]. Additionally, the phosphorous impurity in silicon counts among the most coherent quantum objects found in the solid-state [4]. However, where silicon offers ease of integration with existing semiconductor processing, and diamond offers point defects with extremely long spin decoherence times, a compound of the two called silicon carbide (SiC) offers the best of both. Several promising quantum defects have been identified in SiC, but the perhaps most famous one (and the main focal point of this thesis) is the silicon vacancy (V_{Si}), which is formed by removing a silicon atom from the SiC matrix.

Overall, we will follow the silicon vacancy throughout its life cycle, and elucidate how to form, detect, control, augment and transform the V_{Si} defect, by using a combination of theoretical and experimental techniques. Paper I–Paper IV concern formation, identification, tuning and control of V_{Si} defect ensembles, where Paper I introduces the silicon vacancy in 4H-SiC as a quantum contender by establishing control over its carrier trapping mechanisms. Stark and strain effects are used to manipulate emission from the V_{Si} in 4H-SiC epitaxial layers (epi-layers) and 6H-SiC microcrystals in Paper II and Paper III, respectively. In Paper IV, we investigate a new set of emitters that arise in the near-infrared region of photoluminescence spectra from n-type 4H-SiC epi-layers, and discuss possible origins including vibronic replicas of V_{Si} transitions. In Paper V and Paper VI, the thermal response of V_{Si} is considered, and possible routes for V_{Si} disappearance and transformation are discussed. Paper V reveals that the presence of hydrogen provides an alternate route for out-annealing of V_{Si} , into $V_{\text{Si}}\text{-H}$ complexes, in addition to recombination with interstitial defects or encounters with defect sinks. In Paper VI the thermal degree of

freedom is utilized to transform silicon vacancies into the carbon antisite-vacancy pair and divacancy defect complexes, which also exhibit single-photon emission and spin manipulation characteristics with promising capabilities for quantum applications.

Although the Si vacancy disappears in the 400-800 °C temperature range in n-type 4H-SiC material, as discussed in Paper V and Paper VI, the C vacancy (V_C) is much more stable and remains even after V_{Si} has gone. Paper VII-Paper X investigate the differences between the two vacancy types (V_{Si} and V_C), and explore the different modes of motion of the two atomic species in SiC. Paper VII utilizes low energy muon spin rotation spectroscopy (LE- μ -SR) to map the fundamental differences between C and Si vacancies in 4H-SiC, where slight differences in chemical composition of the local environment lead to strong geometric distortion and short spin lifetimes for V_C , in contrast to the symmetry-conservation, high spin ground states and qubit capabilities shown for V_{Si} . Finally, we reveal the annealing behavior of carbon and silicon vacancies in 4H-SiC, where Paper VIII demonstrates the anisotropic nature of V_C diffusion, Paper IX quantifies and explains the experimental observations regarding V_C migration, and Paper X revisits the mechanism for self-diffusion of Si and C in SiC.

The topic and methodology is introduced in six chapters. First, in Chapter 2, we review relevant quantum technologies from the perspective of point defects in semiconductors ultimately being used as a quantum platform, and discuss semiconductors as a potential quantum host. Silicon carbide is introduced and the available intrinsic point defects therein are discussed in Chapter 3. The theoretical and experimental methods employed in the present work are summarized in Chapters 4 and 5, respectively. A summary of results is provided in Chapter 6, with concluding remarks and outlook following in Chapter 7.

Chapter 2

Semiconductors as a quantum platform

The purpose of this chapter is to provide a glance into the rich world of quantum technology, and illuminate the potential future role of semiconductors in this context. The chapter is not intended as an exhaustive review, and instead contains brief introductions to the concepts most relevant for the present work. First, the three major quantum technologies (communication, sensing and computing) are considered, to outline the properties required of an ideal quantum system. Thereafter follows a generalized introduction to semiconductor physics and the concept of defects is presented, and finally we assemble the pieces to discuss why point defects in semiconductors form a competitive quantum platform.

Before we start, there are a few principles of quantum physics that should be familiar to the reader (see, e.g., Ref. [5] for further details):

- The Heisenberg *uncertainty principle*, $\Delta x \Delta p \geq \hbar/2$, refers to the fact that we cannot accurately predict the position and momentum of a particle at the same time, and must instead compute the *probability* for the particle to be in a certain state. A conceptual illustration of the probability density for where to find an electron close to the nucleus can be found in Figure 2.1(a), with darker color signifying higher probability.
- Quantum states are often treated like waves, and each quantum state can thus be expressed as a sum, or *superposition*, of two or more distinct states. The concept of superposition is illustrated in Figure 2.1(b).
- The act of measuring a superposition of two quantum states forces the system into one of the two states, meaning that the act of measuring destroys the quantum nature of the object.
- A phenomenon called quantum *entanglement* occurs when a pair or group of particles are prepared in such a way that the quantum state of each particle cannot be described as independent of the state of the other particle(s). If you measure the state of one of two entangled particles, you can surmise the state of the other. A schematic of entanglement is included in Figure 2.1(c).
- Quantum *coherence* and *decoherence* arise from the wave-like properties of quantum states, and are closely related to superposition and entanglement. If two waves coherently interfere, a superposition of states which retains a phase relation is created. Loss of coherence is then termed decoherence.

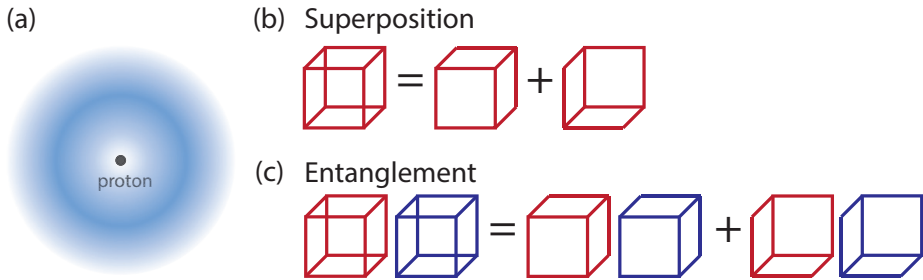


Figure 2.1: (a) Conceptual illustration of the electron cloud surrounding a nucleus, highlighting the differences in probability density over space. Panels (b) and (c) showcase the concepts of superposition and entanglement, respectively.

Coherence must be preserved in order to perform quantum computing operations, and long coherence times require the system to be isolated from its environment. However, this induces a trade-off; a system which is perfectly isolated cannot be manipulated, but a non-isolated system suffers from decoherence. Herein, we will refer to the *coherence time* as the time before decoherence or, in other words, the time before the quantum properties of a qubit system *leak away* into the environment.

2.1 Quantum technology

The term *quantum technology* (QT) refers to practical applications and devices that are engineered with the principles of quantum physics as a foundation, as opposed to devices based on the principles of classical mechanics. Herein, three main sub-categories of QT will be discussed: quantum communication, quantum sensing and quantum computing [6], although they are undoubtedly interconnected. Each technology will be considered briefly, as the main focus of this thesis concerns improving the fundamental building blocks for the final devices. Thus, we will devote our attention to quantum systems with discrete energy levels which can be initialized, controlled and entangled with other systems. Building blocks for quantum computers are called quantum bits or *qubits* and should be available in a superposition of two or more quantum states. A discussion on possible physical implementation schemes will be provided after the technologies are introduced, as any specific quantum system may prove suitable for more than one application area within QT.

2.1.1 Quantum communication

In essence, the term quantum communication refers to the transfer of quantum states over a distance. One can envision *flying qubits* as information being passed between two locations, and the simplest implementation of flying qubits is photons that are either individual or entangled [6, 7]. A popular concept when

discussing quantum communication is that of security: even though someone may intercept the information you are sending or receiving, they cannot interpret it. Today, information that is transferred is encrypted, and most security protocols are constructed from complex codes. For instance, if two people (commonly called Alice and Bob) want to securely communicate, they may encrypt the information they wish to send, and exchange two keys: one public and one private. Everyone can read the public key, but the private key is a long sequence of characters known to Alice and Bob only, and which a spectator should not be able to guess [8]. The security of this scheme relies on the fact that our computer technology is incapable of factoring large numbers within a reasonable amount of time, or, in other words, crack the code and guess the private key. However, as we will see below, a quantum computer could easily deduce the private key and thus render much of current cryptography obsolete, exposing the need for a quantum solution.

Imagine that Alice and Bob are passing information of a quantum nature, e.g., in the form as a qubit, as opposed to classical bits (zeros and ones). The information is encoded in a *superposition* of two quantum states, meaning that if intercepted by an outsider, the process of measuring the state will destroy it. Thus, an eavesdropper (let us call her Eve) has alerted Alice and Bob of her presence merely by attempting to read the information. Alice can therefore send Bob a key by means of qubits encoded in, e.g., the polarization of individual photons, and if the photon states are unperturbed when they are received by Bob, they can be used as a key to encode further information [8]. Alternatively, Eve could intercept the flying qubits and send them on to Bob while keeping a copy for herself. However, quantum states cannot be copied as per the no-cloning theorem [8], which prevents eavesdropping and further strengthens the claim that *quantum key distribution* (QKD), which was just described, is secure. Thus, quantum cryptography involves the use of quantum random number generators to make secret keys, and quantum key distribution to pass them around [6]. It should be noted that the security of QKD has been extensively debated, and relies on the fact that Alice and Bob initially share a short common secret which is later grown, making quantum key *expansion* a more exact term for QKD [7, 8].

Devices for quantum key distribution via photons have been demonstrated, but distance is the main issue, with laboratory limitations still being in the 300 km range. The main reason for this limitation is photon loss in optical fiber cables, as classical repeaters cannot be used to enhance quantum information [6]. Thus, it is important that the source for the optical information generates photons that are compatible with telecommunication wavelengths, in the infrared (IR) or near-infrared (NIR) range, provided that suitable detectors are available.

A more sophisticated approach towards quantum cryptography involves exploiting not only superposition, but also the even stranger quantum feature of *entanglement*, as polarization is short-lived in the optical fiber cables used to transmit the photons. Now, Alice and Bob each have a system of qubits that are entangled with one another, for instance, Alice and Bob each hold one of a pair of entangled photons that are passed through optical fiber cables. Alice encodes her

message and the quantum state is teleported to Bob, who can read it securely [7]. Proof-of-concept measurements have been conducted but, unfortunately, both the generation of large numbers of entangled photons and their transmission over large distances remain a challenge. Taking the idea of spatially separated but entangled emitters a step further, the technology required for quantum key distribution via teleportation also enables the fabrication of larger-scale quantum networks [9], and potentially even a secure quantum internet [6]. To this end, quantum relays which teleport entanglement from node to node, and quantum repeaters consisting of both quantum relays and quantum memories are needed [7]. Quantum repeaters would further enhance the security of QKD, by ensuring signal strength throughout the photon path and thus preventing an eavesdropper from copying the flying qubits sent by Alice, but this technology has yet to mature.

2.1.2 Quantum sensing

Quantum systems are inherently volatile and prone to *decoherence*, and thus susceptible to perturbations of the surrounding environment. Incidentally, quantum systems commonly exist on the nanoscale, and often exhibit detectable responses to extremely small and local changes to their surroundings. The field of quantum sensing seeks to exploit this quantum sensitivity to detect variations in physical quantities such as temperature and electromagnetic fields, and thereby fabricate more precise measurement instruments for use in sensing, metrology and imaging [6, 10]. What separates the quantum sensor from its classical counterpart is the fact that the probe is prepared in a certain quantum state, and we may utilize either the isolated quantum object, coherence of a quantum superposition or quantum entanglement to detect changes in physical quantities [10]. The precision of a quantum sensor can (ideally) scale as the number of particles in the system, N , known as the Heisenberg limit. Comparatively, the precision of a classical sensor can only approach \sqrt{N} [6].

Physical implementation of quantum sensors essentially requires a system that exhibits discrete energy levels, has the potential for controlled initialization and state read-out, coherent manipulation of the sensor by time-dependent fields is available, and finally the system must interact with the physical quantity to be measured via a coupling parameter [10]. Hitherto, the main applications of quantum sensing that have been universally adapted include atomic clocks, magnetic field sensing and nanoscale imaging, but further advancements are expected as quantum technologies progress [10].

Quantum sensing presents an interesting dilemma, as one seeks to exploit the instabilities in the quantum nature of the sensor system. Because the sensor responds rapidly to local fluctuations in the environment we may gain valuable and precise local information. However, at the same time, a quantum system which interacts strongly with the environment will be subject to rapid decoherence [10]. To maximize sensitivity, one should tailor the sensor specifically to the application, by picking a sensor system which couples strongly to the

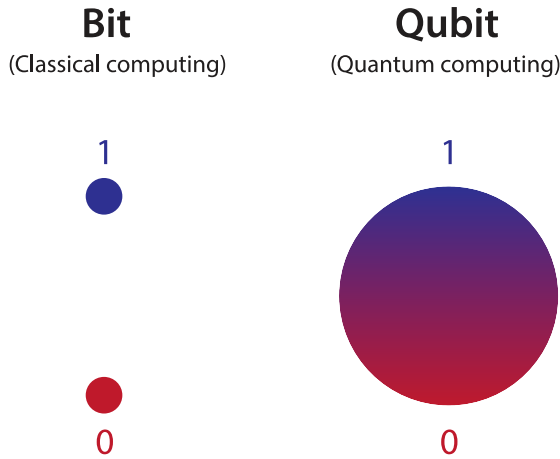


Figure 2.2: Conceptual illustration of the two-level (a) classical bit having the states 0 (OFF) and 1 (ON), and (b) qubit that can inhabit any superposition of the states 0 and 1.

physical quantity to be measured (e.g., a magnetic field) while retaining a long coherence time.

2.1.3 Quantum computing

Finally, we turn to quantum computing, perhaps the most alluring of the quantum technologies. Conventional computer technology has benefited from steadily enhanced computing power over the last 50 years, by continuously increasing the number of transistors comprising a computer's processor. By decreasing the transistor size and thereby increasing the potential transistor count, computers have become more powerful. In accordance with Moore's prediction [1], the amount of transistors on integrated circuit chips has approximately doubled every two years. However, this development is sustainable no longer, as prototype transistors are expected to have critical dimensions approaching 3 nm already in 2021 [11]. Other alternatives for improving computing capabilities must be explored, and quantum computers present an enticing solution.

Quantum computing, which can be described as the ultimate goal of quantum engineering, will herein be compared to what is referred to as *classical* computing. Classical computer logic is based on miniaturized switches (transistors) which are either OFF or ON, where the transistor state can be controlled by means of electrical signals. Where the classical bit can only inhabit the states 0 (OFF) or 1 (ON), the quantum bit (or qubit) can exist in a superposition of 0 and 1. An illustration of the difference between classical bits and qubits can be found in Figure 2.2. Physically, a host of potential qubit implementations exist, but the most promising remain the polarization of photons, the spin of atoms, nuclei or quantum dots, currents running through superconducting

Josephson junctions and the spin or charge of electrons. By combining the quantum principles of superposition and entanglement, computational power far surpassing that of conventional computers can (theoretically) be achieved. In fact, Google very recently demonstrated a drastic speed-up compared to conventional supercomputers when running a random number generator algorithm on a 53-qubit superconductor-based quantum processor [12], prompting further investigation into quantum computer systems.

The art of performing a quantum computation can be described as a controlled quantum evolution, and the dominant quantum computer (QC) architecture relies on a set of universal quantum gates that perform unitary transformations on sets of qubits [2, 13]. An ideal qubit system can facilitate both single-qubit and two-qubit gates (e.g., XOR or cNOT), but the latter requires the presence of two-qubit interactions. Interactions between qubits are, perhaps, the greatest challenge to surmount before quantum computers can be constructed, as they are not always possible to establish, or in some cases may be difficult to switch off at will [13]. However, although the *universal quantum computer* is envisioned to rely on quantum gates (in analogy with classical computers), they are not absolutely necessary [2]. Cluster-state or one-way quantum computers [14] utilize non-universal quantum gates to form the cluster quantum state, and computations are performed by measuring the many-body wavefunction in different ways. Adiabatic quantum computers [15] do not rely on gates at all, instead they employ the adiabatic theorem stating that if a quantum system with discrete energy eigenvalues is subjected to slowly varying external conditions, the system will remain in its instantaneous eigenstate and adapt its functional form [16]. In adiabatic quantum computation, the qubit system is initialized to some state and the answer to the problem is defined to be the ground state of the total wavefunction (this is sometimes referred to as quantum annealing). By controlling the interactions, the complex system of qubits can be adiabatically evolved to the ground state. Herein, we will mainly focus on qubit systems that allow gate-based quantum logic operations.

The speed-up resulting from using quantum computers compared to conventional processors can be attributed to both the superposition of states in each qubit, which yield a drastic increase in degrees of freedom compared to the classical two-level transistors, and the multi-qubit entanglement protocols. Quantum computers are famously known for drastically outperforming (in theory) classical ones when it comes to factoring large numbers, which (as we have seen) is highly relevant for cryptography protocols. This was demonstrated by Shor's algorithm [17], which promises an exponential speed-up on a quantum computer compared to the classical case. Moreover, searching through large data sets may be sped-up quadratically by the arrival of QC, as shown by Grover's algorithm [18]. However, for certain tasks of a more sequential nature, no significant speed-up is expected from exchanging classical computers with their quantum counterparts. In other words, one does not anticipate QC to completely replace modern computer technology anytime soon. Importantly, quantum computers promise not only to speed-up certain well-known tasks, but also capabilities far beyond those currently available. For instance, a quantum computer is ideally

suited for solving extremely complex problems with many variables. Potential application areas include governing traffic and predicting the weather, aiding machine learning technologies, predicting the finance market and (perhaps most relevant to the present work) solving complex quantum chemistry problems and accurately simulating many-body quantum systems [19].

Several challenges must be surmounted to ensure the success of quantum computing advancements, including the task of controlling a complex many-qubit system. Importantly, the volatility of quantum states causes decoherence and other quantum noise, which prevent error-free quantum state manipulation. Hence, decoherence must be mitigated using techniques referred to as *quantum error correction* (QEC), and preliminary QEC protocols are already available for a number of different systems [20]. Below, a short summary of the requirements for physical implementation of quantum computing is provided, followed by a discussion on how a specific qubit design can be performed within that set of rules. The aim of the present work involves gaining a deeper understanding of the building blocks for quantum technology, and the following sections provide the framework these qubit systems should fall within.

2.1.4 Quantum computing requirements

Decoherence is a major obstacle for the realization of fault-tolerant quantum computers. As quantum states are inherently unstable, and may easily interact with the environment, qubit systems should be essentially isolated from their surroundings on a timescale which is longer than that required to perform an operation. At the same time, intentional initialization, control and read-out of the qubit state must be available. To fabricate a fault-tolerant quantum computer, assuming a logic-gate based architecture, the physical qubit system should (for gate-based QC) [13]

1. be scalable
2. have qubits that can be entangled
3. have reliable initialization protocols to a standard state
4. have coherence times much longer than the gate operation time
5. have a set of universal quantum gates to control the quantum evolution
6. have a reliable read-out mechanism for measuring the qubit states.

Although the DiVincenzo criteria above [13] were later rephrased into three more general criteria by Ladd *et al.* [2], of scalability, universal logic and correctability, the original criteria concisely phrase what is physically required from the individual qubits used to build a complete logic-gate based QC. To summarize, based on the ideas of Refs. [2, 13, 21], the qubit system we are searching for

- is a two-level quantum system with discrete energy levels

2. Semiconductors as a quantum platform

- is essentially isolated from its surrounding environment, having quantum levels with decoherence times longer than that needed to perform computation operations
- has an optical initialization cycle
- has a reliable read-out mechanism, for instance by luminescence
- has the potential for error-correction protocols
- is scalable, i.e., exists in a readily available material system, preferably with the potential for large-scale fabrication and electronic and photonic device integration.

Combining the quantum computer with the need to communicate both internally and with other devices, the ideal QC platform also facilitates the translation of stationary qubit states into flying qubits, and the transmission of the flying qubits (for instance photons traveling through optical fiber cables or electrons traveling through a solid) between spatial locations [13].

2.1.5 Available quantum platforms

The physical implementation of a two-level qubit system is possible using quantities such as the photon polarization, the spin of electrons, nuclei or atoms, or the superconducting charge, phase and flux. Below, a selection of quantum platforms that are both available and promising are reviewed.

Superconducting Josephson junctions The characteristic feature of superconducting materials is that at low temperatures, i.e., below a critical value, electrons form Cooper pairs through an effective electron-electron attraction, resulting in zero-loss motion through the material [22]. This intrinsic coherence can be exploited by constructing microwave circuits based on Josephson tunnel junctions, which are loops of two superconducting elements separated by an insulator. Josephson junction-based devices facilitate superconducting qubits based on the charge, flux or phase of the Cooper pair current [2, 6, 23]. The main benefit of superconducting qubits is that they can be controlled electrically while retaining quantum coherence, which would not be possible for non-superconducting electrical circuits. Moreover, both the logic gate-based and adiabatic QC architectures are realizable using a superconductor platform [2]. Entanglement of neighboring superconducting qubits is available via inductive or capacitive proximity coupling, and coupling of distant qubits (which is necessary for large-scale architectures) can be realized via microwave photon pulses [2]. Currently, superconducting qubits constitute the dominant QC technology, and are employed by Google, IBM and D-Wave systems, among others. However, although a quantum speed-up was recently demonstrated for Google's 53-qubit computer [12], a practical quantum advantage has yet to be demonstrated.

Importantly, whether the superconducting platform is capable of satisfying the enormous demand for quantum computing power remains to be seen. The

current devices are associated with relatively short coherence times in the μs range, and larger QC architectures will likely place stricter demands on the qubit stability. Moreover, mK temperatures are currently required to perform quantum computation, increasing the cost of QC systems. To improve connectivity between qubits and facilitate quantum error correction and fault-tolerant quantum computing, we search for qubit systems which promise longer coherence times, better qubit inter-connectivity and a greater potential for scaling.

Single photons The polarization state of single photons traveling through optical fiber cables suffers far less decoherence than solid-state systems, and one-qubit gates can easily be implemented by rotations of the photon polarization [2]. However, photon-photon entanglement and multi-qubit control remain elusive. Schemes for photon-based cluster-state quantum computing do exist, but having high-efficiency single-photon sources and detectors are vital. Regardless, any progress within photonic-based quantum computing will likely benefit the fields of quantum communication, sensing and inter-connectivity within quantum computers having other building blocks equally.

Trapped atoms and ions The hallmark of isolation in matter-based systems is currently the isolated atom platform, where each qubit is based on internal energy levels of a trapped ion or atom. Lattices of ions can be confined in free space by electric fields, or arrays of atoms by laser beams in an optical lattice [2], enabling entanglement via laser-induced spin coupling and initialization via optical pumping. However, scaling to large numbers of ions is challenging due to the need to cool and trap the atoms or ions, the control of a large and complex system, and because cooling becomes inefficient for larger systems which may increase decoherence.

Nuclear magnetic resonance Nuclear spins embedded in molecules, liquid solutions or solid-state systems make excellent gyroscopes and retain long spin coherence times. Qubit manipulation is available via radio-frequency pulses of electromagnetic fields, facilitating one-qubit gates. However, although coherence times are long, the time scales for initialization and control protocols are of comparable sizes, resulting in inefficient gate operation. Solid-state nuclear magnetic resonance does promise enhanced gate efficiencies compared to the liquid and molecular cases, by using nuclear dipole-dipole couplings or the aid of electrons, but an alternative and more promising architecture relies on using nuclear spins for memory applications and employing electron spins for the logic gate operations.

Quantum dots Quantum dots (QDs) are essentially artificial atoms confined in a solid-state host, providing similar coherence capabilities as trapped ions or atoms while evading the cumbersome task of cooling and confining them in free space. A quantum dot can be fabricated in several ways, but overall we consider

a semiconductor nanostructure which traps electrons or holes in a potential with discrete energy levels, similar to that of an atom. The spin degree of freedom exhibits long coherence times, which is seen as promising for QC applications [6]. Importantly, a major source of decoherence for all semiconductor-based quantum technologies is nuclear spins, but potential solutions include isotope purification and dynamic decoupling of nuclear spin noise [2].

Typically, the term quantum dots refers to either systems that are defined lithographically using metallic gates, or nanoparticles that self-assemble during growth. Unfortunately, quantum computers based on the former would require mK operating temperatures, like the superconductor platform, removing much of the advantage. However, liquid-He temperatures would suffice for the nanoparticle QDs [2], which presents a distinct advantage over the superconducting technologies.

Optical transitions in QDs are restricted to discrete energies. Therefore, quantum dots offer the potential for fast voltage control combined with optical initialization and read-out. However, for electrostatically defined quantum dots the exchange interaction is short-range just like for trapped ions, presenting a challenge for large-scale entanglement. Photonic connections could remedy the issue, but reliable two-qubit gates remain the predominant obstacle to overcome [6]. Self-assembled quantum dots, on the other hand, couple strongly to photons, thereby providing photonic connectivity. However, self-assembled nanoparticles form randomly leading to a variety of shapes and sizes, and optical absorption and emission energies will therefore fall into a larger range than desired [2]. A possible solution to ensuring greater optical homogeneity, while retaining the concept and beneficial properties of the artificial atom, is to reduce the system size even further while embedding the qubit into a solid-state matrix: we therefore turn to bulk semiconductors, and point defects situated therein.

Point defects in semiconductors Point defects in semiconductors have comparable properties to QDs in terms of, e.g., discrete optical transitions and coherent spin states that are susceptible to external manipulation. However, point defects are minute changes to the semiconductor lattice (e.g., impurities, vacancies and interstitials), and can therefore be challenging to isolate from the surrounding matrix. On the other hand, the solid-state semiconductor host allows for a degree of isolation that ensures both longer coherence times and greater optical homogeneity compared to QD systems. The remainder of this chapter will be devoted to providing background for why point defects in semiconductors can function as suitable building blocks for quantum technology applications.

2.2 Electronic band structure of semiconductors

Before the intricacies of defect physics can be discussed, the framework of the semiconductor matrix must be in place. Isolated atoms are characterized by discrete energy levels that electrons are allowed to inhabit, where each level can encompass two electrons, one of spin up and one of spin down (in accordance

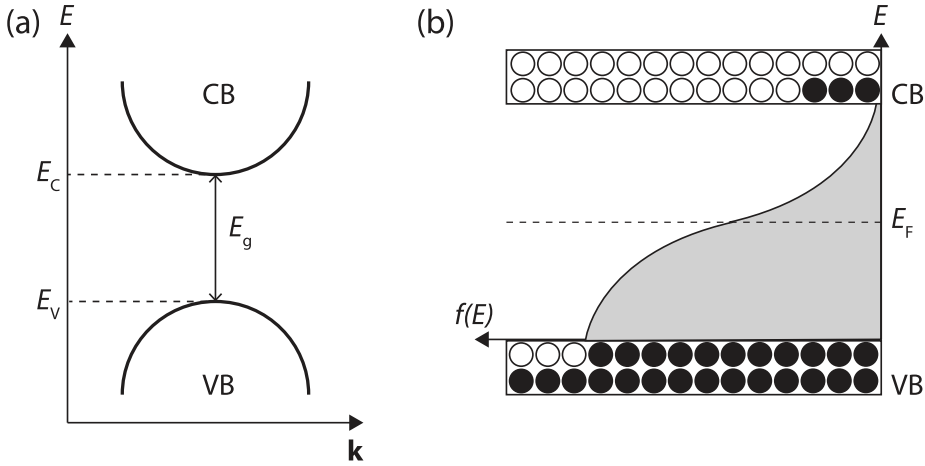


Figure 2.3: Schematic illustration of (a) semiconductor energy bands versus the wavevector \mathbf{k} , and (b) the Fermi-Dirac distribution $f(E)$ for a semiconductor at room temperature. Filled circles signify electrons and empty circles represent holes.

with the Pauli exclusion principle for fermions). In solid materials, on the other hand, the large density of particles being bonded together transforms the discrete energy levels of individual atoms into a set of quasi-continuous energy bands for the solid. These energy bands depend on energy (E) and momentum (\mathbf{k}), and the band structure is material-specific.

The occupation of energy bands by electrons determines many important material properties. The highest energy band that is occupied by electrons at 0 K is termed the valence band (VB), while the lowest unoccupied band is termed the conduction band (CB). Semiconductor materials are usually classified by their room temperature electrical resistivity and *band gap*, which is the energy gap of forbidden energy levels between the valence band maximum and conduction band minimum. Figure 2.3(a) contains a schematic diagram of energy bands versus the wavevector \mathbf{k} , highlighting the valence band, conduction band, valence band edge (E_V), conduction band edge (E_C) and *direct* band gap of energy E_g .

At 0 K, the valence band of a semiconductor will be filled with electrons while the conduction band will be empty. A full (or empty) band cannot conduct electricity, meaning that the band occupation must be manipulated for a current to run through a semiconductor. One solution is excitation of electrons from the VB to CB via temperature, as exemplified by the schematic in Figure 2.3(b). At low temperatures, all electrons would be confined to the valence band, but as the temperature increases, some electrons gain enough energy to traverse the forbidden gap and reach the conduction band. When an electron is excited to the CB a positively charged hole remains in the VB, forming an electron-hole pair (EHP).

The probability for a state to be occupied by an electron is given by the

2. Semiconductors as a quantum platform

Fermi-Dirac distribution,

$$f(E) = \frac{1}{\exp\left(\frac{E-E_F}{k_B T}\right) + 1}, \quad (2.1)$$

where k_B is the Boltzmann constant, T the temperature, E the energy and E_F the Fermi level or chemical potential of the electrons. At $T = 0$ K, all energy levels below E_F are occupied by electrons while those above are empty. At higher temperatures the electrons become able to gain higher-lying states, as illustrated by the conceptual Fermi-Dirac distribution in Fig. 2.3(b). In the case that $|E - E_F| \gg k_B T$, $f(E)$ can be approximated by the Boltzmann distribution,

$$f(E) \sim \exp\left(\frac{E - E_F}{k_B T}\right). \quad (2.2)$$

2.3 Defects in semiconductors

Semiconductors offer control over which energy states are, and are not, allowed. Hence, through clever engineering, one can fabricate a stable and isolated two-level system using the discrete energy states that are induced by a *defect* within the band gap. First, however, we will introduce the concept of a defect in a crystalline material and discuss the effect a defect may have on the electro-optical properties of the semiconductor material.

2.3.1 Defect classification

Defects break the periodicity of an otherwise perfect crystalline lattice, and are present in all real materials. The primary importance of semiconductor defects lies in their perennial and unavoidable presence in semiconductors, and their impact on the electrical and optical properties of the material. *Defect* is a broad term and encompasses a host of different phenomena within semiconductor physics. Herein, we will discuss crystalline semiconductor materials (as opposed to amorphous materials). Crystalline defects can be extended in, e.g., three (*volume defects*) or two (*planar defects*) dimensions, which comprise of, e.g., stacking faults or voids/inclusions, respectively. In one dimension (*line defects*) we can find micropipes and dislocations, while the zero-dimensional defects that will be the topic of the remaining chapters are called *point defects*. Point defects are typically vacancies, where an atom is missing from its lattice configuration, interstitially placed atoms between lattice sites, or an atom substituting a host atom (substitutional). Substitutional defects can be impurities or antisites in the case of compound semiconductors. If the impurity is intentionally introduced, the process is termed *doping*, and enhances either the n-type (excess of electrons) or p-type (excess of holes) conductivity of the material. Figure 2.4 contains a schematic illustration of point defects of vacancy (e.g., Si vacancy or V_{Si}), interstitial (e.g., C interstitial or C_i), antisite (e.g., C on Si antisite or C_{Si}) and impurity types for the case of 4H-SiC.

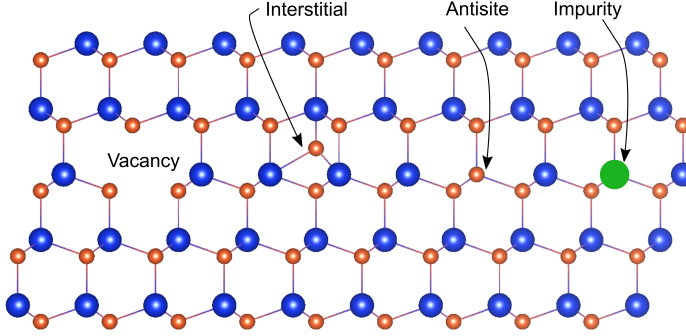


Figure 2.4: Illustration of different point defect types based on the 4H-SiC crystal structure (Si is blue, C orange).

2.3.2 Doping

Point defects of both intrinsic and impurity type may introduce energy levels for carrier capture and emission within the fundamental gap, either close to (within ~ 0.2 eV) the band edges (shallow defects) or near mid-gap (deep level defects). Shallow defects can be described as hydrogen-like, and are often intentionally introduced. In that case they are called *dopants* (as discussed above), and promote excess electrons or holes to the CB or VB. Intrinsic semiconductors are free of dopants and have an equal number of electrons and holes, i.e., the hole and electron concentrations are equal ($n_i = p_i$).

If the dopant atom supplies an additional valence electron compared to the intrinsic semiconductor elements it is called a donor (of concentration N_D) and the doping is n-type, while the opposite case results in an acceptor (of concentration N_A) and the doping is p-type. If the donor or acceptor is electrically active, it introduces an energy level within the semiconductor band gap and close to the conduction or valence band edge, respectively. If sufficient energy is supplied (for instance thermally), the electron or hole from the impurity atom is contributed to the semiconductor. This shifts the Fermi level from mid-gap (intrinsic semiconductor at 0 K) and towards one of the bands, according to

$$E_F = E_{C(V)} - (+)k_B T \ln \left(\frac{N_{C(V)}}{N_{D(A)}} \right) \quad (2.3)$$

for n-type (p-type) semiconductor doping. Here, $N_{C(V)}$ denotes the effective density of states in the conduction (valence) band, and is given by

$$N_{C(V)} = 2 \left(\frac{2\pi m_{n(p)}^* k_B T}{h^2} \right)^{3/2}, \quad (2.4)$$

2. Semiconductors as a quantum platform

where $m_{n(p)}^*$ is the effective mass of electrons (holes) and \hbar is the Planck constant. Note that the effective mass of carriers is determined from the curvature of the $E(\mathbf{k})$ energy bands by

$$\frac{1}{m_{n(p)}^*} = +(-) \frac{1}{\hbar^2} \frac{\partial^2 E}{\partial \mathbf{k}^2}, \quad (2.5)$$

with $\hbar = \hbar/(2\pi)$.

2.3.3 Defect states and charge carriers

Charge carriers (electrons or holes) bound to shallow defects interact strongly with the band edges, and their wavefunctions are therefore *delocalized* with respect to position in the lattice. Deep level defects, on the other hand, cannot be described as hydrogen-like and are instead associated with highly *localized* electron wavefunctions. Deep levels may originate from, e.g., impurities or dangling bonds, and their highly localized nature may ensure the isolation and coherence needed for quantum technology applications. For that reason, deep level defects will constitute the main topic throughout this work and are therefore awarded the most attention in this thesis.

Deep level defects often interact with the semiconductor charge carriers, and can therefore have a significant and potentially detrimental impact on the electro-optical properties of semiconductor devices. For instance, deep level defects may either capture and trap carriers from the bands, or act as a center for electron-hole recombination, in either case potentially hindering the doping process and reducing the net carrier concentration compared to the desired value. The energy levels (E_t) introduced by deep defects within the semiconductor band gap are termed *ionization* or *charge-state transition* levels, and signify the transition between the charge states q and $q-1$, often termed $D(q/q-1)$ where D is some point defect.

Charge-state transition levels for point defects are typically depicted graphically in one of two different ways, as illustrated for a defect D in Figure 2.5. While Fig. 2.5(a) only depicts the positioning of the $D(q/q-1)$ states within the gap, Fig. 2.5(b) contains a *formation energy diagram* which simultaneously displays the transition levels and the relative stability of the different defect charge states depending on the Fermi level. Comparing the formation energies of several defects in the same diagram also provides information on the relative stability of different species and defect complexes, depending on the doping conditions (i.e., the Fermi level). The formation energy of a defect can be extracted experimentally by considering the defect concentration after heat treatments at thermal equilibrium, where the internal free energy of formation is given by the change in Gibb's free energy $\Delta G = \Delta H - T\Delta S$, where H is the enthalpy and S the entropy of the system. Eventually, the equilibrium concentration of the defect D becomes

$$[D] = N_{\text{sites}} \exp\left(\frac{\Delta S_{\text{vib}}}{k_B}\right) \exp\left(-\frac{\Delta H_{\text{form}}}{k_B T}\right), \quad (2.6)$$

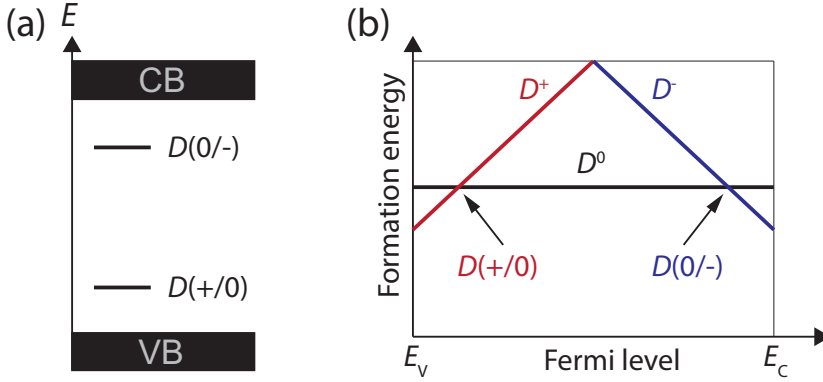


Figure 2.5: Schematic of (a) charge-state transition levels of a defect D , and (b) illustrative formation energy diagram for the same defect.

where N_{sites} refers to the number of possible defect sites and S_{vib} is the vibrational entropy, here assumed to dominate over other entropy terms. However, in this case the formation energy is extracted only for the specific Fermi level that was relevant for the annealing experiment. Alternatively, the formation energy diagram can be computed by theoretical means and for all relevant Fermi levels, as depicted in Fig. 2.5(b) (to be discussed in Section 4.4.2).

2.3.4 Carrier capture kinetics

The charge-state transitions above essentially involve the defect exchanging charge carriers (electrons or holes) with the band edges. Let us now consider the kinetics of carrier capture by, and emission from, a deep defect level situated at an energy E_t below E_C . Imagine that E_t is situated close to mid-gap, and that the probabilities of interchanging a carrier with either band edge are similar. The following discussion applies also to electron traps (E_t is close to E_C) and hole traps (E_t is close to E_v), but in the former case the carrier capture and emission rates for electrons are much larger than those for holes (and vice versa for the latter).

The interchange of carriers by a defect with the band edges is characterized by the defect capture and emission rates for electrons and holes, $c_{n,p}$ and $e_{n,p}$, respectively, and is schematically illustrated in Figure 2.6. The ratio between electron and hole capture determines whether the deep level acts as a trap ($c_n \gg c_p$ or vice versa) or a recombination center ($c_n \sim c_p$). In the former case, E_t is usually located closer to one of the band edges, while for a recombination center E_t typically resides near mid-gap (as exemplified in Fig. 2.6). The capture and emission rates for charge carriers are given by

$$c_{n(p)} = \sigma_{n,p} v_{\text{th},n(p)} n(p) \quad (2.7)$$

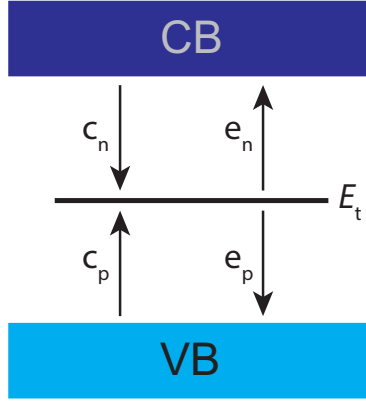


Figure 2.6: Schematic of carrier capture (characterized by $c_{n,p}$) and emission (characterized by $e_{n,p}$) by a deep level defect introducing an energy level E_t within the semiconductor band gap.

and

$$e_{n(p)} = c_{n(p)} \exp\left(-\frac{E_F - E_t}{k_B T}\right) = \sigma_{n(p)} v_{th,n(p)} N_{C(V)} \exp\left(-\frac{E_t - E_{C(V)}}{k_B T}\right), \quad (2.8)$$

where $\sigma_{n(p)}$ is the electron (hole) capture cross-section, $v_{th,n(p)}$ is the thermal velocity of electrons (holes) and n (p) denotes the carrier concentration in the conduction (valence) band. Hence, the carrier emission rate is strongly dependent on temperature, according to (for an electron trap)

$$e_n = \sigma_n \gamma T^2 \exp\left(-\frac{E_C - E_t}{k_B T}\right), \quad (2.9)$$

where γ encompasses the constants that do not rely on temperature and derive from $v_{th,n}$ and N_C .

Note that if a carrier is thermally excited from a deep level and emitted to the VB or CB, the activation energy E_t should be replaced by the change in Gibb's free energy, $\Delta G = \Delta H - T\Delta S$, which is given in terms of the enthalpy (H), temperature (T) and entropy (S). The entropy term can be incorporated by replacing $\sigma_{n(p)}$ by an apparent capture cross-section term, $\sigma_{app,n(p)} = \sigma_{n(p)} \exp(\Delta S/k_B)$, which differs from the real capture cross-section in the cases where the entropy term is not negligible.

2.3.5 Thermodynamic vs. optical defect transitions

Herein, we will discuss two types of defect transitions: thermodynamic and optical. The former transition type was introduced in the previous two sections, and is referred to herein as a thermodynamic charge transition level. Optical transitions, on the other hand, are induced by excitation via, e.g., laser light

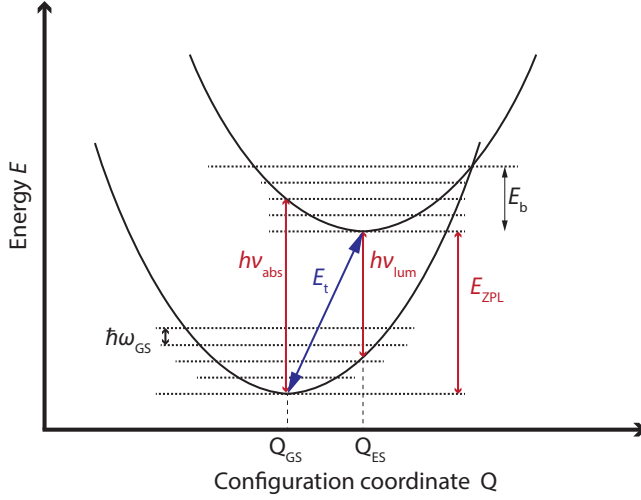


Figure 2.7: Conceptual configuration coordinate (CC) diagram for a defect-related transition. Based on Ref. [24] and adapted from Paper IV.

and electron beams, occur on a short time scale and can be monitored by, e.g., luminescence spectroscopy.

Figure 2.7 demonstrates a conceptual configuration coordinate (CC) diagram (based on the discussion of Ref. [24]) for an arbitrary defect transition. Note that the diagram is general, and that it does not matter whether the transition in question is thermodynamic or optical, or if it involves the exchange of charge carriers with the surroundings or occurs internally between an excited state and the ground state. The lower parabola represents the ground state (GS) while the upper represents the excited state (ES, can be an internal transition or a different charge state). The y -axis denotes energy, with the configuration coordinate Q on the x -axis representing the atomic displacement from the equilibrium position Q_{GS} (see Chapter 4 for a more detailed discussion). The most stable configurations are found at the parabola minima, and the horizontal dashed lines represent vibronic excitations to the quantum state of energy $\hbar\omega_{GS}$ or $\hbar\omega_{ES}$.

Thermodynamic charge-state transitions as discussed above are slow, meaning that the lattice surrounding the defect has enough time to rearrange during the transition event. Let us consider a defect that introduces a deep energy level at $E_C - E_t$ in the semiconductor band gap, and let Fig. 2.7 represent a thermodynamic transition between D^q (lower parabola) and D^{q-1} (upper parabola). Indeed, the energy difference between the two minima equals the ionization energy or positioning of the defect level in the band gap, E_t , and is represented by the blue skewed arrow due to the involvement of phonons as the lattice is rearranged. E_b corresponds to an additional energy barrier for carrier (here electron) capture, which can be extracted experimentally by comparing

the real and apparent capture cross-sections.

Optical transitions are induced by excitation via, e.g., laser light and electron beams, and occur on a shorter timescale than thermodynamic transitions where the lattice does not have time to rearrange. Thus, optical transitions are represented by vertical (red) arrows in Fig. 2.7. Optical transitions may involve both exchange of carriers with the band edges, and excitations to internal excited state of the defect. Focusing now on the latter excitation type, we consider a defect that resides in the ground state (GS) with a configuration coordinate Q_{GS} , and absorbs a photon of energy $h\nu_{\text{abs}}$. The absorption process is fast (on the fs timescale), and is therefore vertical in the diagram of Fig. 2.7. Now, the system occupies an excited vibronic state of the upper (ES) parabola, and will relax towards its bottom via phonon interactions (i.e., lattice reconfiguration occurs). The point defect is still in an excited state, and eventually relaxes to the ground state parabola by emitting a photon of energy $h\nu_{\text{lum}}$ via a second vertical transition. The relaxation energy is known as the Franck-Condon energy, and the CC diagram explains the Stokes' shift where $h\nu_{\text{abs}} \geq h\nu_{\text{lum}}$. Optical transitions between the lowest point of each parabola are called the zero-phonon line (ZPL) of energy E_{ZPL} , while transitions to or from any of the vibronic excitation levels are phonon-related. Phonon features as often referred to as phonon replicas or the phonon side-band (PSB) in luminescence spectra. The strength of the electron-phonon interaction is characterized by the Huang-Rhys factor S [25], and influences the portion of emission that is channeled into the zero-phonon line. Emission into the ZPL can be achieved if the two parabolas in Fig. 2.7 have practically identical locations along Q , or if $S \sim 0$. The value of S quantifies the strength of the electron-phonon coupling, and by estimating S , one can predict the lineshape of luminescence emission from a specific defect center [24]: (i) weak coupling yields a prominent ZPL and a small phonon side-band, (ii) intermediate coupling is associated with a small ZPL and several (~ 10) phonon replicas, and (iii) for strong coupling, the ZPL can hardly be observed, yielding a nearly Gaussian emission band.

2.3.6 Defect-related luminescence

Upon excitation, for instance via laser light (as in photoluminescence or PL spectroscopy) or an electron beam (as in cathodoluminescence or CL spectroscopy), semiconductors may emit *luminescence*. An important feature of semiconductor emission occurs near the band gap energy, and can be related to, e.g., recombination of free and bound (excitons) electron-hole pairs that are formed upon excitation of an electron from the VB to the CB. If the band gap is *direct*, i.e., E_C and E_V are associated with the same momentum \mathbf{k} as exemplified in Fig. 2.3(a), recombination of the EHP results in emission of a photon of energy close to that of the gap (E_g). *Indirect* band gaps do not necessarily hinder luminescence emission, but phonon interactions are required, and EHP recombination may take place via defect states. As demonstrated by the example photoluminescence (PL) spectra from as-grown and proton-irradiated n-type 4H-SiC shown in Figure 2.8(a), emission from semiconductors often encompasses

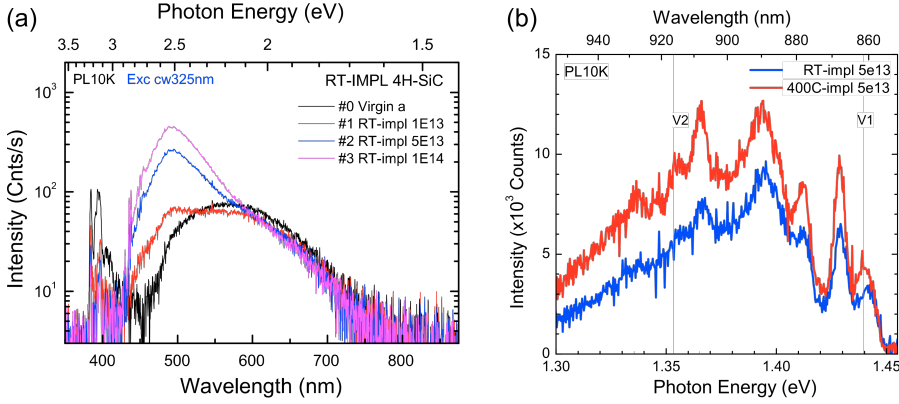


Figure 2.8: Example PL spectra from as-grown (black) and proton-irradiated (1.5 MeV) n-type 4H-SiC samples showcasing (a) near band-edge and broad defect-related emission bands, and (b) sharp defect-related peaks. The figures are based on data from Paper IV.

both the near band edge (NBE) emission related to free EHP recombination and excitons (to the left of spectrum), and broad defect-related bands (to the right of the spectrum).

Defects significantly contribute to the optical properties of the host material (vertical transitions in Fig. 2.7), through both exchange of carriers with the band edges and via internal excited-to-ground state transitions of the defect center in question. The latter process is most relevant for the present work, as we will focus on a type of ES-to-GS transition where single photons are emitted one at a time, with a detectable delay time between each emission process. Defects exhibiting such properties are referred to as single-photon emitters (SPEs) or single-photon sources (SPSs), and are often characterized by a sharp and distinguishable zero-phonon line in addition to the single-photon emission characteristics. Note that we consider only deep optically active defects suitable for optical and spin quantum bits herein, although certain shallow defects may also behave as single-photon sources (e.g., phosphorous in silicon [4]). Experimentally, measurements of the photon statistics based on the Hanbury-Brown and Twiss interferometer [26] are used to assess whether a luminescent defect is also a SPS. A light beam is split in two paths, each with a single-photon counting detector, and an ideal SPS will yield only one detector event at a time. The resulting histogram is described by the auto-correlation function $g^{(2)}(\tau)$, and photon *anti-bunching* features that are characteristic of a SPS are identified when $g^{(2)}(0) < 0.5$.

Single-photon sources are not found in all materials and only some defect types possess the necessary qualities. Importantly, charge-state transitions involve interactions with the VB or CB, and may result in broad bands in the emission spectra. Therefore, SPE processes (as discussed herein) are mostly internal ES-to-GS transitions, and require that both the GS and ES levels are

situated within the band gap. Hence, no change of Fermi level is needed to facilitate ES-to-GS transitions. As a consequence, this transition type mostly occurs for wide-band gap semiconductors, such as diamond and silicon carbide. Example PL spectra showcasing the sharp emission lines that are indicative of single-photon emission are shown in Figure 2.8(b), for n-type 4H-SiC samples that were proton irradiated to the same fluence ($5 \times 10^{13} \text{ cm}^{-2}$) but at different temperatures (RT and 400 °C).

2.4 Point defects in semiconductors for quantum technology

There are several challenges associated with the currently available quantum platforms that must be overcome to realize the universal quantum computer. We need a qubit system with long coherence times, suggesting solid-state spins such as NMR, trapped ions or quantum dots. However, entanglement remains a challenge for trapped ions, and NMR spin initialization is time-consuming. Quantum dots (QDs), on the other hand, promise spin-based quantum computing with rapid initialization and control protocols that are much shorter than the coherence time. However, lithographically defined QDs only operate on the mK temperature scale and nanoparticle QDs self-assemble randomly and thus emit light over a larger wavelength range. Importantly, established quantum error correction (QEC) protocols are compatible with entangled spins [27], making spin-based quantum computing promising for future installment.

As we have seen, point defects may capture charge carriers and introduce energy levels within the semiconductor band gap. Considering the QT aspect, a suitable qubit defect system should have deep energy levels, as this usually corresponds to a high degree of localization of the defect orbitals, and thereby isolation of the defect states from the environment. Combined with low spin-orbit coupling of the material host, this would allow point defects to trap electrons in localized, high-spin states with long coherence times on the millisecond timescale. Furthermore, in addition to stable spin states, an appropriate qubit point defect should facilitate the sharp ES-to-GS transitions that are representative of single-photon emission as described above. To facilitate incorporation of the SPS in, e.g., quantum communication devices, a large portion of the emission should be of the energy E_{ZPL} [28]. Semiconductor materials with wide band gaps would facilitate the sharp ES-to-GS transitions of a single-photon emitter, and if weak electron-phonon coupling is in place, a high-fidelity SPS with a high ZPL fraction can be fabricated. Thus, the point defect can be seen as an artificial atom separate from its surroundings — much like the trapped ion, but with the added benefit of the solid-state matrix. Even though the solid-state environment provides additional routes towards decoherence, it also provides the greatest benefit of the point defect platform, which is integration with opto-electrical devices and on-chip technology.

Spin-selective relaxations enable optical initialization and pumping sequences for the spin state of charge carriers trapped at the point defect, forming

the basis for the gate operations needed to perform quantum computing operations. Overall, the semiconductor platform enables quantum registers based on combinations of nuclear spins, providing long-lived memory and storage, and electron spins trapped at point defects, enabling quantum state manipulation and computation. Moreover, spin-dependent optical transitions from point defect systems facilitate coherent spin-photon connectivity throughout the material, and the well-developed spin-photon interfaces of single-photon sources facilitate the fabrication of modular QCs containing nodes that are interconnected by photonic links and well integrated with devices such as waveguides, optical cavities and on-chip technology [9].

Ideally, point defects in semiconductors combine long spin coherence times with sharp optical transitions. Thus, we must search for a suitable qubit candidate, which combines optical, magnetic and electrical control with high degrees of isolation, single-photon emission and long spin lifetimes. The benchmark point defect system, with potential for quantum communication, sensing, imaging and computing applications, is the nitrogen-vacancy or NV ($N_C V_C$) center in diamond. The negative charge state, NV^- , is a demonstrated single-photon emitter even at room temperature, enabling reliable initialization and read-out of the qubit (spin) state [3, 29]. Moreover, NV centers have been demonstrated as high-sensitivity magnetometers with nanoscale resolution [30], and are excellent quantum sensors for electric fields via the Stark effect [31]. In fact, the nanoscale sensitivity of NV centers even enables optical magnetic imaging of living cells [32]. Finally, the NV center spin can be coherently manipulated at room temperature [3], and entanglement between two NV center spins separated by 3 m has been demonstrated [33], leading to teleportation of the nuclear spin of one NV center onto the electron spin of another [34].

Even though the NV center exhibits numerous exciting properties, several application areas within the fields of quantum communication and computing appear out of reach. Emission from NV centers into the ZPL is low, at only 4 % at 6 K [35], and device fabrication with diamond is famously challenging, making scaling of communication and computing devices problematic. Moreover, the emission from NV centers is in the red wavelength range, complicating integration with optical fiber technology. This has spurred a search for platforms that are more device friendly but offer similar capabilities, including a bound (spin) state that can be used as a qubit, an optical initialization cycle, and an optical read-out mechanism for the qubit state [21]. Semiconductor materials facilitating such properties should have a wide band gap to enable sharp ES-to-GS transitions, small spin-orbit coupling to enhance the spin lifetime, be available as high-quality single crystals, and contain elements having spinless nuclear isotopes. A promising host material, and currently a leading candidate for point defect-based qubits, is silicon carbide (SiC) [21, 36].

Chapter 3

Silicon carbide

Silicon carbide (SiC) is a covalent material, comprising equal amounts of tetrahedrally coordinated Si and C atoms, and a promising host for various power electronics [37] and quantum technology [36] applications. Herein, the important properties of the material system will be discussed, focusing mainly on the 4H polytype, while introducing the key players: the point defects that either facilitate or hinder quantum device fabrication. It is here worth noting that also transition metal impurities in SiC are being researched for quantum applications, but remain outside the scope of the present work.

3.1 Growth and crystal structure

SiC does not exist naturally on earth but has been synthesized since the late 19th century [37]. Si and C bind very strongly in a nearly covalent fashion, however, with a distinct ionic contribution where C is the negatively charged constituent [38]. The strong covalent bonds give rise to an extreme hardness, close to that of diamond, which combined with a high thermal conductivity and stability promote SiC as a candidate for semiconductor devices operating under harsh conditions.

An interesting feature of SiC is its existence in over 200 different atomic structures, labeled polytypes [39]. The crystal structure of SiC consists of stacked Si-C bilayers, where the bilayers are stacked in the positions A, B or C. Herein, three main polytypes will be considered — 3C, 4H and 6H — and are illustrated in Figure 3.1. 3C-SiC has a band gap of 2.39 eV, a cubic ABC stacking sequence and zinc-blende structure (Fig. 3.1a). The 4H (Fig. 3.1b) and 6H (Fig. 3.1c) polytypes both have wurtzite hexagonal structure, and ABCB or ABCACB stacking order, respectively. The 4H polytype is awarded the most attention herein, with a 3.26 eV band gap and two inequivalent lattice sites: the hexagonal (*h*) and the pseudo-cubic (*k*). Similarly, 6H-SiC has a 3.02 eV band gap and three different lattice sites, one hexagonal (*h*) and two pseudo-cubic ones (*k*₁ and *k*₂) [37, 39].

Wafer-grade SiC material typically consists of an epitaxial layer (epi-layer) grown by chemical vapor deposition (CVD) on top of a bulk SiC substrate. The bulk material is usually fabricated by the seeded sublimation method [40], as SiC does not melt, but sublimates at temperatures above 1800 °C for 3C- and 2800 °C for 4H- and 6H-SiC [39]. Doping of SiC epi-layers (not area-selective) is accomplished by introducing precursors during growth, with nitrogen being most commonly employed for n-type doping (substitutes C) and aluminum for p-type doping (substitutes Si).

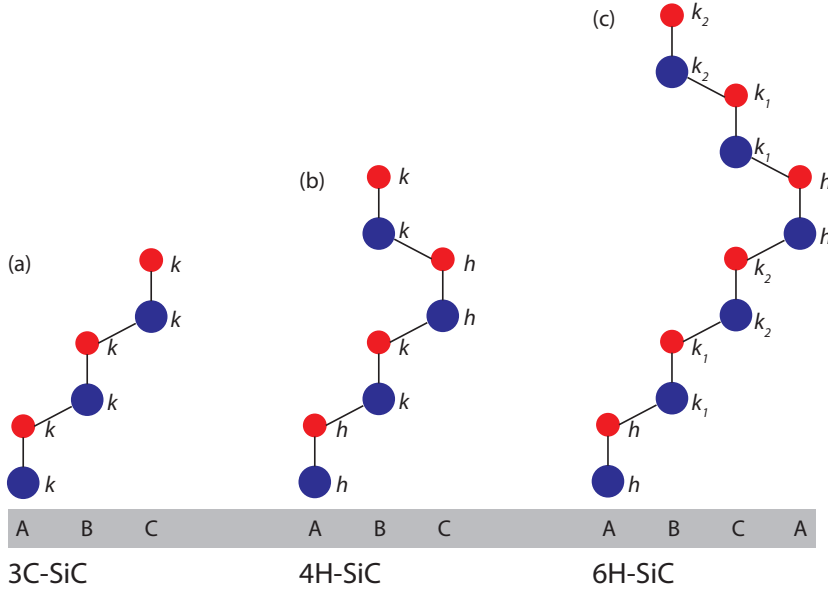


Figure 3.1: Illustration of the SiC crystal structure and stacking sequence for the (a) 3C, (b) 4H and (c) 6H SiC polytype. Si atoms are blue and C atoms red. The h and k labels refer to hexagonal and pseudo-cubic lattice sites, respectively.

3.2 Application

From an application point of view, 4H-SiC is favored by the power electronics industry over the remaining polytypes because both the band gap and thermal stability are high, and the electron mobility is nearly isotropic ($880 \text{ cm}^2/\text{Vs}$ versus $800 \text{ cm}^2/\text{Vs}$ \parallel and \perp to the c -direction, respectively [39]). This has resulted in the availability of high-purity $> 150 \text{ mm}$ diameter 4H-SiC wafers free of micropipe defects, and higher material quality for 4H-SiC epitaxial layers compared to the other polytypes. Importantly, the wide band gap of 4H-SiC allows for fabrication of electronic devices operating at high temperatures while suppressing EHP formation. Moreover, 4H-SiC is associated with a high breakdown electric field (E_B), which facilitates the fabrication of diodes and transistors with high breakdown voltages while retaining a low on-state voltage. Hence, the material properties of SiC are more suitable for power electronics than, e.g., Si, which dominates the markets today.

An important roadblock towards the successful and wide-spread implementation of 4H-SiC power devices is the perennial presence of point defects, even in state-of-the-art epitaxial material [41]. The carbon vacancy (V_C) is the dominant deep-level defect in SiC, acting as a carrier trap. Indeed, the $(0/2-)$ double charge-state transition of V_C is situated at $E_C - 0.67 \text{ eV}$ [42], and effectively limits carrier lifetimes in 4H-SiC material [43]. Even low V_C concentrations of

$\sim 10^{12} \text{ cm}^{-3}$ significantly suppress the carrier lifetime and hence diminish the diode quality, and several strategies have therefore been developed to ensure V_C removal from 4H-SiC epi-layers [44, 45].

Although electrically active defects hinder the development of SiC-based devices for current technology applications, they may in fact promote a whole new class of quantum devices. As previously mentioned, SiC has a wide band gap which facilitates the presence of single-photon emitting defects, while low spin-orbit coupling and the presence of isotopes for both Si and C devoid of nuclear spin enable long spin coherence times. A plethora of different quantum defects may be incorporated in the different polytypes of SiC, and in fact, 3C polytype inclusions into 4H-SiC may themselves act as single-photon emitters due to the lower band gap of 3C compared to 4H SiC [46]. Similar behavior was found for intrinsic defects located at or near the 4H-SiC surface [47]. However, herein, we will focus on developing the understanding of the optical, electronic and thermal properties of native and irradiation-induced point defects in 3C-, 4H- and 6H-SiC.

3.3 Point defects in SiC

Previously, SiC material was plagued by extended defects such as voids and micropipes. State-of-the-art epitaxial material, however, is currently practically devoid of such imperfections, and even stacking faults and polytype inclusions can largely be avoided. Nowadays, the predominant defects in SiC epi-layers are zero-dimensional, and induced either intentionally by for instance ion implantation, or unintentionally during growth, post-processing or device fabrication.

The point defects to be discussed herein exhibit properties that can be both detrimental for devices and quantum friendly. The former description applies to defects acting as carrier traps such as the carbon vacancy (V_C) and silicon vacancy (V_{Si}), and defects that offer pathways for non-radiative recombination during luminescence experiments, such as the V_C , C and Si interstitials (C_i and Si_i , respectively) and C and Si antisites (C_{Si} and Si_C , respectively). The quantum friendly defects exhibit properties such as single-photon emission and long-lived spin states that can be manipulated using magnetic fields and having optical read-out protocols. In this context, we will discuss the silicon vacancy (V_{Si}), the carbon antisite-vacancy pair or CAV ($C_{Si}V_C$), the nitrogen vacancy or NV center (N_CV_{Si}), and the divacancy or VV ($V_{Si}V_C$) in SiC.

Most defects studies in SiC have, over the last few decades, to a large extent been motivated by eventual utilization within power electronics, and the electro-optical signatures of several point defect centers are hence well-known. However, the quantum perspective did not properly manifest until about 5-10 years ago, and was heralded by several seminal papers on the single-photon emission and spin coherence of the silicon vacancy [48], the carbon antisite-vacancy pair [49] and the divacancy [50]. In this section we review the main properties of primary defects in SiC, including formation conditions and annealing behavior, where the aim is to achieve preferential formation of quantum defects at the expense of

their less favorable counterparts such as V_C , interstitials and antisites. Next, the physics giving rise to the different defect types will be reviewed, followed by a glance into the electrical and optical properties of point defects in SiC, focusing mainly on the C and Si vacancies.

3.3.1 Thermal defect formation

Certain defects (like the V_C) are omnipresent in SiC epi-layers. Moreover, the elevated temperatures that manifest during SiC growth may introduce additional defects into the material at a rate governed by the Gibb's free energy (G) for the defect. Defects increase the entropy of a system and must therefore exist to some extent. H is often replaced by the *formation energy* (E^f), which can be extracted both experimentally and theoretically and depends on the defect charge state. In the dilute limit, thermal formation of, e.g., V_C is governed by the relation

$$[V_C] = N_{C\text{-sites}} e^{-E^f/k_B T}, \quad (3.1)$$

where $[X]$ denotes the concentration of a defect species and $N_{C\text{-sites}}$ is (e.g.) the amount of available C sites in the SiC lattice. For instance, the formation energy of the carbon vacancy (V_C) in 4H-SiC is estimated at 4.5-5.0 eV theoretically [51] and 5.0 eV experimentally [52], leading to an induced V_C concentration of $\sim 10^{15} \text{ cm}^{-3}$ after annealing 4H-SiC samples at 1950 °C. Comparably, predicted formation energies for the silicon vacancy (V_{Si}) are around 7.5-8.0 eV for Fermi levels near mid-gap [21, 53], leading to approximately seven orders of magnitude lower V_{Si} concentrations compared to those of V_C under the same annealing conditions. Consequently, thermal formation is a viable route for obtaining certain defects like V_C , while less energetically favorable defects such as V_{Si} must be formed by other means. In SiC, V_C is the main defect that can be formed in large amounts by thermal means alone, with the remainder appearing only after bombardment of the material with high-energy particles.

3.3.2 Irradiation-induced deep-level defects in SiC

Whenever thermal defect formation is not a viable option, or enhanced quantitative control and area-selectivity are desired, ion implantation or irradiation can be employed instead. Proton irradiation is predominantly employed throughout this work, yielding mainly point defects as opposed to large complexes and extended defects, which are often formed when using heavier ions. The interaction between the incoming ion and the lattice results in the formation of a vacancy (V_{Si} or V_C) and its accompanying interstitial (Si_i or C_i) (known as a Frenkel pair), which may subsequently recombine via a process referred to herein as dynamic annealing. An approximate 2-5 % of primary defects, such as Si and C vacancies, are typically estimated to survive an irradiation process. Note that formation of, e.g., antisites (Si_C and C_{Si}), antisite-vacancy pairs ($C_{Si}V_C$ or Si_CV_{Si}) and divacancies ($V_{Si}V_C$) may occur in parallel to that of vacancies and interstitials.

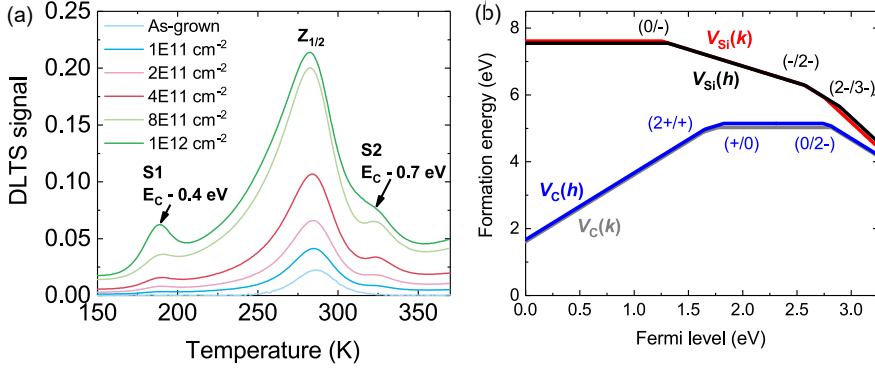


Figure 3.2: (a) Deep level transient spectroscopy (DLTS) spectra of proton-irradiated n-type 4H-SiC epi-layers, adapted from Paper I. (b) Formation energy diagrams for V_C and V_{Si} as calculated using hybrid density functional theory (DFT), adapted from Paper VII.

Let us first consider the Si and C vacancies in 4H-SiC. Both V_{Si} and V_C introduce deep levels within the 4H-SiC band gap, which can be detected by performing deep level transient spectroscopy (DLTS) [54] measurements on n-type 4H-SiC epi-layers. The $(0/2-)$ double charge-state transition of V_C has been ascribed to the well-known $Z_{1/2}$ deep level appearing at $E_C - 0.67$ eV [42] (with E_C denoting the conduction band edge). The $Z_{1/2}$ peak is contained in the DLTS spectra shown in Figure 3.2(a) after proton irradiation to various fluences. Furthermore, the $EH_{6/7}$ level at $E_C - 1.55$ eV arises from the $(+/0)$ transition of V_C [42], and contains contributions from both the $V_C(h)$ and $V_C(k)$ configurations [55].

Fig. 3.2(a) contains two additional signatures to either side of the $Z_{1/2}$ peak assigned to the $V_C(0/2-)$ double electron emission, named S1 and S2, that are known to arise from different charge-state transitions of the same defect center called the S-center [56]. Paper I discusses the assignment of the $V_{Si}(-/2-)$ and $(2-/3-)$ charge-state transitions to the S center, by correlating the dependence of S-center concentration as extracted from DLTS and the V_{Si} photoluminescence (PL) intensity as a function of proton fluence. Moreover, the positioning of the S1 and S2 peaks in the band gap, at $E_C - 0.4$ eV and $E_C - 0.7$ eV, respectively, is compared to the formation energy diagram for V_{Si} calculated using density functional theory (DFT) and shown in Figure 3.2(b). Note that Fig. 3.2(b) also highlights the positioning of the V_C charge-state transitions within the 4H-SiC band gap, and illustrates the difference in formation energy between V_{Si} and V_C (refer back to Section 2.3.3 for further details).

Correspondingly, interstitial defects are perennially present after irradiation or implantation, but both C_i and Si_i are challenging to detect in SiC as they lack unambiguously identified fingerprints. Both interstitial defect types are predicted to have low migration barriers in the 1-2 eV range in 4H-SiC [37,

57], and thus rapidly disappear above room temperature. However, there have been speculations that charge-state transitions of the C interstitial may be contributing to the low-temperature shoulder of the $Z_{1/2}$ DLTS peak (see, e.g., Fig. 3.2a), which disappears upon high-temperature annealing.

Antisite defects are expected to form in substantial amounts during irradiation of SiC. However, no DLTS assignment has yet been made, partly due to the predicted lack of charge-state transition levels of SiC and C_{Si} in n-type material [57, 58]. In the case of antisite formation during irradiation, where, e.g., a Si atom hops into a C vacancy or a C vacancy is formed next to a Si_C antisite, a silicon antisite-vacancy pair ($Si_C V_{Si}$) develops. Although the $Si_C V_{Si}$ complex is predicted to be unstable [59] and has not been detected in SiC, the reciprocal $C_{Si} V_C$ or CAV pair is a prominent single-photon emitter [49] and will be discussed below.

In addition to the defects discussed above, several electrically active and irradiation-induced defects in n-type 4H-SiC have been detected by DLTS but remain to be identified. The most relevant ones for the present work (to be discussed in Paper VI) are EH_4 and EH_5 , at $E_C - 1.0$ eV and $E_C - 1.1$ eV, respectively. EH_4 cannot be formed by low-energy proton irradiation, indicating a complex being the origin [60]. Moreover, hydrogen impurities are perennially present in SiC material, but are also introduced during proton implantation, whereupon the implanted protons may form hydrogen-related defects. A set of DLTS peaks named HR (for hydrogen-related) arise upon proton implantation of n-type 4H-SiC, at $E_C - 0.73$ eV (HR_1), $E_C - 0.69$ eV (HR_2) and $E_C - 0.73$ eV (HR_3) [61]. As both implantation and hydrogen are required to form the HR levels, they likely derive from complexes between one or more H atoms and the Si or C vacancies.

3.3.3 Thermally activated defect migration

Once defects are formed, irrespective of how they were generated, further heat treatments may induce defect migration or transformation into complexes. Defect diffusion or out-annealing can be a first-, second- or higher-order process, where first-order diffusion typically characterizes primary defect migration and second-order diffusion can describe complex formation, both via atomic hops. In SiC, defect migration may occur on or between the two (Si and C) sublattices. Importantly, V_C migration takes place via atomic hops and exclusively on the C sublattice [59], and thus V_C migration should follow Fick's second law [62]

$$\frac{\partial c}{\partial t} = D \frac{\partial^2 c}{\partial x^2}, \quad (3.2)$$

where c represents the defect concentration and D the diffusivity. If the temperature dependence of D then follows an Arrhenius behavior, we can extract the activation energy (E_A) for diffusion of a defect species from

$$D = D_0 e^{-E_A/k_B T}, \quad (3.3)$$

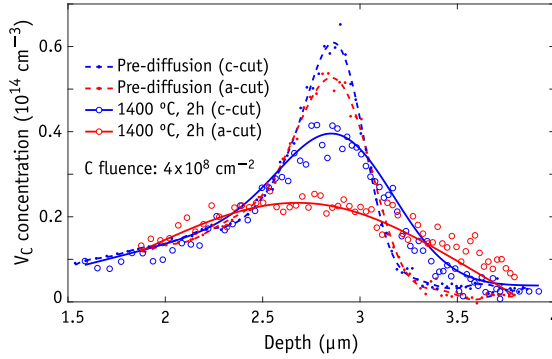


Figure 3.3: Example of the anisotropic V_C diffusion in 4H-SiC as evidenced by DLTS concentration profiles of the $Z_{1/2}$ peak along two different crystallographic directions, a or $[11\bar{2}0]$ and c or $[0001]$, before (pre-diffusion) and after annealing at 1400 °C. Adapted from Paper IX.

where D_0 is the prefactor for diffusion. An example of V_C diffusion in 4H-SiC is illustrated in Figure 3.3, where the broadening of the $Z_{1/2}$ concentration vs. depth profile is monitored by DLTS upon annealing in several stages. Importantly, two different sample types grown showing different crystallographic faces were employed for the experiments (c -face and a -face), and thus the diffusion profiles in Fig. 3.3 evidence that V_C diffusion is distinctly *anisotropic* in 4H-SiC (to be discussed in Paper VIII and Paper IX). Additionally, V_C is exceedingly stable, and does not anneal out until above 1600 °C in 4H-SiC.

Although migration of V_C follows Fick's second law, that of V_{Si} is of a more complex nature and depends strongly on the Fermi level in the sample. Firstly, the DLTS S-center (the relation of which to V_{Si} is discussed in Paper I) anneals out by first-order kinetics and with an activation energy of $E_A = 1.8$ eV [56] in n-type 4H-SiC. Thus, in n-type material, the V_{Si} likely moves by atomic hops on the Si sub-lattice [63, 64], and anneals out by encountering the surface and other sinks, e.g., via Frenkel pair recombination with Si_i or divacancy formation upon encounters with V_C (see Paper VI). In p-type material, on the other hand, V_{Si} is known to anneal out above 400 °C by transforming into the carbon antisite-vacancy pair [49].

Finally, thermally activated migration in SiC can also be trap-limited, as exemplified by hydrogen which diffuses much faster in p-type than n-type SiC [65]. This is explained by a trap limited diffusion mechanism in n-type material [66, 67]. The traps are likely vacancies, as hydrogen readily binds to both V_C and V_{Si} in SiC, regardless of the polytype [68] (further discussed in Paper V).

3.3.4 Physics of vacancy formation in SiC

Hitherto, the carbon vacancy has been discussed as a carrier trap and minority carrier lifetime-limiting defect, while the silicon vacancy is associated with long

spin coherence times and single-photon emission characteristics. SiC is essentially a covalent material, and it may seem surprising that the two different vacancy species exhibit such drastically different properties. However, as it turns out, there are several distinct features that can be identified as typical of a defect that is either quantum compatible or completely devoid of qubit capabilities.

The dominant defects in 4H-SiC are the carbon vacancy (V_C), introducing the (0/2-) double electron emission at $E_C - 0.67$ eV [42], and the silicon vacancy (V_{Si}), with the (2-/3-) and (-/2-) charge-state transitions being assigned to the S-center at 0.4 eV and 0.7 eV below E_C , respectively (see Paper I). Initially, the Si and C vacancies appear similar, with nearly tetrahedral C_{3v} symmetry prior to lattice relaxation, and energy levels introduced within the 4H-SiC band gap. However, the chemical differences in the local environment result in fundamentally different properties: the V_C is a low-spin defect without any detectable optical transitions, while the V_{Si} is a distinguished single-photon emitter with a long-lived and coherent high-spin ground state (in the negative charge state) that holds great promise for quantum applications [48]. Formation of a Si or C vacancy causes the formation of three sets of occupied orbitals within the 4H-SiC band gap: one a_1 -level resonant with the valence band, one a_1 -level within the gap, and a degenerate e -level also within the gap. The degeneracy of the e -orbital paves the way for two different mechanisms: a symmetry-lowering *Jahn-Teller* (JT) distortion to lift the degeneracy competes with the strong *exchange interaction* yielding parallel spin ordering and high-spin states.

Surrounding V_C are four Si atoms with extensive and overlapping dangling bonds, and the bond overlap prompts an inward displacement of the Si atoms and pairwise Si-Si dimer formation. The bond overlap drives a reduction of the V_C symmetry to C_{1h} in the neutral and doubly negative charge states, as illustrated for V_C^0 at h and k sites in the top panel of Figure 3.4 and referred to as a Jahn-Teller (JT) distortion. Intriguingly, the V_C displays a fascinating effective electron-electron attraction known as negative- U behavior [69] and resulting in the (0/-) transition taking place at lower energies than $V_C(-/2-)$ [42], which is caused by the Jahn-Teller distortion driven by the Si dangling bond overlap [70–74].

In contrast to the case for V_C , V_{Si} is surrounded by C atoms having very localized dangling bonds that do not overlap. The lack of nearest neighbor bonding thereby prevents a symmetry-lowering inward atomic displacement, and an energy gain is instead ensured by a shortening of the Si-C bonds. Thus, in the negative charge state (V_{Si}^-), the C_{3v} symmetry is conserved by an outward breathing relaxation, as exemplified by the illustration of V_{Si}^- at h and k sites in the bottom panel of Figure 3.4. The exchange interaction causes the realization of high-spin ordering according to Hund’s rule [70, 72], and hence the negative charge state of V_{Si} exhibits a high-spin ground state with $S = 3/2$. V_{Si}^- is associated with millisecond spin coherence times at cryogenic temperatures [48], and the lower electron-phonon coupling strength of V_{Si} compared to V_C facilitates single-photon emission from V_{Si} even at room temperature (RT) [48].

In summary, negative- U characteristics in point defects are often caused by strong Jahn-Teller distortions that arise to lift degeneracies in the defect states,

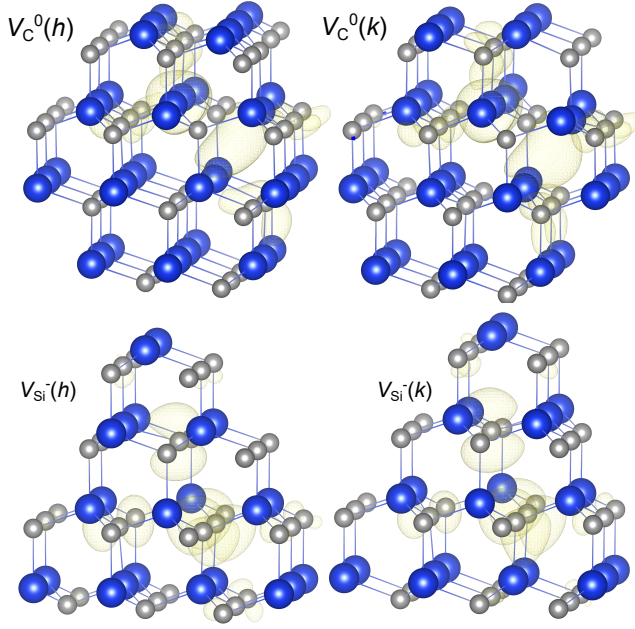


Figure 3.4: Illustrations of the crystal structure surrounding the neutral C vacancy at h and k sites (top), and negatively charged Si vacancy at h and k sites (bottom), in 4H-SiC. Si atoms are blue and C atoms gray, with partial charge densities shown by the yellow isosurfaces.

and both double-electron charge-state transitions and strong geometric relaxation are symptomatic of this defect type. In contrast, single-photon emitting defects with long spin-lifetimes are commonly characterized by lower electron-phonon coupling, preserving the isolation of the qubit system from the environment. Strong geometric reconfiguration of the atoms surrounding a defect is therefore a potent sign that qubit capabilities are unlikely, while highly symmetric defect wavefunctions, small lattice reconfiguration and weak electron-phonon coupling are signs of long-lived spin states and narrow luminescence lineshapes.

3.3.5 Optical properties of quantum defects

Hitherto, optical properties and single-photon emission have been mentioned as important signs of a promising qubit center, but no details have been provided for the SiC candidates. The V1 and V2 emission lines commonly observed in photoluminescence (PL) spectra of irradiated n-type 4H-SiC at 1.44 eV and 1.35 eV, respectively, have been assigned to the negatively charged V_{Si}^- [75–77]. Recently, the V1 ZPL (and accompanying V1' emission from a higher-lying excited state) was assigned to the h configuration of V_{Si}^- , while the V2 line ascribes to $V_{Si}^-(k)$ [78]. Importantly, the V1 and V2 ZPLs are sharp with nearly

40 % of the emission from $V_{\text{Si}}^-(h)$ being channeled into the V1 ZPL [79]. Both V1 and V2 exhibit single-photon emission characteristics, and the V_{Si}^- spin state can be coherently manipulated and optically monitored, even at room temperature [48].

The combination of room temperature single-photon emission, high ZPL fraction [79], near-infrared (NIR) emission wavelength and mature fabrication of SiC marks the V_{Si} as a highly promising candidate for a wide range of quantum applications [36, 48, 80]. Comparing to the NV center in diamond, we note that the V_{Si} emits in a wavelength range more favorable to integration with optical fiber technology, and with a larger fraction of emission (40 % compared to about 4 % [35, 79]) channeled into the ZPL, in addition to the more mature device fabrication of SiC compared to diamond. On the other hand, spin coherence times for the NV center in diamond surpass milliseconds even at RT [3] and entanglement protocols have been demonstrated [33], features that remain to be matched by the V_{Si} in SiC.

The negatively charged Si vacancy adopts spin-3/2 and a 4A_2 quartet state in 4H-SiC [81]. In the hexagonal crystal field of 4H-SiC the point group of the vacancy becomes C_{3v} , and the C dangling bonds surrounding V_{Si} form two a_1 orbitals and one e orbital. The lower-lying a_1 orbital is resonant with the valence band, with the remaining a_1 and e orbitals falling within the fundamental gap [78, 82–85]. Accordingly, the ground state electronic configuration for V_{Si}^- (at h and k lattice sites) corresponds to $a_1^1 e^2$, as illustrated on the left-hand side of Figure 3.5. The lower-lying a_1 state that falls within the valence band does not contribute to the optical activity of the V_{Si} , which instead involves a spin-down electron of the highest occupied valence band state. The V_{Si}^- transitions occur along the minority spin channel (spin-down), resulting in the first and second excited states organizing as 4A_2 and 4E with $a_1^2 e^2$ and $a_1^1 e^3$ configuration, respectively [75, 77, 82, 86]. The excited state configurations of V_{Si}^- at a h site, corresponding to the V1 and V1' emission lines, are shown in the middle and right panels of Figure 3.5. The available optical transitions for the negatively charged V_{Si} are thus $^4A_2 \rightarrow ^4A_2$ (labeled herein $^4A_2^* \rightarrow ^4A_2$ to distinguish the excited state) resulting in V1 and V2 at 1.438 eV and 1.352 eV, respectively, and $^4E \rightarrow ^4A_2$ yielding V1' at 1.443 eV. Note that the V2' transition will be referred to throughout this thesis as the $^4E \rightarrow ^4A_2$ transition of $V_{\text{Si}}^-(k)$, but is currently only a speculation, as no experimental identification has been made.

The most promising (intrinsic) single-photon emitters in SiC in addition to V_{Si} include the CAV pair, the divacancy and the NV center, that all share many properties with the NV center in diamond. The CAV complex has been assigned to the AB-lines arising in the red wavelength range of PL spectra from 4H-SiC, may exist in four different configurations in 4H-SiC (hh , kk , hk and kh), and is a verified ultra-bright single-photon emitter [49]. Although the CAV emission is in the 600-700 nm range and thus less compatible with optical fiber technology than V1 and V2, coherent manipulation of the spin state has been shown [49]. The VV and NV defects in 4H-SiC, on the other hand, have the added benefit of telecom wavelength single-photon emission energies in the 1000-1200 nm range for both centers [50, 87, 88]. Four configurations are available for the

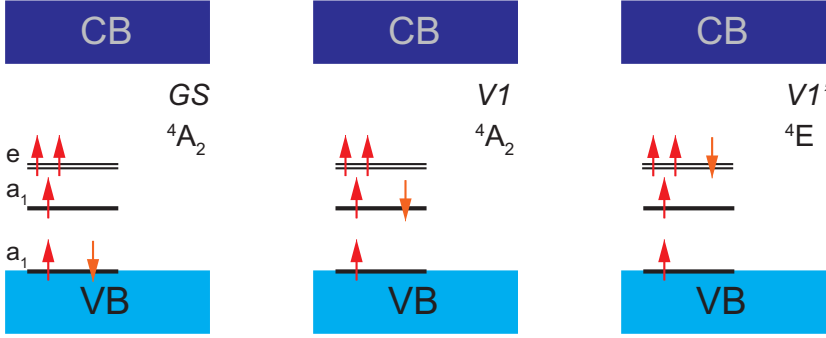


Figure 3.5: Schematic of the orbitals introduced by the negatively charged V_{Si} (at a h site) in the 4H-SiC band gap, and occupation of the levels for the (a) ground state (GS), (b) first excited state (ES) V1 and (c) second excited state V1'. Adapted from Paper IV.

VV and NV complexes (as for CAV), and both room-temperature single-photon emission, coherent spin manipulation and ms spin coherence times (at cryogenic temperatures) have been demonstrated for VV [50] and NV [88] defects in 4H-SiC.

Although optical identification has been performed for the four main quantum defect centers in SiC, electrical identification remains unexplored for all but V_{Si} (see Paper I), and controlling the defect charge state, spin state and emission remains a vibrant field of research. Recently, charge-state control was established for V_{Si} (see Ref. [89] and Paper I), $V_{Si}V_C$ [90, 91] and CAV [92], with Stark tuning of emission wavelengths being demonstrated for divacancy [91, 93] and silicon vacancy (see Ref. [94], Paper I and Paper II) defects. Qubit control via charge-state manipulation, and ensuring that a SPS can produce identical photons on-demand, are vital for a variety of QT applications. Importantly, V_{Si} defects have been successfully embedded into nanopillar waveguides [95] and coupled to optical cavities [96], while photonic device integration has proven detrimental to single-photon emission from divacancies in 4H-SiC and NV centers in diamond [97]. However, divacancies still hold an important advantage over V_{Si} , as ensemble entanglement with nuclear spins has been successfully demonstrated for divacancies in 4H-SiC [27]. Importantly, further advancements related to identification and control over V_{Si} formation and control are needed in order to realize V_{Si} -based quantum devices.

Chapter 4

Modeling of point defects in SiC

Herein, the theoretical methods employed throughout the present work are reviewed. Keep in mind that the theoretical calculations were chosen and specifically designed for comparison with experiment, both to verify the theoretical predictions and to provide an additional depth of understanding to the experimental observations. This chapter will both introduce a toolbox for defect calculations that can be combined with experiment (experimental methods are described in Chapter 5), and discuss the development of new theoretical methods for studying the interplay between defect states and external perturbations such as electric fields. All expressions in this chapter will be quoted using atomic units.

4.1 Introduction to density functional theory

Density functional theory (DFT) has proven to be an immensely powerful approach to predict the physical properties of solid-state systems, and Professors Pople and Kohn shared the 1998 Nobel Prize in Chemistry for the development of computational methods in quantum chemistry and DFT, respectively. Importantly, DFT can be *ab initio*, that is, devoid of empirical assumptions. The success of DFT arises from solving the *many-body Schrödinger equation* (SE) accurately and effectively [98], and therefore, this chapter commences with providing the basics of approximating the many-body SE.

4.1.1 The many-body Schrödinger equation

The properties of any physical system can be comprehensively described by the many-particle wavefunction $\Psi^{\text{en}}(\mathbf{r}, \mathbf{R})$, where (\mathbf{r}, \mathbf{R}) denotes the position of all electrons (e) and nuclei (n), respectively. The wavefunction is obtained by solving the many-body Schrödinger equation [5]

$$H^{\text{en}}\Psi^{\text{en}}(\mathbf{r}, \mathbf{R}) = E^{\text{en}}\Psi^{\text{en}}(\mathbf{r}, \mathbf{R}), \quad (4.1)$$

where H^{en} is the Hamiltonian (operator) and E^{en} the total energy of the system consisting of electrons and nuclei. The Hamiltonian includes the five physical quantities

- kinetic energy of electrons T_j
- kinetic energy of nuclei T_α
- repulsive electron-electron interaction U_{jj}
- repulsive nucleus-nucleus interaction $U_{\alpha\alpha}$

4. Modeling of point defects in SiC

- attractive electron-nucleus interaction $U_{j\alpha}$,

and is described by

$$H^{\text{en}} = T_j + T_\alpha + U_{jj} + U_{\alpha\alpha} + U_{j\alpha} \quad (4.2)$$

$$= -\sum_{j=1}^{N_e} \frac{\nabla_j^2}{2} - \sum_{\alpha=1}^{N_\alpha} \frac{\nabla_\alpha^2}{2m_\alpha} + \sum_{j < j'}^{N_e} \frac{1}{|\mathbf{r}_j - \mathbf{r}_{j'}|} + \sum_{\alpha < \alpha'}^{N_\alpha} \frac{Z_\alpha Z_{\alpha'}}{|\mathbf{R}_\alpha - \mathbf{R}_{\alpha'}|} - \sum_{j=1}^{N_e} \sum_{\alpha=1}^{N_\alpha} \frac{Z_\alpha}{|\mathbf{r}_j - \mathbf{R}_\alpha|}. \quad (4.3)$$

Note that relativistic effects are not accounted for in the above. Here, Z_α refers to the atomic number, N_e is the number of electrons and N_α the number of nuclei, while the summation over $j < j'$ aims to avoid that electrons interact with themselves leading to double counting of the electron interactions.

In practice, solving the many-body Schrödinger equation is an incredibly time-consuming task. Therefore, one often employs the *variational principle* to minimize the total energy (ϵ) by varying the wavefunction (Ψ). The lowest possible energy is the energy of the ground state (ϵ_0), and thus the variational principle states that

$$\epsilon = \langle \Psi | H | \Psi \rangle > \epsilon_0. \quad (4.4)$$

Upon solving the many-body SE, we therefore vary the wavefunction until $\delta\epsilon/\delta\Psi = 0$. As the wavefunction must simultaneously remain normalized, this is often implemented using the method of Lagrange multipliers.

Evidently, the many-body SE quickly becomes incredibly complex as the particle number increases, and in order to solve Eq. 4.2 for a solid-state system, a number of approximations must be implemented. The main approaches to simplifying the many-body SE involve (i) separating the electronic and nuclear parts of the wavefunction, (ii) expressing the total wavefunction (Ψ) in terms of single-electron wavefunctions (ψ_j), (iii) identifying a direct relation between Ψ and the total energy, and (iv) a combination of the above, which constitutes the concept behind modern-day DFT.

In solid-state materials, such as semiconductor crystals, the nuclei are essentially immobile when comparing to electrons because of their much larger mass. Even though the motion of nuclei may influence that of electrons, the opposite is not true in most solid-state problems, and the nuclei can be envisioned as fixed point charges that the electrons move around. Therefore, we perform the *Born-Oppenheimer* (or adiabatic) approximation [5] to split the many-particle wavefunction into separate electronic (Ψ) and nuclear (Φ) parts, according to $\Psi^{\text{en}}(\mathbf{r}, \mathbf{R}) \simeq \Psi(\mathbf{r}, \mathbf{R})\Phi(\mathbf{R})$. The variable separation enables the rewriting of the many-body SE (Eq. 4.2) into a purely electronic expression

$$H^e\Psi(\mathbf{r}, \mathbf{R}) = (T_j + U_{jj} + U_{j\alpha})\Psi(\mathbf{r}, \mathbf{R}) = E^e(\mathbf{R})\Psi(\mathbf{r}, \mathbf{R}), \quad (4.5)$$

where the dependence of Ψ on \mathbf{R} is solely parametric. The total energy $E^e(\mathbf{R})$ thus depends on the atomic positions, and the *potential energy surface* (PES) $E_P(\mathbf{R})$ can be constructed from the sum of $E^e(\mathbf{R})$ and the repulsive interaction

between nuclei ($U_{\alpha\alpha}$). The importance of the PES derives from that nature always strives towards global minima on the free energy surface. In DFT calculations, the PES is utilized by computing the force on each atom according to $\mathbf{F}_\alpha = -\nabla_\alpha E_P(\mathbf{R})$ and iteratively minimizing the force by moving the atoms, in order to identify the minima on the potential energy surface. The main drawback of the Born-Oppenheimer approximation is the decoupling of the electronic and nuclear wavefunctions, which prevents accurate estimates of the electron-phonon coupling in materials.

4.1.2 The Hartree and Hartree-Fock method

Even after separating the electronic and nuclear wavefunctions, the electronic wavefunction $\Psi(\mathbf{r}, \mathbf{R})$ still depends on the position of all electrons of the system. The simplest approximation to the many-particle wavefunction is to assume that each particle can be described independently, and that for two particles (denoted 1 and 2) we can write

$$\Psi(\mathbf{r}_1, \mathbf{r}_2) = A\psi_1(\mathbf{r}_1)\psi_2(\mathbf{r}_2), \quad (4.6)$$

where A is a normalization constant. The *Hartree approximation* in Eq. 4.6 enables the use of single-particle operators, which would simplify solving the many-body SE tremendously. However, the physics of fermions are not fully retained upon implementing the wavefunction according to the Hartree approach, as Eq. 4.6 is symmetric (instead of anti-symmetric) with respect to the particle coordinates. Fermions must be indistinguishable, and hence the total wavefunction must be anti-symmetric upon particle exchange. The *Hartree-Fock* (HF) approach solves the problem of indistinguishable particles by constructing the total wavefunction from a Slater determinant of single-particle wavefunctions, which for a two-particle system reads [5]

$$\Psi(\mathbf{r}_1, \mathbf{r}_2) = \frac{1}{\sqrt{2}} \left(\psi_1(\mathbf{r}_1)\psi_2(\mathbf{r}_2) - \psi_1(\mathbf{r}_2)\psi_2(\mathbf{r}_1) \right). \quad (4.7)$$

By implementing the total wavefunction as a Slater determinant of single-particle states, exact particle exchange can be incorporated when solving the many-body Schrödinger equation. Note that electron correlation (apart from the exchange interaction) is not incorporated in the HF wavefunction.

4.2 Physical principles of the DFT

The task of solving the many-body Schrödinger equation has now been simplified after implementing the variational principle, Born-Oppenheimer approximation and Hartree-Fock method. However, the complexity of solid-state systems remains too high to efficiently solve the many-body SE if many atoms are involved, partly because of the high computational cost of keeping track of the many-particle wavefunction. Herein lies the motivation behind the density functional theory (DFT): we want to rephrase the many-body SE into a problem

which can be solved for fewer variables, while retaining the exactness and *ab initio* nature of Eq. 4.2 [98].

4.2.1 The Hohenberg-Kohn theorems

The DFT is based on the two Hohenberg-Kohn theorems [99], that connect the ground state electron energy (E_0), which we wish to obtain, to the ground state *electron density* $n_0(\mathbf{r}) = |\Psi_0(\mathbf{r}_1, \dots, \mathbf{r}_N)|^2$. The theorems can be phrased as follows [98, 99].

- Hohenberg-Kohn Theorem 1: The ground state energy of an electronic system can be expressed as a unique functional of the electron density, $E_0 = E[n_0]$, and all ground state properties can be obtained from this density. Furthermore, the theorem states that the system resides in an external potential (V_{ext}) that is uniquely defined.
- Hohenberg-Kohn Theorem 2: Using the variational principle, we can identify the true ground state electron density as the density that minimizes the total energy, so that $E[n_0] < E[n]$.

The first Hohenberg-Kohn theorem can be proven by assuming that the opposite is true, that is, by assuming that two different potentials $V_{\text{ext}}^1 \neq V_{\text{ext}}^2$ are associated with the same ground state density $n_0(\mathbf{r})$. Thus, the two potentials result in different Hamiltonians, $H^1 \neq H^2$, that have different ground state eigenfunctions and hence different ground state energies. In the end, the proof yields the relation

$$E_0^1 + E_0^2 < E_0^1 + E_0^2, \quad (4.8)$$

which is an obvious contradiction. In conclusion, the ground state electron density resulting from an external potential must be uniquely defined.

The second Hohenberg-Kohn theorem relies on the variational principle, where the exact ground-state energy E_0 is the global minimum of the energy functional $E[n(\mathbf{r})]$ for a given external potential V_{ext} — provided that the exact forms of the external potential and functional are known. The proof for this theorem is straightforward, and involves dividing the energy functional into the kinetic energy, electron-electron interaction and electron-nuclei interaction, according to

$$E[n] = T_j[n] + U_{jj}[n] + U_{j\alpha}[n]. \quad (4.9)$$

In summary, the DFT is very powerful, as it states that all ground-state properties of a system can be obtained from the system's electron density. Thus, the task at hand is hugely simplified, as instead of identifying the total wavefunction we need to obtain the electron density, which is described by only three variables (x, y, z). However, an important limitation of the Hohenberg-Kohn theorems is that they do not, in fact, identify the functional that maps the relation between the ground-state total energy and the ground-state electron density.

4.2.2 The Kohn-Sham equations

Because the exact formulation of the $E[n]$ functional is unknown, the Hohenberg-Kohn theorems look very limited in terms of practical use. The reformulation of the two theorems by Kohn and Sham [100] into a set of simple single-particle equations, called the Kohn-Sham (KS) equations, revolutionized electronic structure calculations and enabled the form of density functional theory that is widely employed today.

The KS approach requires expressing the total many-electron wavefunction in terms of auxiliary single-electron wavefunctions $\psi_j^{\text{KS}}(\mathbf{r}_j)$ according to

$$\Psi(\mathbf{r}_1, \mathbf{r}_2, \dots, \mathbf{r}_N) = \psi_1^{\text{KS}}(\mathbf{r}_1) \psi_2^{\text{KS}}(\mathbf{r}_2) \cdots \psi_N^{\text{KS}}(\mathbf{r}_N), \quad (4.10)$$

allowing the electron density to take the form

$$n(\mathbf{r}) = \sum_j |\psi_j^{\text{KS}}|^2. \quad (4.11)$$

Although the KS wavefunctions are not, in fact, the true single-electron wavefunctions, we make the *ansatz* that the KS wavefunctions correspond to the true electron density, and thus to the ground state energy (provided that the energy functional is known). The exact total energy is then expressed as

$$E[n] = T_j[n] + U_{jj}[n] + U_{j\alpha}[n] \quad (4.12)$$

$$= T_j[n] + U_{jj}[n] + \int V_{j\alpha}(\mathbf{r}) n(\mathbf{r}) d\mathbf{r}, \quad (4.13)$$

which can be grouped into some terms that are known and some that are not. First, let us rewrite $E[n]$ according to

$$E[n] = U_{j\alpha}[n] + T_s[n] + U_s[n] + \left[(T_j[n] - T_s[n]) + (U_{jj}[n] - U_s[n]) \right], \quad (4.14)$$

where $T_s[n]$ and $U_s[n]$ are the kinetic and interaction energies of the auxiliary wavefunctions, respectively (s refers to single particle). Calculating the first three terms ($U_{j\alpha}[n]$, $T_s[n]$ and $U_s[n]$) is relatively straightforward, while the remaining unknown terms are named the *exchange-correlation energy* $E_{\text{xc}}[n]$. This unknown energy functional, given by

$$E_{\text{xc}}[n] = \Delta T + \Delta U = (T_j[n] - T_s[n]) + (U_{jj}[n] - U_s[n]), \quad (4.15)$$

describes the complex electron exchange and correlation interactions that are not encompassed by the other terms. Thus, by making the *ansatz* of KS wavefunctions providing the true electron density, and grouping the unknown terms into E_{xc} , the total energy of the KS approach to DFT is described according to

$$E[n] = T_s[n] + U_s[n] + U_{j\alpha}[n] + E_{\text{xc}}[n]. \quad (4.16)$$

The true ground state energy can still be determined provided that the exchange-correlation functional is described correctly. We may now formulate the famous

4. Modeling of point defects in SiC

Kohn-Sham equations by using the variational principle to obtain the ground-state energy of the system, resulting in a set of single-electron equations of the form [100]

$$\left\{ -\frac{1}{2}\nabla_s^2 + V_{j\alpha}(\mathbf{r}) + V_H(\mathbf{r}) + V_{xc}(\mathbf{r}) \right\} \psi_s^{\text{KS}}(\mathbf{r}) = \epsilon_s^{\text{KS}} \psi_s^{\text{KS}}(\mathbf{r}), \quad (4.17)$$

where ϵ_s^{KS} denotes the KS energy eigenvalues, the attractive electron-nucleus interaction is given by $U_{j\alpha} = \int V_{j\alpha}(\mathbf{r})n(\mathbf{r})$, and $V_{xc}(\mathbf{r}) = \partial E_{xc}[n]/\partial n(\mathbf{r})$. The term $V_H(\mathbf{r})$ corresponds to the Hartree potential and describes the electron-electron Coulomb interaction, according to $V_H(\mathbf{r}) = \int \frac{n(\mathbf{r}')}{|\mathbf{r}-\mathbf{r}'|} d\mathbf{r}'$. Note that $V_H(\mathbf{r})$ contains an erroneous self-interaction contribution, as it allows an electron to interact with itself. The correction term for the unphysical self-interaction is taken care of in V_{xc} .

Even though the total energy obtained by the KS approach is the true total energy of the system, there is no such guarantee for the KS energy eigenvalues. The exception is the energy of the highest occupied state of a finite system, which corresponds to the ionization energy. The total energy is defined in KS theory as

$$E[n] = \sum_j \epsilon_j^{\text{KS}} - \frac{1}{2} \iint \frac{n(\mathbf{r})n(\mathbf{r}')}{|\mathbf{r}-\mathbf{r}'|} d\mathbf{r}d\mathbf{r}' + E_{xc}[n] - \int V_{xc}(\mathbf{r})n(\mathbf{r})d\mathbf{r}, \quad (4.18)$$

an expression that provides the true total energy despite the fact that the wavefunctions used to obtain E may be wrong — provided that the correct exchange-correlation functional $E_{xc}[n(\mathbf{r})]$ can be identified. And indeed, herein lies the real challenge for conducting DFT calculations on real systems such as semiconductor crystals: the exchange-correlation functional is simply not known.

4.3 Practicalities

In practice, a number of different implementations for the Kohn-Sham DFT exist. Common to them all is an iterative scheme for conducting a calculation known as the *self-consistent field* (SCF) method [98]:

1. The initial atomic structure, potentials and settings are decided.
2. An initial guess for the electron density $n(\mathbf{r})$ is provided.
3. The effective potential $V_{\text{eff}} = V_H + V_{j\alpha} + V_{xc}$ is calculated from $n(\mathbf{r})$.
4. The Kohn-Sham equations are solved and $E[n]$ is determined.
5. The new density is determined from $n'(\mathbf{r}) = \sum_j |\psi_j^{\text{KS}}|^2$.
6. Is the energy self-consistent, that is, is $E[n] \simeq E[n']$?
7. If NO, return to item 3 and repeat until self-consistency is reached.

8. If YES, output energies and forces for the atomic structure.
9. If relaxing atomic configuration, check the maximum force. Revise atomic structure and return to beginning if forces are above some threshold value.
10. When the atomic configuration is satisfactory, output energies, forces etc. and terminate the calculation.

4.3.1 The exchange-correlation energy

Although the DFT is exact in theory, in practice, we must resort to approximations to the exchange-correlation energy. In this section, three main functionals that have been applied (with success) to bulk semiconductor materials are reviewed.

Fortunately, there is one system for which the exchange-correlation functional can be exactly determined: the uniform electron gas [98] or *jellium*, for which $n(\mathbf{r}) = \text{constant}$. Of course, this seems inconvenient for the present purpose, given that the local variations in electron density are exactly what gives rise to interesting material properties. However, the *local density approximation* (LDA) to the exchange-correlation functional relies on the homogeneous electron gas in that the exchange-correlation potential at each point in space is derived from the known exchange-correlation potential of the uniform electron gas for the specific (local) electron density at each position [100]:

$$V_{\text{xc}}(\mathbf{r}) = V_{\text{xc}}^{\text{electron gas}}[n(\mathbf{r})]. \quad (4.19)$$

The LDA (or LSDA when spin is incorporated) is the simplest approximation to $E_{\text{xc}}[n(\mathbf{r})]$ in modern DFT, and provides an efficient way to approximately solving the many-body SE (Eq. 4.2). However, the main drawback of the LDA is that the self-interaction error is not properly accounted for, and the fact that electrons (incorrectly) interact with themselves results in artificial repulsion and thus exaggerated electron delocalization. Moreover, the electron density of atoms and molecules can hardly be seen as nearly constant, and the LDA has therefore been more successful for bulk materials with slowly varying density [98].

Variations in the electron density are profoundly important in material science, and can be accounted for by using the spatial variation in $n(\mathbf{r})$. This is incorporated in the *generalized gradient approximation* (GGA) to DFT [98], where

$$V_{\text{xc}}^{\text{GGA}}(\mathbf{r}) = V_{\text{xc}}[n(\mathbf{r}), \nabla n(\mathbf{r})], \quad (4.20)$$

and is valid when the electron density varies slowly. In the present work, the non-empirical Perdew-Burke-Ernzerhof (PBE) [101] implementation of the GGA was employed.

Even though the GGA and LDA have been highly successful, for instance in predicting structural properties of crystals and binding energies of molecules, an important drawback for the present work is a systematic underestimation of the semiconductor band gap. Additionally, the LDA/GGA approach is associated with large uncertainties when predicting charge localization and charge-state

4. Modeling of point defects in SiC

transition levels in semiconductors, an issue which has been attributed to the self-interaction error [102]. *Hybrid* functionals intermix the exchange-correlation potential of (semi)local functionals based on the LDA or GGA with exact exchange from Hartree-Fock theory, E_x^{HF} [103]. As previously mentioned, the HF method exactly cancels self-interaction errors and thus accounts for exchange correctly, albeit while simultaneously neglecting correlation effects. In the hybrid functional approach to DFT, the exact exchange of HF and correlation of LDA/GGA complement each other, and some of the self-interaction error is canceled. Initially, a half-and-half approach using 50 % each of the HF and LDA energy functionals was proposed [103], but was later revised to 25 % of HF exact exchange [104]. Importantly, exact exchange is non-local, and thus the long-range part of the exchange integral is challenging to compute for large systems [102], making computational demand the main obstacle for wide-spread implementation of the hybrid approach to DFT. A solution to this was proposed by Heyd et al. [105] and involved separating the non-local E_x^{HF} functional into a long-range and a short-range part, mixing exact exchange into the short-range portion only, and replacing the exact exchange by a screened version. The separation is controlled by a parameter ω , and the functional using $\omega = 0.2 \text{ \AA}^{-1}$ and $\alpha = 25 \%$ exact exchange is known as HSE06 (Heyd-Scuseria-Ernzerhof) [105]:

$$E_{\text{xc}}^{\text{HSE}} = \frac{1}{4}E_x^{\text{HF,SR}}(\omega) + \frac{3}{4}E_x^{\text{PBE,SR}}(\omega) + E_x^{\text{PBE,LR}}(\omega) + E_c^{\text{PBE}}. \quad (4.21)$$

The terms SR and LR signify short-range and long-range, respectively.

Importantly, the hybrid functionals cannot strictly be classified as non-empirical (which the LDA and GGA functionals are). Semi-empirical functionals rely on *ab initio* and experimental data, and can be highly accurate, but the screening (ω) and mixing (α) parameters of the HSE06 functionals are commonly adjusted to agree with experimental properties, such as the semiconductor band gap.

4.3.2 Numerical implementation

To implement the KS equations numerically, we express the single-electron KS wavefunctions in a finite basis set

$$\psi_j = \sum_{i=1}^I c_i^j \psi_i^{\text{basis}}, \quad (4.22)$$

which is not exact (due to the truncation at I) but enables numerically efficient implementation. The choice of basis set should be strongly influenced by the system properties, and in crystalline materials it is beneficial to choose a basis which retains the periodicity of the lattice, such as the Bloch function

$$\psi_{n\mathbf{k}}(\mathbf{r}) = e^{i\mathbf{k}\cdot\mathbf{r}} u_{n\mathbf{k}}(\mathbf{r}) \quad (4.23)$$

where the first term is a plane-wave and the second term is the Bloch wave enveloping the lattice periodicity. The calculations conducted in the present work employed the Vienna *ab-initio* simulation package (VASP) [106, 107] and the **Quantum Espresso** [108, 109] codes, which both employ a plane-wave wavefunction basis.

Practically, it is more efficient to solve the KS equations in reciprocal (or \mathbf{k}) space, and the Kohn-Sham equations are thus Fourier transformed into

$$\sum_{\mathbf{G}'} \left((\mathbf{k} + \mathbf{G}) \delta_{\mathbf{G}\mathbf{G}'} + V_{\mathbf{G}-\mathbf{G}'} \right) u_{n\mathbf{k}+\mathbf{G}'} = \epsilon_{n\mathbf{k}} u_{n\mathbf{k}+\mathbf{G}'} \quad (4.24)$$

and solved by matrix diagonalization for the eigenvalues $\epsilon_{n\mathbf{k}}$. Here, the issue of *convergence* should be addressed. Firstly, the sum over \mathbf{G} -vectors is infinite and must be truncated at some appropriate value G_{cutoff} , commonly defined from the plane-wave kinetic energy $E_{\text{cutoff}} = (1/2)G_{\text{cutoff}}^2$. When conducting a DFT calculation, one should be careful to determine an appropriate value for E_{cutoff} , by ensuring that the change in total energy for the system between two different cutoff energies is below some critical value for convergence. Secondly, Fourier transforming the KS equations results in DFT calculations involving a series of integrals over the first Brillouin zone (BZ) of the form [98]

$$A = \frac{V_{\text{cell}}}{(2\pi)^3} \int_{\text{BZ}} g(\mathbf{k}) d\mathbf{k} \quad (4.25)$$

where V_{cell} is the volume of the primitive cell in real space. Carefully considering which \mathbf{k} -points to include in the evaluation of the integrals may therefore profoundly impact the computational demand. Importantly, distances in reciprocal space are inverse to those in real space, and thus using a larger amount of atoms in a calculation results in needing fewer \mathbf{k} -points. Exploiting the symmetry of the system being studied also reduces the required \mathbf{k} -mesh size, and a strategy to this effect was developed by Monkhorst and Pack (MP-type \mathbf{k} -mesh) [110]. Moreover, if the function to be integrated over the BZ has a discontinuity (e.g., metals), a large number of \mathbf{k} -points would be needed, which is solved by implementing a scheme such as the tetrahedron method or the smearing method [98]. In close analogy to the case for the cutoff energy, one should ensure convergence for the \mathbf{k} -mesh density for each specific system. Note that convergence is usually achieved much faster when considering energy differences, e.g., when constructing a formation energy diagram, as compared to total energy calculations, due to cancellation of systematic errors.

The valence electrons in a semiconductor are loosely bound to the nucleus and thus well described as plane-waves. The wavefunctions of the core electrons, on the other hand, oscillate more rapidly and should be described by other means. Fortunately, core electrons are much less important than valence electrons in determining material properties of interest for this thesis, and can therefore be replaced by an effective *pseudopotential*. The calculations encompassed herein employed either norm-conserving pseudopotentials [111] (**Quantum Espresso** calculations) or the Projector Augmented-Wave (PAW) method [112–114] (VASP calculations).

4.3.3 Capabilities and drawbacks of DFT

If we could discover the true nature of $E_{\text{xc}}[n]$, the resulting total energy from density functional theory would be exact. However, the exchange-correlation functional is unknown for most systems, necessitating the use of approximations which may affect the accuracy of DFT calculations. Moreover, advances in describing $E_{\text{xc}}[n]$ accurately are often accompanied by an increase in computational demand. On the other hand, any electronic system can be described by the DFT, and different approximations to E_{xc} can be readily implemented in most codes.

DFT is incredibly powerful in that it allows us to investigate novel and exotic features of nature in a computationally efficient manner. However, one should note that DFT can only ever access local minima, and it is impossible to ascertain whether the correct global minimum has in fact been found. Nature is much too complex for all possible configurations to be investigated, at least with the resources that are currently available, and DFT is therefore most powerful when it can be combined with experimental techniques. The subsequent chapters will therefore outline methods for performing specific calculations on defects in semiconductor materials that can be directly compared with experiment.

4.4 Defect calculations

Point defects can fundamentally alter the electronic, optical and mechanical properties of semiconductor materials, and their understanding is therefore vital for a broad range of applications. First-principles calculations as implemented in Kohn-Sham DFT serve as a powerful supplement to experimental defect studies [102], and the present chapter outlines important tools for predicting electrical and optical defect signatures.

4.4.1 The supercell approach

By relaxing the atomic configurations and minimizing the forces in a semiconductor unit cell, the optimal inter-atomic distances and lattice constants can be identified. By adding or removing atoms at will, a defect can be introduced into the unit cell. However, real-life defect experiments mostly concern the *dilute* limit, where the defects can be separated by several 100 nm. To replicate experimental conditions, we construct *supercells* of up to several hundred atoms and embed a defect, such as a vacancy, therein. Using periodic boundary conditions, the defect system can be repeated indefinitely. However, embedding defects in supercells causes finite-size errors, necessitating the use of corrections in certain cases. The errors that arise due to supercell size can be quantum mechanical, electrostatic, elastic or magnetic [102]. For instance, the use of small supercells may result in unintentional wavefunction overlap between the defect states, causing the formation of defect bands as opposed to discrete defect states. Importantly, if the defect energy depends on the \mathbf{k} -points employed, one should take care to either increase the size of the \mathbf{k} -mesh, avoid using Γ (as the

interaction is strongest here) or increase the supercell size. Ideally, we would need millions of atoms to perfectly capture reality, but computational demand increases rapidly with the supercell size and employing more than 500 atoms, particularly for hybrid DFT calculations, is highly challenging. In the present work, supercells of either 96 or 400 atom size were employed, ensuring at least 10 Å between each periodical image of the defect.

Defects frequently act as carrier traps in semiconductors, necessitating the addition of charge beyond neutral conditions to supercell calculations. The periodic background conditions engender spurious Coulomb interactions between the repeated defect charges, and as electrostatic interactions decay far too slowly for large enough supercells to be feasible, appropriate corrections must be implemented. Firstly, during the DFT calculation a homogeneous background charge (jellium) is added to compensate for the defect charge, as the total energy of a charged periodic system diverges. Secondly, as the Coulomb interaction acts over a long distance, an absolute reference for the potential is needed, which is obtained by aligning the valence band maximum to that of the supercell without the charged defect [102]. Finally, the unphysical interactions between charged defects and with the jellium background charge give rise to a spurious energy contribution, which can be accounted for in the defect total energy by adding a correction term. The correction scheme that was applied in the present work is called the extended Freysoldt-Neugebauer-Van de Walle (FNV) correction scheme [115–117], and accounts for both the potential alignment and corrects the macroscopically screened Madelung energy of a localized charge. The extended FNV scheme assumes a point charge model, is valid for localized charges, and is appropriate for anisotropic materials as the dielectric tensor is employed instead of the dielectric constant. Herein, experimental values for the dielectric tensor of 4H-SiC were employed [118].

4.4.2 Formation energy diagrams

To properly understand the potential effect of a defect on a semiconductor material, the *formation energy diagram* of the defect can be computed, showcasing the stability of different defect charge states versus the Fermi level (i.e., the doping conditions). From the formation energy diagram, several important features can be deduced: (i) by comparing different defect configurations the most stable candidate can be identified, (ii) the formation energy translates into the expected defect concentration at thermal equilibrium, and (iii) the charge-state transition levels of the defect within the band gap can be identified. Charge-state transitions can reveal whether a defect acts as a carrier trap and expose any potential negative- U nature in the transitions, among other properties [102, 119]. The formation energy (E^f) diagram for a defect species X of charge state q can be constructed from

$$E^f[X^q] = E_{\text{total}}[X^q] - E_{\text{total}}[\text{bulk}] - \sum_i n_i \mu_i + qE_F + E_{\text{corr}}, \quad (4.26)$$

4. Modeling of point defects in SiC

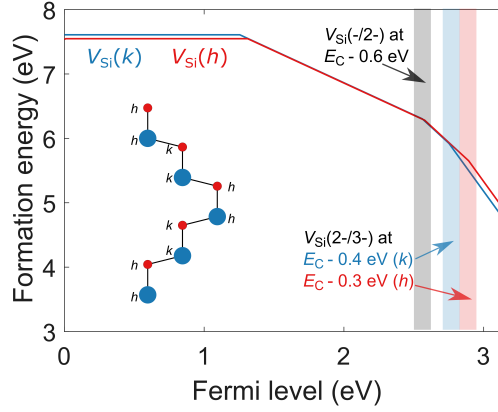


Figure 4.1: Formation energy diagram for the Si vacancy in 4H-SiC computed using a 96-atom supercell. Adopted from Paper I.

where E_{total} refers to the total energy of the relaxed supercell either with or without a defect as determined by DFT calculations, n_i is the number of atoms of chemical species i that are either added to ($n_i > 0$) or removed from ($n_i < 0$) the supercell to form the defect, μ_i refers to the chemical potential of the corresponding atomic species and accounts for the energy cost for exchanging n_i atoms of species i with their reservoir, E_F is the Fermi level and E_{corr} refers to the FNV electrostatic correction term discussed above. Note that this approximation to the formation energy assumes that the supercell volume is fixed, i.e., the formation volume energy is not included and entropy contributions are neglected [102]. The chemical potential depends on the formation conditions for the defect, e.g., if the sample processing occurs in Si rich or Si poor conditions or somewhere in between. Therefore, μ should be carefully chosen when comparing computed formation energies with defect concentrations after heat treatments.

An example formation energy diagram is shown for the Si vacancy (V_{Si}) in 4H-SiC in Figure 4.1. For moderately doped n-type material, the elevated temperatures that manifest during 4H-SiC growth will induce Fermi levels near mid-gap, where the V_{Si} formation energy is approximately 7.5 eV. At thermal equilibrium, this translates roughly into a V_{Si} concentration of $[V_{\text{Si}}] \sim 10^7 \text{ cm}^{-3}$, which is far below the detection limit of characterization techniques wherein the V_{Si} has been identified, including DLTS and PL spectroscopy (see Paper I). Hence, the DFT formation energies can provide valuable hints as to the expected concentration of a specific defect within a sample. If the defect in question is an impurity, techniques such as secondary ion mass spectrometry (SIMS) can be helpful in verifying the defect concentration.

The formation energy diagram in Fig. 4.1 contains another noteworthy feature, and that is the thermodynamic charge-state transition levels that are defined as the Fermi level at the kinks, where the formation energies of two different charge

states are equal. Note that the distance between a defect level and either of the band edges indicates whether a defect can be termed shallow (energy difference approaches the thermal ionization energy) or deep. Importantly, these levels determine the impact of the defect on the electrical properties of a material, and give rise to signals that can be detected experimentally to determine a defect's presence. The transition levels mark where charge carriers are interchanged between the defect and the semiconductor band edges, a process which can be monitored using for instance electrical characterization (such as DLTS) or optical characterization (such as photoluminescence or cathodoluminescence spectroscopy). By combining the theoretical and experimental approaches, defect signatures can be identified.

4.4.3 Defect states and internal transitions

The thermodynamic charge-state transitions of a defect are slow, and occur on a timescale that allows for the lattice to rearrange upon charge carrier exchange with the band edges. Optical transitions, on the other hand, are too fast for atoms surrounding a defect to respond, and the lattice remains frozen during the process. Several commonly discussed optical transitions involve charge carrier exchange with the host matrix, however, an alternative transition path involves internal excitation of the defect wherein the number of charge carriers trapped at a defect remains constant. Herein, the latter transition type will be discussed, and involves transitions between defect ground and excited states and the subsequent emission of a photon (see Section 2.3.5). Using DFT calculations, both the zero phonon line (ZPL) and the phonon side-band (PSB) of defect-related emission can be determined.

Defects may introduce orbital states within the semiconductor band gap. For instance, recall (from Section 3.3.5) that the V_{Si} in 4H-SiC introduces one a_1 state that is resonant with the valence band, one a_1 state within the gap and one degenerate e state within the gap [82, 86], with occupations for the ground and excited states as illustrated by the conceptual diagrams shown in Fig. 3.5 for the negatively charged V_{Si} (V_{Si}^-). The five valence electrons located at V_{Si}^- organize in a high-spin fashion with a total spin of $S = 3/2$ [75, 77, 78, 82, 86]. In the ground state, the lowest-lying a_1 state is fully occupied, and upon excitation, a spin-down electron from the valence band edge is promoted to the higher a_1 orbital for the first excited state (V1 and V2 for h and k V_{Si} , respectively), and to e for the second excited state (V1' and V2').

The schematic diagrams in Fig. 3.5 are based on results obtained from hybrid DFT calculations by investigating the occupation of the single-particle KS states [82, 86]. The total spin state as predicted by DFT calculations has proven to be reliable in many cases, however, the state ordering and energies as determined from the KS single-particle energies do not directly reproduce the physical quasi-particle eigenvalues, because of the self-interaction error. Although comparison to experiment has shown that KS states are indicative of which transitions may occur, the single-particle level occupation should be constrained when considering ES-to-GS transitions. That way, the zero-phonon line energy can be estimated

according to the delta-self consistent field (Δ -SCF) method [120–122], and equals the difference between the excited and ground state total energies. Combined with the HSE06 functional, this method can yield ZPL energies that agree with experimental values to within 0.1 eV for, e.g., the divacancy in SiC [78]. Of course, DFT is inherently a ground state and $T = 0$ K method, and certain systems might necessitate the use of more accurate methods such as many-body perturbation theory, time-dependent DFT, configuration interaction and coupled cluster calculations [119].

4.4.4 Configuration coordinate diagrams

Configuration coordinate (CC) diagrams, as discussed qualitatively in Section 2.3.5, are an important tool when investigating both thermodynamic and optical transitions, and can be quantitatively constructed from DFT calculations [102, 119, 123]. In this context, the configuration coordinate Q represents the displacement of atoms surrounding the defect center, and is taken to be a linear interpolation between the equilibrium configurations of the ground and excited states to be studied. CC diagrams can provide information on both thermodynamic and optical transitions when studying charge carrier exchange between defect states and the band edges.

In the case of a thermodynamic charge-state transition, the energy that must be supplied to add or remove the electron equals the charge-state transition level in the semiconductor band gap. As previously mentioned, DLTS is an excellent tool to probe this parameter. However, the activation energy for charge-state transitions that is acquired using DLTS measurements contains both the ionization energy (that is calculated from DFT) and an additional barrier for carrier capture, which can be large in some cases. By constructing a CC diagram for the charge-state transition from linear interpolation of coordinates, an approximation for the capture barrier can be made. More relevant for the present work is the construction of CC diagrams to investigate internal ES-to-GS transitions of defects such as the V_{Si} in 4H-SiC. The excited state configuration and total energy can be acquired by constraining the KS state occupation, and again the CC diagram is constructed by linear interpolation.

Regardless of whether the optical transition in question involves a change in the charge state of the defect or not, the CC diagram can be used to estimate the Huang-Rhys factor (S) governing the electron-phonon coupling and to form a theoretical prediction for the full luminescence *lineshape*. This is provided that the electron-phonon coupling is sufficiently strong, such that the various types of vibrational modes can be replaced by the single effective modes in the 1D CC model [123, 124]. For weak and intermediate coupling, the PL spectrum is dominated by a strong ZPL and a fine structured phonon side-band, and the 1D CC model is no longer sufficient [119, 125]. Depending on the strength of the electron-phonon coupling for the transition in question, various types of vibrational modes need to be included when computing features such as the Huang-Rhys factor, the Debye-Waller factor (or ZPL weight) and the form of the PL emission.

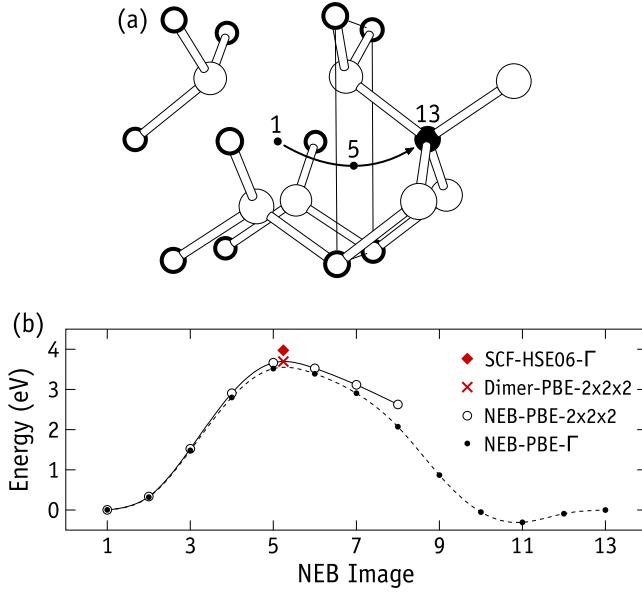


Figure 4.2: V_C migration in 3C-SiC as illustrated by (a) the atomistic structure surrounding a V_C defect (Si in white, C with thick black halos) and the approximate path a C atom (black) will follow when jumping into the vacant site. Dots and numbers indicate the position of the V_C along the path. In (b) we show the energies of intermediate structures along the V_C trajectory as obtained using the nudged elastic band (black dots) and dimer (red cross) methods. Adopted from Paper IX.

4.4.5 Modeling defect migration and complex formation

Defect migration is a vital process to understand when investigating processes such as defect stability, out-annealing and complex formation. Historically, point defect diffusion used to be predicted by fixing potential geometries for the migrating species along a pre-determined path, computing the total energy and thus extracting the potential energy surface (PES) for the process. However, even though several likely pathways can be explored in this fashion, there is no way to know that the true minimum energy path (MEP) has been identified. Both Monte Carlo simulations and Molecular Dynamics calculations can be used to this end, but herein we will focus on the nudged elastic band (NEB) [126, 127] and dimer [128] methods.

The NEB method as implemented in the `VASP` and `Quantum Espresso` codes involves optimizing the geometric structure of the initial and final states of some migration process by DFT calculations, and generating a series of intermediate *images* that form the first guess for the migration path. The images are connected by spring forces to ensure equal spacing between them, and via such constrained optimization, each image obtains its lowest energy along the migration path.

Thus, a snapshot of the PES can be obtained, and the saddle point identified. The climbing image NEB method ensures that the highest energy image on the MEP lies at the top of the curve, and thus promises a better estimate of the transition state [129]. Activation energies (E_A) for migration, or the migration barrier, are defined as the difference in total energy between the saddle-point configuration (the transition state) and the stable configuration (the initial state).

As an alternative to performing a climbing image NEB calculation, the dimer method can be employed to procure the correct transition state geometry. Ideally, the dimer method requires an initial geometry and a direction to search along the MEP as input, but can also start from any minimum and search randomly along the PES. By using first derivatives of the potential energy, the dimer method identifies a nearby saddle point without knowing the final state. The combination of fast NEB calculations with subsequent accurate dimer calculations present an optimized approach to search for the transition state geometry along defect migration pathways.

An example of combining the NEB and dimer methods is illustrated in Figure 4.2 for V_C migration in 3C-SiC, with the V_C migration path shown schematically in Fig. 4.2(a) and the minimum energy path deduced using the NEB method shown in Fig. 4.2(b). First, the initial MEP (dashed line) is identified using the PBE functional and Γ -only BZ sampling, and the activation energy for migration at PBE level is estimated at 3.5 eV. Next, more accurate NEB calculations (solid line) and the dimer method (red cross) are compared, both using 420 eV energy cutoff and $2 \times 2 \times 2$ \mathbf{k} -point sampling and yielding identical migration barriers of 3.7 eV, but with the dimer method being more computationally efficient. Finally, one-shot self-consistent field (SCF) calculations are conducted on top of the transition state geometry using the Γ \mathbf{k} -point and the HSE06 functional (red diamond) to acquire a final activation energy for V_C migration in 3C-SiC of 4.0 eV.

4.4.6 Electric field application

Electric fields have been shown to shift the emission energies from the NV center in diamond [31], and the Si vacancy (see Paper I and Paper II and Ref. [94]) and divacancy [91, 93] in 4H-SiC. To investigate the interplay between defect wavefunctions and external perturbation theoretically, electric fields can in theory be applied to the supercell during DFT calculations. However, this necessitates the incorporation of an electric field in the Hamiltonian, which should preferably be based on first-principles and employs periodic boundary conditions in three dimensions. In Paper II, we discuss a method for evaluating electric field effects on defect states based on including a sawtooth-shaped potential across the periodic supercell [130]. Numerical instabilities due to the superposition of strongly varying potential “teeth” with the atomic potentials are avoided by using periodic slabs separated by thick vacuum layers wherein we place the field “teeth”. At the time of writing, the quadrupole corrections that are required when combining an electric field with a charged system had only been implemented for

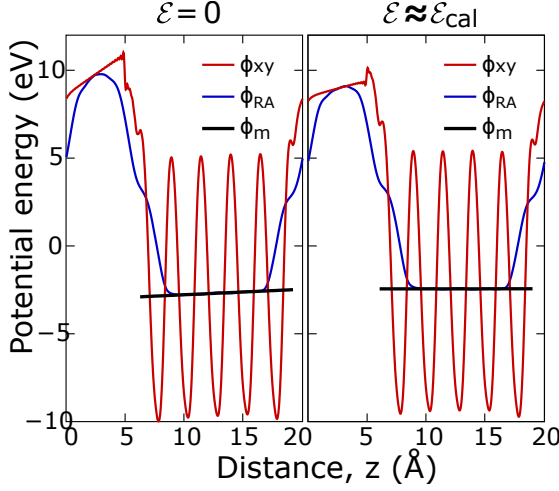


Figure 4.3: Analysis of the electrostatic potential across a defect-free slab for zero electric field (left) and an applied calibration field of $\mathcal{E} \approx \mathcal{E}_{\text{cal}}$ (right). The schematics show the xy -averaged electrostatic potential energy (ϕ_{xy}), the rolling-averaged potential (ϕ_{RA}), and the macroscopic potential in the slab (ϕ_{m}) as found from a linear fit to the ϕ_{RA} data near the center of the slab. Adapted from Paper II.

cubic supercells in the VASP code. Therefore, **Quantum Espresso** was employed for all electric field calculations conducted throughout the course of this work.

Slabs made of non-centrosymmetric materials, such as 4H-SiC, have asymmetric slab surfaces that induce an internal field. This internal field has to be canceled prior to conducting defect calculations by adding an identical but oppositely directed calibration field, \mathcal{E}_{cal} . Figure 4.3 displays the asymmetry in the electrostatic potential over a defect-free (300-atom) slab for zero applied field on the left-hand-side. The red line shows the xy -averaged electrostatic potential energy (ϕ_{xy}), and the blue one the rolling-averaged potential (ϕ_{RA}). A defect embedded within the slab will experience a local macroscopic field

$$\mathcal{F} = -d\phi_{\text{m}}/dz, \quad (4.27)$$

where z is the direction corresponding to the crystallographic c -axis and ϕ_{m} is the macroscopic electrostatic potential over the slab. As illustrated in Fig. 4.3, ϕ_{m} can be identified from a linear fit (black line) to the rolling-averaged potential (ϕ_{RA}). The local *built-in* field over the slab (prior to applying an external field) is herein denoted \mathcal{F}_{bi} . Adding an electric field \mathcal{E} to the slab modifies the local field according to

$$\mathcal{F} = \frac{\mathcal{E}}{\epsilon} + \mathcal{F}_{\text{bi}}, \quad (4.28)$$

where ϵ is the effective slab screening constant. By relaxing a set of pristine slabs under varying electric field conditions, and fitting a set of $(\mathcal{E}, \mathcal{F})$ data

4. Modeling of point defects in SiC

points to Eq. 4.28, \mathcal{F}_{bi} and ϵ can be identified. From there, we can find the neutralization or calibration field that will offset the local field experienced by a defect to zero, according to $\mathcal{E}_{\text{cal}} = \epsilon \mathcal{F}_{\text{bi}}$. The result of such a calibration is shown on the right-hand-side of Fig. 4.3.

The procedure towards identifying the calibration field to offset the local field to zero can be summarized as follows.

1. Estimate the built-field ($\tilde{\mathcal{F}}_{\text{bi}}$) over a defect-free slab from the macroscopic electrostatic potential.
2. Find an estimate for the calibration field according to $\tilde{\mathcal{E}}_{\text{cal}} = \epsilon_{\text{s}} \tilde{\mathcal{F}}_{\text{bi}}$, where we use $\epsilon_{\text{s}} = 10$ for SiC.
3. Choose a suitable local field and corresponding applied field range close to \mathcal{E}_{cal} .
4. Compute a set of $(\mathcal{E}, \mathcal{F})$ data points within the chosen range.
5. Fit the $(\mathcal{E}, \mathcal{F})$ data to Eq. 4.28, and extract the built-in field and screening constant from the linear fit to arrive at \mathcal{E}_{cal} .

Once the calibration field has been identified, a defect can be introduced into the slab and its geometry and electronic structure optimized under the calibration field constraints. The zero-phonon line energy of defect emission is obtained via the delta-self consistent field (Δ -SCF) method [120–122] as the total energy difference between the ground and excited state. We monitor the Stark shift as a second order expansion in the applied field according to

$$\Delta E_{\text{ZPL}} = -\Delta\mu \mathcal{F} - \frac{1}{2} \Delta\alpha \mathcal{F}^2, \quad (4.29)$$

where \mathcal{F} is the local field and $\Delta\mu$ and $\Delta\alpha$ are respective changes in the dipole moment and polarizability between the excited and ground states [131]. Note that Eq. 4.29 is not scalar in general, and may contain additional (or fewer) terms for other problem types.

4.5 Computational details

The defect calculations performed herein on 4H-SiC material can be roughly grouped into three categories depending on the supercell type employed: (i) formation energy diagram construction in 96-atom orthorhombic supercells, (ii) defect diffusion and complex formation studies in hexagonal 400-atom supercells, and (iii) excited state and electric field effect studies on 300-atom slab supercells.

4.5.1 Orthorhombic supercells

The calculations conducted employing 96-atom orthorhombic supercells and the VASP code are quoted in Paper I, Paper V and Paper VII. Note that the HSE06 functional was used to describe valence electrons and the PAW method to describe

core electrons. The supercell was constructed by designing an orthorhombic 96-atom structure from the relaxed 4H-SiC unit cell. The calculated SiC band gap of 3.17 eV at 0 K showed good agreement with the experimental value of 3.27 eV [132]. Si and C vacancies (V_{Si} and V_{C}) were formed by removing a Si or C atom at either the h or k site from the supercell, respectively. Defect calculations were conducted by optimizing forces to below 0.1 eV/Å using Γ -only BZ sampling, and then continuing to below 0.02 eV/Å maximum forces using a $2 \times 2 \times 2$ MP-type \mathbf{k} -mesh. The plane-wave energy cutoff was set to 420 eV and the self-consistent loop criterion was set to 10^{-6} eV.

Formation energy diagrams were constructed for V_{Si} and V_{C} from the total energies of defective and pristine supercells according to Eq. 4.26. The energy of charged systems was corrected using the extended FNV correction scheme [115–117] and employing empirical data for the SiC dielectric tensor. The chemical potentials needed for computing the V_{Si} and V_{C} formation energies were obtained by relaxing Si, diamond and SiC unit cells to have forces below 0.005 eV/Å. Note that the 96-atom supercell is rather small, and mirroring effects may arise. However, the orthorhombic structure ensures ~ 10 Å inter-defect distance in all directions, and the thermodynamic charge-state transitions found for V_{Si} agree within 0.1 eV with those obtained from tests with 400-atom supercells.

4.5.2 Defect diffusion and complex formation

Although the 10 Å defect-defect distance in 96-atom supercells can be sufficient for considering formation energy diagrams of Si and C vacancies, larger supercells were herein employed when studying defect complexes and point defect migration. The calculations conducted employing 400-atom hexagonal supercells and the VASP code are quoted in Paper V, Paper VII and Paper IX. Note that Paper IX also contains calculations that were performed for the 3C-SiC polytype using 216-atom hexagonal supercells.

We consider three separate cases utilizing this supercell type: (i) formation energies of interstitial hydrogen and complexes between $V_{\text{Si}}/V_{\text{C}}$ and hydrogen (Paper V and Paper VII), (ii) migration of interstitial H and V_{Si} -H complex dissociation (Paper V), and (iii) diffusion of V_{C} in 3C- and 4H-SiC (Paper IX).

In Paper V and Paper VII, properties of hydrogen-related defects in 4H-SiC are explored. Hydrogen interstitials and complexes between H and V_{Si} and V_{C} are embedded within 400-atom 4H-SiC supercells, and defect geometry optimization was performed in two stages: (i) PBE-level defect relaxation using a $2 \times 2 \times 2$ \mathbf{k} -mesh and a 0.01 eV/Å force criterion, and (ii) HSE06-level relaxation using Γ -only BZ sampling and relaxing forces to below 0.05 eV/Å. Migration of hydrogen interstitials and dissociation of V_{Si} -H complexes within 4H-SiC (Paper V) was studied using the climbing image nudged elastic band method, 11 intermediate images, the Γ -point for \mathbf{k} -point sampling, the PBE functional and force relaxation to below 0.01 eV/Å. The stopping criterion for the electronic self-consistent loop was set to 10^{-6} eV, the plane-wave energy cutoff to 420 eV, and the extended FNV correction scheme was again employed to remedy spurious electrostatic interactions between charged supercells.

4. Modeling of point defects in SiC

In-depth studies of V_C migration in 3C (216 atoms) and 4H (400 atoms) SiC are conducted in Paper IX. To replicate experimental conditions, the neutral charge state of V_C was studied in both cases. The V_C geometry was optimized using PBE, 420 eV energy cutoff, a 10^{-6} eV energy loop, $2 \times 2 \times 2$ BZ sampling and a force convergence threshold of 0.01 eV/Å. Using this method, initial and final images for V_C migration in 3C- and 4H-SiC were acquired. The migration paths and activation energies for V_C^0 migration were explored in three stages:

1. First, an exploratory NEB calculation (not using the climbing image approach) was conducted using 11 intermediate images, 300 eV cutoff energy and Γ -only BZ sampling.
2. Next, we refined the transition state geometry and energy by (i) higher accuracy NEB calculations surrounding the saddle point, or (ii) using the image of highest energy identified by the initial NEB calculation as a starting point, and conducting a dimer calculation from there. The second round of NEB calculations employed 5 intermediate images, and both the NEB and dimer calculations were conducted using the same calculation parameters (cutoff energy, \mathbf{k} -mesh and force criterion) as the initial V_C relaxations.
3. Finally, following refinements of the transition state, one-shot self-consistent field calculations were used to resolve the energy barrier for V_C migration. In this context, we employed HSE06, 420 eV cutoff energy and the Γ -point.

4.5.3 Electric field effects and excited states

The effect of electric fields on defect states was studied using 300-atom slab supercells and the **Quantum Espresso** software in Paper II. Norm-conserving pseudopotentials (NC-PP) [111, 133] and plane-waves were employed to describe core and valence electrons, respectively. Most of the calculations in Paper II employed the semi-local Perdew, Burke and Ernzerhof (PBE) functional for describing the many-body electronic interactions, however, some calculations were carried out using a non-local hybrid functional as proposed by Song, Yamashita and Hirao [134] (Gau-PBE). The plane-wave energy cutoff was set to 680 eV for the wavefunctions and 2720 eV for the charge density, with force and energy tolerances for the ionic relaxation of 0.01 eV/Å and 1 μ eV, respectively.

The 300-atom hexagonal slab supercells contained 125 C atoms and 125 Si atoms, and were terminated at both ends by 25 H atoms to minimize the charge-transfer between C and Si surfaces. The thickness of the slab and vacuum layers were set to $w_{\text{SiC}} = 2c$ and $w_{\infty} = c$, respectively, making the supercell length along the hexagonal axis equal to $3c$. To optimize the slab geometry (using PBE), the H atoms were relaxed first to find the ideal Si-H and C-H bond lengths, before the Si-H and C-H dimers were kept frozen and the inner slab atoms allowed to move. A $2 \times 2 \times 1$ \mathbf{k} -mesh was employed for all PBE level relaxations while Γ -only Brillouin-zone (BZ) sampling was used for hybrid SCF calculations.

An external electric field (\mathcal{E}) was applied to the slab along the c -axis by adding a sawtooth term to the local potential. The vacuum portion of the supercell geometry was employed to avoid the superposition of artificial charge density singularities with the SiC electronic states, and the potential “teeth” were therefore placed within the vacuum region (see Fig. 4.3). The maximum of the applied electric field was therefore located at 75 % along the c -axis. Electric field calibration resulted in built-in field values and slab dielectric constants of $\mathcal{F}_{\text{bi}} = -3.4$ MV/m and $\epsilon = 10.1$ for h -centered slabs, and $\mathcal{F}_{\text{bi}} = -2.6$ MV/m and $\epsilon = 11.4$ for k -centered slabs. The dielectric constants are quite close to the experimental static dielectric constant parallel to the c -axis of 10.03 [118]. Additionally, we extract calibration fields (to offset the local field to zero) of $\mathcal{E}_{\text{cal}} = 34.3$ MV/m and $\mathcal{E}_{\text{cal}} = 29.6$ MV/m for h - and k -centered slabs, respectively.

Si vacancies were formed by removing either a Si(h) or Si(k) atom from the center of the slab. Two separate slabs were constructed to ensure identical placing of $V_{\text{Si}}(h)$ and $V_{\text{Si}}(k)$. The defect geometry of V_{Si}^- was optimized using the PBE functional and under the constraint of a calibration field (\mathcal{E}_{cal}). The ground state electronic structure of V_{Si}^- organizes as ${}^4A_2 \equiv \Gamma_v(\uparrow\downarrow) + [a_1(\uparrow) + e(x\uparrow, y\uparrow)]$, while first and second excited states are ${}^4A_2^* \equiv \Gamma_v(\uparrow\circ) + [a_1(\uparrow\downarrow) + e(x\uparrow, y\uparrow)]$ and ${}^4E \equiv \Gamma_v(\uparrow\circ) + [a_1(\uparrow) + e(x\uparrow\downarrow, y\uparrow)]$, respectively [82]. Here, square brackets indicate localized states within the gap, doublet states are resolved into x - and y -components, and Γ_v corresponds to mixing between the valence band and defect states. The small circle represents the lack of an electron which has been promoted to a higher state. To resolve Stark shifts of the V_{Si} emission lines, we monitor the field dependencies of the ${}^4A_2^* \rightarrow {}^4A_2$ zero-phonon transition energies of V_{Si} (V1 and V2) within the delta-self consistent field approach. V1' and V2' arise from ${}^4E \rightarrow {}^4A_2$ transitions, but, due to numerical instabilities, the 4E excited states could not be resolved self-consistently in this work. Instead, the V1' and V2' transition energies were ascertained from the energy difference between two spin-down Kohn-Sham eigenvalues of the ground state.

Chapter 5

Point defect generation and characterization

This chapter is dedicated to reviewing the main experimental methods used to characterize point defects in the present work. The first section discusses defect formation via ion implantation and irradiation, while electrical and optical characterization techniques are discussed thereafter, followed by a brief description of muon spin rotation spectroscopy. Additional techniques that have been employed, but will not be discussed in detail herein, are transmission electron microscopy (TEM) and secondary ion mass spectrometry (SIMS). Information on these techniques can be found in, e.g., Ref. [135] for TEM and Ref. [136] for SIMS.

5.1 Ion implantation

Ion implantation is a technique that is commonly used in semiconductor processing, for instance to introduce foreign elements for doping purposes. Here, ion implantation was employed to produce intrinsic point defects on-demand. Native point defects are present in any material to a certain degree, but controlled fabrication is often necessary when performing systemic defect identification studies. The implantation experiments performed herein were designed to predominantly generate point defects as opposed to extended lattice damage. The effect of the implanted species themselves on the generated point defects is also discussed.

Physical principle The ion beam in an ion implanter is accelerated by an electric field and channeled into a semiconductor sample. The depth (or projected range) and distribution of the implanted ions are determined by factors such as the energy and mass of the implanted species, and the angle of the ion beam with respect to the surface normal. The amount of incorporated ions is controlled by the implantation fluence or dose, i.e., the time for which the sample is exposed to the ion beam. As the energetic ions penetrate the sample surface they interact elastically with the target lattice atoms and collide with the surrounding electrons. Interactions between the implanted ions and the lattice atoms and electrons are commonly termed the stopping power, $S = dE/dR_I$, which essentially translates into the change in ion energy with distance traveled. The stopping power can be divided into a nuclear (S_n , elastic collisions with lattice atoms) and an electronic (S_e , the energetic ions excite target electrons) part according to $S = S_n + S_e$. At low ion implantation energies the nuclear stopping will dominate, while electronic stopping dominates for high ionic velocities. Nuclear stopping can be described

by physical models, whereas empirical approximations are needed to predict the electronic stopping.

Following a series of damage events, the implanted ions start to lose their kinetic energy and eventually come to a full stop. The collisions occur randomly, and the resulting implanted ion distribution will have a nearly Gaussian form around some mean projected range (R_P) depending on the ion mass and energy. Note that the above discussion on random collision events assumes that the implanted ion follows a random trajectory through the lattice. For crystalline materials, this is no longer true if the ion follows the open pathways between lattice sites through a process known as *channeling*. To avoid channeling, we ensure that the impinging ion beam hits the surface at an angle that is not parallel to the surface normal.

Ion implantation or irradiation events take place under non-equilibrium conditions, and lattice reorganization may occur via several processes during the experiment. Indeed, upon formation of a Frenkel pair (e.g., $V_{Si} + Si_i$) by ionic collision, one can roughly divide the outcome into two: the Frenkel pair recombines to leave the Si atom in its original place (often referred to as dynamic annealing), or the Si interstitial gains enough kinetic energy from the collision event to migrate away leaving an isolated monovacancy behind. Additionally, the Si atom may gain enough energy to knock out neighboring atoms, resulting in formation of complexes such as the divacancy or the carbon-antisite vacancy pair.

When using ion implantation to modify the semiconductor material properties, predictive power over both the resulting ion distribution and the related damage events is vital. The present work employs Monte Carlo simulations as implemented in the Stopping and Range of Ions in Matter (SRIM) [137] code for predicting the distribution and projected range of carbon, helium and hydrogen implantation into 4H-SiC material. Note that SRIM simulations do not account for dynamic annealing, and only provide information regarding the initial damage events. To predict (e.g.) the concentration of V_{Si} after proton irradiation the percentage of vacancies that survive dynamic annealing should be known. For primary defects such as vacancies, this value falls within the range of 2-5 % in most semiconductor materials.

Experimental conditions The ion implantation experiments conducted in the present work can be grouped into two categories: (i) implantations that leave a Gaussian-like distribution of intrinsic point defects within the 4H-SiC epi-layer with the peak located a few μm from the sample surface, and (ii) irradiation experiments with a projected range far into the substrate and a near-uniform defect concentration profile in the near-surface region. Note that all implantation processes conducted herein employed light atoms to ensure the formation of mainly point defects at the expense of extended lattice damage. All implantations were conducted at an angle 8° off the surface normal to avoid channeling. Two sample types were employed for the implantation processes: $10\mu m$ 4H-SiC epi-layers on top of a SiC substrate, and SiC powder particles of

2-5 μm average diameter (see Section 6.1).

The ion irradiation was conducted using either protons or helium ions, and with the following parameters:

- Energetic protons of energy 1.8 MeV having a projected range of 27 μm as deduced by SRIM were employed in Paper I, Paper III, Paper IV, Paper VI and Paper VII.
- In Paper V, we employed 1.5 MeV proton irradiation resulting in a projected range of 20 μm into the 4H-SiC epi-layer/substrate structure. Irradiation was performed at both room temperature and 400 °C.
- Helium ions of energy 2.5 MeV and having a projected range of 11 μm as deduced by SRIM simulations were employed in Paper IV.

Irradiation was performed at room temperature (RT) only in all cases apart from the 1.5 MeV proton irradiation in Paper V, where so-called hot implantation at 400 °C was also employed. Note that proton irradiation process (energy 1.8 MeV) on the SiC powder (Paper III) resulted in all implanted ions traversing the entire particle layer, due to the small microcrystal diameter of maximum $\sim 5 \mu\text{m}$

The implantation experiments were designed to leave a non-uniform defect distribution within the 4H-SiC epi-layers, and were performed with the following implantation parameters at RT:

- He implantation with energy $E = 300 \text{ keV}$ and a projected range of $R_P \sim 1.5 \mu\text{m}$ was used in Paper IV.
- C implantation of energy $E = 4 \text{ MeV}$ and a projected range of $R_P \sim 2.5 \mu\text{m}$ is exploited in Paper VIII and Paper IX to study V_C migration. Note that C was employed to avoid foreign atoms interfering with the diffusion experiment.

5.2 Electrical characterization

Electrical characterization was employed to monitor the electrically active defects present in the 4H-SiC epi-layer samples, and detect the effect of energy levels introduced by electrically active defects into the 4H-SiC band gap.

5.2.1 Rectifying junctions

Physical principle To probe the properties of a semiconductor in terms of for instance the resistivity, doping concentration or presence of defects, we need to first fabricate a *rectifying junction*. A rectifying junction conducts current in only one direction, as opposed to an Ohmic contact, due to a potential barrier preventing current to pass in the other direction. The two main types of rectifying devices that are commonly used for defect spectroscopy are the pn-junction between a p-type and an n-type semiconductor, and the Schottky barrier diode (SBD) which consists of a metal deposited on a semiconductor.

5. Point defect generation and characterization

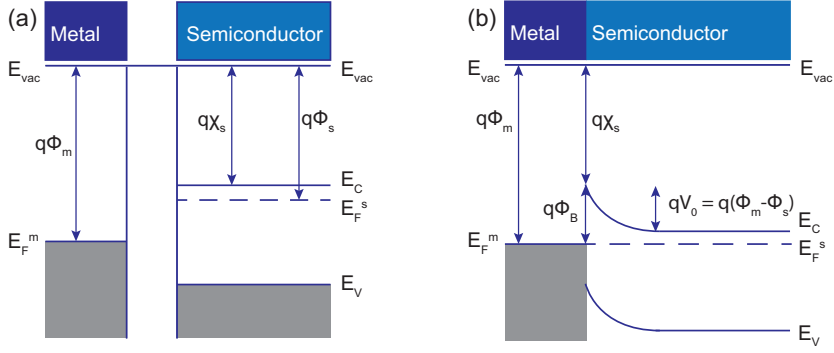


Figure 5.1: Graphics of a Schottky barrier junction between a metal and an n-type semiconductor having $\phi_m > \chi_s$, (a) before and (b) after they are put into contact.

The metal/semiconductor junction forms an Ohmic (non-rectifying) or rectifying contact depending on the work function difference (Φ_{ms}) between the metal and the semiconductor. Herein, we will employ SBDs between a metal (nickel) and an n-type semiconductor (n-type 4H-SiC) as opposed to pn-junctions to probe semiconductor properties, due to ease of fabrication.

Figure 5.1(a) demonstrates the band diagrams of a metal (left) and an n-type semiconductor (right). In Figure 5.1(b) the metal and semiconductor are placed into contact with one another, leading to the formation of a Schottky junction. The characteristic quality of the SBD is the Schottky barrier (Φ_B), which is determined by the work function of the metal (Φ_m) and the electron affinity of the semiconductor (χ_s) according to

$$\Phi_B = \Phi_m - \chi_s. \quad (5.1)$$

In the case that $\Phi_m > \chi_s$, the electrons from the semiconductor conduction band move over to the metal, leading to the formation of a potential barrier which prevents current conduction from the metal into the semiconductor. The work function quantifies the amount of energy needed to remove an electron from the metal to the vacuum level (E_{vac}), while the electron affinity is the difference between E_{vac} and E_C . We commonly employ χ_s instead of the semiconductor's Fermi level as E_F^s depends on the doping concentration and is located within the semiconductor band gap.

Electron motion over to the metal leaves a deficit of electrons on the semiconductor side of the interface which is known as the *depletion region* of width W . W depends on the built-in voltage (V_{bi}),

$$qV_{bi} = \Phi_B - (E_C^s - E_F^s), \quad (5.2)$$

and the applied bias (V) according to

$$W = \sqrt{\frac{2\epsilon_s\epsilon_0(V + V_{bi})}{qN_D}}, \quad (5.3)$$

where N_D is the net donor concentration, q the fundamental charge and $\epsilon_s\epsilon_0$ the semiconductor permittivity. Applying external bias generates an electric field (\mathcal{E}) over the depletion region with a maximum value of

$$\mathcal{E}_{\max} = -\frac{q}{\epsilon_s\epsilon_0}N_D W. \quad (5.4)$$

Experimental conditions Herein, Schottky barrier diodes were employed to facilitate electrical measurements and application of electric fields to defect states. The SBDs were fabricated on the 4H-SiC epi-layer surfaces using electron beam evaporation through a shadow mask. Nickel was employed to ensure a rectifying junction with the n-type 4H-SiC epi-layers, and all Schottky contacts were circular having 1 mm diameter and 150 nm thickness.

5.2.2 Capacitance- and current-voltage measurements

Capacitance-voltage (CV) and current-voltage (IV) measurements are conducted to, among other things, determine the net carrier concentration in a sample, and ascertain the properties and quality of a Schottky barrier junction. See, e.g., Refs. [138, 139] for further details.

During the CV measurements, a step-wise changing external reverse bias (V) is applied to the Schottky contact which alters the depletion region width of the SBD according to Eq. 5.3. The depletion region is reminiscent of a parallel plate capacitor, and according to the *depletion approximation* we formulate the junction capacitance over a SBD space-charge region as

$$C = \frac{\epsilon_s\epsilon_0 A}{W} = A \sqrt{\frac{\epsilon_s\epsilon_0 q N_D}{2(V + V_{bi})}}, \quad (5.5)$$

where A is the Schottky contact area. For the depletion approximation to be valid, there should be no carriers in the depletion region and the depletion region/neutral bulk interface should be abrupt. Reformulating Eq. 5.5 yields

$$\frac{1}{C^2} = -\frac{2}{\epsilon_s\epsilon_0 q N_D A^2} V + \frac{2}{\epsilon_s\epsilon_0 q N_D A^2} V_{bi}. \quad (5.6)$$

Thus, to determine the built-in voltage of a Schottky junction along with the net carrier concentration of the semiconductor material, one can conduct a CV measurement and convert the CV curve into a $1/C^2$ versus voltage plot. Example CV and $1/C^2$ curves are shown in Figures 5.2(a) and 5.2(b), respectively, for a Ni/n-4H-SiC SBD. The built-in voltage of the junction can be deduced from interception of the linear extrapolation to the $1/C^2$ data points with the x -axis,

5. Point defect generation and characterization

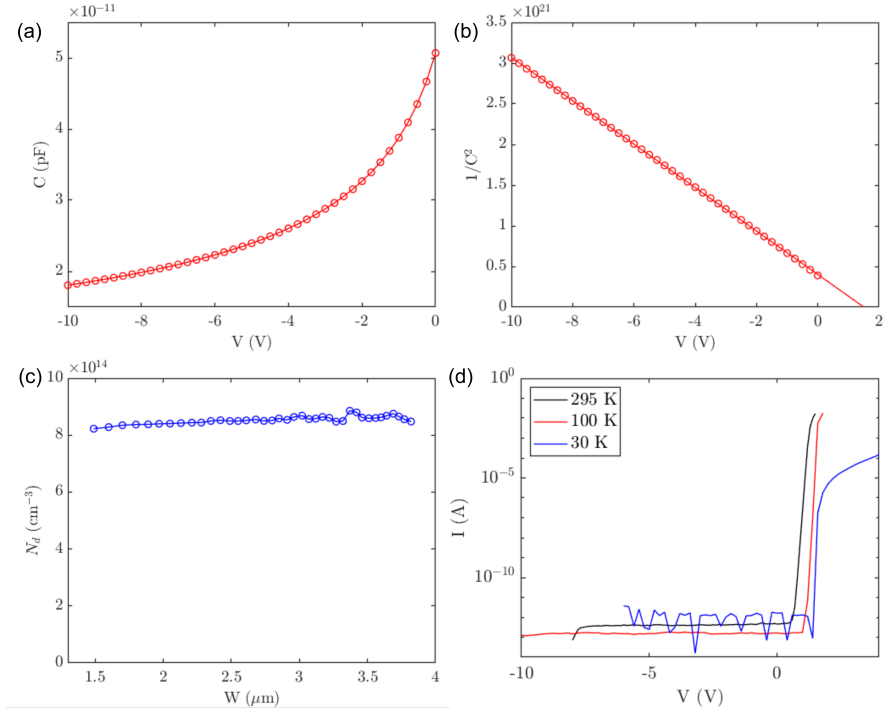


Figure 5.2: Example CV and IV curves for a SBD deposited on a proton-irradiated 4H-SiC epi-layer, showing (a) capacitance (C) versus voltage (V), (b) $1/C^2$ vs. V , (c) the CV curve converted into the net carrier concentration (N_D) versus depletion region depth (W), and (d) example current-voltage (IV) curves collected at different temperatures. Adapted from the Supplementary Information to Paper I.

while the net carrier concentration can be found from the slope, if the doping profile is homogeneous. A depth profile for the net carrier concentration, as shown in Figure 5.2(c), can be determined according to

$$N_D(W) = \frac{2}{q\epsilon_s\epsilon_0 A^2} \left[\frac{1}{d(1/C^2)/dV} \right] \quad (5.7)$$

for both homogeneous and non-homogeneous doping.

The thermionic current (I) through a SBD depends on the voltage (V) according to (neglecting series and shunt resistance)

$$I = AA^*T^2 e^{-q\Phi_B/k_B T} \left(e^{qV/\eta k_B T} - 1 \right) = I_s \left(e^{qV/\eta k_B T} - 1 \right), \quad (5.8)$$

where Φ_B is the Schottky barrier height, A the diode area, I_s the saturation current, A^* denotes Richardson's constant, and η is the ideality factor. The

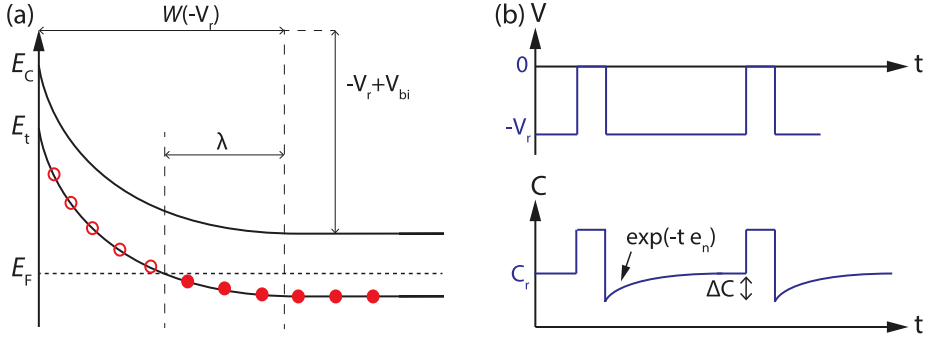


Figure 5.3: Schematic of (a) a band diagram for the Schottky barrier under applied reverse bias $-V_r$ before adding the pulse voltage, and (b) the voltage pulse scheme and resulting capacitance transient of a DLTS measurement cycle.

ideality factor is often $\eta > 1$ due to non-uniform Schottky diodes, and may decrease with temperature. After performing an IV measurement, the barrier height Φ_B for zero bias conditions can be extracted from the saturation current, with the uncertainty arising from the approximate knowledge of Richardson's constant A^* . Example IV measurements for a nickel SBD on n-type 4H-SiC collected at different temperatures are shown in Figure 5.2(d).

5.2.3 Deep level transient spectroscopy

Deep level transient spectroscopy (DLTS), as introduced in the seminal paper by D. V. Lang [54], is a powerful electrical characterization technique capable of detecting electrically active deep level defects in semiconductor materials, and ascertaining properties such as the defect concentration and the energy level positioning in the band gap. Conventional DLTS involves keeping a diode under reverse bias conditions while scanning over a temperature range, and sequentially adding and removing a voltage pulse. Herein, we will also discuss complementary techniques including DLTS depth profiling (isothermal DLTS with varying pulse voltage), Laplace-DLTS (numerical Laplace transformations of capacitance transients) and temperature-dependent capture cross-section measurements (isothermal DLTS with varying pulse duration). The setup employed for conducting DLTS measurements in the present work is similar to that described in Ref. [140].

Consider the band diagram of a Schottky barrier diode (n-type semiconductor) with a deep energy level situated at E_t below E_C . Carrier capture and emission by the deep level depends on the energy E_t , the emission rate, the temperature and the carrier capture cross-section (see Section 2.3.4). By biasing the SBD, an thus inducing non-equilibrium conditions, the charge state of the defect-induced trap level may temporarily change, which subsequently causes a change in the depletion capacitance with amplitude ΔC . The DLTS measurement cycle consists of keeping the sample at reverse bias while applying sequential bias

5. Point defect generation and characterization

pulses. Under reverse bias conditions, as shown in Figure 5.3(a), most traps will reside above the Fermi level (E_F) and thus be empty. The exceptions are the traps within a transition region of width [139]

$$\lambda = \sqrt{\frac{2\epsilon_s\epsilon_0(E_F - E_t)}{q^2N_d}} \quad (5.9)$$

near the edge of the space charge region (W), which remain partly filled.

The DLTS procedure of applying a sequential positive bias pulse while keeping the sample under reverse bias conditions is illustrated in Figure 5.3(b), with the resulting capacitance transient response depicted below. Applying a bias pulse, for instance going to $V = 0$ V, reduces the depletion region width to W_0 . This results in the traps being filled as they are now below the Fermi-level, and an increase in capacitance from the steady-state reverse bias value (C_r). Upon removing the voltage pulse, the depletion region is again extended, but the trap levels remain filled even though $E_t > E_F$. Thus, immediately after reverse bias conditions are restored, the capacitance will differ from C_r by ΔC . As time passes, electrons will be emitted from the filled traps, restoring steady-state conditions. The concentration of filled traps, $N(t)$, depends on the trap concentration (N_t) and emission rate (e_n) according to $N(t) = N_t \exp(-e_n t)$. The time-dependent capacitance then takes a transient form $C(t) = C_r - \Delta C \exp(-e_n t)$, as outlined in Fig. 5.3(b), which can be expressed as

$$C(t) = A \sqrt{\frac{q\epsilon_s\epsilon_0}{2(V_r + V_{bi})}} \left(N_D + N_t \left[1 + e^{-e_n t} \right] \right). \quad (5.10)$$

The above discussion highlights that the emptying and filling of a defect carrier trap is governed by the emission rate, which depends strongly on temperature according to Eq. 2.9. Consequently, a DLTS measurement can be performed by slowly varying the temperature and collecting the capacitance transients. The emission rate of each deep level defect will thus (ideally) be *activated* at different temperatures, allowing the observer to resolve the signature, or fingerprint, of each defect. A set of example capacitance transients at varying temperatures is shown in Figure 5.4(a).

The original DLTS approach that was developed by D. V. Lang [54] employed what is known as the *boxcar weighting function* to construct a DLTS spectrum [138]. In that case, the capacitance transients shown in Fig. 5.4(a) are sampled at two times, t_1 and t_2 . Depending on the temperature, a spectrum can be constructed for $C(t_1) - C(t_2)$ vs. the temperature (T) as exemplified in Figure 5.4(b), resulting in a peak at the largest capacitance difference. At the peak maximum, the emission rate for boxcar-DLTS is given by

$$e_{n,\max} = \frac{\ln(t_2/t_1)}{t_2 - t_1}. \quad (5.11)$$

The main drawback of the boxcar-approach is that only two data points from the capacitance transient contribute to the overall DLTS spectrum. A better

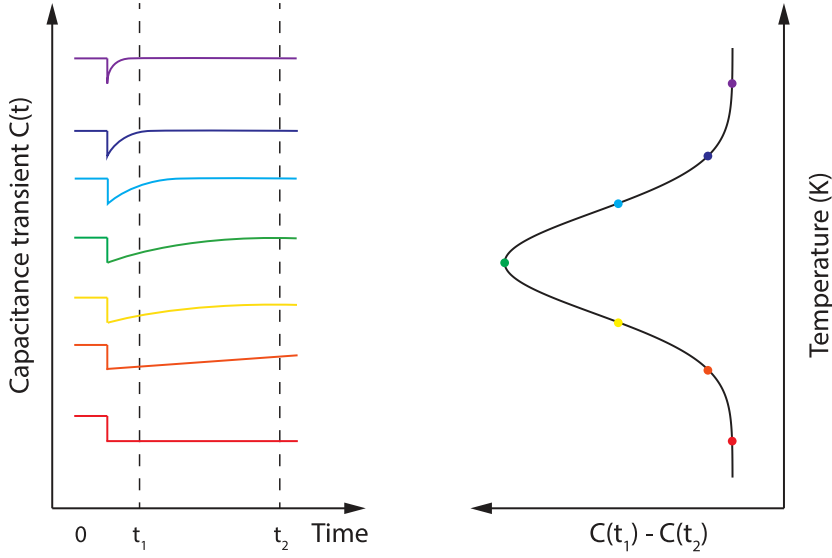


Figure 5.4: Example schematic of DLTS spectrum construction from capacitance transients using the boxcar-approach.

signal-to-noise ratio can be obtained by choosing a different weighting function $w(t)$, and constructing the DLTS signal (S) from the integral

$$S = \int \Delta C(t) w(t) dt. \quad (5.12)$$

The present work employs the *lock-in* weighting function to analyze capacitance transients and construct DLTS spectra, defined as

$$w(t) = \begin{cases} -1 & : 0 < t < t_i/2 \\ 1 & : t_i/2 < t < t_i. \end{cases} \quad (5.13)$$

Other weighting functions may offer better spectral resolution, but at the cost of a lower signal-to-noise ratio.

Regardless of the weighting function employed, the sign of the DLTS signal enables determination of whether a defect level is a majority ($\Delta C > 0$) or minority ($\Delta C < 0$) carrier trap. Only majority carrier traps (electrons for n-type 4H-SiC) are considered herein. Moreover, the activation energy (E_A or E_t) and (apparent) capture cross-section ($\sigma_{n,app}$) for a specific carrier trap can be extracted by performing a DLTS scan and varying the *rate window* ($t_i = t_2 - t_1$). An Arrhenius plot can be constructed for the emission rate at the peak maximum, $e_{n,max}$, versus the inverse temperature. From the relation

$$\ln \left(\frac{e_{n,max}}{T^2} \right) = \ln(\gamma \sigma_{n,app}) - \frac{E_A}{k_B T} \quad (5.14)$$

5. Point defect generation and characterization

we can extract the activation energy from the slope of the fit to the data points, and the (apparent) capture cross-section from the intersection of the extrapolated line with $1/T = 0$. In the case of a uniform defect profile, the trap concentration can also be extracted from the DLTS peak maximum according to

$$\frac{N_t}{N_D} = 2 \frac{\Delta C}{C_r}, \quad (5.15)$$

provided that $N_t \ll N_D$. For the above relation to be valid, the trap concentration should not exceed 10-20 % of the net carrier concentration.

Indeed, the ability to detect trap levels of low concentration (e.g., down to 10^{10} cm^{-3} for $N_D = 10^{15} \text{ cm}^{-3}$) marks DLTS as a highly sensitive technique for detecting defects introducing deep energy levels within the semiconductor band gap, and allowing for precise quantification of parameters such as concentration, activation energy and capture cross-section. However, the defect in question must be electrically active, which is not always the case, and the chemical nature and structure of the defect in question cannot be ascertained by DLTS alone, necessitating comparison to theoretical calculations and other experimental methods. Moreover, the regions both very close to and far away from the diode interface are inaccessible during a DLTS measurement.

5.2.4 DLTS depth profiling

Principle of operation In the case that the defect distribution is not uniform, the simple relation between the trap concentration N_t and the DLTS signal defined in Eq. 5.15 is no longer valid. Instead, concentration versus depth profiles for a certain trap level can be obtained by varying the pulse bias instead of the temperature, and performing an isothermal DLTS measurement. The trap concentration as a function of depth from the surface, $N_t(x)$, is then governed by the relation

$$N_t(x) = - \left(\frac{qW^2N_r}{\epsilon_s\epsilon_0} \right) N_D(x) \frac{\partial(\Delta C/C)}{\partial V}, \quad (5.16)$$

where N_r is the concentration of ionized donors at the end of the depletion region, $N_D(x)$ the concentration of ionized donors versus depth, and the last factor is the derivative of the DLTS signal versus pulse voltage. Note that Eq. 5.16 is an approximation, and neglects the effect of the λ -region (see Fig. 5.3), which is where E_t resides below the Fermi level despite the reverse bias. The extent of this transition region can be estimated according to Eq. 5.9, and should in many cases be accounted for in Eq. 5.16. The assumption commonly made when neglecting the λ -factor is that the transition region is small compared to the depletion region depth during reverse bias, and therefore can be neglected.

Experimental conditions DLTS depth profiles are employed in Paper I, Paper VIII and Paper IX herein. The measurements were conducted employing a 640 ms^{-1} rate window, and the temperature was fixed to within 0.1 K for the duration of transient collection. The reverse bias was kept constant at -10 V ,

while gradually increasing the filling pulse voltage (50 ms duration) from 0 V to 11 V. The ionized donor concentrations, N_{rb} and $N_D(x)$, were determined from capacitance-voltage measurements that were performed prior to each individual DLTS depth profiling procedure.

Note that Paper I accounts for the λ -region when ascertaining trap concentrations, however, the depth profiles for the V_C concentrations in Paper VIII and Paper IX were not λ -corrected. The reason for this was that the high-temperature annealing procedures that are necessary for inducing V_C motion resulted in significant surface degradation. The error associated with neglecting the transition region depends on the depth currently being probed during a DLTS depth profiling measurement (i.e., the applied bias). The error from neglecting this term is smallest at the full depletion region width and largest closest to the sample surface, which coincidentally is where the surface degradation has the greatest impact. Therefore, incorporating the λ -correction term would potentially add systematic errors to the values of the depth measurements that are already the least accurate. Hence, the lambda term was omitted in Paper VIII and Paper IX to keep the measurement data as pristine as possible. Moreover, tests were performed and diffusivities deduced with and without the λ -correction were found to differ by less than 10 %, which is well within the estimated error bars.

5.2.5 Laplace-DLTS

In the event that two different defect centers are associated with similar emission rates, a single DLTS peak may comprise contributions from several trap levels. Employing a weighting function with higher resolution than $w_{lock-in}$ can in certain cases reveal the fine-structure of DLTS peaks, but digital post-processing methods are often necessary. One such method is known as Laplace-DLTS [141], or L-DLTS, which involves averaging over a large number of capacitance transients and subjecting them to a numerical Laplace transform to resolve interlaced emission rates. Numerically, L-DLTS is implemented in a software called CONTIN [142], which is based on the Tikhonov regularization method [143]. L-DLTS measurements are conducted isothermally and necessitate a high degree of temperature stabilization to within ± 0.02 K during the measurement. The capacitance transient is then analyzed as a function of the emission rate at each specific temperature.

In the present work, L-DLTS was employed in Paper I to resolve the fine structure of the S1 peak assigned to the (2-/3-) charge-state transition of the Si vacancy in 4H-SiC, arising from the two possible configurations of V_{Si} at hexagonal (h) and pseudo-cubic (k) lattice sites. The Laplace-DLTS experiment is summarized in Figure 5.5. Fig. 5.5(a) illustrates the DLTS spectrum showcasing the S1, $Z_{1/2}$ and S2 peaks, whereas the Laplace-DLTS spectra resolving the two contributions to the S1 peak at different temperatures (intensity versus emission rate) are illustrated in Fig. 5.5(b). Note that the area under each peak directly translates into the trap concentration, meaning that the two trap levels embedded in the S1 peak, likely relating to the h and k configurations of V_{Si} , are present in approximately equal amounts in the sample. Finally, Fig. 5.5(c)

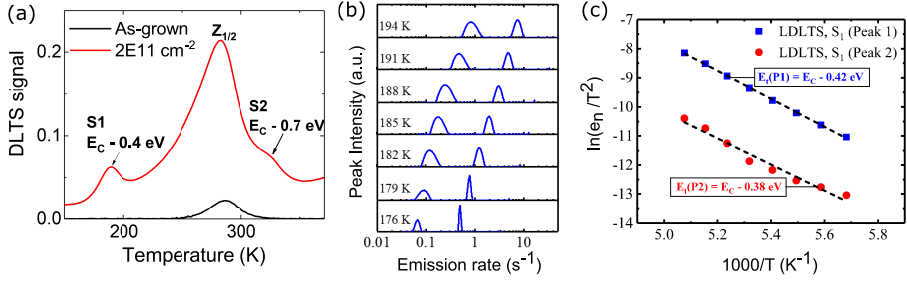


Figure 5.5: (a) DLTS spectra of as-grown (black line) and proton-irradiated (red line) n-type 4H-SiC samples showcasing the S1, S2 and $Z_{1/2}$ peaks. Panels (b) and (c) demonstrate Laplace-DLTS spectra resolving the two contributions comprising the S1 center, which is assigned to the (2-/3-) charge-state transition of the h and k Si vacancy. Adapted from Paper I.

demonstrates the Arrhenius behavior of the two S1 contributions, revealing an activation energy separation of ~ 0.04 eV.

5.2.6 Comparing DLTS and DFT

Formation energies deduced from DFT calculations translate into approximate defect concentrations upon thermal formation, which can often be compared to the defect concentrations deduced from DLTS measurements on as-grown or annealed material. Moreover, DLTS probes charge carrier capture and emission from deep levels introduced by defect states within the semiconductor band gap, which can be readily compared to DFT calculations that allow extraction of charge transition levels from formation energy diagrams (see Section 4.4.2). However, it is important to note the inherent differences between the energy levels that are found using the two methods. Thermodynamic transition levels as extracted from DFT calculations correspond to the defect's ionization energy, i.e., the energy required to interchange a charge carrier with the valence or conduction band at 0 K temperature. The procedure of extracting activation energies from DLTS measurements, on the other hand, is not conducted at 0 K and relies on temperature dependent parameters such as the band energies and capture cross-section (see Eq. 5.14). As a result, E_A extracted from DLTS may differ significantly from that found using DFT for the same defect transition.

The temperature dependence of the capture cross section, and the resulting contribution to E_A found from DLTS, can be determined using both theoretical [144] and experimental means. Experimentally, it is possible to probe the capture kinetics in detail during a DLTS measurement by monitoring the response of the DLTS transient to changes in the pulse duration, t_p [145, 146], which takes the form $\Delta C(t_p) = \Delta C_{\max}(1 - \exp(-t_p/\tau_c))$. Here, the capture time constant evolves as $\tau_c = 1/(\sigma_n v_{th,n} N_D)$, and by fitting the expression for $\Delta C(t_p)$ to the measured data, the true capture cross-section σ_n can be extracted. Firstly, a comparison

between true and apparent capture cross-sections enables an estimation of the entropy contribution via $\sigma_{n,\text{app}} = \sigma_n \exp(\Delta S/k_B)$. However, performing such DLTS versus pulse duration scans at various temperatures may also reveal the temperature dependence of σ_n , which takes the form

$$\sigma_n = \sigma_\infty \exp\left(-\frac{E_b}{kT}\right), \quad (5.17)$$

where σ_∞ is the cross-section at infinite temperature and E_b is an additional barrier for carrier capture. The capture barrier can also be obtained by constructing configuration coordinate (CC) diagrams (see Fig. 2.7) for the charge-state transition, and extracting the barrier E_b as the energy difference between the intersection of the two parabolas, and the energy minimum of the upper parabola [144].

5.3 Optical characterization

Applying excitation, such as photons or an electron beam, to a semiconductor may result in emission of *luminescence*, and the resulting spectrum can be highly valuable in determining semiconductor properties such as the band gap energy, the presence of defects and the electron-phonon coupling strength. While electrical characterization as implemented in the DLTS technique enables reliable estimation of defect-related charge transition levels arising in the semiconductor band gap, optical characterization enables probing of both charge-conserving internal transitions and charge interchanges with the band edges. The photoluminescence (PL) and cathodoluminescence (CL) measurements conducted throughout the course of this work mainly aimed at probing internal transitions (see Sections 2.3.5 and 2.3.6) of qubit defect centers including the Si vacancy, the divacancy and the carbon antisite-vacancy pair in 4H- and 6H-SiC.

Here, we will provide only a brief introduction to emission processes and spectroscopy. Further information can be found in, for instance, Ref. [24], where a comprehensive guide to both the physics of luminescence processes and the technique of luminescence spectroscopy in semiconductor materials is provided.

5.3.1 Luminescence processes in semiconductors

The most straightforward way of describing the process of semiconductor luminescence involves the excitation of an electron from the VB to the CB, and the subsequent formation of an electron-hole-pair (EHP). To achieve EHP formation in a PL measurement, excitation energies above that of the band gap (E_g) are necessary. If the semiconductor band gap is direct, the probability is high for a recombination of the EHP releasing a photon of energy similar to E_g . An alternative excitation pathway involves exchange of charge carriers trapped at defects with the band edges.

Below-gap excitation may promote a carrier residing at a defect system, such as the V_{Si} in 4H-SiC, from the ground state to an excited state while retaining

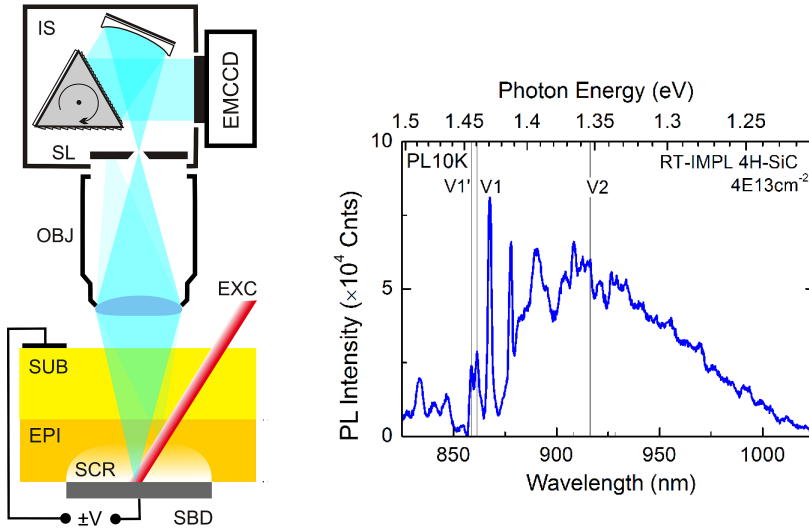


Figure 5.6: Left panel: Micro-imaging PL spectroscopy setup in back-illumination/detection geometry. The laser excitation (EXC) beam is passing through the substrate (SUB) and epilayer (EPI), and is reflected at the Schottky contact (SBD). Right panel: Representative PL spectrum from a proton irradiated n-type 4H-SiC sample showcasing emission related to the Si vacancy (V1, V1' and V2 lines). Adapted from Paper I.

the number of charge carriers associated with the defect center. After excitation, the system will eventually return to the equilibrium or ground state, as the excited electron recombines with a hole either in the valence band or in the defect-induced gap state. The recombination process may be either *radiative* and result in the emission of a photon, or *non-radiative*, where the excess energy supplied by the optical excitation is transferred as, e.g., heat to the lattice via phonons. Radiative transitions can be monitored during PL spectroscopy experiments and provide valuable insight into the various material- and defect-related processes occurring in a sample. Non-radiative transitions, on the other hand, are only detected in an indirect fashion.

5.3.2 Photoluminescence spectroscopy

Photoluminescence (PL) spectroscopy studies as presented in this thesis involve exciting a 4H-SiC sample with laser light and monitoring the resulting emission spectrum. Luminescence emission as described above occurs in all directions simultaneously, meaning that the system to collect and enhance emission may be constructed in several different ways. A schematic of the PL imaging setup mainly employed in the present work is shown in Figure 5.6(a) for a 4H-SiC substrate/10 μm thick 4H-SiC epi-layer/150 nm thick Ni SBD sample stack.

For the specific sample geometry depicted in Fig. 5.6(a), excitation (EXC) was conducted from the substrate (SUB) side of the sample, and the laser beam was focused to within the space charge or depletion region (SCR) at the interface between the 4H-SiC epi-layer (EPI) surface and the Ni Schottky contact (SBD).

For the photoluminescence (PL) spectroscopy measurements, the samples were placed inside a closed-cycle He refrigerator system (CCS-450 Janis Research, Inc.). PL measurements were conducted at temperatures ranging from 10 K to 300 K. Excitation was performed herein using either a 405 nm continuous wave (cw) laser, a 675 nm cw-laser, a 806 nm cw-laser, or a pulsed Ti:sapphire tunable laser operating in femtosecond mode-locked mode for resonant excitation of V_{Si}^- defects at 740 nm wavelength. In all cases, the focused laser beam was impinging on the sample surface at 27° , and yielded an excitation intensity $\leq 1 \text{ kWcm}^{-2}$ and polarization perpendicular to the optic (c) axis of 4H-SiC. The emission was analyzed by fiber-optic (Ocean Optics, HR4000) and imaging spectrometer systems (Horiba iHR320 coupled to Andor iXon888 EMCCD), with a spectral resolution below 0.2 nm. The imaging spectroscopy setup when employing the 405 nm and 806 nm cw-lasers (Paper IV and Paper VI) ensured near-confocal operation, allowing to maximize collection of the emission from the depths $\sim 5 \mu\text{m}$ below the epilayer surface without probing the stopping range regions of H or He implants.

Figure 5.6(b) exemplifies defect-related emission arising from internal transitions of V_{Si}^- in 4H-SiC. The two zero-phonon lines arising from excited-to-ground state transitions of the h and k configurations of V_{Si}^- are marked as V1 and V2, respectively, with V1' having the same chemical origin as V1 but resulting from transitions to a higher-lying excited state. It is possible to distinguish the V1, V1' and V2 ZPLs, however, also a broad phonon side-band overlapping with V2 is clearly visible. See also, e.g., Fig. 2.8 for a PL spectrum that includes both the near-band edge emission related to EHP formation, and broad defect bands related to internal defect transitions and charge carrier exchange between defects and the VB/CB.

5.3.3 Cathodoluminescence spectroscopy

Cathodoluminescence (CL) spectroscopy is similar in principle to PL spectroscopy, and the same physical principles behind excitation and emission hold. The CL setup employed in the present work (see Paper III) is equipped with a focused electron beam, which can excite electron-hole pairs resulting in emission of cathodoluminescence, or be used to scan the sample surface. The forward-scattered electrons are absorbed by the sample, but the secondary and back-scattered electrons can form a scanning electron microscope (SEM) image capable of resolving minute details of the sample being studied.

The CL measurements employed herein were conducted using a Delmic SPARC-system mounted on a JEOL JSM-IT300 scanning electron microscope (SEM). Emission spectra were collected using an Andor Shamrock SR-193i spectrometer and a charge-coupled device (CCD) Andor Newton DU940P-BU2 detector. To control the CL probing depth and excitation power, the experiments

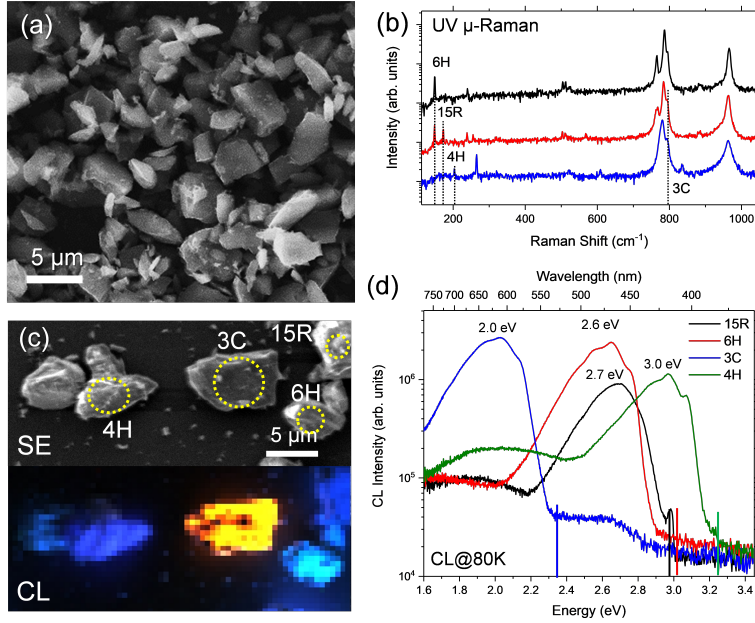


Figure 5.7: (a) SEM image showcasing SiC microparticles. (b) UV μ -Raman spectra measured on a small number of particles highlighting the particle polytypes. (c) SEM micrograph and its corresponding false color map representing the spectral range 1.6-3.3 eV. (d) CL spectra measured at 80 K from selected particles from (c). Adopted from Paper III.

employed acceleration voltages from 2-30 kV and probing currents of 10 pA to 1 nA. The CL measurements were performed at temperatures from 80-300 K, using a Gatan cooling stage equipped with liquid nitrogen.

Example CL spectra showcasing the capabilities of the SEM-CL setup are collected in Figure 5.7 for SiC micro- and nanosized particles, with microcrystal size and shape distributions shown in Fig. 5.7(a). The combination of μ -Raman spectroscopy shown in Fig. 5.7(b), the false CL color map in Fig. 5.7(c) and the near-band edge (NBE) emission spectra in Fig. 5.7(d) demonstrates that the 6H, 4H, 3C and 15R SiC polytypes are present in the powder particles, with 6H being the dominant one. The resolution of CL spectroscopy rivals that of PL, with the added benefit of nm-scale imaging courtesy of the SEM. The main drawback of the CL approach as compared to PL is the somewhat lower sensitivity of the CL setup, in addition to only liquid nitrogen cooling being available in the system employed for the present work.

5.4 Muon spin rotation spectroscopy

Physical principle Muons are elementary particles of the lepton type with charge $\pm q$ and spin-1/2. Muon generation occurs in high-energy proton accelerators, where the collision between protons and a graphite target results in formation of pions with zero spin. After a short timespan of ~ 26 ns, the pion decays into a muon and a muon neutrino, resulting in muons of spin-1/2 with 100 % polarization.

Muon spin rotation (μ SR) spectroscopy is a non-destructive and surface-sensitive technique to study interactions between implanted muons and the solid state. Positive antimuons (μ^+) are most commonly used and can be implanted into a sample of any material type. After a mean lifetime of 2.2 μ s, the μ^+ decays into a positron and two neutrinos. Interestingly, the positron emission occurs preferentially along the direction of the muon spin, meaning that measuring the direction of positron emission as a function of time yields information on the magnetic environment surrounding the muon. The behavior of μ^+ after implantation depends strongly on the material type, where the electron cloud of a metal will efficiently screen the positive charge and the muon will behave as if it were free, while in a semiconductor (or insulator) the muon will usually pick up an electron to form a bound hydrogen-like state called muonium ($\text{Mu} = \mu^+ e^-$). For that reason, the muon has historically been used as a probe for the behavior of hydrogen in semiconductors. Nowadays, hydrogen is commonly used to emulate the behavior of the muon in DFT calculations.

The muon approach is a valuable supplement to the characterization techniques described herein, as PL is not reliably depth-resolved and probing the top ~ 300 nm of a sample is challenging using DLTS. Muon beam spectroscopy is non-destructive, and provides a means to probe the surface-near portion of a sample in a depth resolved manner, depending on the energy of the muons. Importantly, the muon is also a magnetic probe, with excellent sensitivity to small fluctuations in the internal magnetic fields of the sample. Moreover, as revealed in, e.g., Ref. [147], low energy μ SR spectroscopy is capable of detecting carbon vacancies in proton-irradiated 4H-SiC, providing valuable incentive for investigating the sensitivity of the muon beam towards Si and C vacancies in 4H-SiC. Indeed, this is the main focus of Paper VII. For more information on muon spin rotation, and how to employ muon beamline experiments to study the solid state, see, e.g., Refs. [148–150].

Experimental conditions The muon measurements conducted herein on 4H-SiC epi-layers were performed at the low-energy muon (LEM) beamline of the Swiss Muon Source ($S\mu S$) [151, 152] at the Paul Scherrer Institute in Switzerland. The n-type 4H-SiC samples were fixed on a Ni-coated aluminum plate and mounted onto a cryostat placed perpendicular to the muon beam. The final kinetic energy of the implanted μ^+ was in the range 2–18.5 keV, resulting in probing depths of up to 120 nm, as illustrated for a range of muon energies in Figure 5.8 based on Trim.SP simulations [153]. A magnetic field was applied in

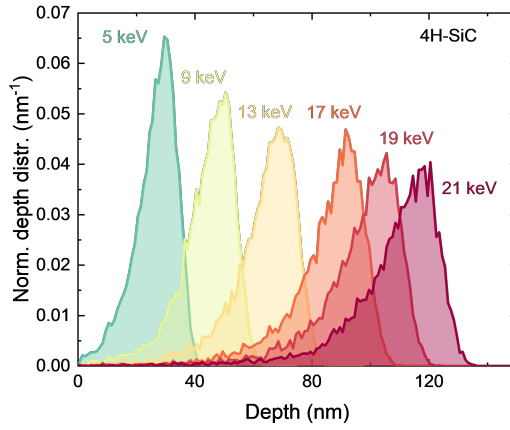


Figure 5.8: Muon implantation profiles versus depth (nm) for muon energies between 5 and 21 keV in 4H-SiC. Simulated with Trim.SP [153]. Adapted from Paper VII.

parallel to the beam axis and the positrons from the muon decay were collected by a set of scintillator detectors placed around the beam axis.

Chapter 6

Summary of results

This chapter serves to summarize the main results obtained over the course of the present work. In order to potentially exploit the vast potential of the silicon vacancy and other qubit defects in SiC for quantum technology applications, we must first establish control over defect formation, utilization and transformation. Until we can reliably predict the effect of various irradiation procedures and heat treatments on the presence of V_{Si} and its counterparts $V_{\text{Si}}V_{\text{C}}$ and CAV, and have established suitable protocols for parameters such as charge-state switching and single-photon emission tuning, we cannot hope to fabricate components for quantum computing and sensing applications based on point defects in SiC. Therefore, this chapter is devoted to exploring the properties of defects in SiC related to formation, identification and quantum control.

Prior to summarizing the results, the samples and processing conditions employed for the experimental portion of this work will be briefly reviewed. Thereafter, the organization of this chapter will follow the lifetime of the Si vacancy:

- Firstly, we will consider identification and control of the silicon vacancy. In Paper I, signatures originating from the V_{Si} are identified in 4H-SiC epi-layers using electrical means, and we employ the newfound electrical degree of freedom to control the V_{Si} charge state.
- Secondly, the effect of perturbation, both external and imposed by the host matrix, on the V_{Si} emission wavelength is investigated. A pronounced Stark effect on the V_{Si} emission energies is revealed in Paper I and explored further (theoretically) in Paper II, while Paper III and Paper IV discuss V_{Si} emission tuning via strain and vibronic effects, respectively.
- Next, different thermally induced transformation pathways of the V_{Si} including complex formation and defect migration are explored, by transformation into hydrogen-related complexes in Paper V and qubit complex formation (VV and CAV) in Paper VI.
- Finally, the inherent difference between silicon and carbon vacancies is investigated in Paper VII, prior to raising the temperature above that where V_{Si} remains and looking into migration pathways for the V_{C} in Paper VIII and Paper IX, and for Si and C self-diffusion in Paper X.

6.1 Experimental details

6.1.1 Sample information

Four sample types were employed for the experimental portion of the present work.

- The predominant sample type employed herein consists of 10 μm thick epitaxial 4H-SiC layers grown 4° off the c -axis on a 4H-SiC substrate, showing the (0001)-face (c -cut) and purchased from CREE Inc. The epi-layers were weakly n-doped with nitrogen to $N_D \sim 1 \times 10^{15} \text{ cm}^{-3}$ as determined by capacitance-voltage measurements, while the substrate n-type doping was about $8 \times 10^{18} \text{ cm}^{-3}$.
- Paper VIII and Paper IX study a -cut 4H-SiC epi-layers of 10 μm thickness in addition to the c -cut ones. The a -cut samples were grown on-axis and showing the (11 $\bar{2}$ 0)-face by chemical vapor deposition (CVD) at the University of Linköping.
- Paper X employs n-type (0001) 4H-SiC substrates holding 7 μm thick isotope purified 4H- $^{28}\text{Si}^{12}\text{C}$ epi-layers. The epi-layers were grown by CVD at the University of Linköping and studied using secondary ion mass spectrometry (SIMS). The isotope purity was approximately $^{28}\text{Si} > 99.85\%$ and $^{12}\text{C} > 99.98\%$. The epi-layer surface was graphitized by covering it with a photoresist and annealing at 900 $^\circ\text{C}$, in order to form a carbon cap (C-cap) to protect the sample surface at high temperatures.
- Paper III utilizes high purity (impurity levels $< 5 \text{ ppm}$) SiC micro- and nanocrystals provided by Washington Mills Co. The particle mean size distributions were in the 2-5 μm range. Approximately 80 % of the particles were of the 6H polytype, while the remainder were divided between the polytypes 3C, 4H and 15R.

6.1.2 Heat treatments

Heat treatments were employed throughout this work to induce the out-annealing of unwanted defects, bring about controlled transformation of the V_{Si} defect, and activate point defect migration. Annealing experiments were conducted using either a hot plate in air (low temperatures at 200-300 $^\circ\text{C}$), a conventional tube furnace in air or N_2 flow (intermediate temperatures from 200-1200 $^\circ\text{C}$) or a RF furnace and in Ar atmosphere (high temperatures from 1200-2450 $^\circ\text{C}$).

The annealing procedures can be grouped into four different categories: (i) low-temperature annealing (200-300 $^\circ\text{C}$) to alleviate implantation damage and reduce the amount of non-radiative channels, (ii) mid-temperature annealing (400-1000 $^\circ\text{C}$) to induce the transformation of V_{Si} into defect complexes, (iii) high-temperature annealing (1200-1600 $^\circ\text{C}$) to ensure removal of V_{Si} and activate migration of V_{C} , and finally (iv) maximum furnace temperature annealing (2300-2450 $^\circ\text{C}$) to engender self-diffusion of Si and C in 4H-SiC.

The low temperature annealing stage was employed after irradiation of SiC samples in all of the included papers (except for the theoretical study in Paper II) to alleviate irradiation damage. Immediately following ion irradiation some lingering atomic displacement may remain, and unstable interstitial defects are likely present. Having migration barriers in the 1-2 eV range [37], both C_i and Si_i may rapidly disappear upon annealing above RT. Therefore, all irradiated samples were annealed at 200 °C or 300 °C for 30 min prior to conducting measurements using either DLTS, PL, CL or LE- μ SR.

The effect of intermediate heat treatments is discussed in Paper V and Paper VI. As outlined in Paper V, performing hot proton irradiation at 400 °C (alternatively post-irradiation annealing) may induce motion of the interstitial hydrogen that was introduced by the proton irradiation, which can result in complex formation between H and intrinsic defects such as V_{Si} and V_C . Furthermore, elevated temperatures can induce the transformation of V_{Si} into corresponding intrinsic defect complexes. Indeed, as discussed in Paper VI, two competing processes may occur: either V_{Si} may transform into the carbon antisite-vacancy (CAV) pair (most important for p-type 4H-SiC), or migration of V_{Si} by atomic hops may ensue, resulting in the eventual formation of divacancy defects (relevant for n-type 4H-SiC). Moreover, CAV complexes that form during ion implantation may anneal out by dissociation at 400-1000 °C in n-type 4H-SiC.

Increasing the temperature above 1200 °C provides enough energy to mobilize the V_C , commonly acknowledged as one of the most prevalent and stable defects in SiC material. Both interstitials and Si vacancies have likely disappeared by this point, while the V_C concentration should exceed that of, for instance, the divacancy and CAV in samples with low defect concentration. Paper VIII and Paper IX monitor the effect of sequentially increasing the temperature in the range 1200-1600 °C on V_C concentration profiles, and reveal the V_C migration mechanism and that V_C anneals out above 1600 °C.

The fourth and final annealing stage involves temperatures in the 2300-2450 °C range to induce self-diffusion of Si and C. Paper X focuses on temperatures above 2300 °C, and employs high temperature annealing steps to elucidate the mechanism for self-diffusion of Si and C atoms in n-type 4H-SiC material covered by a C-cap.

6.2 Identification and control of the silicon vacancy

The V_{Si} in 4H-SiC is a promising single-photon emitter (SPE) and spin center, but is plagued by low emission intensities. Moreover, only one charge state, the singly negative (V_{Si}^-), retains the SPE and high-spin properties desired for quantum technology applications. The remaining charge states are dark and unidentified, with protocols being scarce for ensuring ideal Fermi levels regardless of sample type. The formation energy diagram in Fig. 4.1 showcases the Fermi level dependence of the different V_{Si} charge states available in 4H-SiC, highlighting that the Fermi level range wherein the negative and bright V_{Si} is stable stretches from around mid-gap to $E_C - 0.7$ eV. Consequently, the bright

6. Summary of results

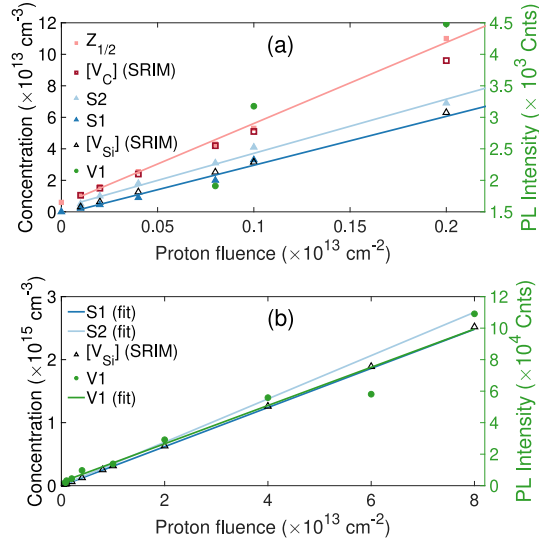


Figure 6.1: Correlating the concentration/intensity dependence of S (blue) and V1 (green) defect centers on the proton irradiation fluence, zooming in on (a) DLTS measurements and (b) PL measurements. Adopted from Paper I.

negative V_{Si} will be predominantly available in intrinsic 4H-SiC only, with both p-type and n-type material favoring other charge configurations.

The first study demonstrating charge-state control over V_{Si} in 4H-SiC was Ref. [90], where an optical approach utilizing dual laser excitation was pursued. Optical processes may involve emission energies over a large range, rendering an exact identification of both the charge states participating in a transition, and the energy at which the transition occurs, challenging. Electrical characterization of charge-state transition levels, on the other hand, for instance as implemented in DLTS, would allow for a more exact estimate of the activation energies for charge-carrier capture and emission processes. Electrical identification of V_{Si} charge transition levels is a vital theme of Paper I, which commences by following up on the suggestion of Ref. [53] that the DLTS S-center indeed originates from the Si vacancy. The S-center is sporadically observed in DLTS spectra of n-type 4H-SiC, and consists of S1 at $E_C - 0.4$ eV and S2 at $E_C - 0.7$ eV (see Fig. 3.2a), having been attributed to different charge-state transitions of the same defect [56]. The transition levels of the S-center are in excellent agreement with those predicted for the Si vacancy, with the $V_{Si}(-/2-)$ transition estimated at $E_C - 0.6$ eV and the $V_{Si}(2-/3-)$ transition at $E_C - 0.4$ eV (see Fig. 4.1). To cement the assignment of S1 and S2 to V_{Si} , we monitor the S-center using DLTS (see Section 5.2.3) and the V1/V1' emission lines using PL spectroscopy (see Section 5.3.2). We correlate the evolution of the S-center concentration to that of the V1 emission intensity (attributed to the negatively charged V_{Si}) as shown in Figures 6.1(a) and 6.1(b), respectively. From the identical linearity in the

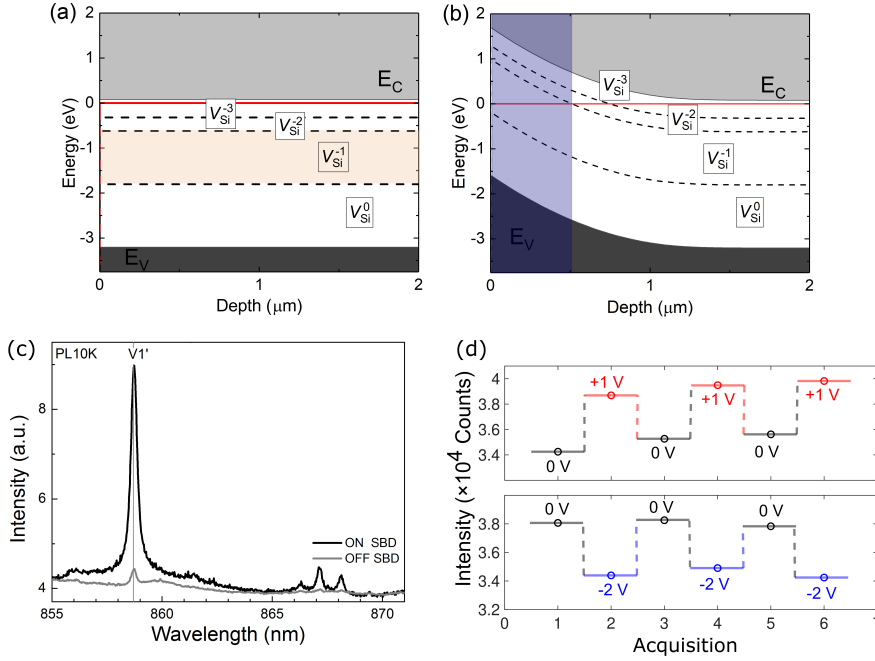


Figure 6.2: Conceptual band diagrams highlighting the V_{Si} charge states (a) in the absence of na SBD at 100 K, and (b) simulated using the Sentaurus Device simulator with deposited SBD, without applied bias and at 100 K. The red line signifies the Fermi level. PL spectra highlighting the $V1'$ emission line associated with the negative V_{Si} are shown (c) comparing the spectrum with (black) and without (gray) SBD, and (d) demonstrating selective charge-state switching of the V_{Si} upon forward (top) and reverse (bottom) biasing of the SBD. Adapted from Paper I.

proton fluence dependence of the S- and V-related signals, we confidently identify the S-center transitions as originating from the Si vacancy in 4H-SiC.

Now that the V_{Si} charge-state transition levels have been estimated, the knowledge can be applied to ensure optimal operation of the V_{Si} . The top row of Figure 6.2 shows the 4H-SiC band diagram and most stable V_{Si} charge state (a) without and (b) with a Schottky contact on the sample surface. Clearly, the singly negative charge state is not favored in the absence of an SBD, but the field-induced band bending illustrated in Fig. 6.2(b) promotes the stability of V_{Si}^{-1} at the expense of the other charge states for a field-dependent volume. To investigate the effect of applying electric fields via SBDs on the V_{Si} emission, we collect emission using a sample geometry as illustrated in the left panel of Fig. 5.6. Figure 6.2(c) highlights the effect of the SBD on V_{Si} -related emission by monitoring the $V1'$ ZPL while emission is collected from beneath (black line) and besides (gray line) a Schottky contact: indeed, the presence of the SBD is

found to enhance the $V1'$ emission intensity by almost an order of magnitude. Further, sequential application of bias to the SBD yields emission modulation that is positive for a small forward bias and negative for all other cases, as illustrated in Figure 6.2(d) for forward (top panel) and reverse (bottom panel) biasing. Combining the band diagram perspective with the observed intensity modulation, we attribute the field dependence of V_{Si} emission to sequential charge-state switching via applied bias. Note that electrical charge-state control was also recently demonstrated for single V_{Si} [89] and $V_{Si}V_C$ [91] defects using 4H-SiC p-i-n diodes instead of the SBD approach, where the latter would offer faster switching frequencies.

6.3 Emission tuning

Having identified the V_{Si} charge-state transitions located in the upper part of the 4H-SiC band gap, and ensured that the V_{Si} inhabits the qubit-friendly charge state, we turn our attention to the V_{Si} emission wavelength. The V_{Si} in its negative charge state is a verified single-photon emitter, with near-IR emission wavelengths suitable for integration with fiber optical technology [48]. However, local inhomogeneities scatter the V_{Si} emission energies, effectively restricting the viability of V_{Si} emitters for, e.g., quantum cryptography applications, where indistinguishable photons are needed. A promising route towards obtaining identical single photons is by emission tuning via controlled perturbation of the defect center. Paper I through Paper IV address this issue by exploiting parameters such as electric fields, local strain variations and vibronic tuning.

Paper I sets the stage for V_{Si} emission tuning by revealing a pronounced Stark effect for the $V1'$ emission line of the V_{Si} , as demonstrated in Figure 6.3(a). The $V1'$ emission wavelength was collected as a function of the applied electric field using PL spectroscopy on a 4H-SiC/SBD structure (see Fig. 5.6), and the Stark shift was found to be of quadratic character as displayed in Figure 6.3(b). Note that Stark shifts were also observed in Ref. [94] for both $V1$ and $V1'$, but revealing different dipole moments (μ) and polarizabilities (α) for the $V1$ and $V1'$ excited states. Interestingly, electric fields were applied both in parallel and perpendicular to the c -axis in Ref. [94], revealing that the Stark effects for $V1$ and $V1'$ depend on the field direction.

Now that both the benefit and opportunity for electric field tuning of single-photon emission are established, we recognize the need for a powerful predictive tool that is capable of capturing the minute differences in ground- and excited-state energetics that are induced by the applied field. Density functional theory is essentially a 0 K and ground-state technique, but approximations can be made to enable examination of excited state properties. In this thesis, we study the effect of applied electric fields on the V_{Si} emission energies by monitoring the evolution of the ground state total energy and KS eigenvalues, and the excited state energetics.

Paper II is devoted to developing a theoretical framework within DFT for studying Stark tuning of single-photon emission from point defects in

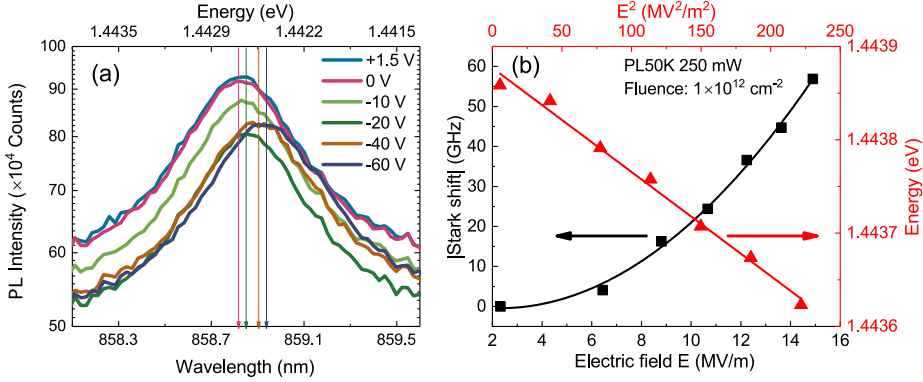


Figure 6.3: Electrically induced shift of the V1' emission line for a proton-irradiated n-type 4H-SiC sample collected at 50 K and for a laser power of 250 mW. Panel (a) shows the Stark shift, and panel (b) shows the V1' peak wavelength (black) and energy (red) versus the applied electric field. Adopted from Paper I.

semiconductors. Relevant physical principles and numerical details are discussed in Sections 4.4.6 and 4.5.3, respectively. Recall that electric fields are applied to a defect embedded in a slab supercell, and that the defect ground and excited state geometries are optimized under zero-field conditions (with the calibration field \mathcal{E}_{cal} applied to account for the polarization induced by the asymmetric slab surfaces) and for varying electric fields. Defect emission properties are studied both by monitoring the evolution of KS states of the ground state with electric fields, and by estimating the zero-phonon line as the difference in total energy between the excited and ground state of a system. The Si vacancy in 4H-SiC is used as a benchmark system to test the validity of the method, exhibiting documented Stark shifts of the V1 and V1' lines as shown in Ref. [94] and Paper I. In Paper II, we monitor the V1 and V2 ZPLs arising from ${}^4A_2^* \rightarrow {}^4A_2$ relaxations, whereas V1' and V2' involve ${}^4E \rightarrow {}^4A_2$ transitions (see Fig. 3.5).

Ground-state calculations were successfully conducted within the slab-and-field model, but excited states were challenging to resolve regardless of whether hybrid- or PBE-level calculations were conducted. Accordingly, the field evolution of the V1 and V2 ZPL energies was monitored using (semi)local ground- and excited state calculations. The ZPL energies were extracted from the total energy difference between the V_{Si}^- ES and GS according to the Δ -SCF method. Conveniently, the electronic confinement resulting from the slab geometry results in a PBE level band gap of $E_g = 2.6$ eV, which is considerably larger than that found ($E_g = 2.0$ eV) using the same theory level for bulk 4H-SiC. Although the larger band gap is an artificial effect, it is nevertheless expected to reduce the self-interaction errors commonly afflicting local and semi-local calculations.

The Δ -SCF calculations employing the PBE functional in Paper II yielded emission energies for V1 and V2 of 1.32 eV and 1.25 eV, respectively, agreeing

6. Summary of results

Table 6.1: Calculated (Calc.) excited-to-ground state relaxation energies E_{ZPL} for the V1/V2 and V1'/V2' transitions of $V_{\text{Si}}^-(h)$ and $V_{\text{Si}}^-(k)$. Quantities outside parentheses were obtained from Δ -SCF calculations, while parentheses refer to the ZPL energies being found from the Kohn-Sham eigenvalues of the respective ground state. Experimental (Exp.) [75] and calculated (Calc.) [78, 85] data from the literature are also included. ND stands for not detected and NC for not calculated, and all values are in eV. Adapted from Paper II.

Defect	ZPL	Calc.	Exp.	Calc. [78]	Calc. [85]
$V_{\text{Si}}^-(h)$	V1	1.32 (1.38)	1.438	1.541	1.450
	V1'	(1.44)	1.443	NC	1.792
$V_{\text{Si}}^-(k)$	V2	1.26 (1.35)	1.352	1.443	1.385
	V2'	(1.39)	ND	NC	1.953

within 10 % with the respective experimental values of 1.438 eV 1.352 eV [75]. The calculated emission energies are summarized in Table 6.1, and simultaneously compared to previous experimental [75] and computed [78, 85] values. Indeed, the ${}^4A_2^* \rightarrow {}^4A_2$ transition energies (V1 and V2) from Paper II show comparable agreement (within 0.1 eV) with experiment to other computational studies, although our PBE level values slightly underestimate the experimental ones.

Unfortunately, for the V1' and V2' excited states resulting in the ${}^4E \rightarrow {}^4A_2$ relaxations of $V_{\text{Si}}^-(h)$ and $V_{\text{Si}}^-(k)$, respectively (see Fig. 3.5), self-consistency of the Kohn-Sham problem proved exceedingly hard to achieve. Instead, the V1' and V2' energies reported in Table 6.1 result from Kohn-Sham eigenvalues of the respective V_{Si}^- ground states. Note that this approach, as opposed to that of the Δ -SCF method, does not account for a Franck-Condon relaxation energy in the excited state. Nonetheless, the KS ZPL energies reproduce the energy ordering of V1 and V2, and suggest that the V2' transition energy is close to that of V1.

The field dependencies of the ${}^4A_2^* \rightarrow {}^4A_2$ transitions reveal approximately linear Stark shifts for V_{Si}^- at h and k lattice sites. Indeed, this is in agreement with the lack of inversion symmetry for the V_{Si} defects at h and k sites [131]. The Stark shift (ΔE_{ZPL}) in the data was fitted according to Eq. 4.29. The fitting procedures resulted in variations in dipole moments and polarizabilities of $\Delta\mu = 1.46$ D and $\Delta\alpha = -640$ Å³ for the V1 transition, and $\Delta\mu = 3.92$ D and $\Delta\alpha = -920$ Å³ for V2 (1 D = 3.34×10^{30} C m and 1 Å³ = $4\pi\epsilon_0 \times 10^{-28}$ C m²V⁻¹). Our results indicate that dipole moment variations dominate for the ${}^4A_2^* \rightarrow {}^4A_2$ transitions of V_{Si} , with the polarizabilities being less important. Regarding agreement with experiment, Ref. [94] reported comparable values for $\Delta\alpha$, but $\Delta\mu$ is overestimated by about a factor of 10 herein.

To summarize, the issues with achieving self-consistency for the V_{Si} excited states must be addressed to advance the present method for calculating Stark shifts in defect transitions. Moreover, the discrepancy with experiment may arise from, e.g., the slab being too thin or the vacuum layer being too small. Note, however, that the determination of local electric fields is a challenging task also experimentally, and may add difficulties to assessing Stark shifts.

Instead of adding external perturbations to tune point defect emission wavelengths, internal degrees of freedom providing coupling with the defect wavefunction may be exploited. Herein, we discuss the potential of two such means: local strain variations in SiC micro- and nanocrystals of predominantly the 6H polytype (Paper III), and vibronic tuning of V_{Si} emission from 4H-SiC epi-layers (Paper IV).

To properly exploit single-photon emission from defect emitters embedded within a solid-state matrix, both controlled tuning of emission wavelengths and ordered placing of the light source should be available. Fortunately, employing nano- and microcrystals deriving from ultra-high purity silicon carbide powder provides access to both features. The micro- and nanosized crystals present a viable alternative to more traditional etching techniques, enabling engineering of structures similar to the two-dimensional waveguide nanopillar array of Ref. [95], but with the added advantage of self-assembly, flexible substrates and scalability. Paper III addresses issues such as V_{Si} formation and placing, characterization, waveguiding effects and V_{Si} emission tuning that are all facilitated by the SiC powder particles, using a combination of cathodoluminescence (CL) spectroscopy (see Section 5.3.3), scanning electron microscopy (SEM) and transmission electron microscopy (TEM). A representative SEM image of the SiC microparticle sample set can be found in Fig. 5.7(a), where the nanoparticle size distribution stretches from some hundred nanometers to above 5 μm , and the morphologies vary from flakes and sheets to nearly round or square. The 6H SiC polytype is predominantly contained in the powder, but also 3C, 4H and 15R can be identified, as shown by Figs. 5.7(b)-(d).

In Paper III, we monitor the V1, V2 and V3 ZPLs that have been attributed to the h , k_2 and k_1 configurations of V_{Si} (in the negative charge state), respectively, in CL spectra of 6H-SiC [86]. Importantly, V_{Si} -related emission can be collected using the SEM-CL setup even in some of the unimplanted SiC particles, but the V_{Si} features are significantly enhanced by proton irradiation. CL spectra focusing on the V1 and V2 emission lines collected at various locations on an implanted square 6H-SiC particle reveal a clear dependence of the V_{Si} -related emission on the defect location with respect to the particle edges. The false color maps in Figures 6.4(a) and 6.4(b) illustrate the distribution and approximate locations of V1 and V2 centers after proton irradiation, where V1 emission is generally located close to particle centers and V2 emitters can be found distributed across the entire particle area. Importantly, Figure 6.4(c) shows the V1 and V2 emission energies for different positions relative to the literature values (dotted lines), and we find considerable peak shifting especially towards the particle edges. In general, the V_{Si} peaks shift collectively, but some cases of asymmetric shifting are found. Additionally, the near-band edge (NBE) emission also displays a variation upon scanning over the particle surface, as shown in Figures 6.4(d) and 6.4(e). Collective shifting of defect- and NBE-related emission is expected in the case that *strain tuning* is causing the emission shifting [85, 154] observed for SiC particles. By comparing the position-dependent V_{Si} emission tuning revealed in Fig. 6.4(c) to strain analysis as implemented in transmission electron microscopy, the observed V_{Si} emission shifts are attributed to compressive strain of 2-3 %

6. Summary of results

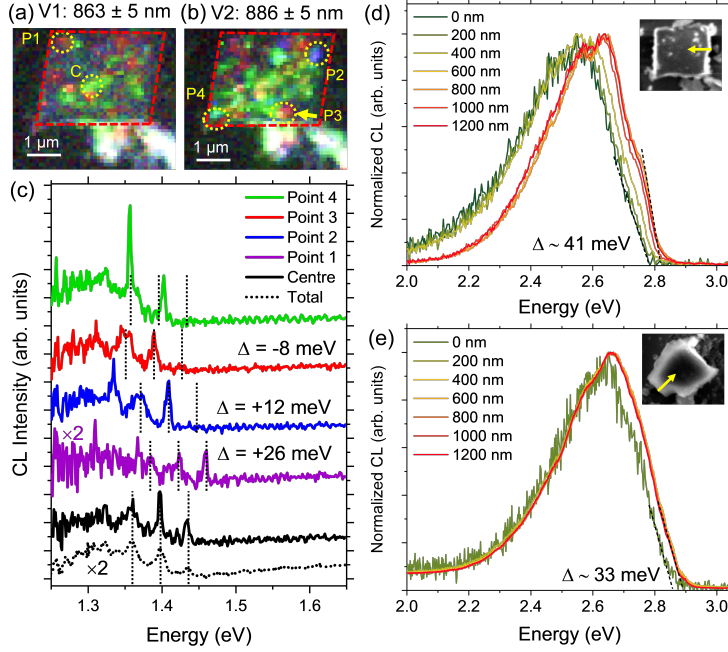


Figure 6.4: V_{Si} -related emission from an implanted square 6H-SiC particle. Panels (a) and (b) show false colour maps revealing the distribution of V1 and V2 centers over the particle surface, (c) shows CL spectra from the different regions marked in (a)-(b), and (d)-(e) reveal position-dependent shifts in V_{Si} emission. Adopted from Paper III.

along the particle a -axis.

Let us now turn our attention back to the n-type 4H-SiC epi-layers that were used for electric field application in Paper I. In Paper IV, we study a set of novel emitters that arise in the near-infrared (NIR) in the vicinity of the V1 and V1' ZPLs in 4H-SiC epi-layers after irradiation. The emission lines are labeled the L-lines herein, and are displayed in Figure 6.5(a). To the best of our knowledge, the L-lines have not been discussed elsewhere in the literature, but appear without mention in spectra shown in Ref. [155] and Paper I (see Fig. 6.2c).

The L-lines appear after irradiation, and regardless of whether H or He is used as the implanted species, thus excluding a hydrogen-related origin. Moreover, combined with a linear increase in intensity with proton irradiation fluence, an intrinsic and primary origin is clearly indicated. The deviation in slope between the two most dominant L-lines, L1 and L2, evidences that a unique origin likely cannot explain all properties of the L-line family. The thermal quenching

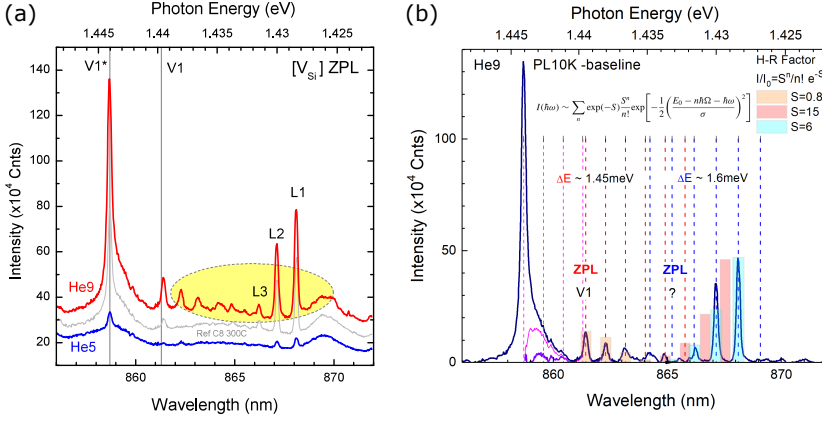


Figure 6.5: (a) PL emission in the near-infrared (NIR) collected from a He-irradiated n-type 4H-SiC epi-layer and showcasing the V1/V1' ZPLs (attributed to V_{Si}) and the L-lines. (b) Background-subtracted spectra for the He-irradiated sample. The periodic nature of the emission lines is evidenced by color-coded sets of equidistantly-spaced vertical markers. The shaded columns are first-approximations for a given Huang-Rhys (HR) factor S . Adapted from Paper IV.

behavior of the L-lines corroborates this interpretation, as $PL(T)$ spectra for V1/V1' and L1-L4 reveals that at least two categories of emission must be considered: V1 and L1 exhibit stable thermal quenching, while for V1' and L3 we observe negative thermal quenching. Again, two sets of deviating characteristics are found, and the relation between V_{Si} and the L-lines is strengthened.

Next, we turn to the electric field dependence of the NIR emission, and find that the L-lines exhibit an intensity increase upon SBD formation that is similar to, but lower than, that found for V_{Si} in Paper I (see Fig. 6.2c). Furthermore, a Stark shift is clearly observed for L2, but not for L1. The small red-shift (~ 1 meV) of the L2 emission line is well described by both a linear and a weakly quadratic behavior, and indicates a link between L2 and V1'. Importantly, sequential biasing of the SBD results in emission intensity modulation for both L1 and L2, in a similar manner to that found for V1' in Paper I (see Fig. 6.2d). Finally, the annealing behavior of the V- and L-lines are compared, revealing similar characteristics for the two emission line families. Annealing at 400 °C either retains or slightly enhances the L-line and V1/V1' intensities, while higher temperatures (600 °C) reduce the L-line emission until they can no longer be distinguished above 800 °C. However, although the V_{Si} emission is significantly reduced at both 600 °C and 800 °C, the V1' emission line is still clearly visible in the samples after the 800 °C annealing step. In sum, these characteristics indicate a shared origin for the L-center and the V-lines: the Si vacancy.

Although the L-lines have been tentatively attributed to the V_{Si} , their true nature has yet to be revealed. The regular and periodic appearance of these sharp

peaks suggests the possible involvement of phonons in the optical transitions. Moreover, as shown in Figure 6.5(b), we find that the energy separation (ΔE) between adjacent peaks is different for the line groups V1-L4 and L1-L3, i.e., 1.45 meV and 1.59 meV, respectively. Indeed, the ordering of the L-peaks in terms of spacing and relative intensity strongly indicates a vibronic origin. Upon considering the conceptual configuration coordinate (CC) diagram shown in Fig. 2.7, it becomes evident that such a model could explain the presence of several closely spaced satellites related to the V1 and V1' zero-phonon lines. Furthermore, as indicated in Fig. 6.5(b), extrapolation of the vertical marker subsets to higher energies predicts potential ZPL positions at V1', V1 and 1.433 eV. Two possible vibrational models are proposed where the fitting of the multi-peak subsets is presented following a common Huang-Rhys simulation approach [156], yielding Huang-Rhys factors (S) in the (0, 15) range. We speculate that the modeled ZPL at 1.433 eV could be related to the V2' transition of $V_{\text{Si}}^-(k)$, in keeping with the suggestion of Paper II that the V2' transition energy is close to that of V1 (see Table 6.1). In conclusion, Paper IV tentatively attributes the L-lines to vibronic replicas of the V1 and V1' emission lines arising from the negatively charged V_{Si} in 4H-SiC.

6.4 Point defect migration and controlled qubit formation

The Si vacancy in 4H-SiC is a promising single-photon emitter and spin center, but exhibits a pronounced instability with respect to temperature compared to, e.g., the V_{C} , as exemplified by the conversion of V_{Si} into CAV above 400 °C in p-type 4H-SiC [49]. The annealing behavior of V_{Si} in n-type 4H-SiC material remains more elusive, and has been suggested to depend strongly on the irradiation procedure and thus degree of dopant compensation in the samples [157]. Indeed, the S-center (assigned to V_{Si} in Paper I) has been shown to anneal out above 400 °C with a barrier of 1.8 eV [56] in samples with low defect concentrations, but V_{Si} defects will be shown below to remain after high-fluence irradiation and 1000 °C annealing in n-type epi-layers. Paper V and Paper VI aim to elucidate the annealing behavior of V_{Si} defects introduced into n-type 4H-SiC samples via proton irradiation to various fluences.

First, consider the case of n-type 4H-SiC epi-layer samples that have been irradiated with protons to different fluences, and thus contain hydrogen within some region. A recent study [158] revealed that V_{Si} -related emission is significantly diminished by implantation of hydrogen as compared to that of helium, indicating that hydrogen somehow quenches V_{Si} emission, perhaps by passivating V_{Si} defects. This interpretation is corroborated by both theoretical [68] and experimental [61] works suggesting that vacancies in SiC (and particularly V_{Si}) may readily capture H. This has motivated the work in Paper V, which is devoted to investigating the interplay between hydrogen and V_{Si} defects by studying the effect of low-temperature annealing on V_{Si} emission in the presence of hydrogen using both experiment and theory.

Paper V explores the concept of complex formation between H and V_{Si} by

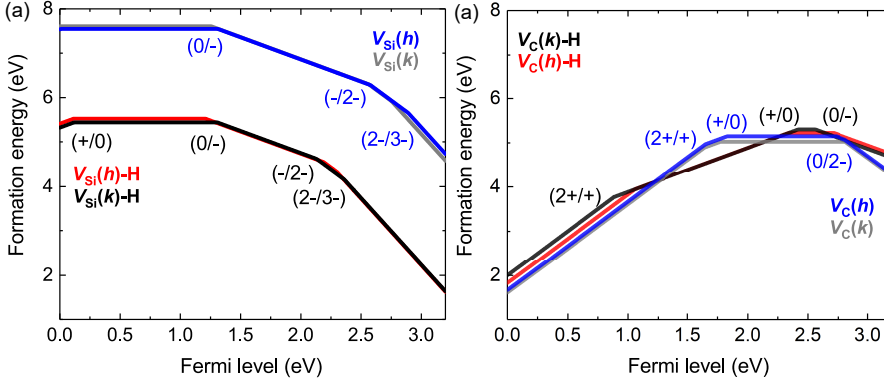


Figure 6.6: Formation energy diagrams comparing (a) V_{Si} and $V_{\text{Si-H}}$, and (b) V_{C} and $V_{\text{C-H}}$. Isolated monovacancies and vacancy-hydrogen complexes were studied using 96-atom and 400-atom 4H-SiC supercells, respectively. Based on data from Paper V and Paper VII.

comparing theory and experiment, and begins by identifying the H interstitial (H_i) as an amphoteric defect in 4H-SiC with the $(+/-)$ transition located near mid-gap, in keeping with previous theoretical works [159] and reinforcing H_i as a negative- U defect in 4H-SiC. Depending on the Fermi level, H_i is prone to locating either in an antibonding-to-C configuration for the $q = +$ charge state, as the C atom is associated with a larger electron density than Si, or in a tetrahedral configuration and forming H-Si bonds for $q = -$. Furthermore, using the NEB method (see Section 4.4.5) and the PBE functional, activation energies (E_A) for interstitial hydrogen migration in 4H-SiC were found to be much lower for H_i^+ ($E_A \sim 0.5$ eV) than H_i^- ($E_A \sim 2.2$ eV). This is in good agreement with experimental works showing that hydrogen migrates much faster in p-type than n-type 4H-SiC material [65]. In fact, Ref. [67] showed that H does not diffuse out of n-type 4H-SiC until above 1300 °C, and attributed the unexpectedly high thermal stability of H to trap-limited diffusion, likely caused by vacancy defects.

To further understand the role of H, we turn to the formation energy diagrams (see Sections 4.4.2 and 4.5.2) calculated for V_{Si} and $V_{\text{Si-H}}$ and shown in Figure 6.6(a), demonstrating that $V_{\text{Si-H}}$ complex formation is energetically favorable in p- and n-type 4H-SiC provided that both hydrogen and Si vacancies are present in the same region. Proton irradiation of 4H-SiC samples is frequently employed to form V_{Si} defects, and both H and V_{Si} will be abundant and in close proximity near the projected range of implanted hydrogen. Under the non-equilibrium conditions that manifest during an irradiation process, $V_{\text{Si-H}}$ complexes are therefore likely created, and their concentration may be enhanced upon post-irradiation annealing.

Experimentally, Paper V probes potential $V_{\text{Si-H}}$ complex formation by monitoring V_{Si} -related emission (using PL spectroscopy, see Section 5.3.2) from n-type 4H-SiC samples that were proton-irradiated ($E = 1.5$ MeV) to different

fluences, and at room temperature and 400 °C (so-called hot implantation). We observe a reduction in the V1 intensity with increasing irradiation temperature (RT compared to 400 °C) when the proton fluence passes some threshold, while V_{Si} emission intensities increase with the hot implantation for lower fluences. Due to a reduction in non-radiative channels with higher temperature, we would initially expect V1 to increase for hot implantation (400 °C) compared to RT for all fluences. In light of the above discussion, we speculate that the reduction in V1 for the high fluence sample is caused by the smaller distance between V_{Si} defects and H atoms, combined with the elevated temperatures (400 °C) that allow H_i diffusion lengths of around 20 nm. Accordingly, hot implantation of H may increase the likelihood of forming V_{Si} -H complexes and hence quenching V_{Si} emission as compared to the room temperature process. In conclusion, hydrogen is likely not a suitable implantation species for ensuring optimal control over the V_{Si} formation process, especially not if the region encompassing the H projected range is to be probed during the experiment.

Importantly, to facilitate utilization of point defects in 4H-SiC for quantum technology, complete control over both formation, stability and out-annealing processes should be attained. We have already established that having H atoms present in the vicinity of V_{Si} may have a detrimental impact on V_{Si} emission, effectively reducing the yield when forming V_{Si} defects and causing additional uncertainty in the V_{Si} placing and abundance. Next, we turn to Paper VI and consider the case where no hydrogen atoms (or other known contaminant species) are present within the region to be probed, and study the effect of temperature and proton irradiation fluence on the evolution of different intrinsic defect species within 4H-SiC epi-layers.

The Si vacancy is known to be metastable with respect to conversion into the carbon antisite-vacancy (CAV) pair in p-type 4H-SiC [49], with a transformation barrier of around 2 eV [64, 160, 161] enabling the $V_{Si} \rightarrow C_{Si}V_C$ transformation to take place at temperatures of 400 °C and above. Fortunately, the CAV complex has shown ultra-bright single-photon emission characteristics [49], and hence the V_{Si} -to-CAV conversion process can be exploited to tune the defect species to the task at hand. However, the process has not been verified in n-type 4H-SiC material, and although electrical charge-state control has been shown [92], the CAV pair is still lacking DLTS identification as shown for V_{Si} in Paper I. Reliable DLTS peak assignments are also missing for the divacancy ($V_{Si}V_C$), which is the alternative intrinsic and qubit-friendly complex formed from V_{Si} . Depending on the V_{Si} charge state, migration barriers for Si monovacancies are predicted in the 2-4 eV range [63, 64], enabling V_{Si} migration at elevated temperatures above (at least) 400 °C. Provided that the temperature is sufficiently high and the distance between V_{Si} and V_C defects is small enough, the divacancy may form by migration of V_{Si} . The divacancy exhibits coherent spin manipulation, entanglement with nearby nuclear spins [27] and single-photon emission in the telecom range, providing a powerful supplement to V_{Si} defect centers. Finally, migrating V_{Si} species may encounter N dopant atoms at C sites and form N_CV_{Si} complexes (not considered in detail in this thesis), or anneal out completely to the surface or other sinks.

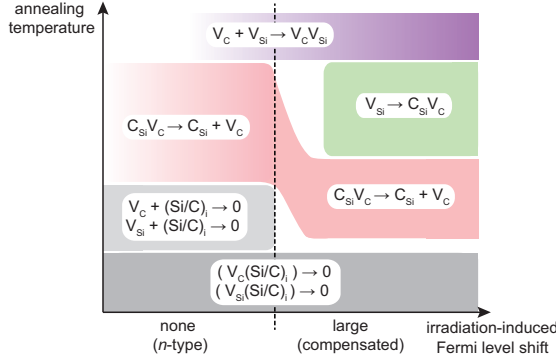


Figure 6.7: Summary of intrinsic defect inter-conversion model in 4H-SiC, where darker colors refer to larger concentration. Adopted from Paper VI.

Paper VI combines DLTS (see Section 5.2.3) and PL spectroscopy (see Section 5.3.2) to monitor the thermal evolution of intrinsic defect species and map the many inter-defect conversion channels available in n-type 4H-SiC. Now, DLTS (as performed herein) collects information from the top $\sim 1\text{-}4\mu\text{m}$ of the epi-layer only, and the PL setup is constructed to be near-confocal and predominantly considers the same region. Thus, we can exclude interference from the H atoms implanted into the substrate, and consider intrinsic defects only. The samples studied are annealed in stages at temperatures ranging from 300-1000 °C, meaning that we are mainly concerned with defects formed during irradiation, that is, vacancies and interstitials but also smaller complexes such as the divacancy and the carbon antisite-vacancy pair. The defects that are considered herein are therefore V_{Si} , V_{C} , C_i , Si_i , $\text{C}_{\text{Si}}V_{\text{C}}$ and $V_{\text{Si}}V_{\text{C}}$. The samples employed during the experiments can be roughly grouped into two categories: in the first sample set, the total defect concentration was approximately $N_t < 0.2N_{\text{D}}$ enabling measurement using DLTS, and in the second set N_t was above the lower detection limit for PL measurements. However, the high-dose samples manifested compensation of dopants and were therefore not suitable for DLTS measurements.

The main findings of Paper VI are summarized by the model illustrated in Figure 6.7 and the following:

- The first annealing stage occurs at 300 °C and below and involves Frenkel pair recombination between vacancies and nearest-neighbor interstitials.
- By monitoring the DLTS signatures of V_{Si} (S1 and S2) and V_{C} ($Z_{1/2}$), a reduction in vacancy concentration is observed by increasing the annealing temperature from 300 °C to 400 °C, and is attributed to recombination with non-nearest neighbor interstitials.
- The Frenkel pair recombination process (alternatively antisite formation) is limited by the diffusivity of C_i and Si_i , and thus effectively hindered in

6. Summary of results

intrinsic (e.g., compensated n-type) and p-type material as opposed to the n-type case.

- The EH_4 and EH_5 DLTS peaks arising in n-type 4H-SiC spectra, at 1.0 and 1.1 eV below E_C , respectively and shown in Figure 6.8(a), are attributed to the $(+/0)$ charge-state transitions of CAV. EH_4 consists of three contributions assigned to the hh , hk and kk configurations of CAV (with the first letter referring to C_{Si}), and EH_5 is correspondingly attributed to $\text{CAV}(kh)$.
- Increasing the annealing temperature above 400 °C causes a reduction in CAV concentration as observed in the DLTS samples. As no new V_{Si} defects appear, we conclude that the $V_{\text{Si}} \rightarrow \text{C}_{\text{Si}}V_C$ conversion channel is blocked in n-type material.
- The decrease in $[\text{CAV}]$ is correlated with a nearly identical increase in the V_C concentration that was also observed in Ref. [60] and is shown in Figure 6.8(b). This annealing stage (above 400 °C) thus results in a dissociation of CAV according to $\text{C}_{\text{Si}}V_C \rightarrow \text{C}_{\text{Si}} + V_C$ in n-type 4H-SiC, where a hop of V_C over a single lattice constant is hypothesized to be enough for the $Z_{1/2}$ DLTS signal to recover.
- In the high-fluence intrinsic samples, where migration of interstitials was delayed and not all V_{Si} defects had annealed out, the CAV concentration (as detected by PL) started to recover upon annealing at 1000 °C, indicating an opening of the V_{Si} -to-CAV conversion channel.
- The PL samples also revealed the development of divacancy defects, which are detectable after 300 °C annealing but increase drastically in concentration above 600 °C due to increased V_{Si} diffusion lengths (V_C is immobile below 1200 °C). A clear dose dependency in the rate of VV formation is observed, where the distance between vacancy defects must be low enough (i.e., the vacancy concentration high enough) for significant divacancy densities to form, even above 600 °C.

Hitherto, we have discussed the lifecycle of the silicon vacancy in SiC from birth to demise. The V_{Si} cannot be formed thermally, instead necessitating irradiation or implantation. To sharpen V_{Si} -related signals as manifested in, e.g., DLTS and PL spectroscopy, a 300 °C annealing stage is employed in the present work, resulting in initial Frenkel pair recombination between vacancies and neighboring interstitial defects. Paper I through Paper IV utilize Si vacancies generated at this stage to achieve electrical identification, charge-state control and emission tuning. The next moderate-temperature annealing stage utilizing 400 °C annealing is discussed in Paper V and Paper VI, and may result in V_{Si} -H complex formation if H is present, and/or recombination between V_{Si} and non-nearest neighbor interstitials. Further annealing can result in formation of the CAV from V_{Si} depending on the temperature and Fermi level, succeeded by migration of V_{Si} defects yielding formation of divacancies, NV centers and

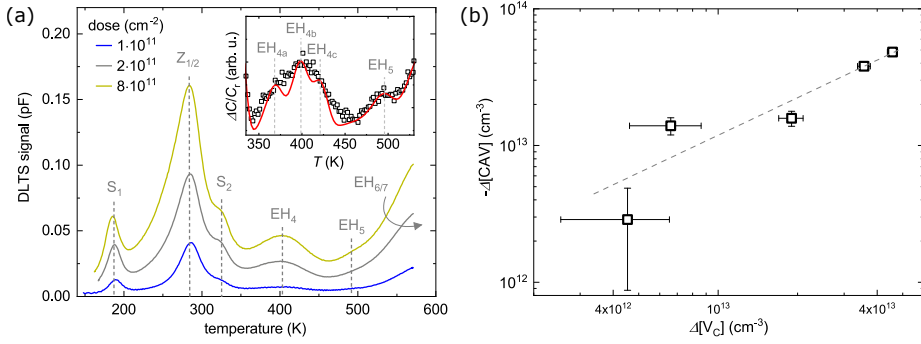


Figure 6.8: (a) High-temperature DLTS spectra of proton-irradiated n-type 4H-SiC epi-layers with the EH₄ fine-structure shown in the inset, and (b) concentration correlation between the V_C increase and CAV decrease upon annealing. Adapted from Paper VI.

out-annealing of V_{Si} to, e.g., the surface and other sinks. After the V_{Si} has gone, V_{Si} -related complexes such as CAV and VV may remain if their formation conditions are favorable, but most importantly, the carbon vacancy continues to survive until temperatures above 1600 °C, and will be discussed next.

6.5 Probing physics and migration of Si and C vacancies

The preceding sections have several times referred to the relative instability of V_{Si} with respect to temperature as compared to V_C , and we have hinted at the fundamental differences between the two vacancy types, leaving V_C as a negative- U and lifetime-limiting defect while V_{Si} in the negative charge state is a single-photon emitter with a high-spin ground state. The time has come to tackle the underlying differences yielding the strikingly contrasting properties of Si and C vacancies in 4H-SiC, and from there we will transition into discussing the thermal behavior of the V_C defect.

The aforementioned differences between V_C and V_{Si} arise from their distinct local chemical environments. Surrounding the V_C are four nearest-neighbor Si atoms that, due to the extended nature of their dangling bonds, have strongly overlapping orbitals. The combination of nearest-neighbor bonding and a degenerate ground state drives a pronounced and symmetry-lowering Jahn-Teller (JT) distortion, resulting in strong inward displacement, C_{1h} symmetry and low spin of $S = 0$ for the neutral charge state of V_C [70–74]. The result is a pronounced negative- U behavior [69] for the $(0/2-)$ charge-state transition of V_C in 4H-SiC [42, 51], leaving the V_C as a prominent charge-carrier trap and lifetime-limiting defect in SiC devices. The Si vacancy, on the other hand, is surrounded by C atoms having highly localized orbitals. As the C dangling bonds are not extended enough to overlap there is no driving force for a JT distortion, and instead, the energy gain arises from a shortening of the C-Si bonds that

6. Summary of results

results in a slight outward-breathing relaxation retaining the C_{3v} symmetry. Moreover, for the case of V_{Si} the exchange interaction wins the competition over JT distortions, yielding a high spin state of $S = 3/2$ for the negative charge state [48, 77]. The structural differences between V_{C} and V_{Si} are illustrated in Fig. 3.4, highlighting the lower symmetry of the V_{C}^0 defect orbitals (top) as compared to those of V_{Si}^- (bottom).

Although we have discussed experimental techniques like DLTS and PL as means to monitor the presence of V_{Si} and V_{C} defects, they are not capable of probing the fundamental physics giving rise to the different defect behaviors (although DLTS combined with illumination can be used to reveal negative- U properties [162]). Paper VII addresses this issue by using low energy muon spin rotation spectroscopy (LE- μ SR, see Section 5.4) to probe the difference between the Si and C vacancies. Proton-irradiated 4H-SiC samples containing both V_{Si} and V_{C} defects were employed, and compared to the results of Ref. [147] where only the V_{C} remained in the epi-layers. The results from the muon measurements are shown in Figure 6.9 and reveal a strong difference in the tendency of the muon to form muonium (Mu) between the samples having many Si vacancies (Figs. 6.9a and 6.9b), having few Si and C vacancies (Fig. 6.9c) and having a large V_{C} density (Fig. 6.9d).

Now, the pronounced difference in the muon tendency of binding to V_{Si} and V_{C} observed with LE- μ SR is investigated using hybrid density functional calculations. Building on the work of Paper V and employing the H atom to model muonium formation ($\text{Mu} = \mu^+ e^-$), we compare complex formation between hydrogen and the two vacancy types in 4H-SiC. Figure 6.6 contains formation energy diagrams calculated for V_{Si} vs. $V_{\text{Si}}\text{-H}$ in 6.6(a), and V_{C} vs. $V_{\text{C}}\text{-H}$ in 6.6(b). While there is a strong tendency for the muon to occupy the V_{Si} site (by forming $V_{\text{Si}}\text{-Mu}$ complexes), the energy gain is smaller for formation of the $V_{\text{C}}\text{-Mu}$ complex, particularly in n-type material. Importantly, the samples employed had large defect densities resulting in compensation of dopants, mid-gap Fermi levels and leaving V_{Si} and V_{C} in the negative and neutral charge states, respectively.

Returning to the experimental findings shown in Fig. 6.9, we observe a marked difference in sensitivity to the two vacancy types, where the muons seem to respond to much lower V_{Si} densities than those needed to detect V_{C} . We speculate that this is due to factors such as the greater V_{Si} charge, the larger space within the Si void, and the pronounced energy gain predicted for $V_{\text{Si}}\text{-Mu}$ complex formation as opposed to that for $V_{\text{C}}\text{-Mu}$ (see Fig. 6.6). We argue that there is a strong tendency for Mu^+ to be trapped by V_{Si} and then capturing an electron to form Mu^0 , as a result of the positive muon being attracted to the negative V_{Si} before reaching an anti-bonding site in the lattice. Oppositely, for a large V_{C} density as shown in Fig. 6.9(d), a mechanism involving a two-electron capture process at the V_{C} is proposed, where Mu^- may form from Mu^+ via a short-lived Mu^0 state.

When μ^+ is attracted to a negative V_{Si} defect, a stable and long-lived Mu^0 state results upon capture of one electron. For V_{C} , on the other hand, a similar initial process takes place, but the strong interaction between V_{C}

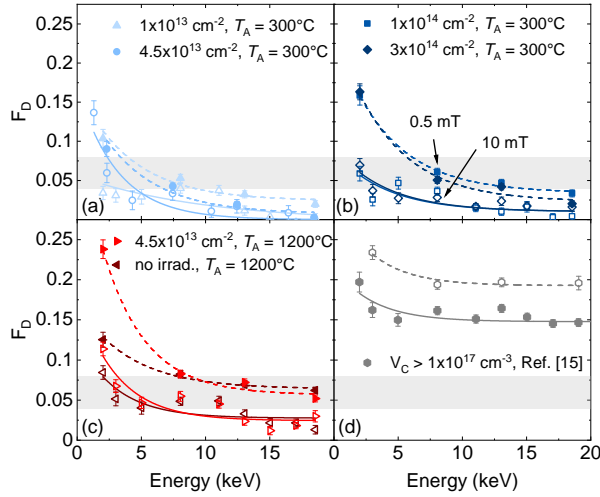


Figure 6.9: Muon measurements to probe differences between V_{Si} and V_{C} defects in 4H-SiC showing the diamagnetic fraction measured for magnetic fields of $B = 0.5$ mT (filled symbols) and $B = 10$ mT (empty symbols). Samples containing both V_{C} and V_{Si} defects are shown after annealing at 300°C in (a)-(b) for different fluences, while low V_{C} and V_{Si} densities are shown after 1200°C annealing in (c). Measurements without V_{Si} defects but with a large V_{C} density are shown in (d), and are from Ref. [147]. Lines are guides to the eyes. Adapted from Paper VII.

and the environment results in a second electron being captured and a delayed Mu^- formation. Remarkably, the muon behavior within each vacancy type is therefore strongly reminiscent of the proclivity of V_{Si} and V_{C} to form localized and isolated high-spin states, or interact strongly with the lattice via electron-phonon coupling yielding a JT distortion, respectively. In summary, Paper VII discusses the capacity of the low energy μSR technique for probing distinct relaxation mechanisms of vacancy defects in semiconductors, while simultaneously providing non-destructive and depth-resolved detection of defects close to the semiconductor surface.

Having established that the fundamental differences between V_{C} and V_{Si} defects in SiC can be probed using the LE- μSR technique in Paper VII, the next stage involves studying low-fluence C-implanted n-type 4H-SiC epi-layers using DLTS, and moving beyond the temperature range where V_{Si} is stable. The goal is to remove all other defect signatures save that of the V_{C} and investigate the mechanism for V_{C} diffusion, in order to both resolve any anisotropy for motion within 4H-SiC, and to predict V_{C} distributions in power devices. Recall that after irradiation the main defects present are Si and C vacancies and interstitials, CAV complexes and divacancies. In n-type 4H-SiC samples (assuming low enough

6. Summary of results

defect concentrations to avoid compensation), Si vacancies mainly anneal out via Frenkel pair recombination with interstitials above 400 °C (see discussion in Paper VI). Moreover, any CAV pairs that arise during irradiation and dynamic annealing will start dissociating into $C_{Si} + V_C$ above 400 °C. V_C defects are highly stable in 4H-SiC, and require temperatures above at least 1000 °C to move. Annealing at temperatures needed for inducing V_C motion may cause formation of the divacancy, however, for the low defect densities studied in this context ($[V_C] \leq 1 \times 10^{14} \text{ cm}^{-3}$) the large inter-defect distances render large VV concentrations unlikely (see Paper VI). Thus, in the temperature range 1200-1600 °C that is studied in Paper VIII and Paper IX, the predominant defect remaining is the carbon vacancy.

Whereas the V_{Si} exhibits well-known PL fingerprints, DLTS is the preferred method for detecting the V_C in this thesis. Paper VIII and Paper IX monitor the evolution of the $Z_{1/2}$ concentration versus depth profiles (see Section 5.2.4) with increasing annealing temperature to elucidate the migration and annealing behavior of V_C . Both papers utilize n-type 4H-SiC epi-layer samples having been implanted with C ions to generate V_C concentration profiles within the SBD depletion region, and compare samples grown showing the *c*-face to ones grown showing the *a*-face to study V_C migration along two crystallographic axes. Paper VIII reveals that the carbon vacancy exhibits anisotropic diffusion in n-type 4H-SiC. By monitoring the distribution of V_C defects along the two different crystallographic directions using DLTS depth profiling, and annealing the samples in several stages, we reveal that the V_C diffuses much further along the *a*-axis than the *c*-axis, as shown in Figures 6.10(b) and 6.10(a), respectively, for 200-1400 °C annealing. Moreover, the V_C was found to be immobile until at least 1200 °C, and was still present in the samples after annealing at 1500 °C for 1 h.

Even though the anisotropic nature of V_C diffusion has been established, no Arrhenius behavior for the V_C diffusivity was demonstrated in Paper VIII, and the mechanisms behind the observed phenomena remain unknown. In Paper IX, we combine theory and experiment to illuminate the mechanisms behind V_C diffusion in 3C- and 4H-SiC, and quantify the carbon vacancy diffusivity by fitting the V_C concentration profiles to the diffusion equation (see Section 3.3.3 and Eq. 3.2). Note that high-temperature annealing induces intrinsic Fermi levels, i.e., near the mid-gap, causing V_C to inhabit the neutral charge state in 4H-SiC. Using the NEB method as implemented in the DFT framework (see Section 4.4.5), 3C-SiC is used as a starting point due to the simpler crystal structure as compared to the 4H polytype. V_C diffusion is found to be isotropic in 3C-SiC, having a barrier of 3.5 eV as deduced using PBE, and a transition state geometry consisting of four C atoms organized as a gate-like structure. This is in agreement with the findings of Ref. [59], and is illustrated in Fig. 4.2. Using the dimer method to refine the transition state geometry and the HSE06 functional to refine the barrier energy, the final E_A for V_C^0 migration in 3C-SiC was found to be 4.0 eV.

The 4H-SiC case is more complex than that for 3C, with V_C having three different jump paths available for each lattice configuration (*h* and *k*). However,

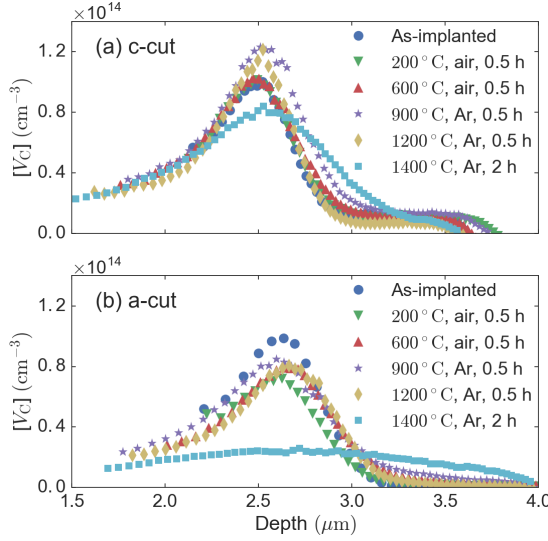


Figure 6.10: V_C depth profiles after annealing at different temperatures as deduced by DLTS depth profiling along the (a) c -axis and (b) a -axis. Adopted from Paper VIII.

before we go into detail on the migration paths available to V_C in 4H-SiC and the migration barriers calculated by NEB, we review the experimental findings. Through Paper VIII and as shown in Fig. 6.10, the fact that V_C diffusion is anisotropic in 4H-SiC has already been established. By collecting similar V_C concentration profiles along the a - and c -axes at different temperatures ranging from 1200-1600 °C, and extracting diffusivities at each temperature by fitting to Fick's second law (Eq. 3.2), Arrhenius plots can be constructed for the V_C diffusivity (D) versus temperature (according to Eq. 3.3). The Arrhenius behaviors for V_C along the a - and c -axes in 4H-SiC are shown in Figure 6.11(a), which emphasizes that V_C diffuses significantly faster along the a - compared to the c -direction, with $D_0^a = 0.02 \text{ cm}^2/\text{s}$ and $E_A^a = 3.6 \text{ eV}$, and $D_0^c = 0.54 \text{ cm}^2/\text{s}$ and $E_A^c = 4.4 \text{ eV}$.

Symmetry considerations reveal that the six different atomic hops a C atom can take to fill a neighboring C vacancy in 4H-SiC can be reduced to four symmetrically inequivalent jumps: two that are in-plane or basal (hh and kk), and two axial hops (labeled kh and kh'). Intriguingly, following the NEB, dimer, and finally hybrid-level SCF calculations (see Section 4.4.5), the energy barriers for V_C^0 migration are found to be 4.2 eV for the axial kh' hop, 4.1 eV for the axial kh hop, 4.0 eV for the in- k -plane or basal kk jump, while the basal hh atomic hop has the lowest barrier of 3.7 eV. Clearly, axial V_C migration along the c -direction has a total barrier of 4.2 eV according to the DFT calculations, while basal or a -axis V_C diffusion is much faster with a 3.7 eV barrier when confined within h -planes. In fact, basal migration within k -planes appears to be identical

6. Summary of results

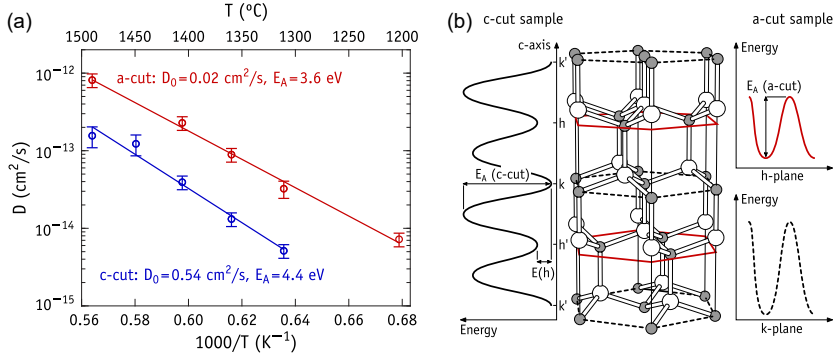


Figure 6.11: (a) Arrhenius behavior of V_C diffusion in 4H-SiC, and (b) microscopic model for anisotropic V_C migration based on NEB calculations. Adapted from Paper IX.

to that found for 3C-SiC, indicating that the anisotropy in V_C diffusion arises from differences in, for instance, cubic and hexagonal crystal fields, or the bond coordination in the h -plane and k -plane transition state.

The 4H-SiC crystal structure, crystallographic axes (a and c), lattice planes (h and k), and finally minimum energy paths (MEPs) for the four available V_C atomic hops are all depicted in Figure 6.11(b). Comparing to the experimental findings shown in Fig. 6.11(a), we attribute V_C diffusion along the c -axis to axial hops between h and k planes on the C sublattice, and V_C diffusion along the a -axis to basal atomic hops within h -planes. Note that the basal V_C migration path within the k -plane is illustrated with a dashed line in Fig. 6.11(b), to emphasize that this migration path is likely blocked at temperatures when axial V_C diffusion has not yet begun. The minimum energy paths for V_C atomic hops, illustrated schematically in Fig. 6.11(b), highlight that V_C prefers to move within h -planes as compared to all other migration paths. The explanation can be found in the transition state geometry: the highest energy path along the c -axis, the kh' jump, hinders V_C migration because the moving C-atom has a low twofold coordination at the saddle point, causing a high energy barrier. Conversely, the transition state of the hh hop exhibits a geometry more similar to perfect Si-C sp³ bonding, yielding a lower activation energy for V_C migration.

The experiments conducted in Paper IX establish that V_C remains present in n-type 4H-SiC also after 1600 °C annealing, however, the V_C depth profiles had broadened sufficiently to indicate that out-annealing of V_C to the surface had commenced at that temperature. Another interesting question that arises when discussing high-temperature annealing and migration is that of self-diffusion, when the lattice atoms themselves become mobile, and is addressed in Paper X. Importantly, at temperatures high enough to induce self-diffusion of lattice atoms, likely pathways for atomic redistribution are caused by Frenkel pair formation in the semiconductor bulk, or vacancy injection from the sample surface. Several experimental [163, 164] and theoretical [59, 165] works have

addressed self-diffusion in SiC, but both the diffusivities and mediating defect species for Si and C self-diffusion remain a subject to some controversy.

Paper X considers a 4H-SiC sample structure consisting of a 4H-SiC substrate holding a 7 μm thick isotope purified epi-layer grown by chemical vapor deposition (CVD). The samples were covered by a carbon cap (C-cap) prior to annealing at 2300-2450 $^{\circ}\text{C}$ in an RF furnace, and SIMS measurements were conducted after each annealing stage to monitor the evolution of the ^{13}C and ^{30}Si concentration versus depth profiles with temperature. Importantly, in the studied temperature range, the diffusion lengths for Si self-diffusion were found to be on the same scale as the surface roughening, indicating that Si hardly moves at ≤ 2450 $^{\circ}\text{C}$ and rendering estimates of the Si diffusivities highly uncertain. Diffusivities for C self-diffusion, on the other hand, are on the same scale as those found in previous works, however, with a higher activation energy of $E_{\text{A}} = 10.4$ eV (comparing to 8.5 eV in Ref. [163] and 7.4 eV in Ref. [164]) and pre-factor for diffusion of $D_0 = 8.3 \times 10^6$ cm^2/s than other works. Therefore, we deduce that diffusivities (D) for Si self-diffusion are at least 100-1000 times smaller than those for C in 4H-SiC.

Intriguingly, exponential pre-factors for self-diffusion in the 10^8 - 10^9 cm^2/s range are predicted to dominate in cases where vacancy formation and injection is suppressed at the surface, instead indicating that self-diffusion commences via Frenkel pair formation in the sample bulk [166]. The C-cap covering the 4H-SiC surface is responsible for continuous injection of C interstitials, and is likely effectively hindering surface vacancy formation by providing a constant supply of C_i for recombination. Hence, we conclude that when a C-cap is present during annealing, surface vacancy formation is suppressed and self-diffusion instead takes place via bulk Frenkel pair formation. In un-capped samples the most likely route for C self-diffusion is therefore via C vacancies that are injected from the sample surface. We have less grounds for concluding on behalf of Si self-diffusion, however, we find it likely that surface injection of Si vacancies prevails over Si Frenkel pair formation in the 4H-SiC bulk in the absence of a capping layer during annealing.

Chapter 7

Concluding remarks

In this work, progress has been made on several aspects related to point defects in silicon carbide. Importantly, protocols for identifying, controlling, and predicting properties of quantum emitters have been established. The silicon vacancy (V_{Si}) has constituted a main focus herein, where the first portion of the thesis concerned the identification and control of V_{Si} charge states. By combining electrical (DLTS) and optical (PL) characterization techniques with hybrid functional calculations, the $V_{\text{Si}}(-/2-)$ and $V_{\text{Si}}(2-/3-)$ charge-state transitions were assigned to the DLTS S-center, yielding control over whether or not the V_{Si} inhabits the bright and high-spin negative charge state. Moreover, sequential electric field application resulted in emission modulation behavior that was interpreted as charge-state switching of the V_{Si} . Extending the notion of control to the V_{Si} emission wavelength, it was further established that the V1 and V1' zero-phonon lines attributed to the negative V_{Si} could be reliably shifted using external electric fields via the Stark effect, local inhomogeneities via strain tuning, and, potentially, vibronic replicas of the V_{Si} emission.

Additionally, we have investigated the fundamental differences between the two vacancy types present in SiC: the single-photon emitting qubit candidate that is the Si vacancy, and the minority life-time limiting carbon vacancy (V_{C}). Where the V_{Si} exhibits little atomic displacement, C_{3v} symmetry and a high spin-state, the V_{C} is optically dark and of low spin. Moreover, the atoms surrounding the V_{C} move significantly yielding lower C_{1h} symmetry, and the large Jahn-Teller distortion for the neutral V_{C} results in negative- U ordering of the V_{C} charge states. Intriguingly, we demonstrate herein that low-energy muons are sensitive to the distinct relaxation mechanisms that are driven by the vacancies' nearest-neighbor dangling bonds, and result in either high-spin and high-symmetry behavior (V_{Si}) or large Jahn-Teller distortions and negative- U characteristics (V_{C}).

Finally, we have illuminated the mechanisms that determine the thermal stability of vacancy defects in SiC. Although the Si and C vacancies anneal out in different temperature ranges, we find two common mechanisms in n-type 4H-SiC: recombination with interstitials, and vacancy migration on the respective sublattice. The V_{Si} disappears above 400 °C in n-type 4H-SiC by recombining with interstitials, out-annealing to the surface or other sinks, or complex formation with H or V_{C} . The transformation of V_{Si} into the carbon antisite-vacancy (CAV) pair, which dominates in p-type material, is blocked in n-type 4H-SiC below 1000 °C. Instead, CAV pairs may dissociate into a V_{C} and an antisite, leading to the recovery of the $Z_{1/2}$ DLTS signal attributed to V_{C} . The V_{C} does not disappear until above 1600 °C, with migration commencing at 1200 °C and above. Migration in 4H-SiC is characterized by a distinct anisotropy,

where the V_C shows a high degree of planar selectivity and migrates more readily within the hexagonal lattice planes as compared to all other migration paths.

7.1 Suggestions for further work

Important correlations have been revealed and methodologies proposed in the present thesis, however, much remains to be discovered, and the techniques presented herein can still be improved. Some suggestions for further work are listed below.

- The technique established herein for relating charge-state transition levels of the V_{Si} and CAV complex to DLTS peaks, by correlating DLTS, PL and DFT, can be extended to other defects in SiC such as the divacancy (VV) and the nitrogen-vacancy (NV) center.
- The V_{Si} charge-state switching of Paper I was demonstrated for defect ensembles. Charge-state switching for single V_{Si} defects has been shown in Ref. [89], but not using Schottky barrier diodes, which provide faster switching frequencies compared to p-i-n diodes. An intriguing platform to embed V_{Si} defects within would be SBDs deposited on nanopillars to combine charge-state switching with a waveguiding effect.
- The framework of Paper II should be extended and improved upon, and applied to different defect species such as VV, CAV and NV in SiC, and the NV center in diamond.
- An important final objective for the future would be to combine the features of the present work: charge-state switching to obtain on-demand single-photon emission, complete with wavelength tunability to achieve indistinguishable photons and waveguiding effects to enhance emission intensities.

7.2 Outlook

While quantum technology may sound like science fiction, recent breakthroughs such as separation of entangled photons over 300 km and Google's recent claim to quantum supremacy [12] strongly imply that the future may be just around the corner. Current quantum computer architectures are based on superconducting materials, but struggle with coherence times and exceeding millikelvin temperatures. Similarly, nitrogen-vacancy (NV) centers in diamond are highly sensitive nanoscale sensors, but diamond is famously challenging to transform into, or combine with, electro-optical device technology.

Si vacancy, divacancy (VV), nitrogen-vacancy (NV) and carbon antisite-vacancy (CAV) defects in SiC, in addition to transition metal impurities, share many properties with NV centers in diamond and already surpass superconducting Josephson junctions in terms of coherence. Additionally, the

point defect platform (in both SiC and diamond) simultaneously provides single-photon emission with the potential for indistinguishability [167], a vital parameter for, e.g., entanglement and quantum cryptography. Single-photon emission has already been shown for these defect centers at room temperature, along with millisecond coherence times at 10 K. Nevertheless, an improved understanding of how the quantum emitters are affected by irradiation, temperature, external perturbation and their host environment is important for the success of such advancements. Finally, the ultimate obstacle towards realizing quantum communication and computation remains to be surmounted: electron-spin entanglement between two different defect centers.

Bibliography

- [1] Moore, G. E., *Electronics* **1965**, vol. 38.
- [2] Ladd, T. D., Jelezko, F., Laflamme, R., Nakamura, Y., Monroe, C., O'Brien, J. L., *Nature* **2010**, vol. 464, 45–52.
- [3] Doherty, M. W., Manson, N. B., Delaney, P., Jelezko, F., Wrachtrup, J., Hollenberg, L. C. L., *Physics Reports* **2013**, vol. 528, 1–45.
- [4] Muhonen, J. T., Dehollain, J. P., Laucht, A., Hudson, F. E., Kalra, R., Sekiguchi, T., Itoh, K. M., Jamieson, D. N., McCallum, J. C., Dzurak, A. S., Morello, A., *Nature Nanotechnology* **2014**, vol. 9, 986–991.
- [5] Griffiths, D. J., *Introduction to quantum mechanics*, Pearson, **2005**.
- [6] Acín, A., Bloch, I., Buhrman, H., Calarco, T., Eichler, C., Eisert, J., Esteve, D., Gisin, N., Glaser, S. J., Jelezko, F., Kuhr, S., Lewenstein, M., Riedel, M. F., Schmidt, P. O., Thew, R., Wallraff, A., Walmsley, I., Wilhelm, F. K., *New Journal of Physics* **2018**, vol. 20, 080201.
- [7] Gisin, N., Thew, R., *Nature Photonics* **2007**, vol. 1, 165–171.
- [8] Gisin, N., Ribordy, G., Tittel, W., Zbinden, H., *Reviews of Modern Physics* **2002**, vol. 74, 145–195.
- [9] Awschalom, D. D., Hanson, R., Wrachtrup, J., Zhou, B. B., *Nature Photonics* **2018**, vol. 12, 516–527.
- [10] Degen, C. L., Reinhard, F., Cappellaro, P., *Reviews of Modern Physics* **2017**, vol. 89, 035002.
- [11] Armasu, L., Samsung Plans Mass Production of 3nm GAAFET Chips in 2021, Online, **2019**.
- [12] Arute, F., Arya, K., Babbush, R., Bacon, D., Bardin, J. C., Barends, R., Biswas, R., Boixo, S., Brandao, F. G. S. L., Buell, D. A., Burkett, B., et al., *Nature* **2019**, vol. 574, 505–510.
- [13] DiVincenzo, D. P., *Fortschritte Phys.* **2000**, vol. 48, 771–783.
- [14] Raussendorf, R., Briegel, H. J., *Physical Review Letters* **2001**, vol. 86, 5188–5191.
- [15] Mizel, A., Lidar, D. A., Mitchell, M., *Physical Review Letters* **2007**, vol. 99, 070502.
- [16] Born, M., Fock, V., *Zeitschrift für Physik* **1928**, vol. 51, 165–180.
- [17] Shor, P. W. in Proceedings 35th Annual Symposium on Foundations of Computer Science, **1994**, pp. 124–134.
- [18] Grover, L. K., *Physical Review Letters* **1997**, vol. 79, 325.

- [19] Cao, Y., Romero, J., Olson, J. P., Degroote, M., Johnson, P. D., Kieferová, M., Kivlichan, I. D., Menke, T., Peropadre, B., Sawaya, N. P. D., Sim, S., Veis, L., Aspuru-Guzik, A., *Chemical Reviews* **2019**, vol. 119, 10856–10915.
- [20] Devitt, S. J., Munro, W. J., Nemoto, K., *Rep. Prog. Phys.* **2013**, vol. 76, 076001.
- [21] Weber, J. R., Koehl, W. F., Varley, J. B., Janotti, A., Buckley, B. B., Van de Walle, C. G., Awschalom, D. D., *Proceedings of the National Academy of Sciences* **2010**, vol. 107, 8513–8518.
- [22] Fossheim, K., Sudbo, A., *Superconductivity: Physics and Applications*, John Wiley & Sons, Ltd, **2004**.
- [23] Nakamura, Y., Pashkin, Y. A., Tsai, J. S., *Nature* **1999**, vol. 398, 786.
- [24] Pelant, I., Valenta, J., *Luminescence Spectroscopy of Semiconductors*, Oxford University Press, **2012**.
- [25] Huang, K., Rhys, A., *Proc. R. Soc. Lond. A* **1950**, vol. 204, 406–423.
- [26] Hanbury Brown, R., Twiss, R. Q., *Nature* **1956**, vol. 177, 27–29.
- [27] Klimov, P. V., Falk, A. L., Christle, D. J., Dobrovitski, V. V., Awschalom, D. D., *Science Advances* **2015**, vol. 1.
- [28] Lohrmann, A., Johnson, B. C., McCallum, J. C., Castelletto, S., *Rep. Prog. Phys.* **2017**, vol. 80, 034502.
- [29] Robledo, L., Childress, L., Bernien, H., Hensen, B., Alkemade, P. F. A., Hanson, R., *Nature* **2011**, vol. 477, 574–578.
- [30] Taylor, J. M., Cappellaro, P., Childress, L., Jiang, L., Budker, D., Hemmer, P. R., Yacoby, A., Walsworth, R., Lukin, M. D., *Nature Physics* **2008**, vol. 4, 810–816.
- [31] Tamarat, P., Gaebel, T., Rabeau, J. R., Khan, M., Greentree, A. D., Wilson, H., Hollenberg, L. C. L., Prawer, S., Hemmer, P., Jelezko, F., Wrachtrup, J., *Physical Review Letters* **2006**, vol. 97, 083002.
- [32] Le Sage, D., Arai, L., Glenn, D. R., DeVience, S. J., Pham, L. M., Rhan-Lee, L., Lukin, M. D., Yacoby, A., Komeili, A., Walsworth, R. L., *Nature* **2013**, vol. 496, 486–489.
- [33] Bernien, H., Hensen, B., Pfaff, W., Koolstra, G., Blok, M. S., Robledo, L., Taminiau, T. H., Markham, M., Twitchen, D. J., Childress, L., Hanson, R., *Nature* **2013**, vol. 497, 86–90.
- [34] Pfaff, W., Hensen, B. J., Bernien, H., van Dam, S. B., Blok, M. S., Taminiau, T. H., Tiggelman, M. J., Schouten, R. N., Markham, M., Twitchen, D. J., Hanson, R., *Science* **2014**, vol. 345, 532–535.
- [35] Barclay, P. E., Fu, K. C., Santori, C., Faraon, A., Beausoleil, R. G., *Physical Review X* **2011**, vol. 1, 011007.
- [36] Castelletto, S., Rosa, L., Johnson, B. C. in *Advanced Silicon Carbide Devices and Processing*, InTech, **2015**.

- [37] Iwamoto, N., Svensson, B. G. in *Defects in Semiconductors*, (Eds.: Romano, L., Privitera, V., Jagadish, C.), Semiconductors and Semimetals, Elsevier, **2015**, pp. 369–407.
- [38] Park, C. H., Cheong, B. H., Lee, K. H., Chang, K. J., *Physical Review B* **1994**, vol. 49, 4485.
- [39] *Properties of Silicon Carbide*, (Ed.: Harris, G. L.), IET, **1995**.
- [40] Kimoto, T., Cooper, J. A., *Fundamentals of Silicon Carbide Technology: Growth, Characterization, Devices and Applications*, Wiley, **2014**.
- [41] Zippelius, B., Suda, J., Kimoto, T., *Journal of Applied Physics* **2012**, vol. 111, 033515.
- [42] Son, N. T., Trinh, X. T., Løvlie, L. S., Svensson, B. G., Kawahara, K., Suda, J., Kimoto, T., Umeda, T., Isoya, J., Makino, T., Ohshima, T., Janzén, E., *Physical Review Letters* **2012**, vol. 109, 187603.
- [43] Klein, P. B., Shanabrook, B. V., Huh, S. W., Polyakov, A. Y., Skowronski, M., Sumakeris, J. J., O'Loughlin, M. J., *Applied Physics Letters* **2006**, vol. 88, 052110.
- [44] Ayedh, H. M., Hallén, A., Svensson, B. G., *Journal of Applied Physics* **2015**, vol. 118, 175701.
- [45] Ayedh, H. M., Nipoti, R., Hallén, A., Svensson, B. G., *Journal of Applied Physics* **2017**, vol. 122, 025701.
- [46] Lohrmann, A., Iwamoto, N., Bodrog, Z., Castelletto, S., Ohshima, T., Karle, T. J., Gali, A., Prawer, S., McCallum, J. C., Johnson, B. C., *Nature Communications* **2015**, vol. 6, 7783.
- [47] Sato, S. ichiro, Honda, T., Makino, T., Hijikata, Y., Lee, S.-Y., Ohshima, T., *ACS Photonics* **2018**, vol. 5, 3159–3165.
- [48] Widmann, M., Lee, S.-Y., Rendler, T., Son, N. T., Fedder, H., Paik, S., Yang, L.-P., Zhao, N., Yang, S., Booker, I., Denisenko, A., Jamali, M., Momenzadeh, S. A., Gerhardt, I., Ohshima, T., Gali, A., Janzén, E., Wrachtrup, J., *Nature Materials* **2014**, vol. 14, 164–168.
- [49] Castelletto, S., Johnson, B. C., Ivády, V., Stavrias, N., Umeda, T., Gali, A., Ohshima, T., *Nature Materials* **2014**, vol. 13, 151–156.
- [50] Christle, D. J., Falk, A. L., Andrich, P., Klimov, P. V., Ul Hassan, J., Son, N. T., Janzén, E., Ohshima, T., Awschalom, D. D., *Nature Materials* **2015**, vol. 14, 160–163.
- [51] Coutinho, J., Torres, V. J. B., Demmouche, K., Öberg, S., *Physical Review B* **2017**, vol. 96, 174105.
- [52] Ayedh, H. M., Bobal, V., Nipoti, R., Hallén, A., Svensson, B. G., *Journal of Applied Physics* **2014**, vol. 115, 012005.
- [53] Hornos, T., Gali, A., Svensson, B. G., *Materials Science Forum* **2011**, vol. 679-680, 261–264.

- [54] Lang, D. V., *Journal of Applied Physics* **1974**, vol. 45, 3023–3032.
- [55] Capan, I., Brodar, T., Pastuović, Ž., Siegele, R., Ohshima, T., Sato, S. ichiro, Makino, T., Snoj, L., Radulović, V., Coutinho, J., Torres, V. J. B., Demmouche, K., *Journal of Applied Physics* **2018**, vol. 123, 161597.
- [56] David, M. L., Alfieri, G., Monakhov, E. M., Hallén, A., Blanchard, C., Svensson, B. G., Barbot, J. F., *Journal of Applied Physics* **2004**, vol. 95, 4728–4733.
- [57] Yan, X., Li, P., Kang, L., Wei, S.-H., Huang, B., *Journal of Applied Physics* **2020**, vol. 127, 085702.
- [58] Kobayashi, T., Harada, K., Kumagai, Y., Oba, F., Matsushita, Y., *Journal of Applied Physics* **2019**, vol. 125, 125701.
- [59] Bockstedte, M., Mattausch, A., Pankratov, O., *Physical Review B* **2003**, vol. 68, 205201.
- [60] Alfieri, G., Monakhov, E. V., Svensson, B. G., Linnarsson, M. K., *Journal of Applied Physics* **2005**, vol. 98, 043518.
- [61] Alfieri, G., Monakhov, E. V., Svensson, B. G., Hallén, A., *Journal of Applied Physics* **2005**, vol. 98, 113524.
- [62] Philibert, J., *Atom movements: Diffusion and mass transport in solids*, Editions de Physique, **1991**.
- [63] Wang, X., Zhao, M., Bu, H., Zhang, H., He, X., Wang, A., *Journal of Applied Physics* **2013**, vol. 114, 194305.
- [64] Defo, R. K., Zhang, X., Bracher, D., Kim, G., Hu, E., Kaxiras, E., *Physical Review B* **2018**, vol. 98, 104103.
- [65] Achtziger, N., Grillenberger, J., Witthuhn, W., Linnarsson, M. K., Janson, M., Svensson, B. G., *Applied Physics Letters* **1998**, vol. 73, 945–947.
- [66] Linnarsson, M. J. K., Doyle, J. P., Svensson, B. G. in *III-Nitride, SiC and Diamond Materials for Electronic Devices*, (Eds.: Gaskill, D. K., Brandt, C. D., Nemanich, R. J.), Material Research Society, Pittsburgh, **1996**, p. 625.
- [67] Linnarsson, M. K., Janson, M. S., Forsberg, U., Janzén, E., *Materials Science Forum* **2006**, vol. 527–529, 637–640.
- [68] Aradi, B., Gali, A., Deák, P., Lowther, J. E., Son, N. T., Janzén, E., Choyke, W. J., *Physical Review B* **2001**, vol. 63, 245202.
- [69] Watkins, G. D. in *Advances in Solid State Physics*, Springer Berlin Heidelberg, **1984**, pp. 163–189.
- [70] Bechstedt, F., Zywietz, A., Furthmüller, J., *Europhysics Letters* **1998**, vol. 44, 309–314.
- [71] Furthmüller, J., Zywietz, A., Bechstedt, F., *Materials Science and Engineering* **1999**, vol. B61–62, 244–247.

- [72] Zywietz, A., Furthmüller, J., Bechstedt, F., *Physical Review B* **1999**, vol. 59, 15166.
- [73] Zywietz, A., Furthmüller, J., Bechstedt, F., *Physical Review B* **2000**, vol. 61, 13655.
- [74] Zywietz, A., Furthmüller, J., Bechstedt, F., *Physical Review B* **2000**, vol. 62, 6854.
- [75] Wagner, M., Magnusson, B., Chen, W. M., Janzén, E., Sörman, E., Hallin, C., Lindström, J. L., *Physical Review B* **2000**, vol. 62, 16555.
- [76] Sörman, E., Son, N. T., Chen, W. M., Kordina, O., Hallin, C., Janzén, E., *Physical Review B* **2000**, vol. 61, 2613–2620.
- [77] Janzén, E., Gali, A., Carlsson, P., Gällström, A., Magnusson, B., Son, N., *Physica B: Condensed Matter* **2009**, vol. 404, 4354–4358.
- [78] Ivády, V., Davidsson, J., Son, N. T., Ohshima, T., Abrikosov, I. A., Gali, A., *Physical Review B* **2017**, vol. 96, 161114(R).
- [79] Nagy, R., Widmann, M., Niethammer, M., Dasari, D. B. R., Gerhardt, I., Soykal, Ö. O., Radulaski, M., Oshima, T., Vucković, J., Son, N. T., Ivanov, I. G., Economou, S. E., Bonato, C., Lee, S.-Y., Wrachtrup, J., *Physical Review Applied* **2018**, vol. 9, 034022.
- [80] Kraus, H., Soltamov, V. A., Riedel, D., Văth, S., Fuchs, F., Sperlich, A., Baranov, P. G., Dyakonov, V., Astakhov, G. V., *Nature Physics* **2014**, vol. 10, 157–162.
- [81] Mizuochi, N., Yamasaki, S., Takizawa, H., Morishita, N., Ohshima, T., Itoh, H., Umeda, T., Isoya, J., *Physical Review B* **2005**, vol. 72, 235208.
- [82] Gali, A., *Materials Science Forum* **2012**, vol. 717–720, 255–258.
- [83] Soykal, Ö. O., Dev, P., Economou, S. E., *Physical Review B* **2016**, vol. 93, 081207(R).
- [84] Udvarhelyi, P., Nagy, R., Kaiser, F., Lee, S.-Y., Wrachtrup, J., Gali, A., *Physical Review Applied* **2019**, vol. 11, 044022.
- [85] Udvarhelyi, P., Thiering, G., Morioka, N., Babin, C., Kaiser, F., Lukin, D., Ohshima, T., Ul Hassan, J., Son, N. T., Vucković, J., Wrachtrup, J., Gali, A., *Physical Review Applied* **2020**, vol. 13, 054017.
- [86] Davidsson, J., Ivády, V., Armiento, R., Ohshima, T., Son, N. T., Gali, A., Abrikosov, I. A., *Applied Physics Letters* **2019**, vol. 114, 112107.
- [87] Koehl, W. F., Buckley, B. B., Heremans, F. J., Calusine, G., Awschalom, D. D., *Nature* **2011**, vol. 479, 84–88.
- [88] Bardeleben, H. J. von, Cantin, J. L., Csóré, A., Gali, A., Rauls, E., Gerstmann, U., *Physical Review B* **2016**, vol. 94, 121202(R).
- [89] Widmann, M., Niethammer, M., Fedyanin, D. Y., Khramtsov, I. A., Rendler, T., Booker, I. D., Ul Hassan, J., Morioka, N., Chen, Y.-C., Ivanov, I. G., Son, N. T., Ohshima, T., Bockstedte, M., Gali, A., Bonato, C., Lee, S.-Y., Wrachtrup, J., *Nano Letters* **2019**, vol. 19, 7173–7180.

- [90] Wolfowicz, G., Anderson, C. P., Yeats, A. L., Whiteley, S. J., Niklas, J., Poluektov, O. G., Heremans, F. J., Awschalom, D. D., *Nature Communications* **2017**, vol. 8, 1876.
- [91] Anderson, C. P., Bourassa, A., Miao, K. C., Wolfowicz, G., Mintun, P. J., Crook, A. L., Abe, H., Ul Hassan, J., Son, N. T., Oshima, T., Awschalom, D. D., *Science* **2019**, vol. 366, 1225–1230.
- [92] Son, N. T., Stenberg, P., Jokubavicius, V., Abe, H., Ohshima, T., Ul Hassan, J., Ivanov, I. G., *Applied Physics Letters* **2019**, vol. 114, 212105.
- [93] de la Casas, C. F., Christle, D. J., Ul Hassan, J., Ohshima, T., Son, N. T., Awschalom, D. D., *Applied Physics Letters* **2017**, vol. 111, 262403.
- [94] Rühl, M., Bergmann, L., Krieger, M., Weber, H. B., *Nano Letters* **2020**, vol. 20, 658–663.
- [95] Radulaski, M., Widmann, M., Niethammer, M., Zhang, J. L., Lee, S.-Y., Rendler, T., Lagoudakis, K. G., Son, N. T., Janzén, E., Oshima, T., Wrachtrup, J., Vucković, J., *Nano Letters* **2017**, vol. 17, 1782–1786.
- [96] Bracher, D. O., Zhang, X., Hu, E. L., *Proc. Natl. Acad. Sci. U.S.A.* **2017**, vol. 114, 4060.
- [97] Nagy, R., Niethammer, M., Widmann, M., Chen, Y.-C., Udvarhelyi, P., Bonato, C., Ul Hassan, J., Karhu, R., Ivanov, I. G., Son, N. T., Maze, J. R., Oshima, T., Soykal, Ö. O., Galí, A., Lee, S.-Y., Kaiser, F., Wrachtrup, J., *Nature Communications* **2019**, vol. 10, 1054.
- [98] Sholl, D. S., Steckel, J., *Density Functional Theory: A Practical Introduction*, John Wiley & Sons, Inc, **2009**.
- [99] Hohenberg, P., Kohn, W., *Physical Review* **1964**, vol. 136, B864–B871.
- [100] Kohn, W., Sham, L. J., *Physical Review* **1965**, vol. 140, A1133–A1138.
- [101] Perdew, J. P., Burke, K., Ernzerhof, M., *Physical Review Letters* **1996**, vol. 77, 3865–3868.
- [102] Freysoldt, C., Grabowski, B., Hickel, T., Neugebauer, J., *Reviews of Modern Physics* **2014**, vol. 86, 253–305.
- [103] Becke, A. D., *Journal of Chemical Physics* **1993**, vol. 98, 1372.
- [104] Perdew, J. P., Ernzerhof, M., Burke, K., *The Journal of Chemical Physics* **1996**, vol. 105, 9982.
- [105] Heyd, J., Scuseria, G. E., Ernzerhof, M., *The Journal of Chemical Physics* **2003**, vol. 118, 8207–8215.
- [106] Kresse, G., Hafner, J., *Physical Review B* **1993**, vol. 47, 558–561.
- [107] Kresse, G., Furthmüller, J., *Computational Materials Science* **1996**, vol. 6, 15–50.
- [108] Giannozzi, P., Baroni, S., Bonini, N., Calandra, M., Car, R., Cavazzoni, C., Ceresoli, D., Chiarotti, G. L., Cococcioni, M., Dabo, I., *Journal of Physics: Condensed Matter* **2009**, vol. 21, 395502.

-
- [109] Giannozzi, P., Andreussi, O., Brumme, T., Bunau, O., Buongiorno Nardelli, M., Calandra, M., Car, R., Cavazzoni, C., Ceresoli, D., Cococcioni, M., *Journal of Physics: Condensed Matter* **2017**, vol. 29, 465901.
- [110] Monkhorst, H. J., Pack, J. D., *Physical Review B* **1976**, vol. 13, 5188.
- [111] Hamann, D. R., *Physical Review B* **2013**, vol. 88, 085117.
- [112] Blöchl, P. E., *Physical Review B* **1994**, vol. 50, 17953–17979.
- [113] Kresse, G., Hafner, J., *Journal of Physics: Condensed Matter* **1994**, vol. 6, 8245.
- [114] Kresse, G., Joubert, D., *Physical Review B* **1999**, vol. 59, 1758–1775.
- [115] Freysoldt, C., Neugebauer, J., Van de Walle, C. G., *Physical Review Letters* **2009**, vol. 102, 016402.
- [116] Komsa, H.-P., Rantala, T. T., Pasquarello, A., *Physical Review B* **2012**, vol. 86, 045112.
- [117] Kumagai, Y., Oba, F., *Physical Review B* **2014**, vol. 89, 195205.
- [118] Patrick, L., Choyke, W. J., *Physical Review B* **1970**, vol. 2, 2255.
- [119] Dreyer, C. E., Alkauskas, A., Lyons, J. L., Janotti, A., Van de Walle, C. G., *Annual Review of Materials Research* **2018**, vol. 48, 1–26.
- [120] Slater, J. C., *Quantum theory of molecules and solids, Vol. 1–4*, McGraw-Hill, New York, **1963–1974**.
- [121] Gali, A., Janzén, E., Deák, P., Kresse, G., Kaxiras, E., *Physical Review Letters* **2009**, vol. 103, 186404.
- [122] Maze, J. R., Gali, A., Togan, E., Chu, Y., Trifonov, A., Kaxiras, E., Lukin, M. D., *New Journal of Physics* **2011**, vol. 13, 025025.
- [123] Alkauskas, A., McCluskey, M. D., Van de Walle, C. G., *Journal of Applied Physics* **2016**, vol. 119, 181101.
- [124] Alkauskas, A., Lyons, J. L., Steiauf, D., Van de Walle, C. G., *Physical Review Letters* **2012**, vol. 109, 267401.
- [125] Alkauskas, A., Buckley, B. B., Awschalom, D. D., Van de Walle, C. G., *New J. Phys.* **2014**, vol. 16, 073026.
- [126] Mills, G., Jónsson, H., *Physical Review Letters* **1994**, vol. 72, 1124–1127.
- [127] Mills, G., Jónsson, H., Schenter, G. K., *Surface Science* **1995**, vol. 324, 305–337.
- [128] Henkelman, G., Jónsson, H., *The Journal of Chemical Physics* **1999**, vol. 111, 7010–7022.
- [129] Henkelman, G., Jónsson, H., *The Journal of Chemical Physics* **2000**, vol. 113, 9901–9904.
- [130] Kunc, K., Resta, R., *Physical Review Letters* **1983**, vol. 51, 686–689.

- [131] Stoneham, A. M., *Theory of Defects in Solids: Electronic Structure of Defects in Insulators and Semiconductors*, Clarendon Press, **2001**.
- [132] Grivickas, P., Grivickas, V., Linnros, J., Galeckas, A., *Journal of Applied Physics* **2007**, vol. 101, 123521.
- [133] Setten, M. J. van, Giantomassi, M., Bousquet, E., Verstraete, M. J., Hamann, D. R., Gonze, X., Rignanese, G.-M., *Computer Physics Communications* **2018**, vol. 226, 39–54.
- [134] Song, J.-W., Yamashita, K., Hirao, K., *Journal of Chemical Physics* **2011**, vol. 135, 071103.
- [135] *Transmission Electron Microscopy: A Textbook for Materials Science*, (Eds.: Williams, D. B., Carter, C. B.), Springer, **2009**.
- [136] van der Heide, P., *Secondary Ion Mass Spectrometry: An Introduction to Principles and Practices*, John Wiley & Sons, Inc., **2014**.
- [137] Ziegler, J. F., Ziegler, M., Biersack, J., *Nuclear Instruments and Methods in Physics Research Section B: Beam Interactions with Materials and Atoms* **2010**, vol. 268, 1818–1823.
- [138] Schroder, D. K., *Semiconductor material and device characterization*, 3rd ed., John Wiley & Sons, Inc, **2006**.
- [139] Blood, P., Orton, J. W., *The Electrical Characterization of Semiconductors: Majority Carriers and Electron States*, Academic Press, **1992**.
- [140] Svensson, B. G., Rydén, K.-H., Lewerentz, B. M. S., *Journal of Applied Physics* **1989**, vol. 66, 1699–1704.
- [141] Dobaczewski, L., Peaker, A. R., Nielsen, K. B., *Journal of Applied Physics* **2004**, vol. 96, 4689.
- [142] Provencher, S. W., *Computer Physics Communications* **1982**, vol. 27, 213–227.
- [143] Groetsch, C. W., *The Theory of Tikhonov Regularization for Fredholm Equations of the First Kind*, Pitman Advanced Pub. Program, London, **1984**.
- [144] Wickramaratne, D., Dreyer, C. E., Monserrat, B., Shen, J.-X., Lyons, J. L., Alkauskas, A., Van de Walle, C. G., *Applied Physics Letters* **2018**, vol. 113, 192106.
- [145] Henry, C. H., Kukimoto, H., Miller, G. L., Merritt, F. R., *Physical Review B* **1973**, vol. 7, 2499.
- [146] Henry, C. H., Lang, D. V., *Physical Review B* **1977**, vol. 15, 989.
- [147] Woerle, J., Prokscha, T., Hallén, A., Grossner, U., *Physical Review B* **2019**, vol. 100, 115202.
- [148] Patterson, B. D., *Rev. Mod. Phys.* **1988**, vol. 60, 69–159.
- [149] Amato, A., Andreica, D. in, (Eds.: Bassani, F., Liedl, G. L., Wyder, P.), Elsevier, **2005**, Chapter Muon Spin Rotation, pp. 41–49.

- [150] Amato, A., Physics with Muons: From Atomic Physics to Solid State Physics, Lecture notes, University of Zürich, **2019**.
- [151] Morenzoni, E., Glückler, H., Prokscha, T., Weber, H. P., Forgan, E. M., Jackson, T. J., Luetkens, H., Niedermayer, C., Pleines, M., Birke, M., Hofer, A., Litterst, J., Riseman, T., Schatz, G., *Physica B: Condensed Matter* **2000**, vol. 289-290, 653–657.
- [152] Prokscha, T., Morenzoni, E., Deiters, K., Foroughi, F., George, D., Kobler, R., Suter, A., Vrankovic, V., *Nuclear Instruments and Methods in Physics Research Section A: Accelerators Spectrometers Detectors and Associated Equipment* **2008**, vol. 595, 317–331.
- [153] Biersack, J. P., Eckstein, W., *Applied Physics A* **1984**, vol. 34, 73–94.
- [154] Deng, S., Wang, L., Xie, H., Wang, Z., Wang, Y., Jiang, S., Guo, H., *AIP Advances* **2018**, vol. 8, 075216.
- [155] Rühl, M., Ott, C., Gätzing, S., Krieger, M., Weber, H. B., *Applied Physics Letters* **2018**, vol. 113, 122102.
- [156] Spindler, C., Babbe, F., Wolter, M. H., Ehré, F., Santhosh, K., Hilgert, P., Werner, F., Siebentritt, S., *Physical Review Materials* **2019**, vol. 3, 090302.
- [157] Steeds, J. W., *Physical Review B* **2009**, vol. 80, 245202.
- [158] Wang, J.-F., Li, Q., Yan, F.-F., Liu, H., Guo, G.-P., Zhang, W.-P., Zhou, X., Guo, L.-P., Lin, Z.-H., Cui, J.-M., Xu, X.-Y., Xu, J.-S., Li, C.-F., Guo, G.-C., *ACS Photonics* **2019**, vol. 6, 1736–1743.
- [159] Kaukonen, M., Fall, C. J., Lento, J., *Applied Physics Letters* **2003**, vol. 83, 923.
- [160] Rauls, E., Lingner, T., Hajnal, Z., Greulich-Weber, S., Frauenheim, T., Spaeth, J.-M., *Phys. Stat. Sol. B* **2000**, vol. 217, R1.
- [161] Rauls, E., Frauenheim, T., Gali, A., Deák, P., *Physical Review B* **2003**, vol. 68, 155208.
- [162] Hemmingsson, C. G., Son, N. T., Ellison, A., Zhang, J., Janzén, E., *Physical Review B* **1998**, vol. 58, R10119–R10122.
- [163] Linnarsson, M. K., Janson, M. S., Zhang, J., Janzén, E., Svensson, B. G., *Journal of Applied Physics* **2004**, vol. 95, 8469–8471.
- [164] Rüschemschmidt, K., Bracht, H., Stolwijk, N. A., Laube, M., Pensl, G., Brandes, G. R., *Journal of Applied Physics* **2004**, vol. 96, 1458–1463.
- [165] Bedoya-Martínez, O. N., Roma, G., *Physical Review B* **2010**, vol. 82, 134115.
- [166] Wager, J. F., *Journal of Applied Physics* **1991**, vol. 69, 3022.

- [167] Morioka, N., Babin, C., Nagy, R., Gediz, I., Hesselmeier, E., Liu, D., Joliffe, M., Niethammer, M., Dasari, D., Vorobyov, V., Kolesov, R., Stöhr, R., Ul Hassan, J., Son, N. T., Ohshima, T., Udvarhelyi, P., Thiering, G., Gali, A., Wrachtrup, J., Kaiser, F., *Nature Communications* **2020**, vol. 11, 2516.

Papers

Paper I

Electrical charge state identification and control for the silicon vacancy in 4H-SiC

**M. E. Bathen, A. Galeckas, J. Müting, H. M. Ayedh, U. Gross-
ner, J. Coutinho, Y. K. Frodason, L. Vines**

Published in *npj Quantum Information*, December 2019, Volume 5 (111).
DOI: 10.1038/s41534-019-0227-y.

ARTICLE OPEN

Electrical charge state identification and control for the silicon vacancy in 4H-SiC

M. E. Bathen¹*, A. Galeckas¹, J. Mütting², H. M. Ayedh¹, U. Grossner², J. Coutinho¹, Y. K. Frodason¹ and L. Vines¹

Reliable single-photon emission is crucial for realizing efficient spin-photon entanglement and scalable quantum information systems. The silicon vacancy (V_{Si}) in 4H-SiC is a promising single-photon emitter exhibiting millisecond spin coherence times, but suffers from low photon counts, and only one charge state retains the desired spin and optical properties. Here, we demonstrate that emission from V_{Si} defect ensembles can be enhanced by an order of magnitude via fabrication of Schottky barrier diodes, and sequentially modulated by almost 50% via application of external bias. Furthermore, we identify charge state transitions of V_{Si} by correlating optical and electrical measurements, and realize selective population of the bright state. Finally, we reveal a pronounced Stark shift of 55 GHz for the V_1^- emission line state of V_{Si} at larger electric fields, providing a means to modify the single-photon emission. The approach presented herein paves the way towards obtaining complete control of, and drastically enhanced emission from, V_{Si} defect ensembles in 4H-SiC highly suitable for quantum applications.

npj Quantum Information (2019)5:111; <https://doi.org/10.1038/s41534-019-0227-y>

INTRODUCTION

Solid-state single-photon emitters (SPEs) and optically addressable spin centers are an emerging technology ideally suited for quantum computing, sensing, and information processing applications.^{1,2} Efficient room-temperature single-photon sources naturally fulfill key requirements for enabling secure communication via quantum key distribution,^{3,4} and offer a platform for optical quantum computing⁵ and communication.⁶ Moreover, single-photon emission from a bound and individually addressable paramagnetic state enables optical manipulation of the spin state and entanglement between quantum systems,⁷ culminating in the feasibility of quantum networks.⁸

The nitrogen-vacancy center in diamond¹ has become a benchmark for implementing semiconductor point defects in quantum technologies, but is suffering from the immaturity of the material and device fabrication. More recently, point defects in silicon carbide (4H-SiC) have gained attention as a more device-friendly alternative, offering a platform to merge existing semiconductor processing capabilities with the quantum technology of the future.^{9,10} Recent testaments to the viability of 4H-SiC as a quantum host include single-photon emission from, and coherent control of, the silicon vacancy (V_{Si}),^{11–13} carbon antisite-vacancy pair ($\text{C}_{\text{Si}}V_{\text{C}}$),¹⁴ transition metal¹⁵ and silicon-carbon divacancy ($V_{\text{Si}}V_{\text{C}}$)¹⁶ spins at room temperature, as well as observations of millisecond spin coherence times for V_{Si} ¹⁷ and $V_{\text{Si}}V_{\text{C}}$ ¹⁸ at cryogenic temperatures.

Hitherto, the desired quantum properties of defects in 4H-SiC have been established for specific charge states only, with the remainder being dark and exhibiting no identified spin signals. In the case of V_{Si} , the negative charge state (V_{Si}^-) exhibits both a high-spin ground state of $S = 3/2$ and two single-photon radiative channels, as observed by photoluminescence (PL), and labeled V_1 and V_2 .¹⁹ Recently, robustness towards detrimental effects such as electron-phonon interactions and fast spin dephasing was established for V_{Si}^- ²⁰ and a large fraction (40%) of optical emission was found in the zero-phonon line (ZPL),²¹ cementing the position

of V_{Si}^- as a promising qubit candidate. However, the overall low photon count rates plague emission from V_{Si} in SiC, and optical signals from isolated defects are challenging to detect without resorting to nanofabricated waveguides,^{11,22,23} or implementation into photonic crystal cavities.²⁴

Charge state conversion between the different V_{Si} and $V_{\text{Si}}V_{\text{C}}$ states in 4H-SiC^{9,25} has been demonstrated by applying electric fields^{26–28} or via laser excitation.^{29–31} Unfortunately, the dark charge states under scrutiny remain largely unknown, and selective charge state population of V_{Si}^- accompanied by reliable switching between known bright and dark states has not been achieved so far.

In the present work, we enhance the V_1 emission from ensembles of negatively charged silicon vacancies via the built-in field generated by Schottky barrier diodes (SBDs), and manipulate the bright state by an external bias. Our findings are discussed in terms of band bending at the SBD/semiconductor interface and the resulting selective charge state population of V_{Si}^- . The charge state transitions $V_{\text{Si}}(-/2-)$ and $V_{\text{Si}}(2-/3-)$ are then identified by combining deep level transient spectroscopy (DLTS), PL spectroscopy, and hybrid density functional theory calculations. The correlation between optical and electrical characterization is rarely seen for qubit candidates, and to the best of our knowledge unique in silicon carbide. Finally, we reveal a Stark shift for V_{Si}^- -related emission with a quadratic field dependency, illuminating the nature of the V_{Si}^- ground and excited states and providing a means of tuning the emission energy. Our findings prove that selective and controlled charge state population and switching is possible for a solid-state quantum bit, and we therefore propose the SBD platform to control the charge state, spin state and luminescence from isolated qubits (or ensembles thereof) in 4H-SiC.

RESULTS

The silicon monovacancy (V_{Si}) remains one of the most extensively studied quantum emitters in 4H-SiC. Two ZPLs observed in the near-infrared region of PL spectra from n-type 4H-SiC exhibit

¹Department of Physics/Centre for Materials Science and Nanotechnology, University of Oslo, N-0316 Oslo, Norway. ²Advanced Power Semiconductor Laboratory, ETH Zürich, Physikstrasse 3, 8092 Zürich, Switzerland. ³Department of Physics and I3N, University of Aveiro, Campus Santiago, 3810-193 Aveiro, Portugal. *email: m.e.bathen@fys.uio.no

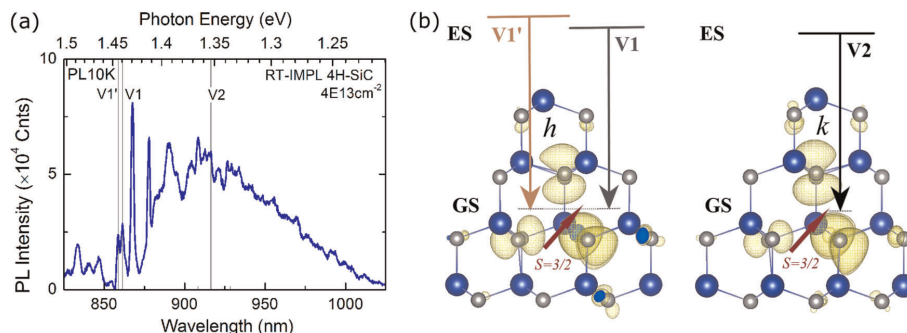


Fig. 1 Internal transitions of V_{Si} in 4H-SiC. **a** Representative PL spectrum highlighting the V1 and V2 silicon vacancy-related emission lines. **b** Ground state (GS) atomic and electronic structures of the negatively charged V_{Si} in both the h and k configurations, with the available internal transitions V1, V1', and V2 highlighted, and showing the partial charge densities of a_1 states.

single-photon emission characteristics and have been attributed to internal transitions of the negatively charged $V_{Si}^{11,19}$, namely V1 at 1.44 eV and V2 at 1.35 eV.³² An exemplar PL spectrum of proton-irradiated n-type 4H-SiC, with the V1 and V2 lines highlighted, is shown in Fig. 1a (see Supplementary Notes 1 for further details). Recently, the V1 and V2 emission lines were attributed to the inequivalent hexagonal (h) and pseudo-cubic (k) V_{Si}^- defect configurations, respectively,^{20,33} in contrast to what was previously suggested.³² Figure 1b illustrates the ground state defect configuration, partial charge density and spin state for $V_{Si}^-(h)$ and $V_{Si}^-(k)$, respectively. In addition, V_{Si}^- manifests single-photon emission, from one excited state accessible for $V_{Si}^-(k)$ (the V2 transition) and two for $V_{Si}^-(h)$ (the V1 and V1' transitions). The presence of V1', a ZPL closely related to V1, but assigned to a second excited state of V_{Si}^- that is slightly higher in energy,^{19,21,24,33} marks the V1/V1' defect center as dichroic. Here, we will focus on the V1/V1' defect, firstly to avoid interference from the broad luminescence band overlapping with V2, and secondly because of the large Debye–Waller factor of the V1 line ($>40\%^{21}$). With a large portion of photons channeled into the V1 ZPL, we are more likely to observe any electrically induced modulation of the V1/V1' emission intensity.

Effect of built-in field on silicon vacancy-related emission

The influence of the SBD-induced built-in field on the V1 emission originating from V_{Si}^- is investigated using an experimental setup as illustrated in Fig. 2a. We study n-type 4H-SiC samples having 10 μm epitaxial layers topped by circular nickel SBDs of 1 mm diameter. The defects are optically addressed at temperatures ranging from 10 to 100 K, and defect-related PL is analyzed using backside imaging geometry, where both laser excitation and PL acquisition are from the substrate side (see Fig. 2a). The dopant concentration in the epitaxial layer was $1 \times 10^{15} \text{ cm}^{-3}$, as determined by capacitance–voltage measurements, with substrate doping being estimated at several orders of magnitude higher (see Supplementary Notes 2 for further information about the samples and SBDs). The silicon vacancies were formed using 1.8 MeV proton irradiation to varying fluences, having a projected range located $\sim 27 \mu\text{m}$ into the sample, which was calculated using collision Monte Carlo models as implemented in the SRIM code³⁴ (see Supplementary Methods 1). At room temperature, the space charge region (SCR, see Fig. 2a) spans approximately 1.5 μm and 4 μm into the sample for zero (0 V) and reverse bias (-10 V), respectively. Consequently, the V_{Si} concentration is assumed constant throughout the probed region, as illustrated by the V_{Si} concentration versus depth profile in Fig. 2c.

The effect of the built-in field induced by the SBD on the V1/V1' emission intensity is displayed in Fig. 2b, where PL spectra obtained at 10 K from the SCR within the SBD and from the nearby area outside the SBD perimeter are put alongside for comparison. One can observe significant, more than by an order of magnitude, enhancement of V1-related emission once collected from the SCR of the SBD (further examples are shown in Supplementary Notes 3). Importantly, this drastic increase is larger than could be expected from purely geometrical considerations that include reflection/scattering from the semiconductor–metal interface along with possible contributions from double-pass excitation and retroreflection. In our opinion, such a significant enhancement can only be adequately explained by assuming that the band-bending induced by the Schottky barrier is affecting the charge state of the silicon vacancies being illuminated, with a larger portion of V_{Si} in the negative charge state inside compared to outside of the space charge region. It is worth noting at this point that the V1-related emission peak is clearly visible up to 150 K, although a significant line broadening occurs at higher temperatures (see Supplementary Notes 1). Moreover, the identity of the two peaks around 867 nm in Fig. 2b are at the present time unknown.

Intriguingly, which excited state V_{Si}^- prefers upon illumination seems to depend on the presence of the SBD. When no SBD is present, both the V1 and V1' lines (with typically reported values of 861.3 nm and 858.7 nm, respectively) are observed, with the V1: V1' ratio depending on factors such as the V_{Si} concentration, the incident laser intensity and polarization, and the temperature. The built-in field of the SBD, however, seems to promote excitation to the higher-lying V1' excited state as shown in Fig. 2b; the lower energy V1 emission line was not detected for any of the tested SBDs. Thus, the promotion of V_{Si}^- to the V1' excited state (see Fig. 1b) appears to be connected to the SBD-induced field. Fortunately, as optical spin manipulation can be improved by selectively exciting the V1' state due to the reduced intersystem crossing rates,²⁰ the straightforward process of depositing a nickel SBD on the sample surface promises both enhanced optical emission and now also augmented control over spin dynamics. Therefore, for the remainder of this manuscript, we have opted to refer to the collected V_{Si}^- emission as V1'.

Intensity modulation

To verify the influence of the SBD-induced built-in field on V1' emission, and to provide a means of tuning the bright state of V_{Si} , we apply external (i) forward and (ii) reverse bias to the SBD and study the resulting V1' PL intensity. Figure 2d showcases representative PL spectra of the proton-irradiated samples with

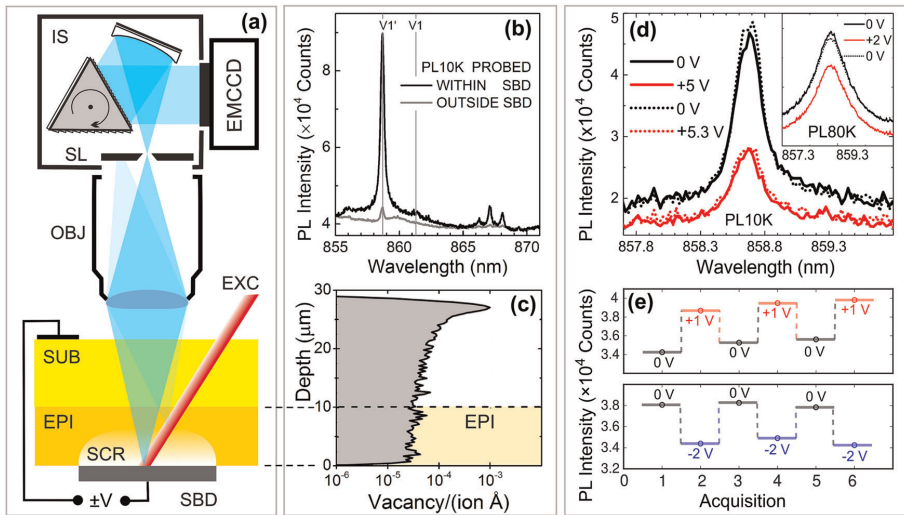


Fig. 2 Experimental considerations and electrical field effects on V1 emission. **a** Micro-imaging PL spectroscopy setup in back-illumination/detection geometry: laser excitation (EXC) beam passing through substrate (SUB) and epilayer (EPI) is reflected at Schottky contact outwards; the confocal approach, ensured by microscope objective (OBJ) and narrow slit (SL) of imaging spectrometer (IS), maximizes pickup of PL signal from the focal plane in the space charge region (SCR) of Schottky barrier diode (SBD). **b** PL spectra obtained at 10 K from SCR or depletion region within SBD, and from nearby area outside SBD perimeter, demonstrating a significant enhancement of V1-related emission by the built-in field of unbiased SBD. **c** Representative depth profile of the 1.8 MeV proton irradiation-induced V_{Si} concentration in the 4H-SiC epilayer/substrate structure. Note that V_{Si} concentration is nearly constant throughout the depletion region and entire epilayer. **d** Electrical modulation of V1' emission for a proton fluence of $2 \times 10^{12} \text{ cm}^{-2}$: by applying an external forward bias the V1' emission is seen to diminish by over 40% at 10 K for $\sim 100 \text{ W cm}^{-2}$ excitation intensity (laser power 25 mW). At 80 K and $\sim 1 \text{ kW cm}^{-2}$ excitation (laser power 250 mW), the modulation is $\sim 25\%$, as shown in the Inset. The reproducibility is verified by consecutive PL acquisitions as specified in the legend, with solid/dotted lines representing the initial and repeated measurements, respectively. **e** Selective switching of V_{Si} luminescence intensity is demonstrated for forward and reverse biased SBD for a proton fluence of $1 \times 10^{12} \text{ cm}^{-2}$. For each acquisition cycle, the intensity level on the plot represents an averaged value over 201 measurements, resulting in minimal standard deviation (within the marker size).

SBD (here for a fluence of $2 \times 10^{12} \text{ cm}^{-3}$) during sequential zero (black) and forward (red) bias conditions. Solid lines denote first acquisition of a given voltage, and dashed lines the second acquisition (acquisitions with time occurred in the order of the legend). Indeed, an intensity modulation is observed when modifying the electric field via biasing of SBD, confirming the influence of the band bending and charge state manipulation of the bright V_{Si} state: emission from the V1' defect can be selectively switched off (lower intensity) and on (higher intensity) by manipulating the electric field at the interface of the Schottky contact and 4H-SiC. While some variation between diodes and applied voltages exists (see also Supplementary Notes 3), unambiguous evidence of V1' emission intensity manipulation via the applied voltage is found. The general trend is clear; for a larger ($> 1.5 \text{ V}$) forward or reverse bias, the intensity of V1' is reduced compared to that without applied bias. For low forward bias conditions up to $\sim 1 \text{ V}$, however, the V1' intensity can be manipulated to increase compared to the 0 V conditions (we will return to this in a moment). The reproducible electrical modulation of the V1' intensity is further confirmed in Fig. 2e, showing a series of cyclic acquisitions for two relevant biasing conditions, forward (top panel) and reverse (bottom panel), obtained for a different proton fluence than that of Fig. 2d. Here, it should be noted that only low to moderate electric fields are required. Once the applied bias exceeds approximately $\pm 5 \text{ V}$, the electrically induced modulation of the V1' emission intensity, demonstrated in Fig. 2d, ceases to be predictable and reproducible, with intensities changing in a more random manner. While the exact reasons for this remain unclear, among the most likely are

charging effects of defects localized at the interface with the Schottky contact. It is also important to point out that both the enhancement and modulation are observed also at higher temperatures, e.g. 80 and 100 K, although the line width of the V1' peak increases.

Finally, Fig. 2d, e also demonstrate the defect concentration dependency of our SBD-centered technique. The sample used to create Fig. 2d was irradiated to a proton fluence twice that of the sample shown in Fig. 2e, which is visualized in the enhanced modulation depth of over 45% in 2d as compared to a 15% modulation in Fig. 2e.

Identifying charge state transitions of the silicon vacancy

To explain the switching demonstrated above, the accessible V_{Si} charge states must be established, including the energy level transitions. Figure 3 displays the formation energy diagram for V_{Si} as calculated using hybrid density functional theory, where the red and blue lines represent hexagonal and pseudo-cubic V_{Si} configurations, respectively. Evidently, V_{Si} is electrically active, with thermodynamic (0/-) transition levels located close to mid-gap for both V_{Si} configurations, ($-2/-$) at $E_c - 0.6 \text{ eV}$ for both V_{Si}(k) and V_{Si}(h), and ($2-/3-$) at $E_c - 0.4 \text{ eV}$ for V_{Si}(k) and $E_c - 0.3 \text{ eV}$ for V_{Si}(h). Note the predicted stability of the triply negative charge state for both the h and k configurations, V_{Si}³⁻, the presence of which has previously been subject to some controversy.^{9,25} The calculations presented in Fig. 3 indicate that $q = 0, 2-$ and $3-$ are likely candidates for the so-called dark states accessed during the electrical modulation of V_{Si} emission demonstrated above (Fig. 2),

and provide upper and lower bounds for the stability region of the negative silicon vacancy.

Deep level transient spectroscopy (DLTS) is a capacitance spectroscopy technique enabling both direct observation of defect charge state transitions as well as extraction of their energetic positions within the band gap. Unfortunately, the quantum-compatible defects in 4H-SiC (V_{Si} , $V_{Si}V_C$, $C_{Si}V_C$) lack reliable identification of their thermodynamic charge transition levels, rendering the dark states generated during both electrical and optical charge state control experiments uncertain. DLTS spectra of irradiated n-type 4H-SiC samples are presented in Fig. 4a and show two main carrier traps in the vicinity of the conduction band edge: the $Z_{1/2}$ double acceptor level arising from the $(0/2-)$ charge state transition of the carbon vacancy (V_C),³⁵ and the S-center consisting of two contributions (S1 and S2) located at 0.4 and 0.7 eV below the conduction band minimum (CBM), respectively. S1 and S2 arise from different charge state transitions of the same defect, and have been tentatively attributed to V_{Si} following theoretical calculations.²⁵ DLTS measurements occur under conditions where the defect can relax fully to its equilibrium configuration after the charge state transition. For this reason, the activation energy for carrier emission from a defect extracted from DLTS should be compared with thermodynamic charge state transition levels,³⁶ i.e., those

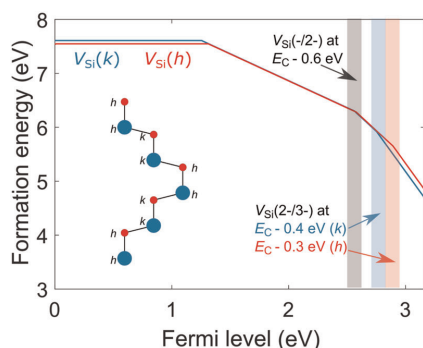


Fig. 3 Charge states of the silicon vacancy. Formation energy diagram for the h and k V_{Si} as a function of the Fermi-level position relative to the VBM under Si rich conditions, with the thermodynamic $(-/2-)$ and $2-/3-)$ charge state transitions highlighted. The inset shows the 4H-SiC crystal structure with alternating h and k lattice sites (C atoms are red, and Si blue).

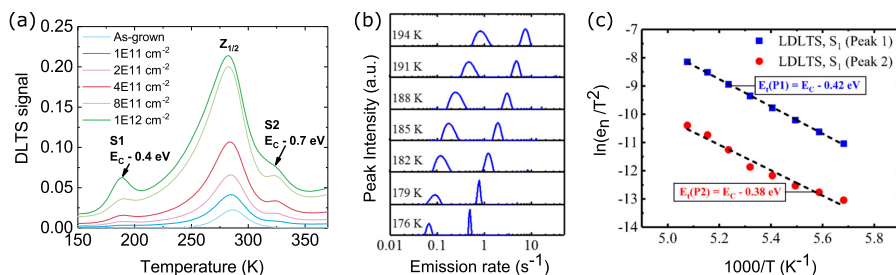


Fig. 4 Experimental characterization of V_{Si} charge state transitions. **a** DLTS spectra of proton-irradiated n-type 4H-SiC samples, evidencing an increase in S1, $Z_{1/2}$ and S2 intensities with proton fluence. **b** Temperature-dependent Laplace-DLTS measurements of the S1 peak, demonstrating that S1 contains contributions from two defect centers, likely $V_{Si}(h)$ and $V_{Si}(k)$. **c** Arrhenius behavior of the two contributions to S1 revealed by the Laplace-DLTS measurements. The confidence intervals for the activation energies are approximately ± 0.01 eV for $E_C(P1)$, and ± 0.02 eV for $E_C(P2)$.

indicated in Fig. 3. However, the activation energies obtained by DLTS may also include a capture barrier, which can be sizable in some cases. An upper estimate for this barrier can be obtained by constructing a one-dimensional configuration coordinate diagram for the transition, as explained in refs. ^{37,38}, i.e., the activation energies for V_{Si} observed by DLTS are predicted to occur within the highlighted ranges in Fig. 3. Here, we observe excellent overlap between the DLTS-deduced activation energies for the S-center (Fig. 4a) and the $V_{Si}(-/2-)$ and $V_{Si}(2-/3-)$ charge state transitions obtained from Fig. 3, and attempt to prove that the S-center indeed arises from V_{Si} .

Interestingly, the S1 DLTS peak accommodates contributions from two distinct defect centers,³⁹ as revealed by the Laplace-DLTS spectra (see Supplementary Methods 2 for details) in Fig. 4b. Recently, $Z_{1/2}$ was also found to contain two distinct signals, which were assigned to the h and k configurations of the carbon vacancy.⁴⁰ Similarly, we infer from Fig. 3 that the h and k $V_{Si}(2-/3-)$ charge state transitions likely have an energy level position difference of up to 0.1 eV. The temperature-dependent Laplace-DLTS signal in Fig. 4b of the S1 peak, and the Arrhenius plot in Fig. 4c, evidence that the two individual S1 contributors are separated in energy by 0.04 eV. Accordingly, we assign the two defect centers encompassed by S1 to $V_{Si}(h)$ and $V_{Si}(k)$, and make a tentative assignment of S1(peak 1) and S1(peak 2) to the $(2-/3-)$ transitions of $V_{Si}(k)$ and $V_{Si}(h)$, respectively. In contrast to what is often found for $Z_{1/2}$,⁴⁰ the two contributions to the S1 defect center have approximately equal integrated intensities. This is as expected for proton-irradiated material, with the h and k V_{Si} configurations formed by displacement caused by the nuclear energy deposition.

Comparing the expected behavior of V_{Si} and S-center, we find a striking similarity (see also Supplementary Discussion 1); the S-center only appears in irradiated n-type material, and anneals out between 400 and 600 °C.^{41,42} Coincidentally, the V_{Si} is a metastable defect in 4H-SiC, transforming into $C_{Si}V_C$ within the same temperature range in n-type material.¹⁴ The calculated barrier for V_{Si} transforming into $C_{Si}V_C$ is 1.8 eV,⁴³ which is identical to the experimentally deduced barrier for S-center annealing.⁴⁴ At these temperatures, self-interstitials should already have annealed out,⁴⁵ while the carbon vacancy remains present and becomes mobile at significantly higher temperatures,⁴⁶ eliminating these defects as contenders for the S-center source. Furthermore, the absence of the Poole-Frenkel effect for S1 indicates an acceptor-like behavior, and the difference of more than an order of magnitude between the capture cross-sections for S1 and S2 is well explained by the large electron repulsion associated with V_{Si}^{2-} capturing an additional electron.⁴⁴ In conclusion, the excellent agreement between calculated and experimental V_{Si} and S-center properties provide compelling evidence for the assignment of the

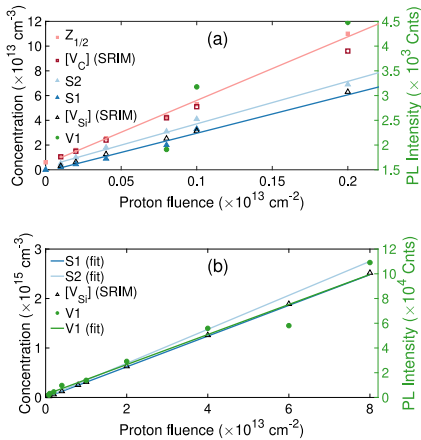


Fig. 5 Correlating the S and V1 defect centers. $Z_{1/2}$ (red) and S1/S2 concentrations (blue) and V1/V1' emission intensity (green) as a function of proton fluence, with (a) zooming in on the S1, $Z_{1/2}$ and S2 concentrations and (b) displaying the complete proton fluence range.

$V_{Si}(-2/-)$ and $V_{Si}(2-/3-)$ charge state transitions to generate the S2 and S1 signals, respectively, and indicate these transitions as accomplices in reducing the single-photon count from V_{Si} .

Proton fluence dependence of the S-center

To unambiguously attribute the DLTS S-center to V_{Si} , and thereby provide experimental verification of the upper boundary for the Fermi level where V_{Si}^- and hence single-photon emission prevails, we relate the DLTS S-center to PL emission from the V1 center. Figure 5a demonstrates a linear dependence of S-center concentration⁴¹ in blue (and V_C in pink) on proton irradiation fluence, as expected for primary point defects. Note that the proton fluence range reflects the detection limits of the DLTS technique, where the defect concentration cannot exceed 20% of net carriers. All defect concentrations were estimated assuming uniform defect concentration profiles within the depletion region as justified by Fig. 2c, and simulated due to overlapping peaks in the 4H-SiC DLTS spectrum (see Supplementary Discussion 2 for details). The slight difference between S1 and S2 concentrations is attributed to the overlap between the S2 and $Z_{1/2}$ peaks (see Fig. 4a). Figure 5a also compares experimentally deduced S-center concentrations to those estimated using SRIM simulations (using displacement energies of 20 eV and 30 eV for C and Si, respectively), with simulated concentrations depicted as red open squares for V_C and black open triangles for V_{Si} . An excellent agreement is found between the experimentally deduced S-center concentration and that estimated for V_{Si} using the SRIM code, using the well known and ever-present V_C as a benchmark.

Correlating the S and V1 centers

Figure 5b correlates the proton fluence dependence of the S-center concentration (fit to experimental data in blue extended from Fig. 5a) and V1/V1' emission intensity (green). The V1/V1' intensities were determined after baseline subtraction, and the deviation from a linear fit for the largest fluences is partly attributed to the strong compensation resulting in a substantial shift in the Fermi level. The match in slope between the S1/S2 and V1/V1' linear fits is excellent, and provides strong support for the optical V1/V1' signals and the electrical S1/S2 signals having the same origin: the silicon vacancy.

To summarize, we combine DFT calculations with DLTS and PL measurements to assign the S1 and S2 DLTS peaks to the $(-2/-)$ and $(2-/3-)$ charge state transitions of the silicon vacancy in 4H-SiC, respectively. Hopefully, the newfound electrical degree of freedom provided by the DLTS technique will yield enhanced control over both V_{Si} formation and placement, and the relation between bright and dark charge states. Indeed, we have identified two new accessible charge states for V_{Si} in 4H-SiC: the doubly and triply negative, and thus experimentally provided an upper bound for the bright V_{Si}^- .

Field effect on band bending

The strong enhancement of the V1' signal under the SBD indicates that emission arises from the depletion region of the junction, and is related to the electric field or the current provided by the junction. However, no electroluminescence has so far been observed, and the strong enhancement also occurs without applied bias. Thus, one can rule out enhancement of the emission by impact excitation⁴⁷ as the only cause for the increased V1' emission, i.e. that charge carriers are accelerated in the electric field and cause excitation resulting in V1' emission when interacting with V_{Si} . Hence, the manipulation of the charge states by the depletion region appears as an important factor for the enhanced emission of V1.

Combining the optical and electrical observations above, we can consider the field-induced switching of V_{Si} luminescence shown in Fig. 2 with respect to the charge state transitions: $V_{Si}(-2/-)$ at $E_C - 0.7$ eV, and $V_{Si}(2-/3-)$ at $E_C - 0.4$ eV. First, consider the band diagram at temperatures above the freeze-out of the main dopant, so that thermally excited charge carriers are still available, i.e., above ~ 50 K in nitrogen doped 4H-SiC. As illustrated in Fig. 6a for a temperature of 100 K, the Fermi level in n-type 4H-SiC, having carrier concentrations in the $\sim 10^{15} \text{ cm}^{-3}$ range or above, is situated $\lesssim 0.1$ eV below the conduction band edge, or lower. Therefore, at 80 K or above, V_{Si} predominantly inhabits the triply negative charge state, with the doubly and singly negative charge states mainly being available through illumination.

Applying a SBD causes band bending in the near surface region, as illustrated in the technology computer-aided design (TCAD) simulation shown in Fig. 6b (further details on the temperature- and voltage dependence can be found in Supplementary Methods 3). The blue colored region in Fig. 6b indicates where V_{Si}^- is predominantly populated. Importantly, at room temperature and zero bias, the depletion region provides conditions where V_{Si}^- is the prevailing charge state, and likely explains the enhancement of the V1' emission demonstrated in Fig. 2b.

Although not directly transferable to the non-equilibrium situation of carrier injection established by external bias and illumination, the conceptual band model presented in Fig. 6 hints at which charge state transitions are occurring during the electrically induced V1' modulation of Figs. 2d, e. Under forward biasing, we approach flat-band conditions. The resulting lowering of the V1' intensity demonstrated in Fig. 2d likely results from transitions between the singly negative and the 2- and 3- charge states of V_{Si} , occurring from the deep end of the depletion region. Furthermore, we speculate that the enhancement of V1' PL intensity shown in Fig. 2e may be explained by a transition from neutral to negative V_{Si} in the near surface region when increasing the voltage slightly. The $V_{Si}(0/-)$ transition is expected at 1.3–1.5 eV above the valence band edge (Fig. 3), but this has not been experimentally verified.

Stark shift of the V1' line

The SBDs also provide opportunities to study the V_{Si} emission under larger electric fields. Although the intensity modulation of the V1' PL peak is no longer accurately predicted for applied

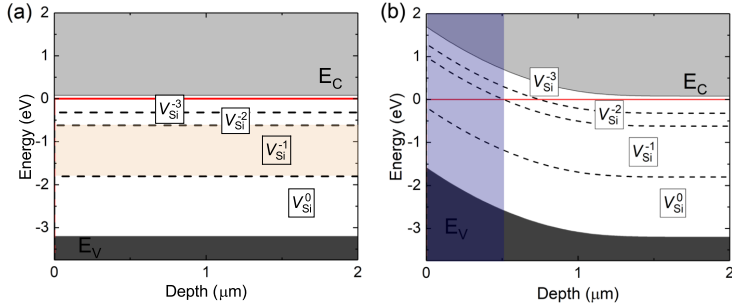


Fig. 6 Field influence on band diagram. The left panel is a conceptual band diagram in the absence of SBD at 100 K, and the right panel diagram was simulated using the Sentaurus Device simulator with deposited SBD, without applied bias and at 100 K.

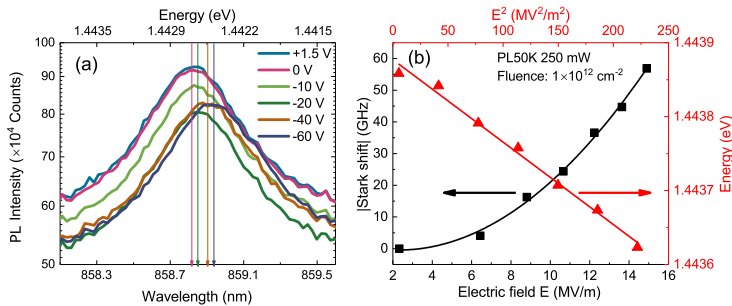


Fig. 7 Electrically induced shift of the V1' line. **a** The Stark effect is clearly observed for the V1' emission line in proton-irradiated 4H-SiC, here demonstrated for a fluence of $1 \times 10^{12} \text{ cm}^{-2}$ at 50 K and a laser intensity of 250 mW, where the vertical lines indicate the peak position. **b** The V1' Stark shift versus electric field (left and bottom axis) and the V1' peak energy vs. square of the electric field (right and upper axis) demonstrate a quadratic Stark effect for the V_{Si} energy levels. The error bars for the peak positions are within the marker size, and the applied bias voltages range up to -60 V .

voltages $\geq \pm 5 \text{ V}$ in our samples, we observe a significant shift in the energy positioning of the V1' ZPL for reverse biasing $>10 \text{ V}$. Figure 7a demonstrates the effect of large electric fields on V1' emission for a sample irradiated to a proton fluence of $1 \times 10^{12} \text{ cm}^{-2}$. Interestingly, the full width half maximum (FWHM) of the V1' peak is consistent as the field increases, although shifted. Thus, one can conclude that a majority of the emitting V_{Si} centers is affected by the electric field, confirming that V1' emission mainly arises from defects within the depletion region of the SBD. Electrically induced shifting or splitting of spectral lines is a phenomenon commonly known as the Stark effect,⁴⁸ and would explain the observed continuous red-shift of the V1' line with increasingly negative applied bias. Forward biasing the sample did not affect the V1' peak position. The extent of the red-shift exhibits a clear dose dependence, and was also influenced by both the carrier concentration and the depth of the depletion region. Indeed, a stronger Stark effect can be attributed to the individual V_{Si} defects experiencing stronger local field (see Supplementary Notes 2 for a discussion on how the electric field strength was estimated from the reverse bias and the SBD characteristics).

The shift in V1' peak position exhibits both quadratic and linear dependences on the applied electric field, as shown in Fig. 7b, regardless of V_{Si} concentration and carrier concentration. Defects in 4H-SiC, V_{Si} included, are non-centrosymmetric, and for such defects both linear and quadratic Stark effects take place.⁴⁹ The V_{Si} has C_{3v} ground state symmetry, and the V1' transition is between the ^4E excited and $^4\text{A}_2$ ground states.¹⁹ This transition is analogous to that of the negatively charged NV center in diamond, for which the quadratic Stark effect was previously

demonstrated.⁵⁰ At the moment, the reason for the quadratic Stark shift of the V1' ZPL remains an open question.

Stark tuning has previously been demonstrated for the divacancy in 4H-SiC,^{26,28} but not for the the silicon vacancy. Consequently, we herein provide a means of tuning the V_{Si} -related emission energy, while simultaneously establishing that the V1' excited state of $V_{\text{Si}}(h)$ seems to be more robust towards stray electric fields than, e.g., the hh configuration of the divacancy.²⁸

DISCUSSION

In summary, we characterize the electric field response of optical emission from V_{Si} ensembles, and find that both a substantial intensity increase as well as controlled modulation of V1' emission are obtainable using highly accessible techniques and voltages. By correlating the PL and DLTS responses of V_{Si} and identifying the DLTS S-center, we identify thermodynamic transition levels of a solid-state qubit candidate, and provide an additional means of detecting and controlling the V_{Si} in 4H-SiC. Having established upper and lower bounds for the Fermi levels ensuring optimal V_{Si} charge state populations, our work promises greater ease of ensuring that all silicon vacancies inhabit the bright state. The results presented herein for charge state modulation of V_{Si} in n-type 4H-SiC apply to a defect ensemble, and we are therefore unable to completely switch the V_{Si} luminescence ON and OFF by manipulating the defect charge state. However, in the event of a single V_{Si} defect being situated at a suitable distance from a Schottky contact, applying external bias is a promising approach

to selectively alter the V_{Si} charge state and effectively switching the quantum-compatible state ON and OFF. In that event, the challenge becomes placing a V_{Si} within a highly localized and easily identifiable depletion region, which can be solved by, e.g., depositing a SBD on top of a nanopillar containing only one or two silicon vacancies.²²

Recently, electric field-dependent manipulation of single silicon vacancies was demonstrated using the intrinsic region of 4H-SiC p-i-n diodes.⁵¹ In the intrinsic region, the Fermi level is close to the middle of the band gap, and switching may occur between the neutral and single negative charge state. In n-type material, on the other hand, the Fermi level is close to the conduction band with V_{Si} predominantly in the 2− or 3− charge states. Hence, the charge states affected by the depletion region will be closer to the metal–semiconductor interface compared to that of the p-i-n diode.

Finally, we reinforce the robustness of the V1 defect center ZPL with respect to stray electric fields by demonstrating a Stark shift that is much smaller than the splitting between the V1 and V1' excited states. Although electric fields above 2×10^4 V/cm are needed to shift the V1' peak position, voltages below ± 5 V can subdue or enhance the intensity by over 40%. Combined with the strong sensitivity of the V_{Si} electron spin to magnetic fields,⁵² we cement the position of V_{Si} in 4H-SiC as a promising quantum sensor with nanoscale resolution, employing V1' intensity for low-field and V1' peak position for high-field applications. Combined with nanofabrication, the SBD approach presents a powerful tool and paves the way towards obtaining complete control of, and drastically enhanced emission from, V_{Si} defect ensembles in 4H-SiC highly suitable for quantum applications.

METHODS

Computational details

First-principles calculations were performed within density functional theory, as implemented in the Vienna ab-initio simulation package (VASP),^{53–56} using the HSE06 hybrid functional⁵⁷ to accurately describe the electronic structure and the Projector-Augmented Wave (PAW) method to consider valence electrons only.⁵⁸ The calculated 4H-SiC 0 K band-gap of 3.17 eV is close to the experimental value of 3.27 eV,⁵⁹ lending support to the calculated charge state transitions. The V_{Si} was created by removing a Si(h) or Si(k) atom from a 96-atom cubic 4H-SiC supercell. The electronic self-consistent energy was minimized to a numerical accuracy of 10^{-6} eV, while atomic coordinates were optimized until forces were below 0.02 eV/Å. A $2 \times 2 \times 2$ Monkhorst-Pack type **k**-mesh and a 420 eV plane-wave energy cut-off were deemed sufficient for capturing defect energetics accurately. Defect formation energies and thermodynamic charge state transition levels were calculated by using the established formalism described in ref. ³⁶ For charged defects, the extended⁶⁰ Freysoldt, Neugebauer, and Van de Walle correction scheme^{60–62} was employed.

Sample preparation

The V_{Si} was studied experimentally using (0001) 4H-SiC samples purchased from Cree, Inc. holding 10 μm thick epitaxial layers with net doping concentrations of $N_D \sim 1 \times 10^{15} \text{ cm}^{-3}$, as determined from capacitance-voltage measurements. The substrates are n-doped with a nominal concentration of $8 \times 10^{18} \text{ cm}^{-3}$. To selectively form the V_{Si} defects, the samples were irradiated at room temperature with 1.8 MeV protons, having a projected range of $\sim 27 \mu\text{m}$ calculated using collision Monte Carlo models as manifested in the SRIM code,³⁴ while being tilted $\sim 8^\circ$ off with respect to the surface normal to reduce channeling effects. Proton irradiation was performed to fluences ranging from 1×10^{11} to $8 \times 10^{13} \text{ cm}^{-2}$ to enable detection using both DLTS (with an upper defect concentration limit of $0.2N_D$) and PL spectroscopy (our setup has a lower V_{Si} detection limit in the 10^{13} cm^{-3} range). Following irradiation, circular nickel (Ni) contacts having 1 mm diameter and 150 nm thickness were deposited on the epitaxial-layer surface using an electron-beam evaporator to form SBDs. To alleviate implantation damage and reduce the concentration of metastable peaks appearing

in the temperature region relevant for DLTS measurements,^{63,64} all samples were annealed at 300 °C in air for 30 min using a conventional tube furnace.

PL spectroscopy and field-dependent intensity modulation

For the PL spectroscopy the samples were placed inside a close-cycled He refrigerator system (CCS-450 Janis Research, Inc.), and the samples were measured at temperatures ranging from 10 to 300 K. Sample excitation was employed using a pulsed Ti sapphire tunable laser operating in a femtosecond mode-locked mode and utilizing an excitation wavelength of 740 nm. The emission was analyzed by a fiber-optic (Ocean Optics, HR4000) and imaging spectrometer systems (Horiba iHR320 coupled to Andor iXon888 EMCCD), with a spectral resolution below 0.2 nm in both cases. Positive and negative bias was applied to the SBD being addressed by individual wires attached to the Ni contact by conductive glue, and the luminescence modulation was investigated at temperatures ranging from 10 to 100 K and with laser intensities of 25 and 250 mW, which correspond to $\sim 100 \text{ W/cm}^2$ and $\sim 1 \text{ kW/cm}^2$ intensities for a given diameter of the excitation beam spot on the sample of $\sim 200 \mu\text{m}$.

Defect identification

Electrical characterization in the form of DLTS was performed in the 77–370 K temperature range to encompass both the S1 and S2 peaks, with the scans starting at low temperature. The reverse bias was kept at -10 V using a 10 V filling pulse. Rate windows in the range 20–640 ms and a standard lock-in weighting function were used to extract the DLTS signal. Optical characterization to obtain correlation with DLTS measurements was performed at 10 K using the PL setup described above with a 25 mW excitation intensity and a wavelength of 740 nm.

SRIM simulations were performed to provide an estimate for the V_{Si} concentration by comparing to that known for V_{C} . For the simulations, we used 20 eV (30 eV) for the C (Si) displacement energy, and for the post-processing we estimated that 3% of all vacancies (both silicon and carbon) survive dynamic annealing during ion implantation and the 300 °C post-irradiation anneal.

Device simulations

Based on TCAD simulations using Sentaurus Device from Synopsys, the Schottky diode was investigated regarding its electrical behavior. A simplified structure including the most important physical models for 4H-SiC was used to replicate the diode's response to various conditions such as the external bias. The simulations were performed for $T = 100 \text{ K}$ and $T = 300 \text{ K}$.

DATA AVAILABILITY

The data that support the findings of this study are available from the corresponding author upon reasonable request.

CODE AVAILABILITY

The code used to analyze the results presented in this paper will be made available from the corresponding author upon reasonable request.

Received: 31 July 2019; Accepted: 10 November 2019;

Published online: 04 December 2019

REFERENCES

- Doherty, M. W. et al. The nitrogen-vacancy colour centre in diamond. *Phys. Rep.* **528**, 1–45 (2013).
- Castelletto, S., Rosa, L. & Johnson, B. C. in *Silicon Carbide Devices and Processing* (InTech, 2015).
- Santori, C., Fattal, D. & Yamamoto, Y. *Single-photon Devices and Applications* (Wiley, 2010).
- Lo, H.-K., Curty, M. & Tamaki, K. Secure quantum key distribution. *Nat. Photonics* **8**, 595–604 (2014).
- Knill, E., Laflamme, R. & Milburn, G. J. A scheme for efficient quantum computation with linear optics. *Nature* **409**, 46–52 (2001).
- Xu, F. et al. Experimental quantum fingerprinting with weak coherent pulses. *Nat. Commun.* **6**, 8735 (2015).

7. Togan, E. et al. Quantum entanglement between an optical photon and a solid-state spin qubit. *Nature* **466**, 730–734 (2010).
8. Humphreys, P. C. et al. Deterministic delivery of remote entanglement on a quantum network. *Nature* **558**, 268–273 (2018).
9. Weber, J. R. et al. Quantum computing with defects. *Proc. Natl Acad. Sci.* **107**, 8513–8518 (2010).
10. Lohrmann, A., Johnson, B. C., McCallum, J. C. & Castelletto, S. A review on single photon sources in silicon carbide. *Rep. Prog. Phys.* **80**, 034502 (2017).
11. Widmann, M. et al. Coherent control of single spins in silicon carbide at room temperature. *Nat. Mater.* **14**, 164–168 (2014).
12. Kraus, H. et al. Room-temperature quantum microwave emitters based on spin defects in silicon carbide. *Nat. Phys.* **10**, 157–162 (2014).
13. Niethammer, M. et al. Coherent electrical readout of defect spins in 4H-SiC by photo-ionization at ambient conditions. Preprint at arXiv:1903.12236 (2019).
14. Castelletto, S. et al. A silicon carbide room-temperature single-photon source. *Nat. Mater.* **13**, 151–156 (2014).
15. Bosma, T. et al. Identification and tunable optical coherent control of transition-metal spins in silicon carbide. *npj Quantum Inf.* **4**, 48 (2018).
16. Koehl, W. F., Buckley, B. B., Heremans, F. J., Calusine, G. & Awschalom, D. D. Room temperature coherent control of defect spin qubits in silicon carbide. *Nature* **479**, 84–88 (2011).
17. Simin, D. et al. Locking of electron spin coherence above 20 ms in natural silicon carbide. *Phys. Rev. B* **95**, 161201(R) (2017).
18. Christle, D. J. et al. Isolated electron spins in silicon carbide with millisecond coherence times. *Nat. Mater.* **14**, 160–163 (2015).
19. Janzén, E. et al. The silicon vacancy in SiC. *Phys. B: Condens. Matter* **404**, 4354–4358 (2009).
20. Nagy, R. et al. High-fidelity spin and optical control of single silicon-vacancy centres in silicon carbide. *Nat. Commun.* **10**, 1054 (2019).
21. Nagy, R. et al. Quantum properties of dichroic silicon vacancies in silicon carbide. *Phys. Rev. Appl.* **9**, 034022 (2018).
22. Radulaski, M. et al. Scalable quantum photonics with single color centers in silicon carbide. *Nano Lett.* **17**, 1782–1786 (2017).
23. Wang, J. et al. Efficient generation of an array of single silicon-vacancy defects in silicon carbide. *Phys. Rev. Appl.* **7**, 064021 (2017).
24. Bracher, D. O., Zhang, X. & Hu, E. L. Selective Purcell enhancement of two closely linked zero-phonon transitions of a silicon carbide color center. *Proc. Natl Acad. Sci. USA* **114**, 4060 (2017).
25. Hornos, T., Gali, A. & Svensson, B. G. Large-scale electronic structure calculations of vacancies in 4H-SiC using the Heyd-Scuseria-Ernzerhof screened hybrid density functional. *Mater. Sci. Forum* **679–680**, 261–264 (2011).
26. de la Casas, C. F., Christle, D. J., Hassan, J. U., Son, T. O. O. T. & Awschalom, D. D. Stark tuning and electrical charge state control of single divacancies in silicon carbide. *Appl. Phys. Lett.* **111**, 262403 (2017).
27. ichiro Sato, S. et al. Room temperature electrical control of single photon sources at 4H-SiC surface. *ACS Photonics* **5**, 3159–3165 (2018).
28. Anderson, C. P. et al. Electrical and optical control of single spins integrated in scalable semiconductor devices. Preprint at arXiv:1906.08328 (2019).
29. Golter, D. A. & Lai, C. W. Optical switching of defect charge states in 4H-SiC. *Sci. Rep.* **7**, 13406 (2017).
30. Wolfowicz, G. et al. Optical charge state control of spin defects in 4H-SiC. *Nat. Commun.* **8**, 1876 (2017).
31. Wolfowicz, G., Whiteley, S. J. & Awschalom, D. D. Electrometry by optical charge conversion of deep defects in 4H-SiC. *Proc. Natl Acad. Sci.* **115**, 7879–7883 (2018).
32. Wagner, M. et al. Electronic structure of the neutral silicon vacancy in 4H and 6H SiC. *Phys. Rev. B* **62**, 16555 (2000).
33. Ivády, V. et al. Identification of Si-vacancy related room-temperature qubits in 4H silicon carbide. *Phys. Rev. B* **96**, 161114(R) (2017).
34. Ziegler, J. F., Ziegler, M. & Biersack, J. SRIM—the stopping and range of ions in matter (2010). *Nucl. Instrum. Methods Phys. Res. B: Beam Interactions Mater. Atoms* **268**, 1818–1823 (2010).
35. Son, N. T. et al. Negative-U system of carbon vacancy in 4H-SiC. *Phys. Rev. Lett.* **109**, 187603 (2012).
36. Freysoldt, C., Grabowski, B., Hickel, T. & Neugebauer, J. First-principles calculations for point defects in solids. *Rev. Mod. Phys.* **86**, 253–305 (2014).
37. Wickramaratne, D. et al. Defect identification based on first-principles calculations for deep level transient spectroscopy. *Appl. Phys. Lett.* **113**, 192106 (2018).
38. Frodason, Y. K., Johansen, M. E., Alkauskas, A. & Vines, L. Negative-U and polaronic behavior of the Zn–O divacancy in ZnO. *Phys. Rev. B* **99**, 174106 (2019).
39. Omotoso, E., Mayer, W. E., Auret, F. D., Paradzhah, A. T. & Legodi, M. J. Electrical characterization of deep levels created by bombarding nitrogen-doped 4H-SiC with alpha-particle irradiation. *Nucl. Instrum. Methods Phys. Res. B* **371**, 312–316 (2016).
40. Capan, I. et al. Double negatively charged carbon vacancy at the h- and k-sites in 4H-SiC: Combined laplace-DLTS and DFT study. *J. Appl. Phys.* **123**, 161597 (2018).
41. Storasta, L., Bergman, J. P., Janzén, E., Henry, A. & Lu, J. Deep levels created by low energy electron irradiation in 4H-SiC. *J. Appl. Phys.* **96**, 4909–4915 (2004).
42. Alfieri, G., Monakhov, E. V., Svensson, B. G. & Linnarsson, M. K. Annealing behavior between room temperature and 2000 °C of deep level defects in electron-irradiated n-type 4H silicon carbide. *J. Appl. Phys.* **98**, 043518 (2005).
43. Rauls, E. et al. Metastability of the neutral silicon vacancy in 4H-SiC. *Phys. Status Solidi B* **217**, R1 (2000).
44. David, M. L. et al. Electrically active defects in irradiated 4H-SiC. *J. Appl. Phys.* **95**, 4728–4733 (2004).
45. Iwamoto, N. & Svensson, B. G. in *Defects in Semiconductors* vol. 91 of *Semiconductors and Semimetals* (eds Romano, L., Privitera, V. & Jagadish, C.) 369–407 (Elsevier, 2015).
46. Bathen, M. E. et al. Diffusion of the carbon vacancy in a-cut and c-cut n-type 4H-SiC. *Mater. Science Forum* **924**, 200–203 (2018).
47. Bringuier, E. Impact excitation in ZnS-type electroluminescence. *J. Appl. Phys.* **70**, 4505–4512 (1991).
48. Stark, J. Beobachtungen über den effekt des elektrischen feldes auf spektrallinien i. quereffekt. *Ann. Physik* **50**, 489 (1914).
49. Stoneham, A. M. *Theory of Defects in Solids: Electronic Structure of Defects in Insulators and Semiconductors* (Clarendon Press, 2001).
50. Tamarat, P. et al. Stark shift control of single optical centers in diamond. *Phys. Rev. Lett.* **97**, 083002 (2006).
51. Widmann, M. et al. Electrical charge state manipulation of single silicon vacancies in a silicon carbide quantum optoelectronic device. *Nano Lett.* **19**, 7173–7180 (2019).
52. Niethammer, M. et al. Vector magnetometry using silicon vacancies in 4H-SiC under ambient conditions. *Phys. Rev. Appl.* **6**, 034001 (2016).
53. Kresse, G. & Hafner, J. Ab initio molecular dynamics for liquid metals. *Phys. Rev. B* **47**, 558–561 (1993).
54. Kresse, G. & Hafner, J. Ab initio molecular-dynamics simulation of the liquid-metal-amorphous-semiconductor transition in germanium. *Phys. Rev. B* **49**, 14251–14269 (1994).
55. Kresse, G. & Furthmüller, J. Efficient iterative schemes for ab initio total-energy calculations using a plane-wave basis set. *Phys. Rev. B* **54**, 11169–11186 (1996).
56. Kresse, G. & Furthmüller, J. Efficiency of ab-initio total energy calculations for metals and semiconductors using a plane-wave basis set. *Comput. Mater. Sci.* **6**, 15–50 (1996).
57. Heyd, J., Scuseria, G. E. & Ernzerhof, M. Hybrid functionals based on a screened coulomb potential. *J. Chem. Phys.* **118**, 8207–8215 (2003).
58. Blöchl, P. E. Projector augmented-wave method. *Phys. Rev. B* **50**, 17953–17979 (1994).
59. Grivickas, P., Grivickas, V., Linnros, J. & Galeckas, A. Fundamental band edge absorption in nominally undoped and doped 4H-SiC. *J. Appl. Phys.* **101**, 123521 (2007).
60. Kumagai, Y. & Oba, F. Electrostatics-based finite-size corrections for first-principles point defect calculations. *Phys. Rev. B* **89**, 195205 (2014).
61. Freysoldt, C., Neugebauer, J. & de Walle, C. G. V. Fully Ab Initio Finite-size corrections for charged-defect supercell calculations. *Phys. Rev. Lett.* **102**, 016402 (2009).
62. Komsa, H.-P., Rantala, T. T. & Pasquarello, A. Finite-size supercell correction schemes for charged defect calculations. *Phys. Rev. B* **86**, 045112 (2012).
63. Nielsen, H., Martin, D., Lévêque, P., Hallén, A. & Svensson, B. Annealing study of a bistable defect in proton-implanted n-type 4H-SiC. *Phys. B: Condens. Matter* **340–342**, 743–747 (2003).
64. Alfieri, G., Monakhov, E. V., Svensson, B. G. & Hallén, A. Defect energy levels in hydrogen-implanted and electron-irradiated n-type 4H silicon carbide. *J. Appl. Phys.* **98**, 113524 (2005).

ACKNOWLEDGEMENTS

The authors would like to sincerely thank the late Professor Bengt G. Svensson for all the enlightening discussion and support, and for initiating the work presented herein. Financial support was kindly provided by the Research Council of Norway and the University of Oslo through the frontier research project FUNDAMENT (no. 251131, FriPro ToppForsk-program), and the Norwegian Micro- and Nanofabrication Facility (NorFAB 245963). The computations were performed on resources provided by UNINETT Sigma2—the National Infrastructure for High Performance Computing and Data Storage in Norway. J.C. thanks the Fundação para a Ciência e a Tecnologia (FCT) for support under project UID/CTM/50025/2019, co-funded by FEDER funds through the COMPETE 2020 Program. J.C. also acknowledges support by the NATO SPS programme (Project No. 985215).

AUTHOR CONTRIBUTIONS

M.E.B. and Y.K.F. performed the calculations. M.E.B, L.V., A.G., and B.G.S. designed the experiments; M.E.B., A.G., and H.M.A performed the experiments. J.M. and U.G. performed the device simulations. All authors analyzed the data and wrote the manuscript.

COMPETING INTERESTS

The authors declare no competing interests.

ADDITIONAL INFORMATION

Supplementary information is available for this paper at <https://doi.org/10.1038/s41534-019-0227-y>.

Correspondence and requests for materials should be addressed to M.E.B.

Reprints and permission information is available at <http://www.nature.com/reprints>

Publisher's note Springer Nature remains neutral with regard to jurisdictional claims in published maps and institutional affiliations.



Open Access This article is licensed under a Creative Commons Attribution 4.0 International License, which permits use, sharing, adaptation, distribution and reproduction in any medium or format, as long as you give appropriate credit to the original author(s) and the source, provide a link to the Creative Commons license, and indicate if changes were made. The images or other third party material in this article are included in the article's Creative Commons license, unless indicated otherwise in a credit line to the material. If material is not included in the article's Creative Commons license and your intended use is not permitted by statutory regulation or exceeds the permitted use, you will need to obtain permission directly from the copyright holder. To view a copy of this license, visit <http://creativecommons.org/licenses/by/4.0/>.

© The Author(s) 2019

Supplementary Information

Electrical charge state identification and control for the silicon vacancy in 4H-SiC

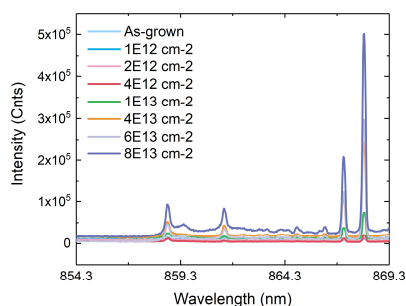
M. E. Bathen¹, A. Galeckas¹, J. Müting², H. M. Ayedh¹, U. Grossner², J. Coutinho³, Y. K. Frodason¹, and L. Vines¹

¹Department of Physics/ Centre for Materials Science and Nanotechnology, University of Oslo, N-0316 Oslo, Norway

²Advanced Power Semiconductor Laboratory, ETH Zürich, Physikstrasse 3, 8092 Zürich, Switzerland

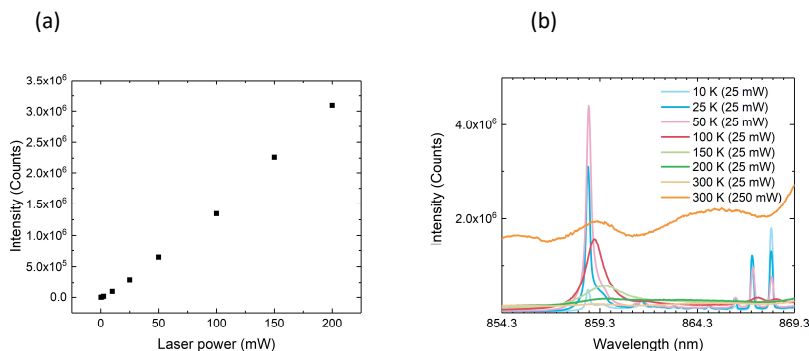
³Department of Physics and I3N, University of Aveiro, Campus Santiago, 3810-193 Aveiro, Portugal

Supplementary Notes 1: Silicon vacancy-related photoluminescence



Supplementary Figure 1: Photoluminescence spectra collected at 10K from several 4H-SiC samples proton irradiated to different fluences, focused around the V1 line.

Supplementary Figure 1 displays the PL spectra obtained after proton irradiation to various fluences, revealing the proton fluence dependence of the V1-related luminescence. The V1 and V1' ZPL intensities clearly increase with the proton fluence. The spectra form the basis for the correlation between the V1/V1' emission and the S1/S2 peaks observed by DLTS and shown in Figure 5 of the main text.



Supplementary Figure 2: (a) Intensity dependence of V1 emission for sample irradiated to a proton fluence of $4\text{E}13\text{ cm}^{-2}$, and (b) temperature dependence of PL in the vicinity of the V1 line for a fluence of $8\text{E}13\text{ cm}^{-2}$.

Supplementary Figure 2(a) demonstrates the intensity dependence of V1 emission for a proton fluence of $4 \times 10^{13}\text{ cm}^{-2}$. The most commonly employed power of the laser excitation in this work is 25 mW, which is substantially below saturation. For a given excitation beam diameter on the sample surface of $\sim 200\mu\text{m}$, the corresponding intensity of such excitation is $\sim 100\text{ W/cm}^2$, which is by far below what is typically reported for confocal systems, in the 100 kW/cm^2 range. Even at the highest excitation power used in our experiments of 250 mW, the intensity merely reaches $\sim 1\text{ kW/cm}^2$, thus a linear dependence is maintained between the PL intensity and the defect concentration. Supplementary Figure 2(b) displays emission close to the V1 line as a function of temperature. The figure reveals that the intensity of V1 decreases and the signature broadens with increasing temperature. However, it remains clearly visible above liquid nitrogen temperatures, until it becomes difficult to distinguish at temperatures above 200 K.

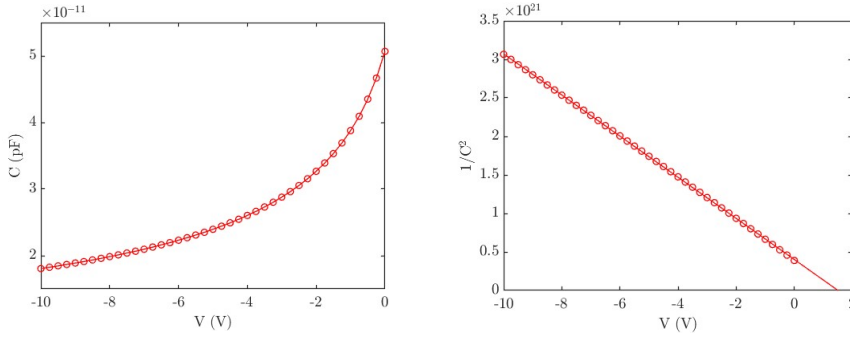
Supplementary Notes 2: Schottky barrier diode characteristics

Capacitance-voltage

The effect of electric fields on silicon vacancy-related emission was studied using n-type 4H-SiC samples having $10\mu\text{m}$ epitaxial layers purchased from Cree, Inc. To enable application of electric fields to the defects, we dipped the samples in 2 % HF to remove the native oxide, and deposited circular Ni contacts using electron beam evaporation to form Schottky barrier diodes (SBDs). The SBDs were 150 nm thick and had diameters of approximately 1 mm, as verified by microscopy.

First, the SBDs were used to determine sample characteristics. By performing capacitance-voltage measurements, we were able to determine the net carrier concentrations in the samples, estimate the depletion region width at different biases, and find the real Schottky barrier height.

Supplementary Figure 3 demonstrates the typical voltage response of an SBD deposited on the n-type proton irradiated 4H-SiC samples studied within this work, with capacitance versus voltage shown in (a) and $1/C^2$ vs voltage shown in (b). Taking the average over eight such CV measurements, we arrived at a mean built-in voltage of 1.5 V, which was later used in the device simulations.

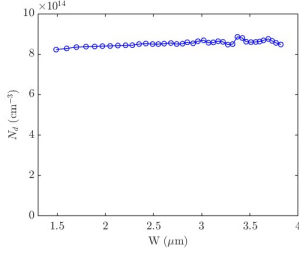


Supplementary Figure 3: representative (a) CV measurement, and (b) $1/C^2$ vs voltage, for a Schottky barrier diode deposited on a n-type 4H-SiC sample proton-irradiated to a fluence of $2 \times 10^{11} \text{ cm}^{-2}$.

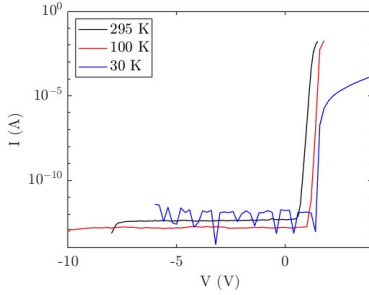
The capacitance of an SBD is given as $C = \frac{\epsilon A}{W}$, where ϵ is the semiconductor permittivity, A is the diode area and W is the depletion region width. W is given by

$$W = \sqrt{\frac{2\epsilon(V_{\text{built-in}} - V_{\text{applied}})}{qN_d}}, \text{ where } N_d \text{ is the donor concentration. The net carrier}$$

concentration (N_d) as a function of the depletion region width (W) is estimated from the CV measurement demonstrated in Supplementary Figure 3(a), and plotted in Supplementary Figure 4. As an average value, we estimate that the net carrier concentration in the n-type 4H-SiC samples is approximately $N_d = 1 \times 10^{15} \text{ cm}^{-3}$. Now that we have an estimate of the built-in voltage and N_d , we can find the Schottky barrier height according to $\Phi_B = V_{\text{bi}} + \frac{E_c - E_{Fs}}{q} = V_{\text{bi}} + 0.2 \text{ V} = 1.7 \text{ V}$.



Supplementary Figure 4: Net carrier concentration versus depletion region depth, as estimated from CV measurements obtained from a 4H-SiC sample proton-irradiated to a fluence of $2 \times 10^{11} \text{ cm}^{-2}$.



Supplementary Figure 5: Temperature-dependent current-voltage characteristic for a representative SBD deposited onto an n-type 4H-SiC sample proton-irradiated to a fluence of $2 \times 10^{11} \text{ cm}^{-2}$.

Current-voltage

Supplementary Figure 5 illustrates the temperature-dependent IV characteristics of a representative Schottky diode. The difference is small between the room temperature and the 100 K curves, but increases as the temperature drops to 30 K. However, the diode is clearly rectifying also at a temperature of 30 K. The noise present for the 30 K IV curve can be ascribed to the cryogenic pump.

Electric field

The maximum applied electric field depends on the depletion region width, and thereby the applied bias voltage, according to

$$\xi_0 = -\frac{q}{\epsilon} N_d W.$$

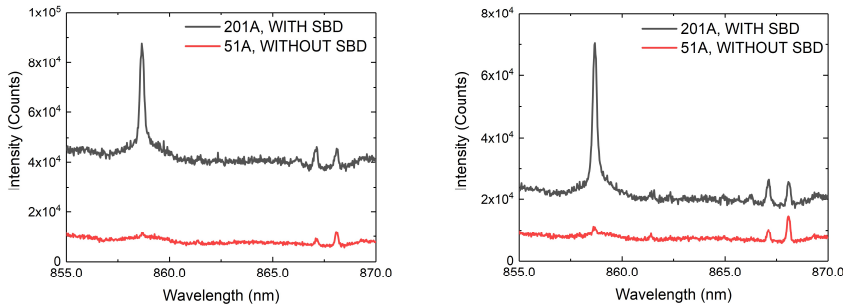
Within this work, the applied electric field cited in Figure 7 of the main text (concerning the Stark effect) refers to the maximum applied electric field, and not the local field experienced by the individual defect.

Forming a Schottky barrier diode on the 4H-SiC sample surface results in an electric field over the depletion region, which is further modified by applying external bias. The electric field strength has been estimated under the depletion approximation and the doping concentration extracted from the CV measurements. Consequently, contributions from local space charge or laser excitation has been assumed to be negligible. In this regard, it is worth noting that no significant change was observed in the measured current during the sub-bandgap excitation performed here.

As defect distribution and concentration within the depletion region differed for different samples, the electric field experienced by each individual defect may differ from the presented electric field values.

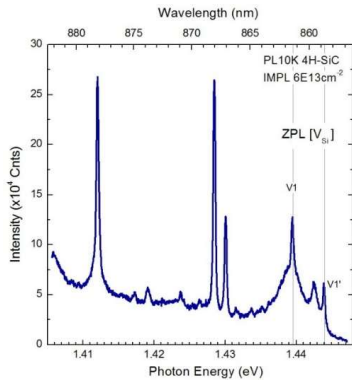
Supplementary Notes 3: Field effect on emission from V_{Si} ensembles in 4H-SiC

Effect of built-in field



Supplementary Figure 6: Effect of built-in field imposed by Schottky barrier diode on the V1 PL signal originating from V_{Si}^{-1} in two different 4H-SiC samples proton irradiated to a fluence of (a) $1 \times 10^{12} \text{ cm}^{-2}$ and (b) $2 \times 10^{12} \text{ cm}^{-2}$.

Supplementary Figure 6 demonstrates how the presence of the SBD drastically increases V1 emission for two different fluences: (a) $1 \times 10^{12} \text{ cm}^{-2}$, and (b) $2 \times 10^{12} \text{ cm}^{-2}$. The first fluence is represented in the main text by Figure 2(e), and the second by Figure 2(d). In each



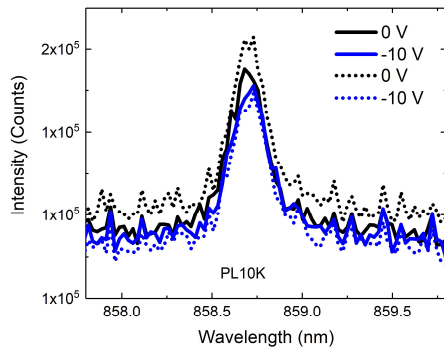
Supplementary Figure 7: PL spectrum obtained at 10 K from proton irradiated epilayer clearly revealing presence of both ZPL V1 lines. Note the prevailing V1 over V1', which is in contrast to what is observed in the case of probing SBD.

case the PL was collected from two different samples: one with and one without SBD, but both irradiated at the same time and to the same fluence. A stands for acquisition and each acquisition lasted 1 second. Indeed, integration over 201 acquisitions does lead to larger peak intensities in total, but affects the background equally. With SBD, we clearly see a much larger V1 peak as compared to the SBD-free case. On the other hand, in the case of a bare implanted surface (without SBD), the spectral contents include both V1' and V1 signatures, as can be observed in Supplementary Figure 7.

The drastic increase demonstrated in Supplementary Figure 7, and in Figure 2(b) of the main text, is larger than expected from geometrical considerations, where the main factor is reflection from the semiconductor-

metal interface. Hence, an increase no more than a factor two would be expected, while about an order of magnitude is observed. The band bending due to the Schottky barrier must therefore cause the increase.

Effect of external field



Supplementary Figure 8 demonstrates that while intensity modulation of V1' is still obtainable for larger biases, here for -10 V, the modulation depth becomes less predictable.

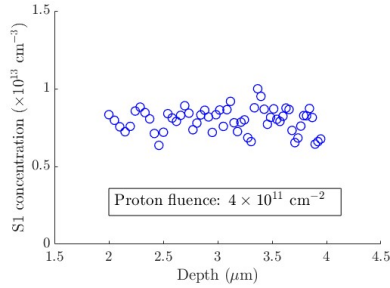
Supplementary Figure 8: Effect of sequential application of -10 V reverse bias on V1' emission intensity. The sample was proton-irradiated to a fluence of $1 \times 10^{12} \text{ cm}^{-2}$.

Proton fluence dependence

As mentioned in the manuscript, we observe a pronounced proton fluence dependence for the V1' emission modulation. For the lower proton fluence of $1 \times 10^{12} \text{ cm}^{-2}$, we can modulate the photon counts by up to 20 %. For the higher proton fluence of $2 \times 10^{12} \text{ cm}^{-2}$, the modulation is twice as large and exceeds 45 % (see Figure 2 of the main text).

Supplementary Discussion 1: DLTS investigation of the S1 peak

The DLTS spectra [1] were obtained using a DLTS setup as described in Ref. [2]. Previous works have established that the measured capture cross sections for S1 and S2 differ from the apparent ones, and are $\sigma = 8 \times 10^{-1} \text{ cm}^{-2}$ for S1, and $\sigma = 3 \times 10^{-15} \text{ cm}^{-2}$ for S2 [3]. The significant difference of more than an order of magnitude resonates with S1 corresponding to the (2-/3-) transition, as a large electron repulsion would be associated with V_{Si} capturing the additional electron.

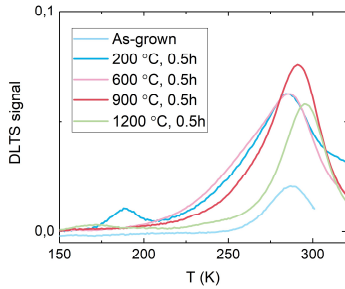


Supplementary Figure 9: S1 concentration depth profile for a proton irradiation fluence of $4 \times 10^{12} \text{ cm}^{-2}$, demonstrating a uniform trap distribution throughout the depletion region.

Supplementary Figure 9 demonstrates that the S1 concentration is uniform throughout the depletion region, as expected for a primary point defect (such as the silicon vacancy) after proton irradiation. The concentration versus depth profiles of the S1 defect was determined according to the relation [4]

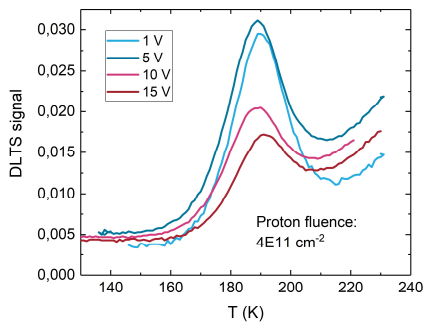
$$N_t(x) = \left(\frac{qW^2N_d}{\epsilon} \right) N_d(x) \frac{\partial \left(\frac{\Delta C}{C} \right)}{\partial V},$$

where N_t is the defect concentration, q the elementary charge, W the depletion region depth, N_d the concentration of ionized donors, ϵ the semiconductor permittivity, and the last factor is the derivative of the DLTS signal versus voltage. As only the uniformity of the S1 concentration profile was to be considered, we disregarded the lambda correction [5].



Supplementary Figure 10: Temperature dependence of the S1 defect center.

Supplementary Figure 10 shows the temperature dependence of the S center, as represented by the S1 peak. S1 is not present in as-grown material, appears after ion implantation (here using 4 MeV Carbon ions to a fluence of $4 \times 10^8 \text{ cm}^{-2}$) and annealing at 200 °C for 30 minutes in air. Annealing the sample at 600 °C or above removes the S1 peak, perfectly in line with behavior commonly associated with the silicon vacancy.



Supplementary Figure 11: Voltage dependence of the S1 peak (normalized), displaying the absence of the Poole-Frenkel effect, indicating an acceptor-like nature for the S1 defect.

Supplementary Figure 11 shows the voltage dependence of the S1 peak, demonstrating no Poole Frenkel effect and therefore an acceptor-like behavior of the S1 defect center.

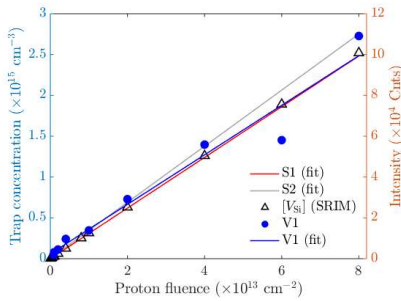
Supplementary Discussion 2: Determining silicon vacancy concentrations

Knowing that the S center has a uniform concentration profile in the proton irradiated samples, its concentration can be determined according to

$$N_t = 2N_d \frac{\Delta C}{C_r},$$

where ΔC is the capacitance transient in the peak. For S1 this is relatively straightforward, while for S2 and $Z_{1/2}$ the overlap between the two peaks renders extraction of the peak amplitude difficult. Accordingly, the DLTS spectrum was simulated to extract all trap concentrations for each proton irradiation fluence, using known parameters for the activation energy and capture cross section [3]. The lambda-effect [5] was accounted for when determining the trap concentrations.

The V1/V1' emission intensities for each proton fluence were determined after a linear baseline subtraction.



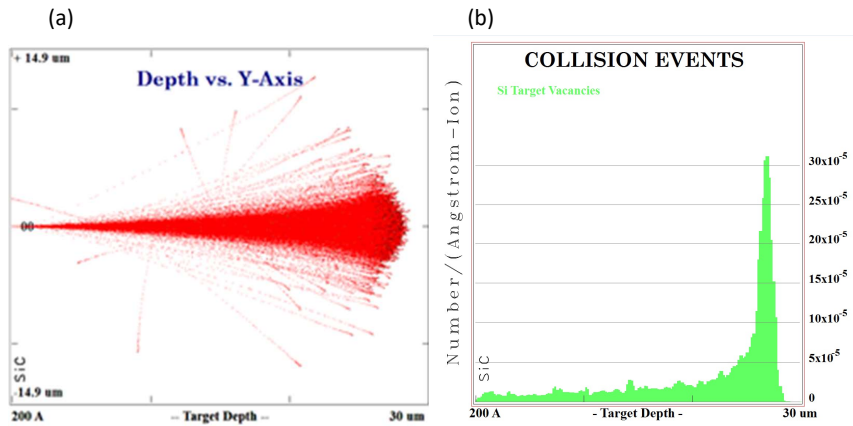
Supplementary Figure 12: S center concentration, and V1 emission intensity, dependence on the proton fluence.

Supplementary Figure 12 illustrates the same behavior as in Figure 5 of the main paper. The main features summarized by the figure that support the assignment of V_{Si} as the S center are:

- The S1 and S2 concentrations increase linearly with the proton fluence, as expected for primary point defects such as vacancies that are created by ion implantation in the dilute limit.
- When fitting the dynamic annealing factor to the known carbon vacancy concentration, the S center concentrations match those predicted for V_{Si} using SRIM very well.

- The extracted dynamic annealing factor says that 3 % of the Si vacancies survive ion implantation and the subsequent heat treatment. The factor of 3 % falls within the range we expect for primary point defects created by ion implantation.
- The slopes of the proton fluence dependence of the S center, the V1 center, and V_{Si} as predicted by SRIM, overlap very well, as seen by Supplementary Figure 12.

Supplementary Methods 1: SRIM simulations of proton irradiation

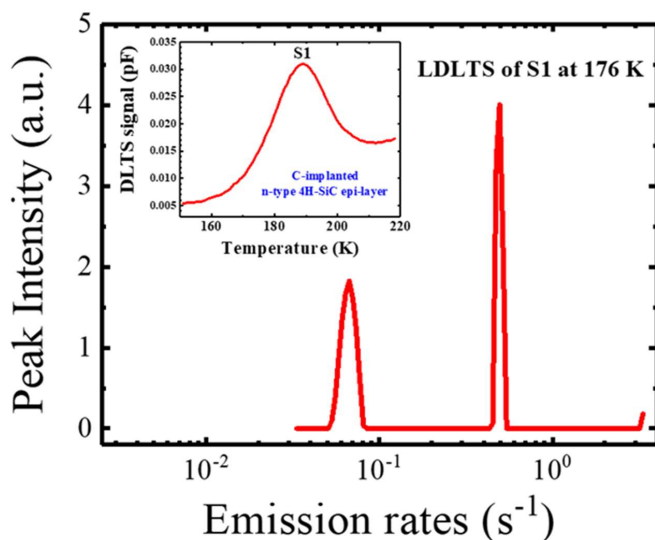


Supplementary Figure 13: Generated silicon vacancies follow 1.8 MeV proton irradiation, as estimated using the SRIM code, showing (a) the lateral distribution and ion trajectories, and (b) the average vacancy generation as a function of target depth.

SRIM 2013 [6] was used to provide an initial estimate of both the target silicon vacancies, and their projected range, following irradiation with 1.8 MeV protons to different fluences. The collision events of the protons are illustrated in Supplementary Figure 13(a), with Supplementary Figure 13(b) showing the predicted Si vacancy concentration profile. We find that the Si vacancy peak is situated approximately 27 μm into the sample, with the near-surface defect tail being approximately uniform.

Moreover, the SRIM simulations were used to estimate the expected silicon vacancy concentration after irradiation to varying proton fluences. By comparing the SRIM simulation to the DLTS measurements of the $Z_{1/2}$ level assigned to the well-known carbon vacancy, we were able to estimate the number of silicon and carbon vacancies surviving dynamic annealing during ion implantation, and the 300 °C post-irradiation anneal, at 3 %.

Supplementary Methods 2: Laplace-DLTS investigation of the S1 peak



Supplementary Figure 14: Laplace-DLTS measurement of the S1 deep center at 176 K in n-type 4H-SiC epi-layer implanted by C-ions. The inset Supplementary Figure shows the conventional DLTS spectrum of S1 in the same sample. The LDLTS measurement clearly separates the signals from two closely separated deep levels of S1 which are indistinguishable by conventional DLTS.

If two closely spaced energy levels have similar emission rates (time constants), it is extremely difficult to distinguish these levels by means of conventional DLTS, where two closely overlapping peaks will be monitored as a single broad peak in the DLTS spectra. A numerical methods using Laplace transformation was developed to better separate the interlaced emission rates of these close energy levels from the recorded capacitance transients; this is known as Laplace DLTS (LDLTS) [7]. This powerful technique has been successfully employed to resolve overlapping defects in semiconductors [8]. The relevant mathematical details are rather complex and to facilitate utilizing LDLTS, the numerical calculations are done by a software procedure called CONTIN [9], based on the so-called Tikhonov regularization method [10]. LDLTS measurements are very sensitive to the temperature change, and LDLTS systems use isothermal measurements with high thermal stability, maintaining the temperature at the range ± 0.02 K during the measurement. The Laplace DLTS method analyzes emission rates at a specific temperature and provides a spectrum of capacitance transient signal against the emission rate rather than against temperature. In order to extract the energy positions of closely spaced deep levels, an Arrhenius plot can be produced by the repetition of LDLTS measurements at a number of different temperatures.

LDLTS Measurement details

In LDLTS measurements, capacitance transients were recorded at a series of temperatures; 176, 179, 182, 185, 188, 191, and 194 K, by keeping the temperature stability within ± 0.02 K. Reverse bias of -5V and a filling pulse voltage to 0 V of 50 ms width were applied. The transient length (scan time) has been adjusted at each measurement until the maximum amplitude of the capacitance transient is displayed and a full shape of saturated transient is shown. During the LDLTS measurements, each capacitance transient consisted of 10^6 points and the recorded transient for Laplace transform was obtained by averaging a total of 500 - 1000 capacitance transients, in order to increase the signal-to-noise ratio. The Laplace transform was then computed from the averaged transient and the raw data of 10^6 points were compacted to 1000 points representing the entire transient using CONTIN software that employs Tikhonov regularization.

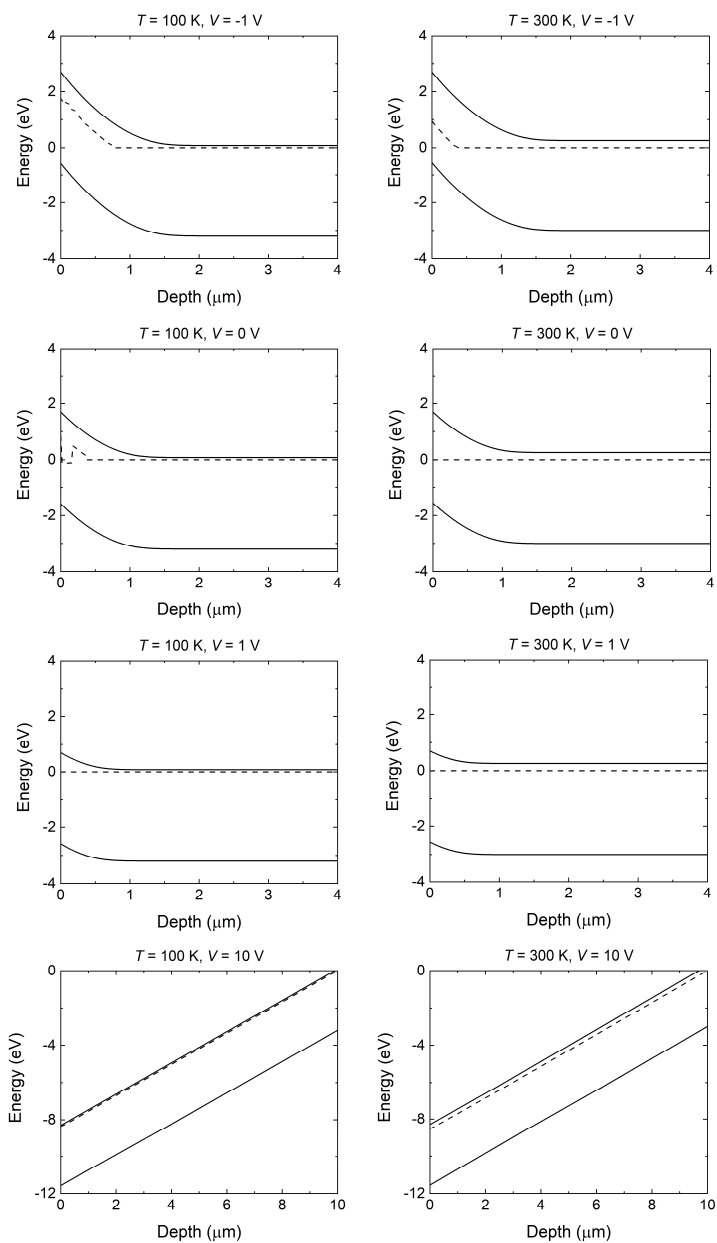
In this study, the high energy resolution LDLTS technique was employed in an attempt to resolve the emission rates of closely spaced deep states of S1 defect that are attributed to the hexagonal and cubic contributions of the silicon vacancy (V_{Si}) in 4H-SiC epilayers implanted by C ions (4 MeV, C fluence of $6E8 \text{ cm}^{-2}$). Indeed, two distinct signals of the S1 peak could be clearly resolved, as illustrated in Supplementary Figure 14 for LDLTS measurement performed at sample temperature 176 ± 0.02 K. The conventional DLTS spectrum of S1 peak is shown as an inset at the top of Supplementary Figure 14. The broad peak centered at 188 K for the DLTS rate window ($(640 \text{ ms})^{-1}$) is due to electron emissions from both the hexagonal and the cubic sites of V_{Si} .

LDLTS spectra of S1 deep levels at different temperatures are shown in Figure 4(b) in the main article, and Figure 4(c) displays Arrhenius plots of the two LDLTS peaks of the S1 contributions. The energy separation for the two contributions to S1 deduced using Laplace-DLTS is 0.04 eV, as seen in Figure 4(c), is somewhat below the 0.1 eV estimated by hybrid DFT calculations. However, the difference of 0.06 eV is well within the error bar of both techniques. Although the two peaks in Supplementary Figure 14 have different peak intensities, their integrated areas are approximately identical. During irradiation, both *h* and *k* silicon vacancies are formed. As the two configurations of V_{Si} differ in formation energy by only 0.1 eV in most charge states (see Figure 3 of the main text), high-energy proton irradiation is expected to form approximately equal amounts of both defect types. Accordingly, the Laplace-DLTS study of the S1 peak reinforces our belief that the S1 defect center in fact originates from the (2-/3-) charge-state transition of V_{Si} .

Supplementary Methods 3: Device simulations

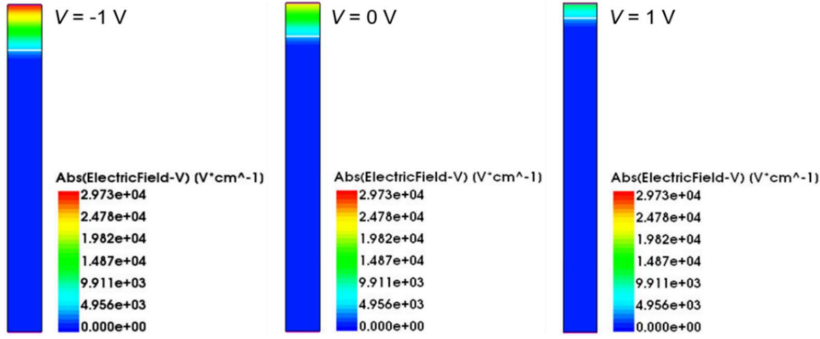
The device simulations yielding band structures were performed using Sentaurus Device from Synopsys. For simplicity reasons, the geometry (4H-SiC, $1 \times 10 \mu\text{m}$, $N_{D,\text{const}} = 1\text{E}15 \text{ cm}^{-3}$) was created with Sentaurus Editor, only taking the n-type epilayer into account. Simulations of the full device including the substrate showed identical results, but consumed much more computational time. Within Sentaurus Device the Schottky contact was introduced with a barrier height of 1.7 eV. In order to achieve a realistic simulation, the following physical models were used with specific 4H-SiC parameters: incomplete ionization of nitrogen, doping dependence of the mobility, Auger and Shockley-Read-Hall recombination. Constant defect levels at $E = 0.4 \text{ eV}$ and $E = 0.7 \text{ eV}$ (to emulate the (-2/-3) and (-1/-2) charge state transitions of the V_{Si} , respectively) with a concentration of $C = 1\text{E}13 \text{ cm}^{-3}$ were additionally included. To achieve convergence at lower temperatures a very fine mesh was used.

Supplementary Figure 15 shows several band diagrams of the Schottky contact for varying biases and temperatures.

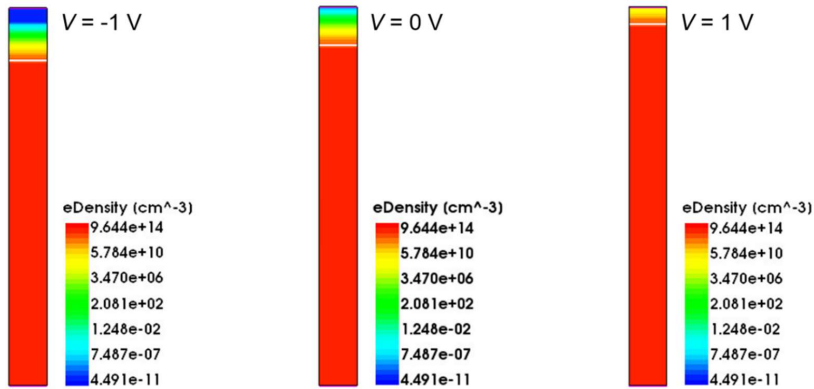


Supplementary Figure 15: Simulated band diagrams with different biases for $T = 100$ K (left) and $T = 300$ K (right). The upper solid line is the conduction band, the lower solid line the valence band and the dashed line the Fermi level. Zero depth corresponds to the Schottky contact.

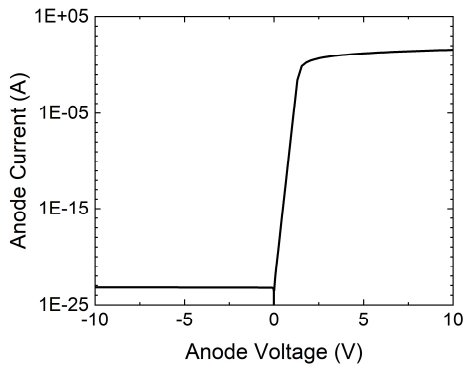
Supplementary Figure 16 and 17 show the distribution of the absolute electric field and the electron density for small biases at $T = 300$ K. The current voltage relation of the Schottky diode at $T = 300$ K can be seen in Supplementary Figure 18. A leakage current of around 10^{-23} A can be estimated, as shown in Supplementary Figure 18.



Supplementary Figure 16: Absolute electric field within simulated structure for different biases at $T = 300$ K. The Schottky contact is at the top of the structure, which is $1\ \mu\text{m} \times 10\ \mu\text{m}$.



Supplementary Figure 17: Electron density within simulated structure for different biases at $T = 300$ K. The Schottky contact is at the top of the structure, which is $1\ \mu\text{m} \times 10\ \mu\text{m}$.



Supplementary Figure 18: Anode current over voltage of the Schottky diode at $T = 300$ K. The simulation uses an appropriate area factor to scale the simulation.

Supplementary References

- [1] D. V. Lang, *Journal of Applied Physics* **45**, 3023 (1974).
- [2] B. G. Svensson, K.-H. Rydén, and B. M. S. Lewerentz, *Journal of Applied Physics* **66**, 1699 (1989).
- [3] M. L. David, G. Alfieri, E. M. Monakhov, A. Hallén, C. Blanchard, B. G. Svensson and J. F. Barbot, *Journal of Applied Physics* **95**, 4728 (2004).
- [4] P. Blood and J. W. Orton, *The Electrical characterization of Semiconductors: Majority Carriers and Electron States* (Academic Press Limited, London, 1992).
- [5] S. D. Brotherton, *Solid-State Electronics* **26**, 987 (1983).
- [6] J. F. Ziegler, M. Ziegler, and J. Biersack, *Nuclear Instruments and Methods in Physics Research Section B: Beam Interactions with Materials and Atoms* **268**, 1818 (2010).
- [7] L. Dobaczewski, P. Kaczor, I. D. Hawkins, and A. R. Peaker, *J. Appl. Phys.* **76**, 194 (1994).
- [8] L. Dobaczewski, A. R. Peaker, and K. Bonde Nielsen, *J. Appl. Phys.* **96**, 4689-4728, (2004).
- [9] S. W. Provencher, *Comput. Phys. Commun.* **27**, 213 (1982).
- [10] C. W. Groetsch, *The Theory of Tikhonov Regularisation for Fredholm Equations of the First Kind* (Pitman Advanced Pub, London, 1984).

Paper II

First-principles calculations of Stark shifts of electronic transitions for defects in semiconductors: The Si vacancy in 4H-SiC

M. E. Bathen, L. Vines, J. Coutinho

Accepted in *Journal of Physics: Condensed Matter* (2020).

DOI: 10.1088/1361-648X/abc804.



First-principles calculations of Stark shifts of electronic transitions for defects in semiconductors: The Si vacancy in 4H-SiC

Marianne Etzelmüller Bathen,^{1,*} Lasse Vines,¹ and José Coutinho²

¹*Department of Physics / Centre for Materials Science and Nanotechnology, University of Oslo, N-0316 Oslo, Norway*

²*13N, Department of Physics, University of Aveiro, Campus Santiago, 3810-193 Aveiro, Portugal*

(Dated: November 13, 2020)

Point defects in solids are promising single-photon sources with application in quantum sensing, computing and communication. Herein, we describe a theoretical framework for studying electric field effects on defect-related electronic transitions, based on density functional theory calculations with periodic boundary conditions. Sawtooth-shaped electric fields are applied perpendicular to the surface of a two-dimensional defective slab, with induced charge singularities being placed in the vacuum layer. The silicon vacancy (V_{Si}) in 4H-SiC is employed as a benchmark system, having three zero-phonon lines in the near-infrared ($V1$, $V1'$ and $V2$) and exhibiting Stark tunability via fabrication of Schottky barrier or p-i-n diodes. In agreement with experimental observations, we find an approximately linear field response for the zero-phonon transitions of V_{Si} involving the decay from the first excited state (named $V1$ and $V2$). However, the magnitude of the Stark shifts are overestimated by nearly a factor of 10 when comparing to experimental findings. We discuss several theoretical and experimental aspects which could affect the agreement.

I. INTRODUCTION

Point defects in semiconductors are rapidly becoming contenders for a host of quantum applications, with properties such as spin manipulation and single-photon emission at room temperature, enabling technologies that range from quantum sensing and information processing to quantum cryptography and communication. Hitherto, the nitrogen-vacancy (NV) center in diamond has been at the forefront, enabling high-sensitivity magnetometers with nanoscale resolution [1], and exhibiting both coherent spin manipulation at room temperature [2] and entanglement between two NV center spins [3]. However, as far as device processing and fabrication is concerned, diamond technology lacks maturity, the fraction of the total NV emission channeled into the zero-phonon line (ZPL) is low (at about 4%) [4], and coupling NV centers to waveguides to enhance emission intensities was shown to have a detrimental effect on spin and emission stability [5,6].

Over recent years, silicon carbide (and the 4H polytype in particular) has emerged as a competitive alternative to diamond, offering a more mature fabrication technology and greater ease of combining defect centers with various devices [7]. Several candidate defects exist, with the silicon vacancy (V_{Si}), the silicon-carbon divacancy ($V_{\text{Si}}V_{\text{C}}$), the nitrogen-vacancy center ($N_{\text{C}}V_{\text{Si}}$) and the carbon-antisite vacancy pair ($C_{\text{Si}}V_{\text{C}}$) all being room-temperature single-photon sources and exhibiting millisecond spin coherence times under cryogenic conditions [8–13]. However, only one charge state of each defect center exhibits the required properties, with the others remaining *dark* and without the option of optically controlling and reading out the spin state. For the case of the Si vacancy, the bright charge state is the negative one (represented as V_{Si}^-).

Charge-state control over qubit contender defects in 4H-SiC was first demonstrated for V_{Si} and $V_{\text{Si}}V_{\text{C}}$ by employing dual excitation [14], but the optical approach lacks the option of selective and controlled toggling between specific defect charge states. Recently, electrical charge-state control over V_{Si} and $V_{\text{Si}}V_{\text{C}}$ was optically detected by monitor-

ing the photoluminescence (PL) emission intensity from defects situated within 4H-SiC membranes in the vicinity of electrodes [15] or in the intrinsic region of 4H-SiC p-i-n diodes [16,17], and embedded within the depletion region of Ni/4H-SiC Schottky barrier diodes (SBDs) [18]. The electrical approach is particularly interesting as it enables control over not only the intensity, but also the energy, of single-photon emission from qubit defects via the Stark effect [19]. This has been demonstrated for defects such as NV in diamond [20,21], and also V_{Si} [18,22] and $V_{\text{Si}}V_{\text{C}}$ [15,17,23] in 4H-SiC.

Importantly, emission from solid-state systems is highly susceptible to local fluctuations related, for instance, to strain and electromagnetic fields. Thus, local inhomogeneities surrounding a defect center will diminish the uniformity of photon energies originating from that specific emitter. Emission tuning, for example via the Stark effect, therefore presents a means towards obtaining high-fidelity and identical photons from solid-state light sources, enabling integration with present and future quantum technologies and facilitating operation of relevant defects as electric field sensors. Moreover, the nature of the Stark shift may help to elucidate defect-related properties such as the local environment, the defect symmetry and the degeneracy of its electronic states. With that in mind, we report on a theoretical method for studying Stark shifts of transitions between electronic states of defects in semiconductors. We will use the negatively charged Si vacancy in 4H-SiC as a model system, and compare the results with observations reported in the literature.

A Si vacancy can inhabit two distinct lattice locations in 4H-SiC, namely the hexagonal (*h*) and pseudo-cubic (*k*) sites. These sites have C_{3v} point group symmetry and essentially differ on the relative positions of their second neighbors and farther atoms. In the ground state, both the $V_{\text{Si}}^-(h)$ and $V_{\text{Si}}^-(k)$ defects have spin 3/2 and adopt a 4A_2 spin-quartet state [24]. To simplify our analysis, we will disregard any fine structure of the many-body states due to spin-orbit and zero-field effects. Within a one-electron picture, the ground state corresponds to a $a_1^1e^{\uparrow\uparrow}$ configuration as shown on the left-hand side of Figure 1(a), with the

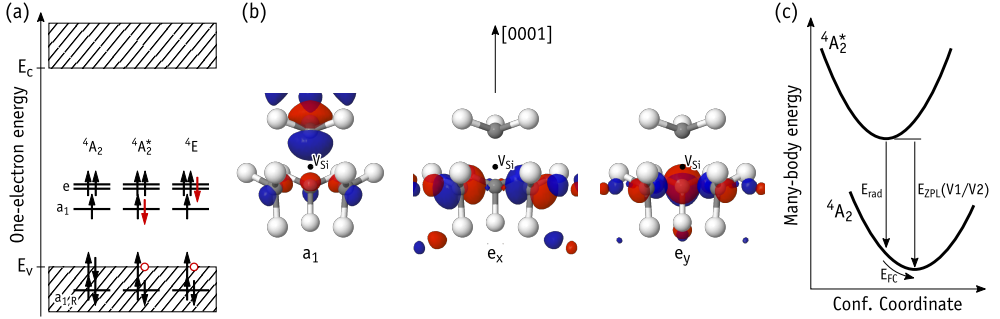


FIG. 1: (a) Schematics of the one-electron configurations involved in the luminescent transitions from excited states, $4A_2^*$ and $4E$, into the $4A_2$ ground state. Arrows (pointing upwards and downwards) and circles correspond to electrons (with spin-up and spin-down) and holes bound to V_{Si}^- . The symmetry character of the one-electron states is also indicated. Hatched areas represent crystalline states limited by the valence band top (E_v) and conduction band bottom (E_c). (b) Isosurfaces of the a_1 and e states in the gap for $\psi = \pm 0.03$ at $\mathbf{k} = \Gamma$. Si and C atoms are represented as white and gray spheres, respectively. The location of the missing Si atom is indicated as a black dot. (c) Configuration coordinate diagram representing two possible luminescent transitions from the $4A_2^*$ excited state into $4A_2$ ground state. The system either combines a radiative decay (with energy E_{rad}) with a non-radiative relaxation step (releasing a Franck-Condon energy E_{FC}), for instance via multi-phonon emission, or it undergoes a *zero-phonon* transition maximizing the energy of the emitted photon (E_{ZPL}).

corresponding one-electron states being depicted in Figure 1(b). Besides the singlet and doublet states in the gap, the four carbon radicals of V_{Si} (represented as gray spheres) give rise to a fourth one-electron state which is resonant with the valence band, and is labeled $a_{1,R}$. This state does not participate in the optical activity of the center.

Three different zero phonon lines (ZPLs) are attributed to V_{Si}^- in 4H-SiC. They are labeled V1 and V1', arising from the decay of two different but close-lying excited states of the same defect center, and V2. V1/V1' and V2 have been assigned to the h and k configurations of V_{Si} , respectively [25]. The corresponding ZPL energies fall in the near-infrared range (860 – 916 nm), and are thus far better suited for integration with fiber optical communication than, e.g., the NV center in diamond which emits in the red. All three lines have been interpreted as arising from spin-down channel radiative relaxations involving two close-lying excited states, namely $4A_2^*$ and $4E$. Their corresponding one-electron configurations are depicted in Figure 1(a). While $4A_2^* \rightarrow 4A_2$ transitions, which involve $V_{Si}^-(h)$ and $V_{Si}^-(k)$, give rise to the V1 ($E_{ZPL} = 1.438$ eV) and V2 ($E_{ZPL} = 1.352$ eV) ZPLs, respectively, $4E \rightarrow 4A_2$ in $V_{Si}^-(h)$ leads to the V1' emission line ($E_{ZPL} = 1.443$ eV) [26]. It is expected that analogously to $V_{Si}^-(h)$, $V_{Si}^-(k)$ should produce a V2' counterpart. So far, and despite many attempts, such a signal has escaped detection.

In Figure 1 we suggest that the excited states of V_{Si}^- possess a pseudo-acceptor character. Accordingly, they consist of an electron strongly bound to V_{Si}^- (red colored downward arrows) whose negative charge secures a weakly bound hole (red circles). This picture, where the $4A_2^*$ state is effectively a double negatively charged vacancy (V_{Si}^{2-}) perturbed by a diffuse hole, is coherent with the fact that the V1 and V2 ZPL energies are very close to the calculated energy difference between the first and

second acceptor levels of V_{Si} in 4H-SiC, $E(= /-) - E(-/0) = 1.4$ eV [18,27] (the small discrepancy being accounted for by a meV-range hole binding energy).

In Ref. [18], a pronounced quadratic Stark shift was shown for the V1' ZPL upon application of a bias to SBD devices along the hexagonal crystallographic axis (0001). Similar behavior was subsequently reported in Ref. [22], but now adding the effect of the electric field applied along the crystallographic basal direction as well. Here, the observation of a two-fold splitting of the V1' line nicely accounted for the double degeneracy of the $4E$ excited state. A Stark shift was also reported for the V1 ZPL [22]. In this case, approximately linear and quadratic shifts were observed when the field was along the main axis and parallel to the basal plane, respectively.

Despite several reports on the calculation of Stark shifts using first principles methods (see for instance Refs. [28] and [29]), this effect has not been addressed for the case of defects in solids. In principle, the combination of reasonable accuracy with the ability to account for the electronic structure of thousands of atoms makes the Kohn-Sham formalism to density functional theory (DFT) the method of choice for such a calculation. However, a major difficulty arises upon the incorporation of a macroscopic field into the Hamiltonian, which desirably should be constructed from first-principles, and mostly uses three-dimensional periodic boundary conditions. Additionally, since we may be dealing with defects with open-shell or metallic-like states, we cannot employ the Berry-phase theory of polarization [30]. While a possible approach involves the incorporation of a sawtooth-shape potential across the periodic cell [31], in the case of a solid, numerical instabilities hamper the calculations due to the superposition of strongly varying potential “teeth” with the atomic potentials. Note that according to the Poisson equation, this method effectively translates into placing two parallel sheets of high charge density with opposite sign within the supercell.

Of course, the above is not an issue for the calculation of molecules within open boundary conditions [28], not even for defects in surfaces and 2D-materials calculated in 3D-supercells [29,32], where the potential “teeth” can be placed within vacuum regions.

Herein, we propose that Stark shifts of defect states in bulk semiconductors can still be evaluated using 3D periodic boundary conditions. To that end, we use periodic slabs separated by thick vacuum layers wherein we place the field “teeth” (Section II). Semi-local and hybrid DFT calculations are employed to investigate the effect of macroscopic fields on the ground and excited states of $V_{\text{Si}}^-(h)$ and $V_{\text{Si}}^-(k)$. We describe a calibration step that should be performed for the case of non-centrosymmetric materials (like 4H-SiC), where a polarization is induced by the asymmetric slab surfaces (Section III). The field dependence of the ${}^4A_2^- \rightarrow {}^4A_2$ zero-phonon transition energies is obtained within the delta-self consistent field approach (Δ -SCF), and the results are compared to experimental data (Section IV). Finally, we draw several remarks and conclusions in Section V.

II. METHODOLOGY

The calculations reported below employ the Kohn-Sham density functional method as implemented in the Quantum ESPRESSO software [33,34]. Importantly, this particular code allows for simultaneously (i) constraining the occupation of the one-electron states (needed for studying ground and excited states of V_{Si}^-), (ii) the use of supercells with arbitrary shape (hexagonal for the case of 4H-SiC), (iii) applying an external periodic electric field, (iv) solving the Kohn-Sham problem self-consistently (subject to the external field and occupancy constraints), (v) the use of charged supercells, and finally (vi) calculating the forces on atoms, relaxing the atomistic structure and finding the total energy. Most results reported below employ the semi-local functional of Perdew, Burke and Ernzerhof (PBE) [35] for describing the many-body electronic interactions. A limited number of calculations were carried out using a non-local hybrid functional as proposed by Song, Yamashita and Hirao [36], and in this case they are flagged with the “Gau-PBE” label. Unfortunately, due to the complexity of the calculations, numerical instabilities frustrated any attempt to obtain self-consistent hybrid-DFT energies for the excited states when subject to electric fields. Hence, calculated transition dipole and polarizability values were found within the PBE level.

The effect of core electrons was accounted for by using norm-conserving pseudopotentials [37,38], whereas the valence was described by a plane-wave basis. Accordingly, energy cut-offs of $E_{\text{cut}}^{\text{wf}} = 680$ eV and $E_{\text{cut}}^{\text{pot}} = 4E_{\text{cut}}^{\text{wf}}$ were found sufficient to provide convergence with respect to the quality of the Kohn-Sham wave functions and potential/density fields, respectively. An external electric field with magnitude \mathcal{E} was applied by adding a sawtooth term to the local potential along the z -coordinate (parallel to the c -axis of 4H-SiC). The slope of the sawtooth potential was $-\mathcal{E}$ across the whole cell, except within a short 0.1 Å interval where it ramped-up to comply with the pe-

riodic boundary conditions. In order to avoid the superposition of artificial charge density singularities (induced by the potential “teeth”) with the SiC electronic states, we employ vacuum-separated 4H-SiC periodic slabs with Si and C surface atoms saturated by hydrogen. The potential “teeth” were therefore placed inside the vacuum region.

Figure 2(a) shows a side view of a hydrogen-terminated slab used in this study with a hexagonal (h) lattice plane at its center. The figure also shows a $V_{\text{Si}}(h)$ defect as indicated by a black dot. An analogous slab with a pseudocubic middle layer was employed to study $V_{\text{Si}}(k)$. The limits of the whole supercell are indicated by the box, which in the case of a pristine slab encloses a total of 300 atoms, including 25 hydrogen atoms on each face. The primitive lattice vectors of bulk 4H-SiC ($\mathbf{a}_1 = \mathbf{a}_2$ and \mathbf{a}_3) and positive direction of the applied electric field are also shown. The lateral size of the supercell was $5a_1 = 15.356$ Å, whereas the axial length was $2a_3 = 20.103$ Å. The vacuum width was about 1/3 of the total length of the supercell. For sampling the Brillouin zone, we used a $2 \times 2 \times 1$ mesh of \mathbf{k} -points for all PBE-level calculations, while Γ -sampling was used for the hybrid Gau-PBE calculations.

The coordinates of the hydrogen atoms saturating the surfaces were optimized in a first step (keeping all SiC atoms locked to their crystalline coordinates). This avoided the appearance of any spurious gap states due to residual strain in the Si-H and C-H bonds. During all subsequent atomic relaxations, the Si-H and C-H surface pairs were kept frozen and only inner layer atoms were allowed to move. Further constraints included the charge state (negative), the one-electron occupancy (for excited states) and the presence of the external field. Tolerances for the largest force during ionic relaxations and for the self-consistent total energy were 0.01 eV/Å and 1 μ eV, respectively. Finally, we computed the zero-phonon line energy, E_{ZPL} , according to the delta-self consistent field (Δ -SCF) method [39–41]. As depicted in Figure 1(c), E_{ZPL} is found from the energy difference between the minimum energy configurations of excited and ground states under the effect of an external field. This approach naturally accounts for any Frank-Condon relaxation contribution, E_{FC} , to the ZPL energies.

III. ELECTRIC FIELD CALIBRATION

The effect of the polarization induced by the asymmetric slab surfaces can be seen on the left-hand-side graph of Figure 2(b), where we plot the xy -averaged electrostatic potential, $\phi_{xy}(z)$, across a pristine slab (red line) and its rolling average, $\phi_{\text{RA}}(z)$, obtained within a window of width $a_3 = 10.05$ Å. The presence of an induced dipole is demonstrated by a non-vanishing slope of ϕ_{RA} within the slab under zero-field conditions ($\mathcal{E} = 0$). Here, any defect introduced into the slab will be subject to a local macroscopic field

$$\mathcal{F} = -d\phi_m/dz, \quad (1)$$

where ϕ_m is the macroscopic electrostatic potential across the slab. In the present context, the expression *macroscopic* refers to a space-averaged quantity that is free of

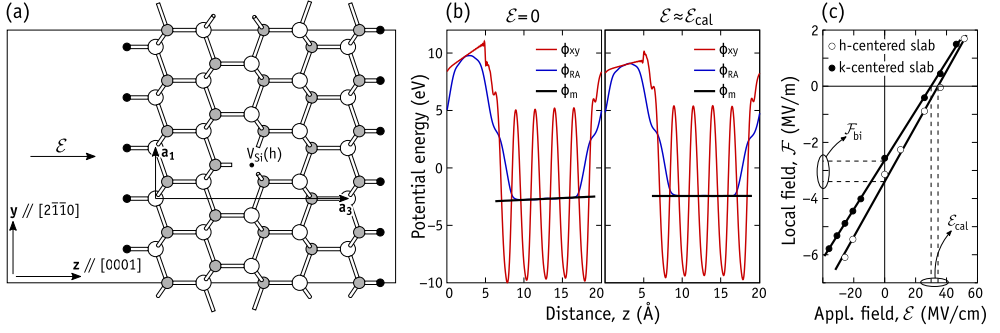


FIG. 2: (a) Side view of a hydrogen-terminated h -plane centered 4H-SiC slab used in this study with a $V_{Si}(h)$ defect located in the middle (black dot). The limits of the supercell are indicated by the box. Primitive lattice vectors (a_1 and a_3), crystallographic directions and positive direction of the applied electric field (\mathcal{E}) are also shown. Silicon, carbon and hydrogen atoms are represented as white, gray and black spheres, respectively. (b) Analysis of the electrostatic potential across a pristine slab for zero electric field (left) and when the applied field is $\mathcal{E} \approx \mathcal{E}_{cal}$ (right, see text). The data presented includes the xy -averaged electrostatic potential energy (ϕ_{xy}), the rolling-averaged potential (ϕ_{RA}) and the macroscopic potential in the slab (ϕ_m) as found from a linear fit to the ϕ_{RA} data near the center of the slab. (c) Calculated local field in the middle of h - and k -centered pristine slabs against the applied electric field, $\mathcal{F}(\mathcal{E})$. Best linear fits to the data are also shown (see Eq. 2).

atomic-scale variations. We found ϕ_m from a linear fit to ϕ_{RA} in the central region of the slab (straight black line in Figure 2(b)).

To first order (linear media), a change in an externally applied electric field ($\Delta\mathcal{E} = \mathcal{E} - \mathcal{E}_0$) induces a proportional variation in the local field within the slab ($\Delta\mathcal{F} = \mathcal{F} - \mathcal{F}_0$),

$$\mathcal{F} - \mathcal{F}_0 = \frac{\mathcal{E} - \mathcal{E}_0}{\epsilon}, \quad (2)$$

where \mathcal{E}_0 and \mathcal{F}_0 are arbitrary and ϵ is the effective slab screening constant. For the sake of convenience we rewrite the above as

$$\mathcal{F} = \frac{\mathcal{E}}{\epsilon} + \mathcal{F}_{bi}, \quad (3)$$

where we set $\mathcal{E}_0 = 0$ and $\mathcal{F}_0 = \mathcal{F}_{bi}$, the latter representing the *built-in* field induced across the slab mentioned above. Both ϵ and \mathcal{F}_{bi} can be found by linear fitting of Eq. 3 to a set of $(\mathcal{E}, \mathcal{F})$ data points from defect-free slab calculations. Importantly, we can calibrate the applied field, that is, we can find the field $\mathcal{E}_{cal} = -\epsilon\mathcal{F}_{bi}$ which neutralizes the built-in field, as well as its effect on defects introduced in the slab. The result of this condition is shown on the right-hand-side plot in Figure 2(b). Of course, calibration of \mathcal{E} is only necessary when the slab surfaces induce an internal field (e.g., slabs made of non-centrosymmetric materials). Although not unique, the procedure can be summarized by the following steps:

1. From a zero-field calculation (using a pristine slab), estimate the spurious built-in field as $\tilde{\mathcal{F}}_{bi} \approx -d\phi_m/dz$;
2. Find an estimate for \mathcal{E}_{cal} as $\tilde{\mathcal{E}}_{cal} = -\epsilon_s\tilde{\mathcal{F}}_{bi}$, where ϵ_s is the static dielectric constant of the material. For SiC we employ $\epsilon_s = 10$;

3. Chose a local field range $\pm\delta\mathcal{F}$ and corresponding applied field range $\tilde{\mathcal{E}}_{cal} \pm \epsilon_s\delta\mathcal{F}$ (see below for further details);
4. Calculate from first-principles a set of $(\mathcal{E}, \mathcal{F})$ data points within the selected \mathcal{E} -field range;
5. Fit Eq. 3 to the calculated data points, extract \mathcal{F}_{bi} and ϵ , and finally obtain $\mathcal{E}_{cal} = -\epsilon\mathcal{F}_{bi}$.

After obtaining the values of \mathcal{F}_{bi} and ϵ (for h - and k -centered slabs), we are ready to introduce a silicon vacancy into the slab and probe its response to an arbitrary field \mathcal{F} . For that, we set the applied field to $\mathcal{E} = \epsilon(\mathcal{F} - \mathcal{F}_{bi})$ and monitor the Stark shift using a second-order expansion in the local field,

$$\Delta E_{ZPL} = -\Delta\mu\mathcal{F} - \frac{1}{2}\Delta\alpha\mathcal{F}^2, \quad (4)$$

where $\Delta\mu$ and $\Delta\alpha$ are the respective changes in dipole moment and polarizability between the excited and ground states [42]. Although in general the dipole moment and polarizability of a defect state are, respectively, vectorial and second-rank tensorial quantities, Eq. 4 is reduced to a scalar form, reflecting the fact that we will analyze the Stark shifts for fields along the c -axis of the crystal.

Figure 2(c) shows the best linear fits to the calculated $\mathcal{F}(\mathcal{E})$ data points obtained for h -centered and k -centered pristine slabs. The built-in fields in the slabs, as found from the fittings to Eq. 3, are $\mathcal{F}_{bi} = -3.4$ MV/m and -2.6 MV/m (horizontal dashed lines), while the slab dielectric constants are $\epsilon = 10.1$ and 11.4 for the h - and k -centered slabs, respectively. The calculated values of ϵ are rather close to the measured static dielectric component parallel to the c -axis for bulk 4H-SiC ($\epsilon_{||} = 10.03$ [43]). We emphasize that the geometry of the inner layers of the slabs are fully relaxed for each value of \mathcal{E} . This

implies that the screening response accounts for both electronic polarization (ion-clamped conditions) as well as for ionic polarization effects.

The bare field that has to be imposed in order to offset the local field to zero is $\mathcal{E}_{\text{cal}} = -\epsilon\mathcal{F}_{\text{ind}} = 34.3$ MV/m and 29.6 MV/m for h - and k -slabs, respectively (vertical dashed lines in Figure 2(c)). Hence, if we consider probing V_{Si}^- defects with fields $|\mathcal{F}| \lesssim 10$ MV/m, the applied field \mathcal{E} will be in the range $|\mathcal{E} - \mathcal{E}_{\text{cal}}| \lesssim 100$ MV/m.

Before moving on to the results section, we leave a few remarks regarding accuracy issues. According to experiments [18,22], local fields of up to about $|\mathcal{F}| \sim 50$ MV/m led to Stark shifts of the V1 and V1' lines in the meV range. These correspond to changes in the electric dipole and polarizability of the order of $\Delta\mu \sim 1$ D and $\Delta\alpha \sim 10^3$ Å³. From the point of view of conducting the calculations, the convergence tolerance of the total energy should be tight enough as to provide us with a sub-0.1 meV numerical error in energy differences. Among the most important issues to take care of, we single out (i) keeping the Si-H and C-H units frozen during all calculations and (ii) when finding the ground state of a defect under a particular field, one should start the self-consistent calculation with the solution found from a previous calculation, ideally from one with a close electric field.

Another important issue is to make sure that electrons do not *leak out* from nor get *poured into* defect states upon the application of the field (ex. into surface states or into excited states). This can be inspected by closely monitoring the population of the band structure, to ensure that the V_{Si}^- defect state ordering envisaged in Figure 1(a) is maintained throughout the calculations.

Due to electronic confinement along the direction perpendicular to the slab surfaces, the calculated band-gap (within PBE) is $E_g = 2.6$ eV. This is considerably larger than the gap width of bulk 4H-SiC ($E_g = 2.0$ eV using the same theory level), but closer to the experimental figure (3.2 eV). This artificial, albeit convenient, effect is expected to reduce the overestimated and detrimental resonances between gap states and crystalline states that typically affect local and semi-local calculations.

Single determinant calculations of E_{ZPL} values usually yield absolute accuracies of around ~ 0.1 eV [44]. This figure is at least two orders of magnitude larger than the largest Stark shifts observed for V1/V1' and V2 lines [18,22]. However, we are actually interested in the shift ΔE_{ZPL} , whose calculation involves the energy difference between two systems which differ only by a slight perturbation of the electron density, due to a small change in the electric field magnitude. As for other differential quantities, such as vibrational mode frequencies with typical error bars of a few tens of cm⁻¹, the geometries and electronic structure of the differentiating states remain very similar and the results benefit from cancellation of systematic errors (e.g., due to finite size effects or basis incompleteness).

Finally, the nearly linear behavior of $\mathcal{F}(\mathcal{E})$ in Figure 2(c) and the screening response of the slabs to external fields (showing values of ϵ close to the experimental figure), give us confidence in the method.

IV. RESULTS AND DISCUSSION

We now report on the application of the above methodology for the case of V_{Si} in 4H-SiC. After calibration of the field, we calculated the change in the zero-phonon transition energies with the local field amplitude. The one-electron occupancy was kept fixed to enforce the electronic configurations of the $S = 3/2$ states of V_{Si}^- (see Figure 1(a)). The optical transitions referred to as V1/V1' and V2/V2', respectively attributed to $V_{\text{Si}}^-(h)$ and $V_{\text{Si}}^-(k)$, are spin-conserving and involve changes in the occupancy of the minority-spin channel. Although V2' has not been detected experimentally, possibly due to a lifetime- or dynamical-related broadening effect or overlap with the phonon-side bands of V1 and V2, we still consider it in our analysis for the sake of completeness.

V1 and V2 arise from ${}^4A_2^* \rightarrow {}^4A_2$ relaxations, whereas V1' and V2' involve ${}^4E \rightarrow {}^4A_2$ transitions. The ground state organizes as ${}^4A_2 \equiv \Gamma_v(\uparrow\downarrow) + [a_1(\uparrow) + e(x\uparrow, y\uparrow)]$, while first and second excited states are ${}^4A_2^* \equiv \Gamma_v(\uparrow\circ) + [a_1(\uparrow\downarrow) + e(x\uparrow, y\uparrow)]$ and ${}^4E \equiv \Gamma_v(\uparrow\circ) + [a_1(\uparrow) + e(x\uparrow\downarrow, y\uparrow)]$, respectively [45]. In this notation, localized states in the forbidden gap are enclosed within square brackets, upward and downward arrows stand for occupied spin-up and spin-down states, respectively, while the small circle refers to the lack of an electron which has been promoted to a higher-lying state. Doublet states are resolved into x and y components. The label Γ_v identifies a state that results from mixing between valence band states with a resonating $a_{1,R}$ state of the defect (see Figure 1(a)). In the excited state configurations, Γ_v holds a diffuse hole overlapping the vacancy. In practice, Γ_v is taken as the highest occupied valence band state of the pristine slab, i.e., just below a_1 in the energy scale. Notably, the V1' and V2' luminescent transitions involve a degenerate and open-shell initial (excited) state. In this case, a Jahn-Teller distortion is expected to take place. To account for that, we allowed the structures to relax without symmetry constraints. The distortion is not affected by the electric field — the latter is invariant with respect to all operations of the C_{3v} point group of the V_{Si} defect. Further details of this problem have been addressed elsewhere [26] and fall outside the scope of the present work.

Table I reports the calculated ZPL energies for the ${}^4A_2^* \rightarrow {}^4A_2$ and ${}^4E \rightarrow {}^4A_2$ transitions of $V_{\text{Si}}^-(h)$ and $V_{\text{Si}}^-(k)$ in the slabs. The calculations reported in Table I were all carried out with $\mathcal{F} = 0$, i.e., the field in the vacuum layer was $\mathcal{E} = \mathcal{E}_{\text{cal}}$. Quantities outside parentheses were obtained according to the Δ -SCF method using fully relaxed structures. On the other hand, results within parentheses were found from the energy difference of two spin-down Kohn-Sham eigenvalues of the 4A_2 ground state, which involve the electron exchange during the transition. Unfortunately, self-consistency of the Kohn-Sham problem proved exceedingly difficult to achieve for excited state calculations. While this was still possible for the lower energy ${}^4A_2^* \rightarrow {}^4A_2$ transitions, ${}^4E \rightarrow {}^4A_2$ transition energies could not be obtained, except when using the Kohn-Sham energies from V_{Si}^- ground states alone (quantities enclosed in parentheses in Table I). Within the latter

TABLE I: Calculated (Calc.) excited-to-ground state relaxation energies E_{ZPL} for the ${}^4A_2^* \rightarrow {}^4A_2$ and ${}^4E \rightarrow {}^4A_2$ transitions of $V_{Si}^-(h)$ and $V_{Si}^-(k)$. Quantities outside parentheses were obtained from total energies of fully relaxed defects in the ground and excited states of V_{Si}^- . Quantities within parentheses were found from the Kohn-Sham eigenvalues of the respective ground state. Assignments of V1/V1' and V2 to the experimental data (Exp.) are also included [46]. ND stands for not detected. All values are in eV.

Defect	Transition	Calc.	Exp.	ZPL
$V_{Si}^-(h)$	${}^4A_2^* \rightarrow {}^4A_2$	1.32 (1.38)	1.438	V1
	${}^4E \rightarrow {}^4A_2$	(1.44)	1.443	V1'
$V_{Si}^-(k)$	${}^4A_2^* \rightarrow {}^4A_2$	1.26 (1.35)	1.352	V2
	${}^4E \rightarrow {}^4A_2$	(1.39)	ND	V2'

approach, we found a ~ 50 meV monoclinic splitting of the two degenerate ${}^4E \rightarrow {}^4A_2$ transitions due to Jahn-Teller unfolding of the e -states. Table I reports only the lower transition energy counterpart.

The experimental values from Ref. [46] are shown next to the calculations in Table I. In general, the calculated figures match rather well the experimental data and they differ by less than 10 %. As discussed at the end of Section III, this agreement benefits from the artificial opening of the band gap due to the slab boundary conditions. Notably as well, in agreement with the experiments, all calculated ZPL energies related to $V_{Si}(h)$ are invariably higher than the analogous quantities for $V_{Si}(k)$. Hybrid-DFT calculations of the ${}^4A_2^* \rightarrow {}^4A_2$ transitions using the Gau-PBE functional overestimate experimental data by about 0.2 eV. For the sake of comparison, we calculated selected ZPL transition energies using bulk orthorhombic (hexagonal) supercells without vacuum comprising 96 (400) atoms. Accordingly, the $V_{Si}(h)$ transition energies were 1.414 eV (1.412 eV) for the ${}^4A_2^* \rightarrow {}^4A_2$ transition, and 1.428 eV for ${}^4E \rightarrow {}^4A_2$. Comparing with the literature, our zero-field transition energies land slightly below other computed values [25,26], but show similar agreement (below ~ 10 % difference) with experiment. Indeed, the slight underestimation of experimental data found herein (see Table I) can be attributed to the use of a semi-local functional. Ref. [25] reported hybrid-level values of 1.541 eV for V1 and 1.443 eV for V2, the overestimation likely arising from the use of the HSE06 functional. Ref. [26] computed ZPL energies of 1.450 eV and 1.385 eV for V1 and V2, respectively, but reported higher transition energies for the second electronic ${}^4E \rightarrow {}^4A_2$ excitations at 1.792 eV and 1.953 eV, respectively, for V1' and V2'.

Regarding the Kohn-Sham based results, besides being derived from quantities with a weak physical meaning, they do not account for a small Franck-Condon relaxation energy in the excited state. This explains why they slightly overestimate their Δ -SCF counterparts. Despite the insufficiencies, they reproduce the observed V1 and V2 energy ordering and they allow us to suggest that the V2' transition energy is a few tens of meV below V1' and close to V1.

Figure 3 represents the field dependence of the ${}^4A_2^* \rightarrow {}^4A_2$ transitions of V_{Si}^- at h - (Figure 3(a)) and k -sites (Fig-

ure 3(b)) as calculated using the Δ -SCF method at PBE level. The solid lines represent the best fits of Eq. 4 to the first-principles data (black circles). Considering the magnitude of the fields applied, approximately linear Stark shifts were found for both $V_{Si}(h)$ and $V_{Si}(k)$. A strictly linear Stark effect is often not observed in non-centrosymmetric defects. A notable example is the NV center in diamond [20]. The weak parabolic dependence of ΔE_{ZPL} on \mathcal{F} could be explained by field-induced couplings of defect and crystalline states [42]. From the fittings to the data we found variations of the electric dipole moment and polarizability as $\Delta\mu = 1.46$ D and $\Delta\alpha = -640 \text{ \AA}^3$ for $V_{Si}(h)$, and $\Delta\mu = 3.92$ D and $\Delta\alpha = -920 \text{ \AA}^3$ for $V_{Si}(k)$ (1 D = 3.34×10^{30} C m and $1 \text{ \AA}^3 = 4\pi\epsilon_0 \times 10^{-28} \text{ C m}^2 \text{ V}^{-1}$). The relative error bars for dipole and polarizability changes are less than 1 % and about 10 %, respectively. We note that because of the nearly linear dependence of $E_{ZPL}(\mathcal{F})$, the offset applied to the field of $\mathcal{F}_{bi} \approx -3$ MV/m during the calibration step (see Sec. III) has little impact on the results.

Our results indicate little contribution from the polariz-

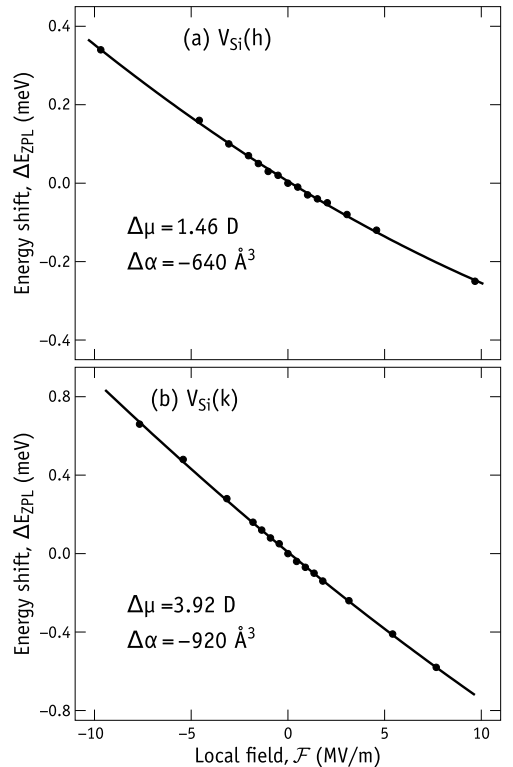


FIG. 3: Calculated Stark shift (black circles) of the ${}^4A_2^* \rightarrow {}^4A_2$ zero-phonon transition involving the decay from the first excited state into the ground state of (a) $V_{Si}(h)$ and (b) $V_{Si}(k)$. Solid lines represent the best fits of Eq. 4 to the data, from which the transition dipole moment and polarizability changes ($\Delta\mu$ and $\Delta\alpha$, respectively) were extracted.

ability change to the Stark effect, instead hinting towards a dominance of the dipole moment difference between excited and ground states. While a small $\Delta\alpha$ value (which leads to an approximately linear character) has been observed for V1 with the field along the c -axis [22], the calculated value of $\Delta\mu$ for $V_{\text{Si}}(h)$ overestimates the respective measured figure for V1 by about a factor of 10.

We can only hypothesize several reasons for the above discrepancy. Firstly, it is possible that the slab employed is too thin (additional SiC layers should be included) or the vacuum width should be increased. Further, the semi-local treatment of the many-body electronic exchange correlation interactions could be insufficient to accurately describe the difference in coupling of the electric field to the 4A_2 and $^4A_2^*$ electronic configurations. Another possibility is the inherent inaccuracy of the simple single-determinant wave functions to describe excited states. These are among the issues that need to be addressed in the future in order to further investigate the applicability of the present method for the calculation of Stark shifts of electronic transitions for defects in semiconductors.

In comparison to other centers, we note that the calculated $\Delta\mu$ values are close to those observed for the divacancy in 4H-SiC ($\Delta\mu \approx 2$ D) [15] and to the NV center in diamond ($\Delta\mu \approx 0.8$ -1.5 D) [20,21]. Regarding the polarizability, we know that small molecules [47] and quantum dots [48] usually yield positive values for $\Delta\alpha$. This is in line with the view that excited states are generally nodal and therefore more polarizable than ground states. However, we found $\Delta\alpha < 0$ for the $^4A_2^* \rightarrow ^4A_2$ transitions of V_{Si}^- in 4H-SiC. Considering the error bars of the measurements, we cannot consider a disagreement with the observations [22]. As a matter of fact, negative values for $\Delta\alpha$ are also possible for defects in semiconductors, one prominent case being NV in diamond [20].

Finally, we should keep in mind that the theoretical approximations and limitations discussed above are not exclusively accountable for the discrepancies between theory and measurements. Several difficulties affect the measurement of Stark shifts as well. Perhaps the most severe is the determination of the electric field that is actually acting on a specific defect. For instance, the often used Lorentz local field approximation may turn out to be inadequate, or the complexity of the sample structure combined with the scatter of the defect distribution can easily frustrate an accurate quantification of $\Delta\mu$ and $\Delta\alpha$.

V. CONCLUDING REMARKS

We present a first-principles methodology to calculate Stark shifts of electronic transitions of defects in semiconductors using periodic boundary conditions. The method is applied to the silicon vacancy in 4H-SiC, with the electric field response of its photoluminescence transition energies being investigated by density functional theory within the Δ -SCF method.

Our approach involves the use of a periodic supercell

comprising a semiconductor slab adjacent to a vacuum layer. The surfaces of the slab were passivated by hydrogen termination, and an external electric field with variable amplitude was applied along the surface normal (in parallel to the (0001)- or c -axis). To this end, we added a sawtooth potential to the Hamiltonian, placing the potential “teeth” in the vacuum region to avoid the superposition of induced charge density singularities with the electronic states of the slab.

For the case of non-centrosymmetric materials (like 4H-SiC), the presence of inequivalent surfaces on the 4H-SiC slab induce a built-in field. A calibration of the external field is carried out to neutralize the built-in field and find the zero-field condition in the slab bulk.

The calculated zero-field transition energies for $V_{\text{Si}}(h)$ and $V_{\text{Si}}(k)$ account for the experimental data (V1/V1' and V2 PL lines) within an error bar of about 0.1 eV. The energy ordering of the transitions are also in line with the measurements. Such an agreement exceeds the expectations for the present level of theory — typical semi-local approximated exchange correlation functionals underestimate excitation energies by a factor of 0.5-0.6. We suggest that the agreement artificially profits from the opening of the band gap due to electronic confinement in the slab terminated by hydrogen and vacuum.

Regarding the Stark shifts, within the range of electric fields considered ($|\mathcal{F}| < 10$ MV/m), we found approximately linear Stark shifts for the $^4A_2^* \rightarrow ^4A_2$ transitions of both $V_{\text{Si}}(h)$ and $V_{\text{Si}}(k)$. These corresponded to transition dipole changes of $\Delta\mu = 1.46$ D and $\Delta\mu = 3.92$ D, respectively, with a numerical error bar below 1 %. While an approximately linear Stark shift was observed for V1 [22], the calculated $\Delta\mu$ overestimates the measurement by about a factor of 10. We discuss several reasons which could affect the quality of the theory and should be addressed in the future (for instance, slab geometry and exchange-correlation description level), but also aspects that impact on the interpretation of the observations, in particular the knowledge of the magnitude and direction of the field directly affecting the defects.

Acknowledgments

Financial support was kindly provided by the Research Council of Norway and the University of Oslo through the frontier research project FUNDAMeNT (no. 251131, FriPro ToppForsk-program). The Research Council of Norway is acknowledged for the support to the Norwegian Micro- and Nano-Fabrication Facility, NorFab, project number 245963. Some of the computations were performed on resources provided by UNINETT Sigma2 - the National Infrastructure for High Performance Computing and Data Storage in Norway. J.C. thanks the support of the i3N project, Refs. UIDB/50025/2020 and UIDP/50025/2020, financed by the Fundação para a Ciência e a Tecnologia in Portugal and support by the NATO SPS programme (Project No. 985215).

* Electronic address: m.e.bathen@fys.uio.no

- ¹ J. M. Taylor, P. Cappellaro, L. Childress, L. Jiang, D. Budker, P. R. Hemmer, A. Yacoby, R. Walsworth, and M. D. Lukin, *Nature Physics* **4**, 810 (2008).
- ² M. W. Doherty, N. B. Manson, P. Delaney, F. Jelezko, J. Wrachtrup, and L. C. L. Hollenberg, *Physics Reports* **528**, 1 (2013).
- ³ H. Bernien, B. Hensen, W. Pfaff, G. Koolstra, M. S. Blok, L. Robledo, T. H. Taminiau, M. Markham, D. J. Twitchen, L. Childress, et al., *Nature* **497**, 86 (2013).
- ⁴ P. E. Barclay, K. C. Fu, C. Santori, A. Faraon, and R. G. Beausoleil, *Physical Review X* **1**, 011007 (2011).
- ⁵ Y. Shen, T. M. Sweeney, and H. Wang, *Physical Review B* **77**, 033201 (2008).
- ⁶ A. Faraon, C. Santori, Z. Huang, V. M. Acosta, and R. G. Beausoleil, *Physical Review Letters* **109**, 033604 (2012).
- ⁷ S. Castelletto, L. Rosa, and B. C. Johnson, in *Advanced Silicon Carbide Devices and Processing* (InTech, 2015).
- ⁸ M. Widmann, S.-Y. Lee, T. Rendler, N. T. Son, H. Fedder, S. Paik, L.-P. Yang, N. Zhao, S. Yang, I. Booker, et al., *Nature Materials* **14**, 164 (2014).
- ⁹ H. Kraus, V. A. Soltamov, D. Riedel, S. Văth, F. Fuchs, A. Sperlich, P. G. Baranov, V. Dyakonov, and G. V. Astakhov, *Nature Physics* **10**, 157 (2014).
- ¹⁰ D. Simin, H. Kraus, A. Sperlich, T. Ohshima, G. V. Astakhov, and V. Dyakonov, *Physical Review B* **95**, 161201(R) (2017).
- ¹¹ W. F. Koehl, B. B. Buckley, F. J. Heremans, G. Calusine, and D. D. Awschalom, *Nature* **479**, 84 (2011).
- ¹² D. J. Christle, A. L. Falk, P. Andrich, P. V. Klimov, J. Ul Hassan, N. T. Son, E. Jánzén, T. Oshima, and D. D. Awschalom, *Nature Materials* **14**, 160 (2015).
- ¹³ S. Castelletto, B. C. Johnson, V. Ivády, N. Stavrias, T. Umeda, A. Gali, and T. Oshima, *Nature Materials* **13**, 151 (2014).
- ¹⁴ G. Wolfowicz, C. P. Anderson, A. L. Yeats, S. J. Whiteley, J. Niklas, O. G. Poluektov, F. J. Heremans, and D. D. Awschalom, *Nature Communications* **8**, 1876 (2017).
- ¹⁵ C. F. de las Casas, D. J. Christle, J. Ul Hassan, T. Ohshima, N. T. Son, and D. D. Awschalom, *Applied Physics Letters* **111**, 262403 (2017).
- ¹⁶ M. Widmann, M. Niethammer, D. Y. Fedyanin, I. A. Khramtsov, T. Rendler, I. D. Booker, J. Ul Hassan, N. Morioka, Y.-C. Chen, I. G. Ivanov, et al., *Nano Letters* **19**, 7173 (2019).
- ¹⁷ C. P. Anderson, A. Bourassa, K. C. Miao, G. Wolfowicz, P. J. Mintun, A. L. Crook, H. Abe, J. Ul Hassan, N. T. Son, T. Ohshima, et al., *Science* **366**, 1225 (2019).
- ¹⁸ M. E. Bathen, A. Galeckas, J. Mütting, H. M. Ayedh, U. Grossner, J. Coutinho, Y. K. Frodason, and L. Vines, *Submitted* (2019).
- ¹⁹ J. Stark, *Annalen der Physik* **50**, 489 (1914).
- ²⁰ P. Tamarat, T. Gaebel, J. R. Rabau, M. Khan, A. D. Greentree, H. Wilson, L. C. L. Hollenberg, S. Praver, P. Hemmer, F. Jelezko, et al., *Physical Review Letters* **97**, 083002 (2006).
- ²¹ V. M. Acosta, C. Santori, A. Faraon, Z. Huang, K.-M. C. Fu, A. Stacey, D. A. Simpson, K. Ganesan, S. Tomljenovic-Hanic, A. D. Greentree, et al., *Physical Review Letters* **108** (2012).
- ²² M. Rühl, L. Bergmann, M. Krieger, and H. B. Weber, *Nano Letters* **20**, 658 (2020).
- ²³ K. C. Miao, A. Bourassa, C. P. Anderson, S. J. Whiteley, A. L. Crook, S. L. Bayliss, G. Wolfowicz, G. Thiering, P. Udvarhelyi, V. Ivády, et al., *Science Advances* **5** (2019).
- ²⁴ N. Mizuochi, S. Yamasaki, H. Takizawa, N. Morishita, T. Ohshima, H. Itoh, T. Umeda, and J. Isoya, *Physical Review B* **72**, 235208 (2005).
- ²⁵ V. Ivády, J. Davidsson, N. T. Son, T. Ohshima, I. A. Abrikosov, and A. Gali, *Physical Review B* **96**, 161114(R) (2017).
- ²⁶ P. Udvarhelyi, G. Thiering, N. Morioka, C. Babin, F. Kaiser, D. Lukin, T. Ohshima, J. Ul Hassan, N. T. Son, J. Vučković, et al., *Physical Review Applied* **13**, 054017 (2020).
- ²⁷ T. Hornos, A. Gali, and B. G. Svensson, *Materials Science Forum* **679-680**, 261 (2011).
- ²⁸ B. F. Garrett, I. Azuri, L. Kronik, and J. R. Chelikowsky, *The Journal of Chemical Physics* **145**, 174111 (2016).
- ²⁹ G. Noh, D. Choi, J.-H. Kim, D.-G. Im, Y.-H. Kim, H. Seo, and J. Lee, *Nano Letters* **18**, 4710 (2018).
- ³⁰ I. Souza, J. Íñiguez, and D. Vanderbilt, *Physical Review Letters* **89**, 117602 (2002).
- ³¹ K. Kunc and R. Resta, *Physical Review Letters* **51**, 686 (1983).
- ³² S. Selçuk and A. Selloni, *The Journal of Chemical Physics* **141**, 084705 (2014).
- ³³ P. Giannozzi, S. Baroni, N. Bonini, M. Calandra, R. Car, C. Cavazzoni, D. Ceresoli, G. L. Chiarotti, M. Cococcioni, and I. Dabo, *Journal of Physics: Condensed Matter* **21**, 395502 (2009).
- ³⁴ P. Giannozzi, O. Andreussi, T. Brumme, O. Bunau, M. Buongiorno Nardelli, M. Calandra, R. Car, C. Cavazzoni, D. Ceresoli, and M. Cococcioni, *Journal of Physics: Condensed Matter* **29**, 465901 (2017).
- ³⁵ J. P. Perdew, K. Burke, and M. Ernzerhof, *Physical Review Letters* **77**, 3865 (1996).
- ³⁶ J.-W. Song, K. Yamashita, and K. Hirao, *Journal of Chemical Physics* **135**, 071103 (2011).
- ³⁷ D. R. Hamann, *Physical Review B* **88**, 085117 (2013).
- ³⁸ M. J. van Setten, M. Giantomassi, E. Bousquet, M. J. Verstraete, D. R. Hamann, X. Gonze, and G.-M. Rignanese, *Computer Physics Communications* **226**, 39 (2018).
- ³⁹ J. C. Slater, *Quantum theory of molecules and solids*, vol. 1-4 (McGraw-Hill, New York, 1963-1974).
- ⁴⁰ A. Gali, E. Jánzén, P. Deák, G. Kresse, and E. Kaxiras, *Physical Review Letters* **103**, 186404 (2009).
- ⁴¹ J. R. Maze, A. Gali, E. Togan, Y. Chu, A. Trifonov, E. Kaxiras, and M. D. Lukin, *New Journal of Physics* **13**, 025025 (2011).
- ⁴² A. M. Stoneham, *Theory of Defects in Solids: Electronic Structure of Defects in Insulators and Semiconductors* (Clarendon Press, 2001).
- ⁴³ L. Patrick and W. J. Choyke, *Physical Review B* **2**, 2255 (1970).
- ⁴⁴ J. Davidsson, V. Ivády, R. Armiento, N. T. Son, A. Gali, and I. A. Abrikosov, *New J. Phys.* **20**, 023035 (2018).
- ⁴⁵ A. Gali, *Materials Science Forum* **717-720**, 255 (2012).
- ⁴⁶ M. Wagner, B. Magnusson, W. M. Chen, E. Jánzén, E. Sörman, C. Hallin, and J. L. Lindström, *Physical Review B* **62**, 16555 (2000).
- ⁴⁷ C. Brunel, P. Tamarat, B. Lounis, J. C. Woehl, and M. Orrit, *J. Phys. Chem. A* **103**, 2429 (1999).
- ⁴⁸ S. A. Empedocles and M. G. Bawendi, *Science* **278**, 2114 (1997).

Paper III

Strain modulation of Si vacancy quantum emission from SiC micro- and nanoparticles

C. G. Vásquez, M. E. Bathen, A. Galeckas, C. Bazioti, K. M. Johansen, D. Maestre, A. Cremades, Ø. Prytz, A. M. Moe, A. Yu. Kuznetsov, L. Vines

Accepted in *Nano Letters* (2020).



Strain modulation of Si vacancy quantum emission from SiC micro- and nanoparticles

G. C. Vásquez^{a*,**}, M. E. Bathen^a, A. Galeckas^a, C. Bazioti^a, K. M. Johansen^a, D. Maestre^b,
A. Cremades^b, Ø. Prytz^a, A. M. Moe^c, A. Yu. Kuznetsov^a, L. Vines^a

^a Centre for Materials Science and Nanotechnology, University of Oslo, N-0318 Oslo, Norway

^b Departamento de Física de Materiales, Facultad de CC. Físicas, Universidad Complutense de Madrid, 28040, Madrid, Spain

^c Washington Mills AS, NO-7300 Orkanger, Norway

*Present address: Jülich Centre for Neutron Science (JCNS-I), Forschungszentrum Jülich GmbH, Leo-Brandt-Straße, 52425 Jülich, Germany

**email: c.vasquez@fz-juelich.de

ABSTRACT

Single-photon emitting point defects in semiconductors have emerged as strong candidates for future quantum technology devices. Typically, these phenomena are studied in bulk materials, however, in the present work we exploit crystalline particles to investigate relevant defect localizations, emission tuning and waveguiding. Specifically, emission from 6H-SiC micro- and nanoparticles ranging from 100 nm to 5 μm in size is collected using cathodoluminescence (CL), and we monitor signals attributed to the Si vacancy (V_{Si}) as a function of its location. Clear shifts in the emission wavelength are found for emitters localized in the particle center and at the edges. By comparing spatial CL maps with strain analysis carried out in transmission electron microscopy, we attribute the emission shifts to compressive strain of 2-3% along the particle a -direction. Thus, embedding V_{Si} qubit defects within SiC nanoparticles offers an interesting and versatile opportunity to tune single-photon emission energies, while simultaneously ensuring ease of addressability via a self-assembled SiC nanoparticle matrix.

KEYWORDS: Color centers, SiC, cathodoluminescence, micro- and nanoparticles, strain tuning

Point defects in semiconductors present a viable route for realization of several different quantum technologies, including quantum sensing, computing and communication. Common to these is the need for single-photon emitters (SPEs), which convey information on the local environment surrounding the emitter, interconnect qubits and sections in a quantum computing environment, provide a means for secure communication, and enable spin-photon entanglement in solid-state systems [1]. However, SPEs are vulnerable to local inhomogeneities, and obtaining high-fidelity and completely identical photons on-demand is a proven challenge.

The benchmark quantum candidate is the nitrogen-vacancy center in diamond, but its zero-phonon line (ZPL) emission is relatively low although it can be improved by coupling to microcavities [2]. Meanwhile, silicon carbide (SiC) in its different polytypes can boast of superior nanostructuring capabilities and waveguide integration potential compared to diamond, and hosts a plethora of promising color centers [3], including the Si vacancy (V_{Si}). Stable emission from V_{Si} centers is important for many SiC-based quantum technologies [3–6], however, the methods for integration of quantum emitters in electrically and optically controlled devices are still immature [4].

Recently, spectral tuning of single-photon emission via the Stark effect was demonstrated for the V_{Si} [7,8] and divacancy ($V_C V_{Si}$) [9,10] in 4H-SiC, via fabrication of Schottky barrier or p-i-n diodes. Electrical tuning allows the inhomogeneous broadening of SPEs to be circumvented, and provides a means to tailor the photon energy to each specific application. Alternatively, the challenge of obtaining identical photons can be tackled from a different angle, by exploiting the strain arising from local imperfections. Strain has been shown to affect emission from V_{Si} in 4H and 6H-SiC [11], and theoretically predicted shifts in the ZPL

energy for V_{Si} [12] and $V_C V_{Si}$ [13] are in the range of several meV, exceeding that achieved via Stark tuning.

Micro- and nanoparticle engineering can be an alternative to traditional etching methods, allowing for large-scale fabrication of SPEs ready for further processing. For example, SiC-based composites with self-assembly ability can be deposited, similar to the two-dimensional single-photon arrays achieved by Radulaski *et al.* in 4H-SiC [14], with the advantage of flexible substrates and scalability. Nevertheless, an improved understanding of how the V_{Si} defects are affected in their micro- and nanocrystal host environment is important for the success of such advancements.

Herein, we investigate the effect of local strain on emission from silicon vacancies embedded within proton-irradiated SiC micro- and nanocrystals of predominantly the 6H polytype by combining scanning electron microscopy (SEM) with hyperspectral cathodoluminescence (CL) measurements. We reveal that the V_{Si} emission energy can be tuned within 10-20 meV depending on its specific position within the particle as well as on the shape and size. By comparing the SEM-CL data to transmission electron microscopy (TEM) strain maps, we reveal correlating compressive strain variations along the particle *a*-axis, thereby unambiguously identifying these local strain variations as the cause for the V_{Si} emission tuning, controlled by the local nano- and microcrystal morphology.

We study SiC micro- and nanoparticles provided by Washington Mills Co. and deriving from ultra-high purity silicon carbide powder, specially manufactured to reduce impurities to extremely low levels of < 5 ppm [15]. These powder species (having an average size of 2 and $5\ \mu\text{m}$) were deposited and mechanically dispersed on flat Si substrates, irradiated with 1.8 MeV protons to a fluence of $8 \times 10^{13}\ \text{cm}^{-2}$ to form V_{Si} centers, and annealed at 300 °C for 30 min in air to clear out interstitial defects (similar to that performed in Ref. [7]). The particle

morphology and emission properties were studied in a SEM-CL system at room temperature (RT) and 80 K, using acceleration voltages from 5 to 10 kV and probing currents of 100-200 pA. To investigate the structural composition of the powder, we performed micro-Raman analysis using a 325-nm He-Cd laser, and supplemented our findings with (Scanning) Transmission Electron Microscopy investigations at 300 kV. Finally, Geometric Phase Analysis (GPA) was applied on high-resolution images for nanoscale strain measurements. See the Supporting Information for further details.

The SiC powder is composed of particles of sizes ranging from approximately 5 μm down to a few hundred nm as shown by the SEM micrograph in Figure 1(a). Using a combination of CL and micro-Raman spectroscopy, we identify and determine the main spectral signatures of various SiC polytypes that are present in the initial powder. Figure 1(b) shows micro-Raman spectra of individual or small agglomerates of particles identifying the 6H, 15R and 4H SiC polytypes [16,17], with the 6H polytype being predominant over all measured particles. Additionally, the Raman spectra show a shoulder at $\sim 796\text{ cm}^{-1}$ that can be attributed to stacking faults [18] or the presence of 3C polytype particles [19].

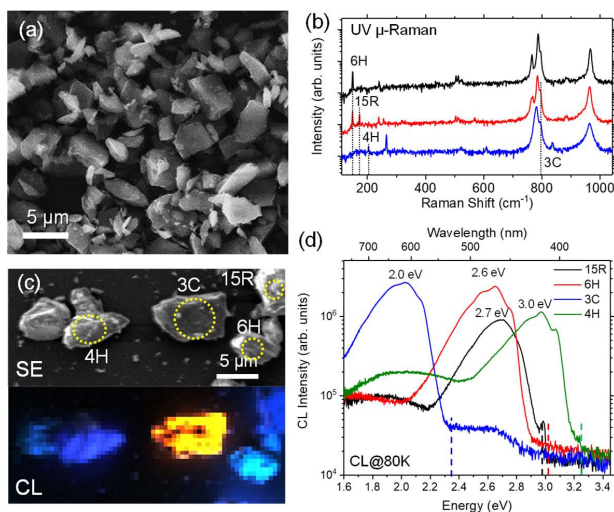


Figure 1. (a) SEM micrograph of a dense region ($\sim 30 \times 30\text{ }\mu\text{m}^2$) of SiC microparticles. (b) UV μ -Raman spectra measured on single particles and small agglomerates. The dotted lines indicate the position of

characteristic Raman modes of the 3C, 15R, 4H and 6H polytypes. (c) SEM micrograph and its corresponding CL false color map representing the spectral range 1.6–3.3 eV. (d) CL spectra measured at 80 K from selected particles as shown in panel (c).

Figure 1(c) shows a SEM micrograph of select particles (top) and their CL false color map (bottom), with corresponding CL spectra (at 80 K) shown in Figure 1(d) and highlighting the excitonic energy gap (E_{gx}) for the 3C, 15R, 6H and 4H polytypes, respectively [20,21] (see Supporting Information for further details). Focusing now on the 6H polytype, similar features are presented in Figure 2(a), which correspond to the average CL spectrum from a relatively large area ($30 \times 30 \mu\text{m}^2$) with hundreds of particles. Thus, the CL spectrum from the as-received (non-irradiated) powder consists of a dominant luminescence band ranging from 2.0 to 2.9 eV and peaking at around 2.6 eV. Note that each particle contains only one polytype, i.e., the 6H-SiC particles do not exhibit inclusions of the other polytypes, as evidenced by TEM measurements (see Supporting Information Figure S1).

Figure 2(a) also shows the luminescence from a proton-irradiated and annealed set of particles. Despite a lower intensity caused by an increase in non-radiative recombination, the averaged CL spectrum shows a similar shape in the UV and visible regions. Importantly, however, the near IR (NIR) region now clearly contains a new band ranging around 1.2–1.4 eV, which is enlarged in the inset of Fig. 2(a); the narrow emission lines – as indicated by arrows in the inset to Fig. 2(a) – are attributed to V_{Si} [11]. The signals peaking at 1.43, 1.40 and 1.36 eV are in good agreement with the V_{Si} centers reported for 6H-SiC and labelled V1, V2 and V3, respectively [11]. Note that V2 is more intense and sharper than V1 and V3, and has a full width at half maximum (FWHM) of around 14 meV. In addition, V3 is reported at 1.368 eV at 20 K, but in our case (at 80 K) is detected at 1.36 eV, and might be partially overlapping with a phonon-assisted sideband of V1 near V3 [11,22].

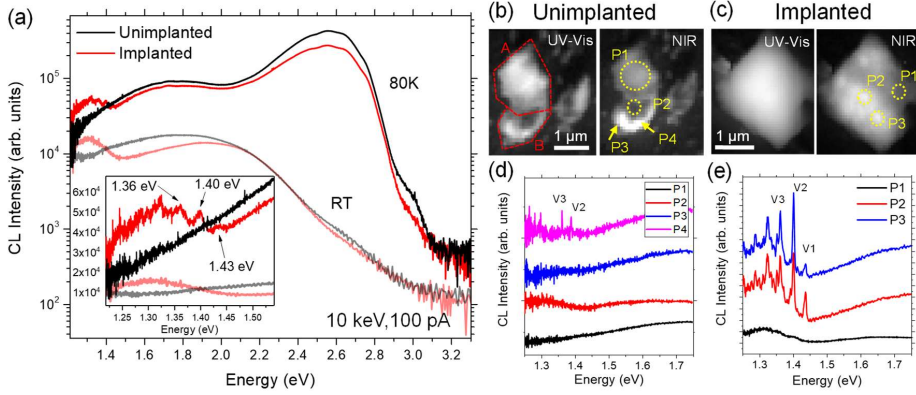


Figure 2. (a) CL spectra at 80K and room temperature (RT) from areas of $\sim 30 \times 30 \mu\text{m}^2$ of non-irradiated and irradiated SiC particles. The near IR (NIR) region has been enlarged in the inset. (b)–(c) UV-Visible and NIR intensity maps of non-irradiated and irradiated particles, respectively. (d)–(e) CL spectra from the regions marked in panels (b)–(c).

A more detailed analysis of the luminescence response of non-irradiated and irradiated particles is shown in the CL maps in Figures 2(b) and 2(c) and their corresponding spectra at 80 K in Figures 2(d) and 2(e), respectively. In general, non-irradiated particles show similar luminescence contrast in both the UV-Visible (2.0–3.0 eV) and NIR (1.2–1.5 eV) regions, as in particle A (contours marked by dashed line) in Fig. 2(b). However, occasionally, despite the featureless NIR signal in the averaged CL spectrum (Fig. 2a), some of the non-irradiated particles show a weak NIR emission band, as in particle B. The corresponding CL spectra in Fig. 2(d) reveal that, although particle A shows no evidence of V_{Si} -related features, we find sharp peaks at the V2 and V3 positions (P4 spectrum in Fig. 2d) in particle B. This indicates that V_{Si} defects were formed naturally during the microcrystal production process, and highlights the strong localization of V_{Si} emission. Thus, this represents an intriguing approach to single-photon source (SPS) control and design at the micro and nanoscale.

In irradiated particles, the UV-Vis and NIR contrasts show clear differences as demonstrated by Fig. 2(c), where the NIR map exhibits heterogeneous luminescence as

compared to the UV-Vis map. Intriguingly, the spectra in Fig. 2(e) suggest that the presence of the structured NIR band in irradiated particles strongly depends on the localization of the probe. For instance, the luminescence around location P1 (Fig. 2c) does not exhibit such V_{Si} -related structure, while P2 and P3 show a well-structured band with sharper (i.e., FWHM of 6.7 meV) and more intense V_{Si} peaks as compared with those in the averaged CL spectrum (see the inset to Fig. 2a). It should be mentioned that the relative intensity of the V1 and V2 peaks vary in this case, where V1 is more intense in spot P2 and V2 clearly dominates in P3 over all V_{Si} centers, indicating local changes in the luminescence efficiency for these emission lines. Importantly, Fig. 2(e) reveals a clear variation in the V_{Si} emission wavelength, which represents both a challenge and an opportunity for devices utilizing V_{Si} as SPEs. Ideally, the wavelength emission should be identical for various V_{Si} centers, but by controlling the local environment of the defect center, there is an opportunity to tune the emission accordingly.

A representative example of V_{Si} emission tuning is the irradiated square particle in Figure 3, in which the NIR maps (Figs. 3a and 3b) present significantly higher contrast compared to the UV-Vis map (see Supporting Information Figure S2). The particle contour has been marked with a dashed line (note that there is a slight horizontal drift during CL acquisition). By mapping the V1 and V2 lines, as shown by the false color maps in Figures 3(a)–(b), we can directly observe the location of the different V_{Si} luminescence centers. The color maps represent the wavelength in spectral windows of 10 nm around the V1 and V2 ZPLs, with the corresponding ZPL in green color. Fig. 3(a) illustrates that the V1 centers emit photons generally in regions localized at the central area of the particle rather than at or closer to the edges, while V2 (and similarly V3 in Figure S3 of the Supporting Information) exhibits heterogeneous distribution almost covering the entire area of the particle. Additionally, both the V1 and V2 maps clearly show red, blue or purple dots indicating considerable peak shifting, especially towards the particle edges.

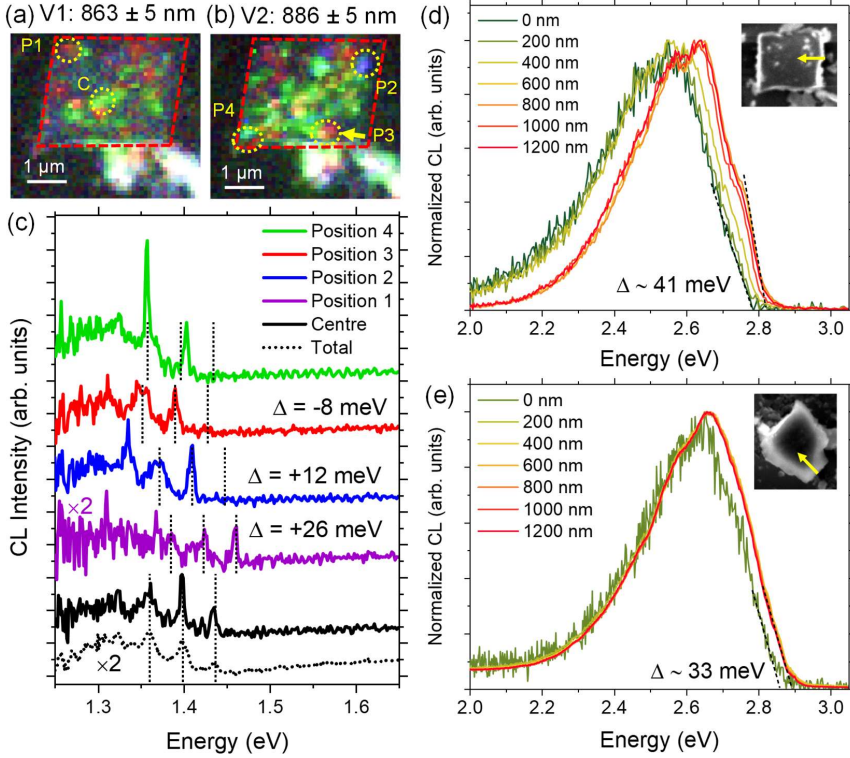


Figure 3. (a) and (b) CL false color maps obtained for the V1 and V2 centers of an irradiated square particle using wavelength windows of 10 nm around the zero-phonon line (ZPL). (c) CL spectra from the different regions marked in panels (a)–(b), and the total CL. Vertical dotted lines indicate the position of the V_{Si} centers. (d) and (e) Normalized CL spectra at the Visible-UV region of the particles shown in the SEM micrograph of the inset. The arrow indicates the direction of the linescan.

To investigate the origin of the V_{Si} emission variation in the SiC microcrystals, we turn to the CL spectra in Figure 3(c), which were obtained from the different regions marked in Figs. 3(a)–(b). The vertical dotted lines at the bottom of Fig. 3(c) indicate the position of the V_{Si} lines reported in the literature, while the dotted lines above refer to the corresponding spectrum. The positions of the V_{Si} peaks at the center of the particle (region C in Fig. 3a) agree well with reported energies, where V2 is the dominant center and significantly narrower compared with the total CL spectrum. Spectra from the points 1, 2 and 3 correspond to regions where the

detected V_{Si} peaks are shifted (note that $V1$ is weak or undetected in some cases), where points 1 and 2 exhibit a significant blue-shift of 26 and 12 meV, respectively, and point 3 a red-shift of 8 meV. It is important to mention that, in general, the V_{Si} peaks are blue- or red- shifted collectively. However, in some cases we can observe an asymmetric shifting as in point 4 near the particle corner, where a very intense sharp peak at 1.357 eV that agrees well with the $V3$ center is slightly red-shifted (-3 meV) with respect to its reported energy at 1.360 eV, while the $V2$ peak at 1.403 eV is blue-shifted ($+5$ meV).

A noticeable luminescence shifting near the particle edge is also observed at the high-energy side of the CL spectra, as demonstrated by the linescan of Figure 3(d). The linescan was performed with an e-beam energy of 5 keV in steps of 200 nm starting from the particle edge, and the CL spectra in Fig. 3(d) were normalized for simplicity. The SEM micrograph of the particle is displayed in the inset of Fig. 3(d) where the arrow indicates the scanning direction. Since there are no apparent near band edge (NBE) emission features, the high-energy slope of the defect band with the onset at around 2.8–2.9 eV has been used to monitor variations of the bandgap. In this way, a gradually increasing red shift up to 41 meV is observed as the e-beam approaches the particle edge. Figure 3(e) shows a similar analysis performed in the particle where the V_{Si} -line shifting was negligible (see Figs. 2d and 2e). The maximum deviation for this particle is around 33 meV, which is lower compared to that of the particle in Fig. 3(d). Interestingly, such a spectral shifting is only significant if measured at the particle's edge, while the lowest deviation is observed at distances > 200 nm from the edge.

In general, surfaces and particle boundaries are regions with a high density of structural and point defects, thus, corresponding changes in the CL features are expected [23,24]. In general, impurities or dopant concentration gradients towards the particle edge could locally modulate the bandgap. However, even a reasonably high presence of dopants and/or impurities should not have dramatic impacts on the V_{Si} -line positions unless there are strain effects

involved. Under strain conditions both NBE and deep level emission (DLE), including that from V_{Si} , have similar trends with respect to the emission energy variations [12,22,25]. Indeed, both the broad DLE and V_{Si} -related emission (see Fig. 3) display a variation between the particle center and particle edge, making strain a strong candidate for the wavelength tuning.

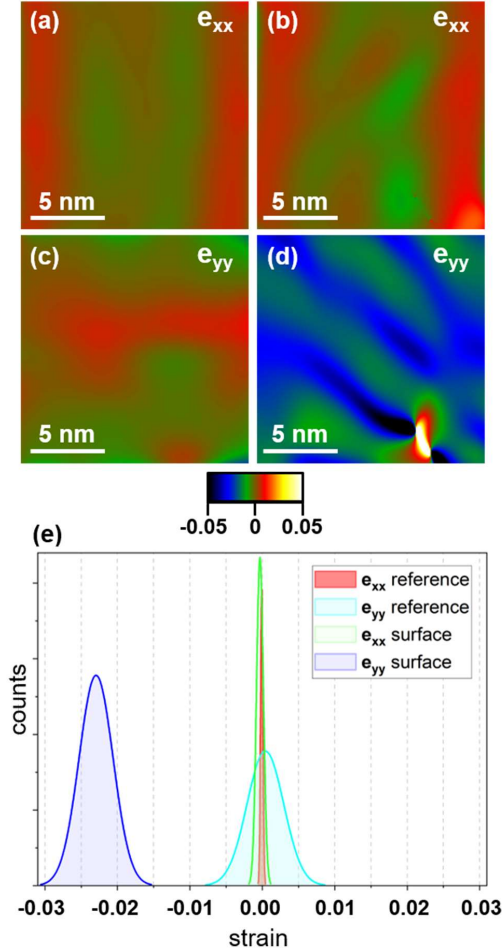


Figure 4. e_{xx} and e_{yy} strain maps from the middle-reference area of the particle (panels (a) and (c)) versus the surface of the particle ((b) and (d)). (e) The corresponding graph shows the distribution of the calculated strain values. Compressive e_{yy} lattice strain at the edge with respect to the middle area is detected, with a mean value -2.3%. The e_{xx} strain component was close to zero.

To verify this hypothesis, strain analysis on the nano-scale was performed by applying GPA in high-resolution scanning TEM images that were acquired continuously, starting from the middle towards the edges of the 6H-SiC particles. Figure 4 shows e_{xx} and e_{yy} strain maps measured at the middle ((a) and (c)) and surface area ((b) and (d)), respectively. The measured strain values show the deviation of the lattice with respect to the middle area of the particle that was used as a reference, according to: $\frac{d^{ROI} - d^{REF}}{d^{REF}}$, where ROI and REF denote the region of interest and reference area, respectively. Compressive e_{yy} strain was detected (along the a -axis of the hexagonal structure) with a mean value of -2.3 %, while the e_{xx} strain component was almost zero (along the c -axis). This strain trend was systematic and representative of the surface area until ~ 200 nm from the particle edge, after which the strain was significantly reduced.

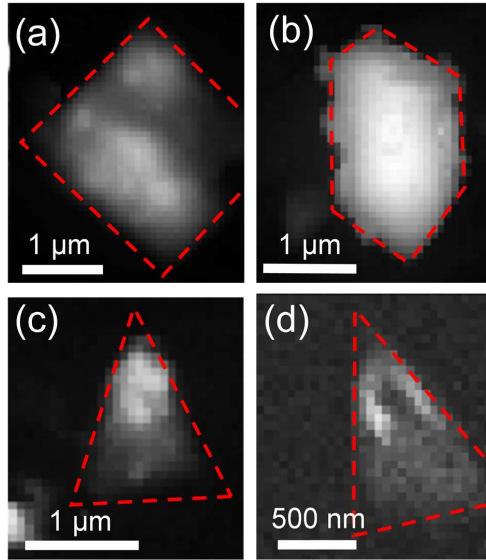


Figure 5. CL intensity maps of the NIR region, showing V_{Si} -related emission from particles of different shapes: (a) square, (b) irregular, (c) and (d) triangular.

Optimizing small-scale quantum emitters for quantum applications requires an advanced understanding of the changes in the optical properties under strain. The spin and strain coupling dependence was studied for 3C and 4H-SiC polytypes [12,26,27], but the 6H polytype

has been less explored. Nonetheless, it is known that V1 and V2 luminescence centers in 4H-SiC show a larger response for axial strain (along the c -axis) compared to transverse tensile strain [12], which would indicate an even larger potential for emission tuning than that shown herein for strain along the a -axis of 6H-SiC. Another important characteristic is that, in contrast to the variable luminescence wavelength, the V_{Si} spin state is immune to strain fluctuations [28,29]. Similar characteristics can be expected for the 6H polytype, making these centers quite robust and advantageous for quantum sensing technology [30] and integration in quantum photonic circuits [4,6,14], which require a stable spin state.

Finally, we investigate the impact of particle shape, with Figure 5 displaying the NIR emission attributed to V_{Si} for four particles having different shapes, where the emission is representative of the particle shape. Figure 5(a) shows a square particle where the NIR emission can be seen as bright regions originating from individual centers or ion tracks, while the irregularly shaped particle in Figure 5(b) exhibits uniform emission. On the other hand, the triangular shapes in Figures 5(c) and 5(d) reveal a stronger emission from the tip of the particle, indicating a pronounced waveguiding effect. Thus, the shape of the particles can be utilized to control and enhance the single-photon emission similar to that exploited in nanostructuring [14].

In summary, we have studied quantum emission from Si vacancies embedded in SiC micro- and nanoparticles using cathodoluminescence. Focusing on particles of the 6H polytype, prominent shifts in the emission wavelength – up to 26 meV – were revealed as a function of the V_{Si} localization. These shifts were correlated with compressive strain systematically occurring along the particle a -axis as observed by strain analysis in TEM. Moreover, we observed that the particle shape can be utilized to control, guide, and enhance the emission similarly to that exploited by nanostructuring of bulk samples. As such, we conclude that

embedding V_{Si} qubit defects into microparticles offers an interesting and versatile opportunity to tuning single-photon emission energies, and identify the SiC microcrystal platform as a suitable host for quantum applications.

Acknowledgements

Financial support was kindly provided by the Research Council of Norway and the University of Oslo through the frontier research project FUNDAMeNT (no. 251131, FriPro ToppForsk-program). The Research Council of Norway is acknowledged for the support to the Norwegian Micro- and Nano-Fabrication Facility, NorFab, project number 245963, and the Norwegian Center for Transmission Electron Microscopy (NORTEM) (no. 197405/F50). DM and AC thank the MINECO/FEDER/M-ERA.Net Cofund projects: RTI2018-097195-B-I00 and PCIN-2017-106.

Supporting Information. Materials and methods. Polytype identification, crystal structure and additional CL maps.

References

- [1] T. D. Ladd, F. Jelezko, R. Laflamme, Y. Nakamura, C. Monroe, and J. L. O'Brien, Quantum computers, *Nature* **464**, 45 (2010).
- [2] C. F. Wang, R. Hanson, D. D. Awschalom, E. L. Hu, T. Feygelson, J. Yang, and J. E. Butler, Fabrication and characterization of two-dimensional photonic crystal microcavities in nanocrystalline diamond, *Appl. Phys. Lett.* **91**, 201112 (2007).
- [3] S. Castelletto, L. Rosa, and B. C. Johnson, Silicon Carbide for Novel Quantum Technology Devices, in *Adv. Silicon Carbide Devices Process.* (InTech, 2015).
- [4] S. Castelletto and A. Boretti, Silicon carbide color centers for quantum applications, *J.*

- Phys. Photonics **2**, 022001 (2020).
- [5] A. L. Falk, B. B. Buckley, G. Calusine, W. F. Koehl, V. V. Dobrovitski, A. Politi, C. A. Zorman, P. X.-L. Feng, and D. D. Awschalom, Polytype control of spin qubits in silicon carbide, *Nat. Commun.* **4**, 1819 (2013).
 - [6] F. Peyskens, C. Chakraborty, M. Muneeb, D. Van Thourhout, and D. Englund, Integration of single photon emitters in 2D layered materials with a silicon nitride photonic chip, *Nat. Commun.* **10**, 4435 (2019).
 - [7] M. E. Bathen, A. Galeckas, J. Müting, H. M. Ayedh, U. Grossner, J. Coutinho, Y. K. Frodason, and L. Vines, Electrical charge state identification and control for the silicon vacancy in 4H-SiC, *Npj Quantum Inf.* **5**, 111 (2019).
 - [8] M. Rühl, L. Bergmann, M. Krieger, and H. B. Weber, Stark Tuning of the Silicon Vacancy in Silicon Carbide, *Nano Lett.* **20**, 658 (2020).
 - [9] C. F. de las Casas, D. J. Christle, J. Ul Hassan, T. Ohshima, N. T. Son, and D. D. Awschalom, Stark tuning and electrical charge state control of single divacancies in silicon carbide, *Appl. Phys. Lett.* **111**, 262403 (2017).
 - [10] C. P. Anderson, A. Bourassa, K. C. Miao, G. Wolfowicz, P. J. Mintun, A. L. Crook, H. Abe, J. Ul Hassan, N. T. Son, T. Ohshima, and D. D. Awschalom, Electrical and optical control of single spins integrated in scalable semiconductor devices, *Science* **366**, 1225 (2019).
 - [11] M. Wagner, B. Magnusson, W. M. Chen, E. Janzén, E. Sörman, C. Hallin, and J. L. Lindström, Electronic structure of the neutral silicon vacancy in 4H and 6H SiC, *Phys. Rev. B* **62**, 16555 (2000).
 - [12] P. Udvarhelyi, G. Thiering, N. Morioka, C. Babin, F. Kaiser, D. Lukin, T. Ohshima, J. Ul-Hassan, N. T. Son, J. Vučković, J. Wrachtrup, and A. Gali, Vibronic States and Their Effect on the Temperature and Strain Dependence of Silicon-Vacancy Qubits in

- 4H-SiC, *Phys. Rev. Appl.* **13**, 054017 (2020).
- [13] P. Udvarhelyi and A. Gali, Ab Initio Spin-Strain Coupling Parameters of Divacancy Qubits in Silicon Carbide, *Phys. Rev. Appl.* **10**, 054010 (2018).
- [14] M. Radulaski, M. Widmann, M. Niethammer, J. L. Zhang, S.-Y. Lee, T. Rendler, K. G. Lagoudakis, N. T. Son, E. Janzén, T. Ohshima, J. Wrachtrup, and J. Vučković, Scalable Quantum Photonics with Single Color Centers in Silicon Carbide, *Nano Lett.* **17**, 1782 (2017).
- [15] See <https://www.washingtonmills.com>
- [16] D. W. Feldman, J. H. Parker, W. J. Choyke, and L. Patrick, Phonon Dispersion Curves by Raman Scattering in SiC, Polytypes 3C, 4H, 6H, 15R and 21R, *Phys. Rev.* **173**, 787 (1968).
- [17] X. Qin, X. Li, X. Chen, X. Yang, F. Zhang, X. Xu, X. Hu, Y. Peng, and P. Yu, Raman scattering study on phonon anisotropic properties of SiC, *J. Alloys Compd.* **776**, 1048 (2019).
- [18] S. Nakashima, Y. Nakatake, H. Harima, M. Katsuno, and N. Ohtani, Detection of stacking faults in 6H-SiC by Raman scattering, *Appl. Phys. Lett.* **77**, 3612 (2000).
- [19] H. Okumura, E. Sakuma, J. H. Lee, H. Mukaida, S. Misawa, K. Endo, and S. Yoshida, Raman scattering of SiC: Application to the identification of heteroepitaxy of SiC polytypes, *J. Appl. Phys.* **61**, 1134 (1987).
- [20] P. J. Wellmann, Review of SiC crystal growth technology, *Semicond. Sci. Technol.* **33**, 103001 (2018).
- [21] W. van Haeringen, P. A. Bobbert, and W. H. Backes, On the Band Gap Variation in SiC Polytypes, *Phys. Status Solidi* **202**, 63 (1997).
- [22] A. Niilisk, A. Laisaar, and A. V. Slobodyanyuk, Effect of pressure on near-infrared abc photoluminescence spectrum of 6H SiC crystal, *Solid State Commun.* **94**, 71 (1995).

- [23] G. C. Vásquez, K. M. Johansen, A. Galeckas, L. Vines, and B. G. Svensson, Optical signatures of single ion tracks in ZnO, *Nanoscale Adv.* **2**, 724 (2020).
- [24] W. T. Ruane, K. M. Johansen, K. D. Leedy, D. C. Look, H. von Wenckstern, M. Grundmann, G. C. Farlow, and L. J. Brillson, Defect segregation and optical emission in ZnO nano- and microwires, *Nanoscale* **8**, 7631 (2016).
- [25] S. Deng, L. Wang, H. Xie, Z. Wang, Y. Wang, S. Jiang, and H. Guo, Strain-assisted band gap modulation in intrinsic and aluminum doped p-type SiC, *AIP Adv.* **8**, 075216 (2018).
- [26] S. J. Whiteley, F. J. Heremans, G. Wolfowicz, D. D. Awschalom, and M. V. Holt, Correlating dynamic strain and photoluminescence of solid-state defects with stroboscopic x-ray diffraction microscopy, *Nat. Commun.* **10**, 3386 (2019).
- [27] A. L. Falk, P. V. Klimov, B. B. Buckley, V. Ivády, I. A. Abrikosov, G. Calusine, W. F. Koehl, Á. Gali, and D. D. Awschalom, Electrically and Mechanically Tunable Electron Spins in Silicon Carbide Color Centers, *Phys. Rev. Lett.* **112**, 187601 (2014).
- [28] H. Kraus, V. A. Soltamov, F. Fuchs, D. Simin, A. Sperlich, P. G. Baranov, G. V. Astakhov, and V. Dyakonov, Magnetic field and temperature sensing with atomic-scale spin defects in silicon carbide, *Sci. Rep.* **4**, 5303 (2015).
- [29] R. Nagy, M. Widmann, M. Niethammer, D. B. R. Dasari, I. Gerhardt, Ö. O. Soykal, M. Radulaski, T. Ohshima, J. Vučković, N. T. Son, I. G. Ivanov, S. E. Economou, C. Bonato, S.-Y. Lee, and J. Wrachtrup, Quantum Properties of Dichroic Silicon Vacancies in Silicon Carbide, *Phys. Rev. Appl.* **9**, 034022 (2018).
- [30] J. Davidsson, V. Ivády, R. Armiento, T. Ohshima, N. T. Son, A. Gali, and I. A. Abrikosov, Identification of divacancy and silicon vacancy qubits in 6H-SiC, *Appl. Phys. Lett.* **114**, 112107 (2019).

Supporting Information

Strain modulation of Si vacancy quantum emission from SiC micro- and nanoparticles

G. C. Vásquez^{a*}, M. E. Bathen^a, A. Galeckas^a, C. Bazioti^a, K. M. Johansen^a, D. Maestre^b, A. Cremades^b, Ø. Prytz^a, A. M. Moe^c, A. Yu. Kuznetsov^a, L. Vines^a

^a *Centre for Materials Science and Nanotechnology, University of Oslo, N-0318 Oslo, Norway*

^b *Departamento de Física de Materiales, Facultad de CC. Físicas, Universidad Complutense de Madrid, 28040, Madrid, Spain*

^c *Washington Mills AS, NO-7300 Orkanger, Norway*

*Corresponding author

G. Cristian Vasquez

Present address: *Jülich Centre for Neutron Science (JCNS-1), Forschungszentrum Jülich GmbH, Leo-Brandt-Straße, 52425 Jülich, Germany*

E-mail: c.vasquez@fz-juelich.de

Contents: Methods, supporting analyses, and additional results and discussion

Supporting Methods

SiC micro- and nanoparticles were provided by Washington Mills Co. Crystals having an average size of 2 and 5 μm were deposited and mechanically dispersed on flat Si substrates. To intentionally create the V_{Si} defects, a sample with SiC particles was irradiated with 1.8 MeV protons to a fluence of $8 \times 10^{13} \text{ cm}^{-2}$ and at an angle 8° off the surface normal to reduce channelling effects. The protons have a projected range of around 27 μm , that is, the Bragg peak of implanted hydrogen is situated far beyond the micron-sized SiC particles. Therefore, we anticipate no involvement of hydrogen in the CL measurements. The irradiation was followed by thermal annealing on a hot plate at 300 $^\circ\text{C}$ for 30 min in air to clear out interstitial defects, similar to that performed in Ref. [7] of the main text.

The samples were studied with a JEOL JSM-IT300 SEM equipped with a Delmic SPARC Cathodoluminescence (CL) System. CL spectra were measured at room temperature (RT) and 80 K with acceleration voltages from 5 to 10 kV and probing currents of 100-200 pA. Hyperspectral data was collected with an Andor Shamrock 303i spectrometer with a 300 l/mm grating and a charged couple device (CCD) Andor Newton DU940P-BU2 detector. Long pass filters with cut-off wavelengths of 550 nm were used to block second order diffractions to record the NIR region. Note that the CL spectra have been filtered in order to minimize the etaloning effect caused by optical interference on the back-illuminated CCD detectors in the range 700-1000 nm.

The micro-Raman analysis was performed at room temperature using a Horiba Jobin-Yvon LabRAM HR800 confocal microscope equipped with a 325-nm He-Cd laser source. The laser power density of about $8 \times 10^4 \text{ W} \cdot \text{cm}^{-2}$ was attenuated by using a neutral filter to avoid thermal heating effects.

(Scanning) Transmission Electron Microscopy (S)TEM investigations were conducted on a FEI Titan G2 60-300 kV equipped with a CEOS DCOR probe-corrector and Super-X EDX detectors. Observations were performed at 300 kV with a probe convergence angle of 24 mrad. The camera length was set at 77 mm and simultaneous STEM imaging was conducted with three detectors: high-angle annular dark-field (HAADF) with collection angles of 98.7-200 mrad, annular dark-field (ADF) with collection angles of 21.5-98.7 mrad, and annular bright-field (ABF) with collection angles of 10.6 - 21.5 mrad. The resulting spatial resolution achieved was approximately 0.08 nm. Geometric Phase Analysis (GPA) was applied on high-resolution images for nanoscale strain measurements in the GMS Gatan software suite. Energy-Dispersive X-ray Spectroscopy (EDX) was applied to identify the chemical composition of the particles. The powder samples were mixed with Epofix glue, and were prepared by mechanical grinding and polishing (Allied MultiPrep). Final thinning was performed by Ar ion milling with a Fishione Model 1010, and plasma cleaning was applied before the STEM investigations with a Fishione Model 1020.

Particle polytype identification

Figure 1 of the main text details the microcrystals employed for the present work, by highlighting the large variation in the particle size and shape distribution (see Figure 1a of the main text). Furthermore, Fig. 1 (main text) reveals that the microcrystal sample set is composed of both the 4H, 6H and 15R polytypes, by using a combination of CL and micro-Raman spectroscopy to identify and determine the main spectral signatures of the different SiC polytypes that are present in the initial powder. The spectra in Figure 1(b) (main text) correspond to Raman measurements from individual or small agglomerates of particles (few micron size) acquired at room temperature with an UV laser source of 325 nm. We identify the 6H, 15R and 4H polytypes with reported active Raman modes at 149, 172 and 204 cm^{-1} , respectively, with 6H-SiC being the dominant polytype over all measured particles.

The near band edge emission as collected by CL spectroscopy also provides important information regarding the polytype of each particle. Figure 1(c) of the main text shows a SEM micrograph of select particles (top) and their corresponding CL false colour maps (bottom) displaying the spectral range from 1.6 to 3.3 eV. The hyperspectral CL measurements were recorded at 80 K and the spectra of the marked particles in Fig. 1(c) (main text) are shown in Figure 1(d) (main text). Vertical bars at 2.39, 2.98, 3.02 and 3.26 eV in Fig. 1(d) of the main text illustrate the excitonic energy gap ($E_{g\chi}$) reported in the literature for the 3C, 15R, 6H and 4H polytypes, respectively. In general, 3C or 4H polytypes can be easily identified because of the dominant luminescence band centred at around 2.0 or 3.0 eV, respectively, and extending up to or close to their corresponding $E_{g\chi}$. In contrast, since 15R and 6H polytypes possess similar $E_{g\chi}$, an assignment based on the luminescence band extension would be imprecise. However, we observe that 15R particles generally show a narrow peak at 2.98 eV consistent with its $E_{g\chi}$.

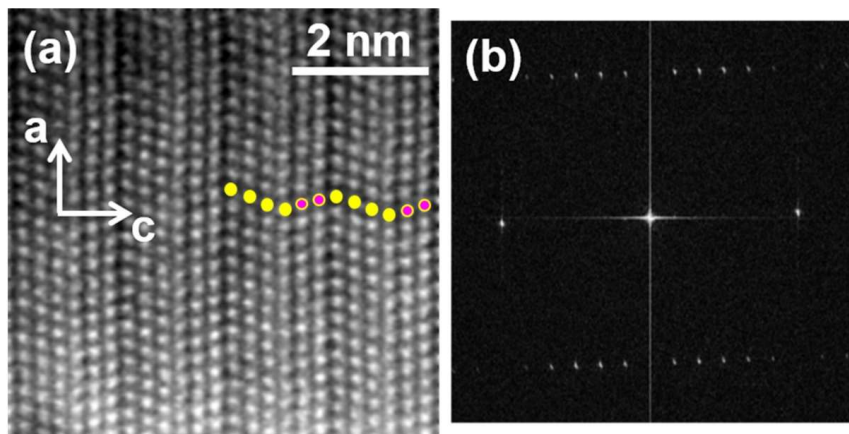
Particle crystal structure

Figure S1. (a) High resolution ADF-STEM image from the edge of the microparticle and (b) fast Fourier transform diffractogram from a larger area, verifying that the particle is of the 6H polytype without other polytype inclusions.

With 6H being identified as the dominant SiC polytype over all studied particles, we now turn to an in-depth investigation of the crystal structure of a representative 6H-SiC microcrystal. Figure S1 illustrates the stacking sequence of a microparticle as collected using scanning transmission electron microscopy, and demonstrates that the particle contains only one polytype. That is, a particle of 6H-SiC polytype will not exhibit polytype inclusions. The characteristic ABCACB stacking sequence of the hexagonal 6H-SiC polytype along the c-axis ([0001] direction) is clearly resolved in Fig. S1. The microparticles were single crystals, and no polytype transformations or extended defects were observed. The fast Fourier transform diffractogram in the inset of Fig. S1 also verifies that the particle is of the 6H polytype without other polytype inclusions.

Distribution of V_{Si} defects after proton irradiation and annealing

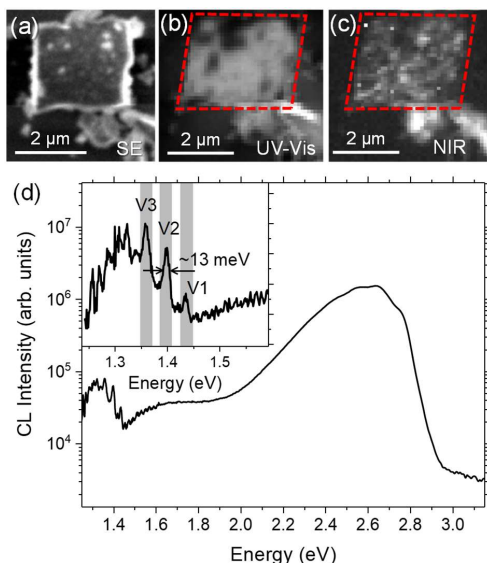


Figure S2. (a) SEM micrograph of a proton-irradiated square particle and its corresponding (b) UV-Visible and (c) NIR intensity maps. The dashed lines in (b) and (c) contour the particle edge. (d) Total CL spectrum at 80 K from the particle in (a). The NIR region has been enlarged in the inset of (d).

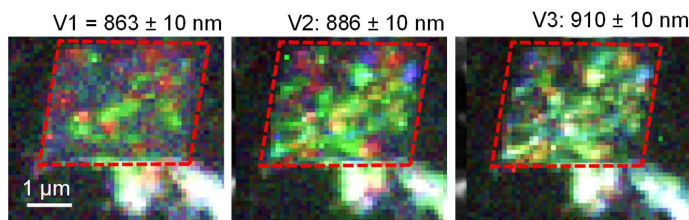


Figure S3. False colour maps demonstrating the distribution of V1, V2 and V3 centres within the proton-irradiated square particle shown in Figure S2, using wavelength windows of 10 nm around the zero phonon line (ZPL).

Next, let us consider the portion of CL emission from the particles that is related to Si vacancies in the 6H SiC polytype. Figure S2(a) shows the SEM micrograph of an irradiated square particle. The particle contour has been marked with a dashed line (note that there is a slight horizontal drift during CL acquisition) in the UV-Vis and NIR CL maps of the Figures S2(b) and S2(c), respectively. The NIR maps present significantly rougher contrast with respect to the UV-Vis map of Fig. S2(b). The CL spectrum acquired from the entire particle is shown in Figure S2(d), with similar characteristics for 6H-SiC as observed the Figure 2(a) of the main text. Details of the NIR region can be observed

in the inset of Fig. S2(d), with the V1, V2 and V3 lines peaking at 1.435, 1.399 and 1.359 eV, respectively. Note that the V2 line dominates over V1, and to a lesser extent over V3. Interestingly, the full width at half maximum (FWHM) of V2 and V3 is around 13–14 meV, similar to the FWHM observed averaging over a great number of particles (Figure 2(a) in manuscript). The false colour maps in Figure S3 show the distribution of the different V_{Si} centres embedded within the particle. Note that V3 shows similar distribution as compared to V2.

Paper IV

Near-IR emitters related to the silicon vacancy in n-type 4H-SiC

M. E. Bathen, A. Galeckas, R. Karsthof, A. Yu. Kuznetsov, L. Vines

In manuscript (2020).

IV

Paper V

Influence of hydrogen implantation on emission from the silicon vacancy in 4H-SiC

M. E. Bathen, A. Galeckas, J. Coutinho, L. Vines

Published in *Journal of Applied Physics*, February 2020, Volume 127 (085701).
DOI: 10.1063/1.5140659.

V

Influence of hydrogen implantation on emission from the silicon vacancy in 4H-SiC

Cite as: J. Appl. Phys. **127**, 085701 (2020); <https://doi.org/10.1063/1.5140659>

Submitted: 29 November 2019 . Accepted: 05 February 2020 . Published Online: 24 February 2020

M. E. Bathen , A. Galeckas , J. Coutinho , and L. Vines 

COLLECTIONS

Paper published as part of the special topic on [Defects in Semiconductors 2020](#)

Note: This paper is part of the Special Topic on Defects in Semiconductors 2020.



View Online



Export Citation



CrossMark

ARTICLES YOU MAY BE INTERESTED IN

[Iron and intrinsic deep level states in Ga₂O₃](#)

Applied Physics Letters **112**, 042104 (2018); <https://doi.org/10.1063/1.5020134>

[Applied Physics Letters welcomes papers in Quantum Technologies](#)

Applied Physics Letters **116**, 010401 (2020); <https://doi.org/10.1063/1.5142832>

[Self-trapped hole and impurity-related broad luminescence in \$\beta\$ -Ga₂O₃](#)

Journal of Applied Physics **127**, 075701 (2020); <https://doi.org/10.1063/1.5140742>

Lock-in Amplifiers

Find out more today



 Zurich
Instruments

Influence of hydrogen implantation on emission from the silicon vacancy in 4H-SiC

Cite as: J. Appl. Phys. 127, 085701 (2020); doi: 10.1063/1.5140659

Submitted: 29 November 2019 · Accepted: 5 February 2020 ·

Published Online: 24 February 2020



M. E. Bathen,^{1,a)} A. Galeckas,¹ J. Coutinho,² and L. Vines¹

AFFILIATIONS

¹Department of Physics/Centre for Materials Science and Nanotechnology, University of Oslo, N-0316 Oslo, Norway

²Department of Physics and I3N, University of Aveiro, Campus Santiago, 3810-193 Aveiro, Portugal

Note: This paper is part of the Special Topic on Defects in Semiconductors 2020.

a) Author to whom correspondence should be addressed: m.e.bathen@fys.uio.no

ABSTRACT

The silicon vacancy (V_{Si}) in 4H-SiC is a room temperature single-photon emitter with a controllable high-spin ground state and is a promising candidate for future quantum technologies. However, controlled defect formation remains a challenge, and, recently, it was shown that common formation methods such as proton irradiation may, in fact, lower the intensity of photoluminescence (PL) emission from V_{Si} as compared to other ion species. Herein, we combine hybrid density functional calculations and PL studies of the proton-irradiated n-type 4H-SiC material to explore the energetics and stability of hydrogen-related defects, situated both interstitially and in defect complexes with V_{Si} , and confirm the stability of hydrogen in different interstitial and substitutional configurations. Indeed, V_{Si} -H is energetically favorable if V_{Si} is already present in the material, e.g., following irradiation or ion implantation. We demonstrate that hydrogen has a significant impact on electrical and optical properties of V_{Si} , by altering the charge states suitable for quantum technology applications, and provide an estimate for the shift in thermodynamic transition levels. Furthermore, by correlating the theoretical predictions with PL measurements of 4H-SiC samples irradiated by protons at high (400 °C) and room temperatures, we associate the observed quenching of V_{Si} emission in the case of high-temperature and high-fluence proton irradiation with the increased mobility of H_i , which may initiate V_{Si} -H complex formation at temperatures above 400 °C. The important implication of hydrogen being present is that it obstructs the formation of reliable and efficient single-photon emitters based on silicon vacancy defects in 4H-SiC.

Published under license by AIP Publishing. <https://doi.org/10.1063/1.5140659>

I. INTRODUCTION

Solid-state single-photon emitters and controllable spin centers are currently in high demand for applications within quantum computing, communication, imaging, and sensing. Silicon carbide, and the 4H polytype, due to its mature material processing and fabrication, in particular, is a promising host for qubit defects. 4H-SiC harbors several candidate defects exhibiting desirable properties such as single-photon emission in the near-infrared and stable and controllable spin states, even at room temperature (RT).^{1,2} However, although isolated point defects can be detected and identified in 4H-SiC, both controlled formation and fully reliable detection of the defects remain a challenge.

Promising qubit contenders in 4H-SiC include the silicon vacancy (V_{Si}),³ the silicon-carbon divacancy ($V_{\text{Si}}V_{\text{C}}$),⁴ the carbon antisite-vacancy pair ($C_{\text{Si}}V_{\text{C}}$),⁵ and the nitrogen-vacancy center

($N_C V_{\text{Si}}$).⁶ The high fraction of V_{Si} emission directed into the zero-phonon line (ZPL),⁷ along with the higher stability of V_{Si} emission energies toward stray electric fields^{8–10} and device fabrication¹¹ as compared to the complexes, mark the silicon vacancy as a front-runner for quantum technology applications.

V_{Si} can inhabit two different lattice sites in 4H-SiC, the hexagonal (h) and pseudo-cubic (k), and, therefore, exists in two configurations. Accordingly, photoluminescence (PL) spectra from n-type 4H-SiC typically showcase two ZPLs related to V_{Si} : V1 at 1.438 eV assigned to the negative V_{Si} at a hexagonal lattice site, $V_{\text{Si}}^-(h)$, and V2 at 1.352 eV attributed to $V_{\text{Si}}^-(k)$.^{8,12} Despite the promising properties of V_{Si} , emission from V_{Si} remains low and is commonly enhanced by nanostructuring of the 4H-SiC surface to form waveguides for single-defect spectroscopy.^{13,14} Furthermore, only the negative charge state of V_{Si} manifests single-photon emission and millisecond spin coherence times.¹³ Recently, the 2– and 3– charge

states were shown to be more stable than V_{Si}^- in n-type material, by correlating density functional theory (DFT) calculations to deep level transient spectroscopy (DLTS) measurements.⁹ Indeed, substantial enhancement of emission from V_{Si} ensembles⁹ and control of the charge state of isolated V_{Si} defects¹⁵ was recently demonstrated via application of electric fields, and this was attributed to selective population of the bright and dark charge states.

In contrast to the carbon vacancy, which is commonly present even in the state-of-the-art epitaxial 4H-SiC material,¹⁶ the silicon vacancy is challenging to form thermally. With a formation energy of ~ 7.5 eV in the neutral charge state,^{1,9} which is predominant under the intrinsic conditions that manifest at high temperatures, only approximately 10^7 cm^{-3} of silicon vacancies can be formed by annealing 4H-SiC at 2000 °C. Accordingly, irradiation and ion implantation are the methods of choice for silicon vacancy formation. Unfortunately, the placement of isolated defects during an irradiation procedure is inherently randomized, but proton beam writing¹⁷ or irradiation through nano-scale apertures¹⁸ enhances the reproducibility when single defects are desired. To successfully employ silicon vacancies as efficient single-photon sources for quantum cryptography or reliable multi-level single spins for quantum computing, comprehensive investigations into the effects of processing conditions on V_{Si} formation and emission are needed.

Recently, it was shown that V_{Si} -related PL is substantially weaker when the silicon vacancies are formed by hydrogen implantation compared to that of, e.g., helium.¹⁸ A possible explanation involves the implanted hydrogen atoms preferentially occupying V_{Si} sites, thereby altering the optoelectronic properties of the defect and effectively quenching the V1 and V2 emission lines. Helium, on the other hand, is inert and may have a reduced impact on the V_{Si} emission. A theoretical study suggested that hydrogen is readily captured by silicon and carbon vacancies in 3C-SiC, while preferring the V_{Si} site over that of V_{C} .¹⁹ However, vacancy-hydrogen complex formation is possible also in the 4H polytype, motivating for further investigation. Indeed, a deep-level defect at 0.73 eV below the conduction band edge, observed by DLTS, was tentatively attributed to the $V_{\text{Si}}\text{-H}$ complex.²⁰

In the present work, we explore the impact of hydrogen on the formation and properties of V_{Si} in 4H-SiC theoretically, by employing density functional calculations, and interpret our findings in light of photoluminescence measurements. We propose that the interstitial H configuration is lowest in energy and that formation of the $V_{\text{Si}}\text{-H}$ complex is energetically favorable during, e.g., irradiation and subsequent heat treatments. Complex formation likely results in a quenching of V_{Si} -related emission, and we propose hydrogen as an obstacle for efficient creation of reliable single-photon emitters using silicon vacancies in 4H-SiC. Moreover, we reaffirm that H migrates substantially slower in n-type than p-type material and find that 400–500 °C is likely sufficient for H to react with V_{Si} in n-type 4H-SiC. Finally, we study V_{Si} -related emission experimentally in n-type 4H-SiC samples, irradiated with protons to different fluences and at different temperatures, and attempt to explain our observations in light of the theoretical findings presented herein.

II. METHODOLOGY

A. Theory

Hydrogen-related defects in 4H-SiC were studied using density functional theory as implemented in the *Vienna ab initio simulation package*, or VASP, code.^{21–24} The electronic ground state was obtained within the Kohn–Sham formalism, using the projector augmented-wave (PAW) method²⁵ and plane waves to describe core and valence electrons, respectively. 400-atom hexagonal supercells were constructed from $5 \times 5 \times 2$ primitive cells along the main axes. The lattice constants used for 4H-SiC were obtained using the Perdew–Burke–Ernzerhof functional (PBE²⁶), and PBE-level lattice parameters were chosen because PBE was mainly used when studying H diffusion.

Defect formation was accomplished by adding one hydrogen (H) atom to form a hydrogen interstitial (H_i) and removing a Si atom to form a silicon vacancy (V_{Si}) or a $V_{\text{Si}}\text{-H}$ complex. The defect geometries were first optimized at the PBE-level by employing $2 \times 2 \times 2$ Γ -centered Brillouin-zone (BZ) sampling and relaxing until the maximum force was below 0.01 eV/Å. Starting from the resulting defect configuration, a Γ -only relaxation succeeded within screened hybrid density functional theory (HSE06^{27,28}) until maximum forces were below 0.05 eV/Å. From these results, formation energy diagrams for all defects were constructed. The stopping criterion for the electronic self-consistent loop was set to 10^{-6} eV and the plane-wave energy cut-off to 420 eV.

For the silicon monovacancy, the formation energies are based on calculations from Ref. 9, where we employed a 96-atom orthorhombic supercell, the HSE06 functional and $2 \times 2 \times 2$ Monkhorst–Pack type BZ-sampling. Note that mirroring effects might influence the defect energetics for smaller supercells. However, the minimum distance between defects is 10 Å for V_{Si} in the 96-atom supercell, and the calculated thermodynamic charge-state transition levels agree with those obtained for V_{Si} in tests with 400-atom supercells, and when comparing to experiment,⁹ within ~ 0.1 eV. During migration, the defect strain field extends over a larger volume and particularly when a complex is involved. A larger 400-atom supercell was, therefore, used to study the migration of interstitial hydrogen and the formation of hydrogen-vacancy complexes herein. This method was previously successfully employed to study the migration of the carbon vacancy (V_{C}) in 3C- and 4H-SiC,²⁹ and excellent overlap between theory and experiment was found.

Electronic structure calculations employing the HSE06 functional appear to adequately capture the energetics of defects within 4H-SiC, as demonstrated in Refs. 9 and 29 by combining DFT calculations with DLTS measurements for V_{Si} and V_{C} , respectively. The bandgap of the orthorhombic supercell becomes 3.17 eV when employing the $2 \times 2 \times 2$ MP k-mesh, which is close to the experimental value of 3.27 eV.³⁰ The Γ -only HSE06 calculations employing hexagonal supercells yield a bandgap of 3.48 eV. When discussing charge state transition levels herein, the calculated figures will refer to the valence band edge.

The formation energy of a semiconductor point defect is given by^{31,32}

$$E^f(q) = E_{\text{defect}}^{\text{total}}(q) - E_{\text{bulk}}^{\text{total}} - \sum_i \Delta n_i \mu_i + q(\epsilon_{\text{VBM}} + \epsilon_{\text{F}}) + E^{\text{FNV}}. \quad (1)$$

Here, E^{total} refers to the total energies of the defective and pristine supercells, Δn_i is the number of atoms added (positive) or removed (negative), μ_i is the chemical potential for a particular species (Si, C, or H), ϵ_{VBM} is the valence band maximum (VBM) and ϵ_{F} is the Fermi level position relative to VBM. Within this work, the chemical potentials were estimated by relaxations of bulk diamond, Si and hydrogen gas (H_2 in a periodic box) until all forces were below 0.005 eV/Å. E^{FNV} is a correction term to account for the use of charged and finite-sized supercells, and we have employed the extended Freysoldt, Neugebauer, and Van de Walle (FNV) correction scheme^{33–35} herein.

From the formation energy diagrams of the different defects, we can estimate the binding energy of a corresponding complex, here exemplified by $V_{\text{Si}}\text{-H}$,

$$E^{\text{b}}[(V_{\text{Si}}\text{-H})^{3-}] = E^{\text{f}}(V_{\text{Si}}^{2-}) + E^{\text{f}}(\text{H}_i^-) - E^{\text{f}}[(V_{\text{Si}}\text{-H})^{3-}]. \quad (2)$$

The binding energy depends on the charge state of the final defect complex, and thereby the Fermi level, and must be positive to ensure the stability of the complex in question. To obtain the complete dissociation energy needed to break up the complex, the migration barrier of the most mobile constituent (here H_i) is added to E^{b} .

Minimum energy paths (MEPs) for defect migration were studied at the PBE-level using the climbing image nudged elastic band (CI-NEB) method,^{36,37} Γ -only BZ sampling, 420 eV cut-off energy and between seven and 11 intermediate images. The forces were relaxed until the maximum force was below 0.01 eV/Å for all migration paths. NEB calculations require fixed initial and final geometries, and a chain of intermediate images is formed to provide an initial guess for the path of the migrating species. The images are connected via spring forces to keep them at a suitable distance and are then collectively optimized, with the climbing image approach ensuring that the highest-energy image lands at the MEP maximum. Finally, the transition state electronic structure was refined by self-consistent field (SCF) calculations employing HSE06 for select migrational pathways.

Within the present work, we study seven different configurations of H_i , and eight different migration paths involving axial and basal migration for two charge states (+ and -). This is not exhaustive, as a fully comprehensive investigation into the nature of H_i in 4H-SiC is outside the scope of this work. We leave a full qualitative summary of H_i to other works,^{19,38,39} although one should note that semi-local functionals are employed and Ref. 19 concerns the 3C polytype. Instead, our aim is to determine if hydrogen is likely to alter the electronic structure and optical transitions of V_{Si} when both defects are present in the 4H-SiC material, and explore the likelihood of the $V_{\text{Si}}\text{-H}$ complex formation. Therefore, to understand the recent experimental findings, we focus on illuminating a representative behavior for H in 4H-SiC and consider closely how hydrogen interacts with silicon vacancies. Higher-order complexes between V_{Si} and more than one H atom were not considered herein, but could contribute to the overall picture.

B. Experiment

Experimentally, we study PL emission from 4H-SiC samples that are proton-irradiated to different fluences and at different temperatures, to better understand the optimal formation conditions for V_{Si} . 4H-SiC samples holding 10 μm epitaxial layers purchased from Cree, Inc. were employed. The epi-layers were n-doped (nitrogen) with net carrier concentrations in the epi-layer of $1 \times 10^{15} \text{ cm}^{-3}$, as determined by capacitance-voltage measurements. We study n-type 4H-SiC samples implanted with 1.5 MeV protons having a projected range of $\sim 20 \mu\text{m}$, according to collision Monte Carlo calculations as manifested in the SRIM (Stopping and Range for Ions in Matter) code.⁴⁰ The samples were irradiated to fluences of $1 \times 10^{13} \text{ cm}^{-2}$, $5 \times 10^{13} \text{ cm}^{-2}$, and $1 \times 10^{14} \text{ cm}^{-2}$, dubbed low, medium, and high fluence, respectively. All implantations were performed with the samples tilted $\sim 8^\circ$ off with respect to the surface normal to reduce channeling, and at either room temperature (RT) or 400 °C (so-called hot implantation). Note that hot implantation is common in silicon carbide device processing and is used to alleviate damage during implantation of dopants. Employing the dynamic annealing figure of 3% for V_{Si} estimated in Ref. 9, we arrive at V_{Si} concentrations in the $10^{16}\text{--}10^{17} \text{ cm}^{-3}$ range at the Bragg peak maximum.

Photoluminescence measurements were carried out at 10 K using a closed-cycle He refrigerator system (Janis, CCS450) and 675 nm wavelength cw-laser of 1 mW power as an excitation source. The focused laser beam, impinging on the sample surface at $\sim 27^\circ$ angle, yielded an excitation intensity of $< 100 \text{ W cm}^{-2}$ and polarization perpendicular to the optical c -axis of 4H-SiC. PL signal was collected in a back-scattering geometry by a microscope objective (Mitutoyo, LWD 10 \times), spectrally filtered (long-pass LP 750 filter) and analyzed by imaging spectrometer (Horiba, iHR320) coupled to EMCCD camera (Andor, LM658M) with a spectral resolution below 2 nm.

As 4H-SiC is virtually transparent to below-bandgap illumination, the luminescence can be collected from the whole sample depth.⁹ Consequently, in the experiments described herein, we are probing both the proton irradiation tail and the Bragg peak of implanted hydrogen ions and can collect luminescence deriving from defects located in either region. The V1 and V2 ZPLs are associated with the negative charge state of h and k V_{Si} , respectively,^{3,7} but no PL signal has (to the best of our knowledge) been attributed to complexes between V_{Si} and H. V_{Si} requires high energies, and therefore irradiation, to form,^{1,29} and post-irradiation annealing is commonly performed to alleviate implantation damage and remove non-radiative channels. As this effect was something we wanted to probe herein, no post-irradiation annealing was performed.

III. RESULTS

A. Theory

1. The hydrogen interstitial

A selection of H_i configurations is presented in Fig. 1, where Fig. 1(a) displays the preferred lattice sites with hexagonal and pseudo-cubic sites labeled as h and k , respectively, and Fig. 1(b) contains formation energy diagrams for H_i . We find that interstitial

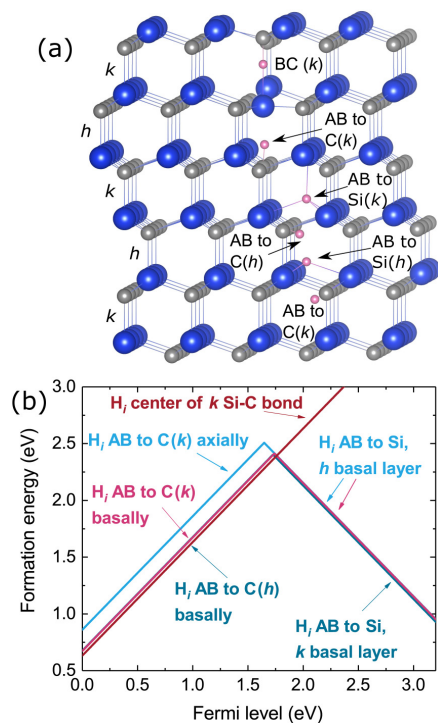


FIG. 1. (a) Favorable positions for H_i in the 4H-SiC lattice, with the different lattice site configurations (h and k) highlighted to the left. Si atoms are shown in blue, C in gray, and H in pink. The anti-bonding (AB) to C and bond-centered (BC) configurations reflect the positive charge state, while negative H is AB to Si. (b) Formation energy diagrams for various configurations of H_i . The energy of VBM is offset to zero.

hydrogen is amphoteric in 4H-SiC, with a negative- U character for the $(+/-)$ transition near midgap. Upon altering the charge state, the H_i configuration also changes. The most stable configuration for H_i^+ is at (approximately) the center of a Si-C bond (bond-centered or BC), in contrast to the finding of Ref. 38. However, the antibonding (AB) state (to C), which is most stable in Ref. 38, lies less than 0.05 eV higher in energy and should be attainable at room temperature. Generally, H_i^+ attaches to a location with high electron density, i.e., either at the bond-centered site or at the AB site to the C atom, which is the anion species in SiC. In an n-type material, on the other hand, H_i^- will dominate, preferring the AB to Si configuration. For both V_C^{41} and V_{Si}^9 , the k site is more stable than the h site in an n-type material, by ~ 0.1 eV. However, regarding sub-lattice site preference, no unified trend has been identified for H_i herein.

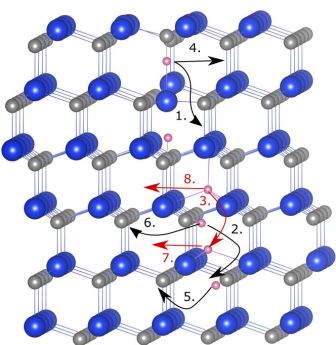


FIG. 2. Migration pathways for H_i in 4H-SiC. The jumps correspond to those of Table I. Black arrows designate migration of H_i^+ and red arrows that of H_i^- .

Interstitial hydrogen migration in 4H-SiC was studied for eight different atomic hops (both axial and basal) using the CI-NEB method, the PBE functional and Γ -only k -point sampling. The migration pathways for various jumps of H_i are illustrated in Fig. 2, with black arrows symbolizing H_i^+ and red arrows H_i^- . Activation energies for the corresponding pathways of H_i in the $+$ and $-$ charge states, and explanations for the numbering in Fig. 2, are summarized in Table I. The table contains migration barriers for H_i deduced from PBE-NEB, and select activation energies are refined by hybrid-SCF calculations. The charge state of H_i is found to significantly impact the migration barrier, with $E_A \geq 0.5$ eV for both axial and basal migration of H_i^+ (at PBE-level), and $E_A \geq 2.2$ eV for basal and ≥ 2.4 eV for axial H_i^- migration. This agrees with experiments, which have demonstrated that hydrogen migrates much faster in p-type than

TABLE I. Activation energies (E_A) for different axial and basal jumps of H_i^+ and H_i^- in 4H-SiC (see Fig. 1 for the notation and Fig. 2 for illustrations of the migration paths). The PBE and HSE data columns refer to the two steps of the calculation, namely, (1) the climbing image NEB run and (2) the SCF calculation to refine the transition state within HSE06. All activation energies for individual jumps are calculated with respect to the energy of the initial state.

Jump	Activation energy, E_A (eV)			
	$q = +1$		$q = -1$	
Charge state	PBE	HSE	PBE	HSE
Functional				
1. Axial BC(k) \rightarrow BC(h)	0.49	0.61		
2. Axial AB C(h) \rightarrow C(k)	0.65			
3. Axial AB Si(k) \rightarrow Si(h)			2.36	2.67
4. Basal BC(k)	0.51			
5. Basal AB to C(k)	0.51			
6. Basal AB to C(h)	0.50	0.45		
7. Basal AB to Si(h)			2.19	2.28
8. Basal AB to Si(k)			2.62	

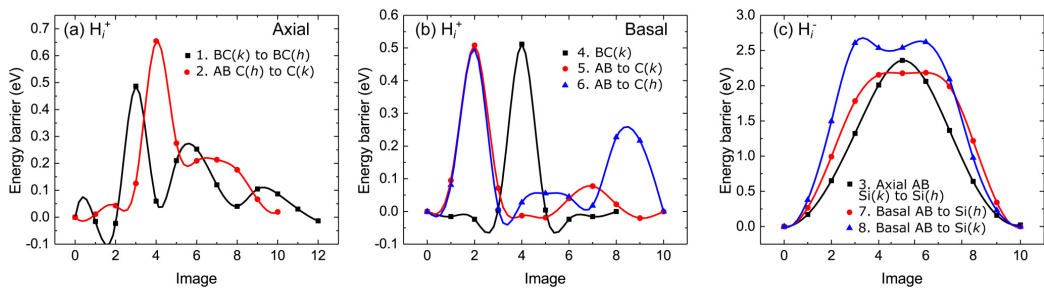


FIG. 3. Potential energy surfaces for migration of H_i in 4H-SiC. The migration paths are as outlined in Fig. 2 and are calculated using the CI-NEB method at the PBE-level. Panel (a) shows the minimum energy path (MEP) for H_i^+ migrating axially and (b) for H_i^+ moving basally, while (c) depicts basal and axial migration of H_i^- . The solid lines are cubic-spline interpolations of the data obtained from CI-NEB calculations and are intended as eye-guides.

n-type material.⁴² Moreover, the migration barriers found herein for H_i^+ are very similar to those of Refs. 38 and 43, while the ones for H_i^- are lower than the ~ 3 eV found in Ref. 38. It is also interesting to note that like V_C ,²⁹ we find that the migration of interstitial H in 4H-SiC is anisotropic, with H traveling faster along the basal directions than along the main crystalline axis. Assuming a jump frequency in the 10^{13} s^{-1} range, a migration barrier of 0.5 eV translates into room temperature hydrogen motion, while a ≥ 2.2 eV barrier prevents H diffusion (beyond $\sim 1 \mu\text{m}$) below 500°C .

The charge state of H_i impacts not only the activation energy for diffusion, but also the form and nature of the pathway of motion. The minimum energy paths (MEPs) for H_i migration in 4H-SiC are illustrated in Fig. 3, with Figs. 3(a) and 3(b) showcasing the potential energy surfaces for H_i^+ migrating axially and basally, respectively, while Fig. 3(c) contains the MEPs for axial and basal H_i^- jumps. The pathways are identified with numbers in the legends, corresponding to those in Table I. H_i^+ prefers to reside either at a bond center or in an antibonding configuration to a C atom, which is accompanied by MEPs with several intermediate transition states and local minima [Figs. 3(a) and 3(b)]. The oscillations largely correspond to rotations of the C–H bonds, while the highest-lying transition state structures are often similar to the ground-state configurations of H_i^- , and involve AB to a Si site. Note that the differences in x -coordinates between the different atomic hops in Fig. 3 only correspond to the number of intermediate images employed in the CI-NEB calculations and do not reflect absolute distances in the supercell.

The potential energy surfaces for H_i^- migration [Fig. 3(c)] are strikingly different from those of H_i^+ , having either a single transition state near mid-way along the path (axial jump), or two transition states similar in energy with a small local minimum in between (both basal jumps). In the former case, the transition state occurs as H_i^- passes through a square constructed of two C and two Si atoms. For basal(k) migration (blue curve), the first transition state of H_i^- is anti-bonded to C(h), while the subsequent local minimum and second barrier involve a rotation of the bond, and passing between two Si atoms on the way to the final configuration

[AB to Si(k)]. The transition state for H_i , that is, AB to Si(h) [red curve in Fig. 3(c)] is, in fact, similar to the AB to Si(k) configuration, with the difference being that the former is stable when the three basal atoms are Si(h), while the latter is stable when they are Si(k). Therefore, for the negative charge state in particular, we find a pronounced effect of the crystal field (depending on whether the H atom resides in a h or k lattice plane) on the preferred configuration of interstitial hydrogen.

2. The $V_{Si^-}H$ complex

If a silicon vacancy is present in the material, H may prefer the substitutional over the interstitial configuration. The formation energy diagrams of $V_{Si^-}H$ (calculated as described in Sec. II) and V_{Si} (calculated as in Ref. 9) are presented in Fig. 4. We observe that while the formation energy of H_i is significantly lower than that of

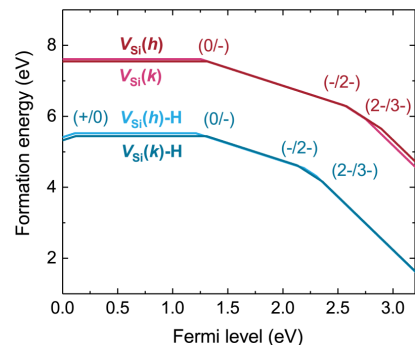


FIG. 4. Formation energy diagram for the silicon vacancy and the $V_{Si^-}H$ complex, in both the h and k configurations. The total energies of V_{Si} are from Ref. 9, and the VBM energy is offset to zero.

the $V_{\text{Si}}\text{-H}$ complex for all Fermi levels, the $V_{\text{Si}}\text{-H}$ complex will be energetically favorable if V_{Si} is present in the material. Indeed, after proton implantations, both V_{Si} and H, are present, and the formation of $V_{\text{Si}}\text{-H}$ is likely.

For the $V_{\text{Si}}\text{-H}$ complex, we find that the H atom prefers to sit closer to the axial or one of the three basal C atoms (termed the axial and basal configurations, respectively). The four configurations differ in energy by less than 0.1 eV for $V_{\text{Si}}(h)\text{-H}$, and all configurations are expected to be available to both complexes (h and k) at room temperature. The C-H bond length is between 1.10 and 1.11 Å for all charge states and both h and k V_{Si} , in close agreement with the 1.12 Å found for C-H bonds in 3C-SiC.¹⁹ Similarly to that for V_{Si} , the C atoms surrounding the $V_{\text{Si}}\text{-H}$ complex experience a slight breathing relaxation, which is more prominent for the positive and neutral charge states than for the three acceptor states. Contrary to what is found for V_{Si} , the $V_{\text{Si}}\text{-H}$ complex is more stable in the k than h configuration in a p-type and slightly n-type material, and vice versa in a highly n-type material, although the difference in stability is minor (see Fig. 4). Interestingly, the shape of the formation energy diagram is strikingly similar for V_{Si} and $V_{\text{Si}}\text{-H}$, with only minor differences apart from the predicted stability of $(V_{\text{Si}}\text{-H})^+$ in highly p-type 4H-SiC.

Next, we consider the binding energy of $V_{\text{Si}}\text{-H}$. Importantly, to ensure that silicon vacancies do not inadvertently disappear, processing steps intended for quantum applications utilizing V_{Si} should not involve heat treatments exceeding 400–600 °C.^{5,9,44,45} In this temperature range, the Fermi level resides around 0.5 eV below the conduction band edge in an n-type material, and the $V_{\text{Si}}\text{-H}$ complex will likely inhabit the 3[−] charge state (see Fig. 4). If the defect dissociates into $(V_{\text{Si}}\text{-H})^{2-} + \text{H}_i^-$, the energy raises by 4.35 eV (binding energy). Of course, the dissociation kinetics are limited by a dissociation barrier, which must be at least as high as the binding energy plus the migration barrier of the faster-diffusing product. These figures ensure that $V_{\text{Si}}\text{-H}$ will remain stable in n-type 4H-SiC at most operating conditions. Interestingly, Refs. 46 and 47 predicted that the dissociation of complexes between V_{Si} and H is the rate limiting step for H diffusion in irradiated n-type 4H and 6H SiC, with dissociation energies being in the 3.5–4.9 eV range. The relevant experimental conditions involve temperatures above 1300 °C,⁴⁸ resulting in Fermi levels around midgap and leaving H_i in the positive charge state. The binding energy of $V_{\text{Si}}\text{-H}$ will then likely differ from the n-type case.

Dissociation of $(V_{\text{Si}}\text{-H})^{3-}$ into the relevant constituents was studied using CI-NEB and a starting configuration with the H atom situated approximately two lattice vectors away from the vacancy (to enable relaxation). The resulting MEP is shown in Fig. 5, and we find that the dissociation barrier is indeed the binding energy plus the migration barrier of H_i , with no large capture barriers being present. In n-type 4H-SiC, where migration of H_i was found to have E_A above 2.2 eV (at the PBE-level), we anticipate that migration of interstitial hydrogen is the limiting reaction for $V_{\text{Si}}\text{-H}$ complex formation.

The silicon vacancy is a promising candidate for quantum technology applications, having millisecond spin coherence times and single-photon emission associated with the negative charge state. It is thus relevant to consider the effect of hydrogen on the electro-optical properties of V_{Si} when an isolated vacancy is

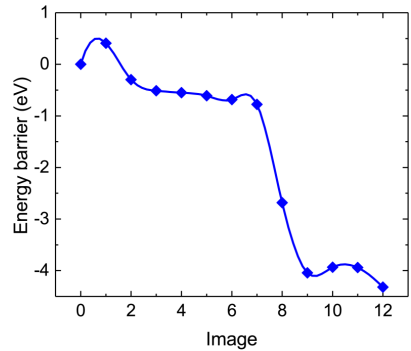


FIG. 5. Minimum energy path for dissociation of $(V_{\text{Si}}(k)\text{-H})^{3-}$, as calculated using the CI-NEB method, the PBE functional, and the Γ -only BZ sampling. The starting image was $V_{\text{Si}}(k)$ with a H atom two lattice vectors away. The solid lines are cubic-spline interpolations of the data obtained from CI-NEB calculations and are intended as eye-guides.

transformed into the $V_{\text{Si}}\text{-H}$ defect complex. As only the negative charge state (V_{Si}^-) has well-known opto-spin signals, it is particularly interesting to scrutinize the energetics of $V_{\text{Si}}\text{-H}$ as compared to that of V_{Si}^- .

Table II summarizes the ground state total spin of both V_{Si} configurations and the $V_{\text{Si}}\text{-H}$ complexes for all relevant charge states. Interestingly, $(V_{\text{Si}}\text{-H})^+$ appears to change spin states between the h and k V_{Si} configurations. This happens because the electronic structure of $(V_{\text{Si}}(k)\text{-H})^+$ organizes as $a_1^2 e^0$, while in $(V_{\text{Si}}(h)\text{-H})^+$, the a_1 and e levels become very close, resulting in a parallel spin configuration.

In the negative charge state, the ground state spin of V_{Si} (h and k) is $S = 3/2$. We observe that a corresponding high-spin configuration does exist for the $V_{\text{Si}}\text{-H}$ complex, but now in the neutral charge state. This is so because the reaction of V_{Si}^- with H^+ displaces one of the singlet gap states of V_{Si}^- into the valence band (due to C-H bond formation), along with two electrons. However, magnetic and optical manipulation of the V_{Si} spin state, as needed for quantum applications, relies on optical detection of the V1 and V2 ZPLs. Accordingly, a crucial question is whether photoluminescence from $V_{\text{Si}}\text{-H}$ follows that of V_{Si} . Although they do not provide

TABLE II. Spin state of V_{Si} and the $V_{\text{Si}}\text{-H}$ complexes, as calculated using hybrid DFT for different charge states. The results for $V_{\text{Si}}(h)$ and $V_{\text{Si}}(k)$ are from Ref. 9.

Charge state	$V_{\text{Si}}(k)$	$V_{\text{Si}}(h)$	$V_{\text{Si}}(k)\text{-H}$	$V_{\text{Si}}(h)\text{-H}$
$q = +$	N/A	N/A	0	1
$q = 0$	1	1	3/2	3/2
$q = -$	3/2	3/2	1	1
$q = 2 -$	1	1	1/2	1/2
$q = 3 -$	1/2	1/2	0	0

the full picture, the Kohn-Sham single-particle states that the result from DFT calculations may illuminate how the electronic structure of V_{Si} changes upon addition of H to form the $V_{\text{Si}}\text{-H}$ complex.

The five upper electrons inhabiting the V_{Si}^- defect states are expected to distribute in an $a_1^2 a_1^1 e^2$ configuration in the ground state, with the first excited state (V1 and V2) being $a_1^1 a_1^2 e^2$.⁴⁹ Accordingly, the optical transitions are minority spin-channel transitions. The relevant charge states of $V_{\text{Si}}\text{-H}$ are $q = -, 2-, \text{ and } 3-$, as these are most likely present in an n-type material. V_{Si} is metastable in p-type 4H-SiC and rapidly transforms into $\text{C}_{\text{Si}}\text{V}_{\text{C}}$ for Fermi levels below midgap. The electronic structures of $V_{\text{Si}}\text{-H}$ are $a_1^2 e^2$, $a_1^2 e^3$, and $a_1^2 e^4$ for the charge states $-, 2-, \text{ and } 3-$, respectively. Indeed, the $-$ and $2-$ states could have excited states similar to V1,⁵ where an electron from the singlet is promoted to the doublet. However, upon comparing, e.g., $V_{\text{Si}}(k)^-$ to $(V_{\text{Si}}(k)\text{-H})^0$, we observe that there are no longer any occupied spin-down energy levels within the bandgap for the complex. All spin-down electrons are confined to the valence band. Moreover, there are only two unoccupied levels within the gap, as compared to four for V_{Si} . Upon complex formation, the energy difference between the highest occupied and lowest unoccupied Kohn-Sham energy levels is lowered by ~ 0.6 eV, indicating a drastic change in emission when V_{Si} transforms into $V_{\text{Si}}\text{-H}$. Moreover, the $3-$ state does not have excited states because the levels are fully occupied, and thus the formation of $(V_{\text{Si}}\text{-H})^q$ complexes may explain the PL quenching.

To summarize, we find from theoretical considerations that the $V_{\text{Si}}\text{-H}$ complex is stable in n-type 4H-SiC, with thermal formation (given the presence of V_{Si}) restricted by the migration barrier of interstitial hydrogen. Even though high-spin configurations likely exist for the $V_{\text{Si}}\text{-H}$ complex, capturing an H atom is found to significantly impact the electronic configuration of V_{Si} , resulting in an alteration of the optical transition and quenching of V_{Si} -related photoluminescence.

B. Experiment

In Ref. 18, the effect of H implantation on V_{Si} -related PL was compared to that of He implantation. Considering the reported results, the assumption that the formation of the $V_{\text{Si}}\text{-H}$ complex quenches luminescence from V_{Si} in turn necessitates that He does not complex with V_{Si} , or that $V_{\text{Si}}\text{-He}$ complexes retain the luminescence properties of isolated V_{Si} . Herein, we investigate the effect of fluence and temperature during hydrogen implantation on the V_{Si} luminescence intensity, to corroborate the theoretical predictions above.

Figure 6 shows the effect of different proton fluences on V_{Si} -related emission for (a) RT and (b) 400 °C hydrogen implantation. One can observe dramatic developments in the PL spectra of 4H-SiC upon irradiation, with the broad background emission (gray band) representing the virgin material being quenched after the lowest fluence irradiation and then gradually recovering at higher fluences. The intensity of the silicon vacancy-related signal is increasing with the proton fluence, and such a dependency remains linear within the 10^{11} – 10^{14} cm^{−2} fluence range, as shown earlier in Ref. 9. Upon comparing Figs. 6(a) and 6(b), we notice that the signal intensity overall increases for the 400 °C implant,

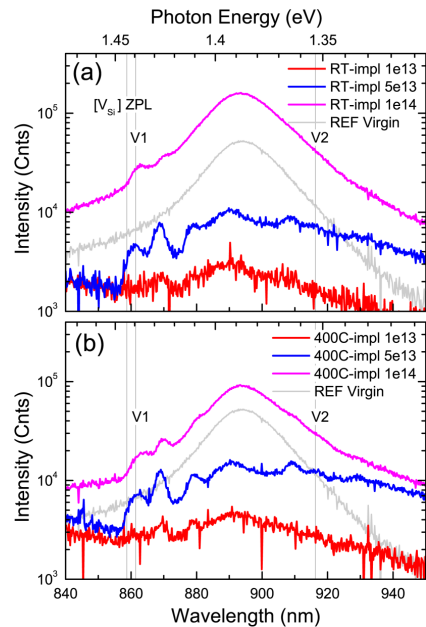


FIG. 6. Emission from n-type 4H-SiC (proton implanted to different fluences) collected at 10 K, for implantation at (a) RT and (b) 400 °C, with the V_{Si} -related emission lines V1 and V2 highlighted.

while V_{Si} -related features seem to sharpen. This effect can be attributed to the reduction in non-radiative channels at elevated temperatures.

Figure 7 displays a baseline-subtracted and zoomed-in version of Fig. 6 and compares RT and 400 °C irradiation for the three different proton fluences [(a)–(c)]. In Fig. 7(a), for the lowest proton fluence, the V1 and V2 ZPLs are barely visible as the V_{Si} concentration is below the detection level, but the elevated temperature seems to enhance the overall signal. Both V1 and V2 are clearly visible in Figs. 7(b) and 7(c), with V1 being much more prominent than V2. The total luminescence and amount of features appear greater for the 400 °C implant in all three cases. For the intermediate case, illustrated in Fig. 7(b), irradiating at 400 °C clearly impacts the V_{Si} content in the sample compared to that of the RT sample. The V1 peak is almost twice as strong for the high temperature irradiation. The moderate proton fluence of 5×10^{13} cm^{−2} falls within the scope studied in Ref. 9, where we correlate the proton fluence dependence of the V1 emission intensity to the same dependence of the S center observed in DLTS spectra of n-type 4H-SiC. Therefore, we can conclude that an increase in V1 intensity is accompanied by a similar increase in the V_{Si} concentration. Consequently, for the medium fluence (5×10^{13} cm^{−2}), we can

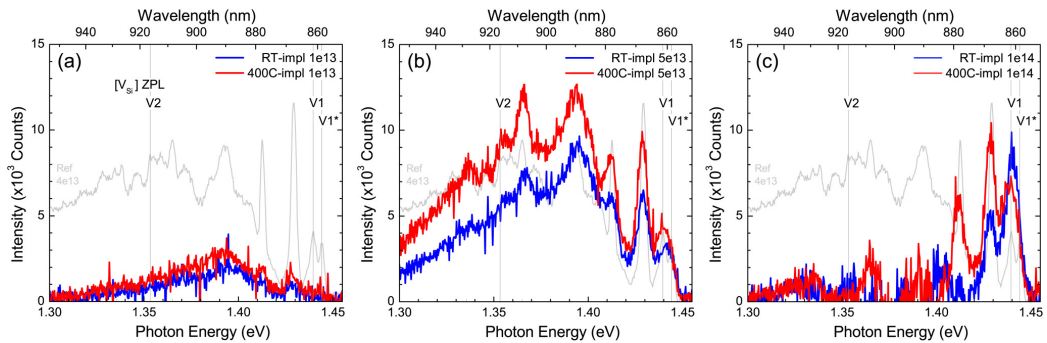


FIG. 7. Emission from n-type 4H-SiC, proton implanted at RT (blue lines) and 400 °C (red lines), collected at 10 K, for proton fluences of (a) $1 \times 10^{13} \text{ cm}^{-2}$, (b) $5 \times 10^{13} \text{ cm}^{-2}$, and (c) $1 \times 10^{14} \text{ cm}^{-2}$, with the V_{Si} -related V1 and V2 emission lines highlighted. The gray PL spectra in the background are for reference and derived from a V_{Si} -rich sample from Ref. 9.

anticipate more silicon vacancies and fewer non-radiative channels for the sample irradiated at 400 °C than the one irradiated at RT.

Interestingly, Fig. 7(c) demonstrates the opposite behavior for V1 when comparing to Fig. 7(b). In fact, the V1 peak is found to be stronger after implanting at RT than at 400 °C for the highest proton fluence. The discrepancy in temperature dependence between Figs. 7(b) and 7(c) is intriguing and challenging to explain from standard considerations concerning irradiation and temperature alone.

IV. DISCUSSION

The DFT calculations corroborate that hydrogen migrates faster in the p-type material than in an n-type material, as previously established experimentally.⁴² However, raising the temperature above 400 °C during implantation could render the H atoms mobile, even in an n-type material. Accordingly, during hot implantation, H is likely to migrate and potentially encounter an implantation-induced and nearby V_{Si} and form $V_{\text{Si}}\text{-H}$ complexes, resulting in reduced emission from V_{Si} centers. Indeed, H migration in the irradiated material is expected to be limited by dissociation of H-related complexes,^{46,47} with out-diffusion of H not commencing until above 1300 °C.⁴⁸

Post-implantation annealing should result in a similar effect on V_{Si} as that of hot implantation. Indeed, Wang *et al.*¹⁸ demonstrated that the V_{Si} -related PL increased in intensity after post-H-implantation anneals up to 300 °C, while He-implantation resulted in increasing PL intensities up to 500 °C. Importantly, silicon vacancies are metastable in n-type 4H-SiC and anneal out between 400 and 600 °C.⁵ Hence, one may speculate that the lower stability of V_{Si} after H implantation as compared to that of He may be related to formation of $V_{\text{Si}}\text{-H}$, and larger complexes thereof, assuming that H becomes mobile at or above 400 °C.

The experiments demonstrate different effects of temperature on V_{Si} -related emission, depending on the proton fluence used for

hydrogen implantation (Fig. 7). First, C and Si interstitials are expected to migrate rapidly at 400 °C, but not at RT, due to migration barriers of $\sim 1 \text{ eV}$ ⁵⁰ resulting in fewer non-radiative channels in the samples irradiated at 400 °C as compared to the RT ones. Second, V_{Si} defects may start to anneal out in this temperature range, due to the migration of H_i , recapturing of self-interstitials or transformation into $\text{C}_{\text{Si}}\text{V}_{\text{C}}$.⁵ The migration of H_i and subsequent complex formation would be dependent on the average distance between V_{Si} s and hence fluence dependent.

The diffusivity D of hydrogen is expected to follow an Arrhenius behavior in 4H-SiC, according to

$$D = D_0 e^{-E_A/kT}, \quad (3)$$

where D_0 is the exponential prefactor, E_A is the activation energy for migration, k is the Boltzmann constant, and T is the temperature.²⁹ If we assume that $D_0 = 4 \times 10^{-3} \text{ cm}^2/\text{s}$ for H_i ⁵¹ and $L = \sqrt{Dt}$ and estimate that the samples are at 400 °C for $t = 1$ hour, the diffusion length of H_i becomes $L = 22 \text{ nm}$ for a migration barrier of $E_A = 2.2 \text{ eV}$ (see Table I). Using SRIM, we estimate that the V_{Si} concentration at the top of the implantation Bragg peak is $1.3 \times 10^{16} \text{ cm}^{-3}$ for the low fluence (10^{13} cm^{-2}), $7 \times 10^{16} \text{ cm}^{-3}$ for the medium fluence ($5 \times 10^{13} \text{ cm}^{-2}$), and $1.3 \times 10^{17} \text{ cm}^{-3}$ for the high fluence (10^{14} cm^{-2}), assuming a dynamic annealing factor of 3 % for V_{Si} .⁹ These concentrations translate into mean distances between silicon vacancies (in all directions) of approximately 45 nm, 25 nm, and 20 nm, respectively. As the peak concentration of H is 3–4 times larger than that of Si vacancies, we assume that the formation of $V_{\text{Si}}\text{-H}$ is limited by the V_{Si} distribution. Hence, for the low fluence (10^{13} cm^{-2}) and medium fluence ($5 \times 10^{13} \text{ cm}^{-2}$), the diffusion length of H_i is not sufficient to efficiently form $V_{\text{Si}}\text{-H}$, while for the high fluence (10^{14} cm^{-2}), complex formation is viable and is one potential explanation for the fluence dependence observed in Fig. 7, and the temperature dependence observed in Ref. 18.

In conclusion, we find that the likelihood of a hydrogen atom diffusing far enough to encounter, and potentially form a complex with, a silicon vacancy increases with the proton irradiation fluence. Hence, hot hydrogen implantation might render H mobile and increase the amount of $V_{\text{Si}}\text{-H}$ complexes as compared to the corresponding RT process. If a maximum yield of isolated V_{Si} defects is desired and a sample volume containing the Bragg peak of H is to be probed, hydrogen should be avoided as the implantation species, with He being a more promising candidate. Alternatively, the issue can be circumvented by laser creation of point defects, as was recently demonstrated for V_{Si} in silicon carbide.^{32,33}

So far, no optical signal has been unambiguously assigned to complexes of V_{Si} and H, as the H-lines, which are located around 3.15 eV in hydrogen-rich 4H-SiC and were originally assigned to $V_{\text{Si}}\text{-H}$,⁵⁴ were later attributed to a hydrogen dimer bound to a carbon antisite ($\text{C}_{\text{Si}}\text{H}_2$).³⁵ Hence, we remain unable to directly probe the $V_{\text{Si}}\text{-H}$ formation. Electrical characterization may offer a viable alternative, as deep level transient spectroscopy (DLTS) measurements of n-type 4H-SiC have shown that hydrogen-related and irradiation-induced defects introduce deep levels within the 4H-SiC bandgap.²⁰ Recently, we demonstrated that the silicon vacancy is electrically active in n-type 4H-SiC, by assigning the $(-2-)$ and $(2-3-)$ charge state transitions of h and k V_{Si} to the S-center, a deep-level defect consisting of two different transition levels that are sporadically observed in DLTS spectra of n-type 4H-SiC.⁹ Interestingly, the predicted transition levels of $V_{\text{Si}}\text{-H}$ are ~ 0.1 eV, 1.2–1.3 eV, 2.2 eV, and 2.3–2.4 eV above the valence band maximum (Fig. 4), which is within the range found for hydrogen-related deep levels using DLTS.²⁰ However, complexes between hydrogen and carbon vacancies ($V_{\text{C}}\text{-H}$) may also be electrically active³⁶ and are thus potential candidates for the measured defect levels.

The contribution of the zero-point (vibrational) energy has not been considered herein. Indeed, H is very light, and the energy of each configuration should have the contribution of approximately $\hbar\omega/2$, where ω is the vibrational frequency of the stretch mode for the Si–H or C–H bond. Although it should have a limited impact on the calculated location of electronic levels, zero-point motion affects formation and migration energies (see, for instance, Ref. 57). For migration, the contribution of vibration to the energy barrier is expected to be found mainly in the ground state, as the transition state bonds are weaker than the ground state ones. Thus, we expect the absolute error bar of our calculations, arising from vibrations of light H atoms, to be in the 0.1–0.2 eV range (see Ref. 19).

V. CONCLUDING REMARKS

In summary, we study hydrogen-related defects in 4H-SiC and find that H_i may exist both interstitially and embedded in defect complexes. As previously found, H_i is expected to migrate much faster in a p-type than an n-type 4H-SiC material, and migration of H may be limited by the formation of complexes such as $V_{\text{Si}}\text{-H}$ in n-4H-SiC. In fact, the $V_{\text{Si}}\text{-H}$ complex is more stable than the isolated V_{Si} defect, and we find it likely that hydrogen may alter the spin and luminescence properties of V_{Si} in

n-type 4H-SiC. Upon comparing to PL emission from n-type 4H-SiC samples that are proton irradiated to different fluences and at different temperatures, we find that elevated temperature implantations may induce H_i motion, causing formation of $V_{\text{Si}}\text{-H}$ complexes and a reduction in the V_{Si} -related emission intensity. In conclusion, we predict that hydrogen could present an important obstacle toward the reliable formation of, and optimal luminescence yield from, V_{Si} defects highly suitable for quantum technology applications.

ACKNOWLEDGMENTS

Financial support was kindly provided by the Research Council of Norway and the University of Oslo through the frontier research project FUNDAMeNT (No. 251131, FriPro ToppForsk-program) and the Norwegian Micro- and Nanofabrication Facility (No. NorFAB 245963). The computations were performed on resources provided by UNINETT Sigma2—the National Infrastructure for High Performance Computing and Data Storage in Norway. J.C. acknowledges the Fundação para a Ciência e a Tecnologia (FCT) for support under Project No. UID/CTM/50025/2019, co-funded by FEDER funds through the COMPETE 2020 Program.

REFERENCES

- ¹J. R. Weber, W. F. Koehl, J. B. Varley, A. Janotti, B. B. Buckley, C. G. V. de Walle, and D. D. Awschalom, "Quantum computing with defects," *Proc. Natl. Acad. Sci. U.S.A.* **107**, 8513–8518 (2010).
- ²S. Castelletto, L. Rosa, and B. C. Johnson, "Silicon carbide for novel quantum technology devices," in *Advanced Silicon Carbide Devices and Processing* (InTech, 2015).
- ³E. Janzén, A. Gali, P. Carlsson, A. Gällström, B. Magnusson, and N. Son, "The silicon vacancy in SiC," *Phys. B Condens. Matter* **404**, 4354–4358 (2009).
- ⁴D. J. Christle, A. L. Falk, P. Andrich, P. V. Klimov, J. U. Hassan, N. T. Son, E. Janzén, T. Oshima, and D. D. Awschalom, "Isolated electron spins in silicon carbide with millisecond coherence times," *Nat. Mater.* **14**, 160–163 (2015).
- ⁵S. Castelletto, B. C. Johnson, V. Ivády, N. Stavrias, T. Umeda, A. Gali, and T. Oshima, "A silicon carbide room-temperature single-photon source," *Nat. Mater.* **13**, 151–156 (2014).
- ⁶H. J. von Bardeleben, J. L. Cantin, A. Csóré, A. Gali, E. Rauls, and U. Gerstmann, "NV centers in 3C, 4H, and 6H silicon carbide: A variable platform for solid-state qubits and nanosensors," *Phys. Rev. B* **94**, 121202(R) (2016).
- ⁷R. Nagy, M. Widmann, M. Niethammer, D. B. R. Dasari, I. Gerhardt, Ö. O. Soykal, M. Radulaski, T. Oshima, J. Vucković, N. T. Son, I. G. Ivanov, S. E. Economou, C. Bonato, S.-Y. Lee, and J. Wrachtrup, "Quantum properties of dichroic silicon vacancies in silicon carbide," *Phys. Rev. Appl.* **9**, 034022 (2018).
- ⁸R. Nagy, M. Niethammer, M. Widmann, Y.-C. Chen, P. Udvarhelyi, C. Bonato, J. U. Hassan, R. Karhu, I. G. Ivanov, N. T. Son, J. R. Maze, T. Oshima, Ö. O. Soykal, A. Gali, S.-Y. Lee, F. Kaiser, and J. Wrachtrup, "High-fidelity spin and optical control of single silicon-vacancy centres in silicon carbide," *Nat. Commun.* **10**, 1054 (2019).
- ⁹M. E. Bathen, A. Galeckas, J. Mütting, H. M. Ayedh, U. Grossner, J. Coutinho, Y. K. Frodason, and L. Vines, "Electrical charge state identification and control for the silicon vacancy in 4H-SiC," *npj Quant. Inform.* **9**, 111 (2019).
- ¹⁰C. P. Anderson, A. Bourassa, K. C. Miao, G. Wolfowicz, P. J. Mintun, A. L. Crook, H. Abe, J. U. Hassan, N. T. Son, T. Oshima, and D. D. Awschalom,

"Electrical and optical control of single spins integrated in scalable semiconductor devices," *Science* **366**, 1225–1230 (2019).

¹¹C. F. de la Casas, D. J. Christle, J. U. Hassan, T. Ohshima, N. T. Son, and D. D. Awschalom, "Stark tuning and electrical charge state control of single divacancies in silicon carbide," *Appl. Phys. Lett.* **111**, 262403 (2017).

¹²M. Wagner, B. Magnusson, W. M. Chen, E. Janzén, E. Sörman, C. Hallin, and J. L. Lindström, "Electronic structure of the neutral silicon vacancy in 4H and 6H SiC," *Phys. Rev. B* **62**, 16555 (2000).

¹³M. Widmann, S.-Y. Lee, T. Rendler, N. T. Son, H. Fedder, S. Paik, L.-P. Yang, N. Zhao, S. Yang, I. Booker, A. Denisenko, M. Jamali, S. A. Momenzadeh, I. Gerhardt, T. Ohshima, A. Gali, E. Janzén, and J. Wrachtrup, "Coherent control of single spins in silicon carbide at room temperature," *Nat. Mater.* **14**, 164–168 (2014).

¹⁴M. Radulaski, M. Widmann, M. Niethammer, J. L. Zhang, S.-Y. Lee, T. Rendler, K. G. Lagoudakis, N. T. Son, E. Janzén, T. Ohshima, J. Wrachtrup, and J. Vucković, "Scalable quantum photonics with single color centers in silicon carbide," *Nano. Lett.* **17**, 1782–1786 (2017).

¹⁵M. Widmann, M. Niethammer, D. Y. Fedyanin, I. A. Khramtsov, T. Rendler, I. D. Booker, J. U. Hassan, N. Morioka, Y.-C. Chen, I. G. Ivanov, N. T. Son, T. Ohshima, M. Bockstedte, A. Gali, C. Bonato, S.-Y. Lee, and J. Wrachtrup, "Electrical charge state manipulation of single silicon vacancies in a silicon carbide quantum optoelectronic device," *Nano. Lett.* **19**, 7173–7180 (2019).

¹⁶B. Zippelius, J. Suda, and T. Kimoto, "High temperature annealing of n-type 4H-SiC: Impact on intrinsic defects and carrier lifetime," *J. Appl. Phys.* **111**, 033515 (2012).

¹⁷H. Kraus, D. Simin, C. Kasper, Y. Suda, S. Kawabata, W. Kada, T. Honda, Y. Hijikata, T. Ohshima, V. Dyakonov, and G. V. Astakhov, "Three-dimensional proton beam writing of optically active coherent vacancy spins in silicon carbide," *Nano. Lett.* **17**, 2865–2870 (2017).

¹⁸J.-F. Wang, Q. Li, F.-F. Yan, H. Liu, G.-P. Guo, W.-P. Zhang, X. Zhou, L.-P. Guo, Z.-H. Lin, J.-M. Cui, X.-Y. Xu, J.-S. Xu, C.-F. Li, and G.-C. Guo, "On-demand generation of single silicon vacancy defects in silicon carbide," *ACS Photonics* **6**, 1736–1743 (2019).

¹⁹B. Aradi, A. Gali, P. Deák, J. E. Lowther, N. T. Son, E. Janzén, and W. J. Choyke, "Ab initio density-functional supercell calculations of hydrogen defects in cubic SiC," *Phys. Rev. B* **63**, 245202 (2001).

²⁰G. Alfieri, E. V. Monakhov, B. G. Svensson, and A. Hallén, "Defect energy levels in hydrogen-implanted and electron-irradiated n-type 4H silicon carbide," *J. Appl. Phys.* **98**, 113524 (2005).

²¹G. Kresse and J. Hafner, "Ab initio molecular dynamics for liquid metals," *Phys. Rev. B* **47**, 558–561 (1993).

²²G. Kresse and J. Hafner, "Ab initio molecular-dynamics simulation of the liquid-metal–amorphous-semiconductor transition in germanium," *Phys. Rev. B* **49**, 14251–14269 (1994).

²³G. Kresse and J. Furthmüller, "Efficiency of ab-initio total energy calculations for metals and semiconductors using a plane-wave basis set," *Comput. Mater. Sci.* **6**, 15–50 (1996).

²⁴G. Kresse and J. Furthmüller, "Efficient iterative schemes for ab initio total-energy calculations using a plane-wave basis set," *Phys. Rev. B* **54**, 11169–11186 (1996).

²⁵P. E. Blöchl, "Projector augmented-wave method," *Phys. Rev. B* **50**, 17953–17979 (1994).

²⁶J. P. Perdew, K. Burke, and M. Ernzerhof, "Generalized gradient approximation made simple," *Phys. Rev. Lett.* **77**, 3865–3868 (1996).

²⁷J. Heyd, G. E. Scuseria, and M. Ernzerhof, "Hybrid functionals based on a screened Coulomb potential," *J. Chem. Phys.* **118**, 8207–8215 (2003).

²⁸A. V. Krutau, O. A. Vydrov, A. F. Izmaylov, and G. E. Scuseria, "Influence of the exchange screening parameter on the performance of screened hybrid functionals," *J. Chem. Phys.* **125**, 224106 (2006).

²⁹M. E. Batten, J. Coutinho, H. M. Ayedh, J. U. Hassan, I. Farkas, S. Öberg, Y. K. Frodason, B. G. Svensson, and L. Vines, "Anisotropic and plane-selective migration of the carbon vacancy in SiC: Theory and experiment," *Phys. Rev. B* **100**, 014103 (2019).

³⁰P. Grivickas, V. Grivickas, J. Linnros, and A. Galeckas, "Fundamental band edge absorption in nominally undoped and doped 4H-SiC," *J. Appl. Phys.* **101**, 123521 (2007).

³¹S. B. Zhang and J. E. Northrup, "Chemical potential dependence of defect formation energies in GaAs: Application to Ga self-diffusion," *Phys. Rev. Lett.* **67**, 2339 (1991).

³²C. Freysoldt, B. Grabowski, T. Hickel, J. Neugebauer, G. Kresse, A. Janotti, and C. G. V. de Walle, "First-principles calculations for point defects in solids," *Rev. Modern Phys.* **86**, 253–305 (2014).

³³C. Freysoldt, J. Neugebauer, and C. G. V. de Walle, "Fully ab initio finite-size corrections for charged-defect supercell calculations," *Phys. Rev. Lett.* **102**, 016402 (2009).

³⁴Y. Kumagai and F. Oba, "Electrostatics-based finite-size corrections for first-principles point defect calculations," *Phys. Rev. B* **89**, 195205 (2014).

³⁵H.-P. Komsa, T. T. Rantala, and A. Pasquarello, "Finite-size supercell correction schemes for charged defect calculations," *Phys. Rev. B* **86**, 045112 (2012).

³⁶G. Mills and H. Jónsson, "Quantum and thermal effects in H₂ dissociative adsorption: Evaluation of free energy barriers in multidimensional quantum systems," *Phys. Rev. Lett.* **72**, 1124–1127 (1994).

³⁷G. Mills, H. Jónsson, and G. K. Schenter, "Reversible work transition state theory: Application to dissociative adsorption of hydrogen," *Surf. Sci.* **324**, 305–337 (1995).

³⁸M. Kaukonen, C. J. Fall, and J. Lento, "Interstitial H and H₂ in SiC," *Appl. Phys. Lett.* **83**, 923 (2003).

³⁹X.-Y. Yang, Z. Wang, Y. Lu, Z. Sun, S. Hussain, and P. Zhang, "First-principles study of hydrogen retention and diffusion behaviors in 4H-SiC," *Superlatt. Microstruct.* **122**, 362–370 (2018).

⁴⁰J. F. Ziegler, M. Ziegler, and J. Biersack, "SRIM—the stopping and range of ions in matter (2010)," *Nucl. Instrum. Methods Phys. Res. Sec. B* **268**, 1818–1823 (2010).

⁴¹J. Coutinho, V. J. B. Torres, K. Demmouche, and S. Öberg, "Theory of the carbon vacancy in 4H-SiC: Crystal field and pseudo-Jahn-Teller effects," *Phys. Rev. B* **96**, 174105 (2017).

⁴²N. Achtziger, J. Grillenberger, M. Witthuhn, M. K. Linnarsson, M. Janson, and B. G. Svensson, "Hydrogen passivation of silicon carbide by low-energy ion-implantation," *Appl. Phys. Lett.* **73**, 945–947 (1998).

⁴³B. Aradi, P. Deák, and A. Gali, "Diffusion of hydrogen in perfect, p-type doped, and radiation-damaged 4H-SiC," *Phys. Rev. B* **69**, 233202 (2004).

⁴⁴L. Storasta, J. P. Bergman, E. Janzén, A. Henry, and J. Lu, "Deep levels created by low energy electron irradiation in 4H-SiC," *J. Appl. Phys.* **96**, 4909–4915 (2004).

⁴⁵M. L. David, G. Alfieri, E. M. Monakhov, A. Hallén, C. Blanchard, B. G. Svensson, and J. F. Barbot, "Electrically active defects in irradiated 4H-SiC," *J. Appl. Phys.* **95**, 4728–4733 (2004).

⁴⁶M. J. K. Linnarsson, J. P. Doyle, and B. G. Svensson, "Diffusion of hydrogen in 6H silicon carbide," in *Proceedings in Materials Research Society Symposium: III-Nitride, SiC and Diamond Materials for Electronic Devices*, edited by D. K. Gaskill, C. D. Brandt, and R. J. Nemanich (Materials Research Society, Pittsburgh, 1996), Vol. 423, p. 625.

⁴⁷M. Janson, M. K. Linnarsson, A. Hallén, and B. G. Svensson, in *Proceedings in Materials Research Society Symposium: Hydrogen in Semiconductors and Metals*, edited by N. H. Nickel, W. B. Jackson, and R. C. Bowman (Materials Research Society, Pittsburgh, 1998), Vol. 513, p. 439.

⁴⁸M. K. Linnarsson, M. S. Janson, U. Forsberg, and E. Janzén, "In-diffusion, trapping and out-diffusion of deuterium in 4H-SiC substrates," *Mater. Sci. Forum* **527–529**, 637–640 (2006).

⁴⁹V. Ivády, J. Davidsson, N. T. Son, T. Ohshima, I. A. Abrikosov, and A. Gali, "Identification of Si-vacancy related room-temperature qubits in 4H silicon carbide," *Phys. Rev. B* **96**, 161114(R) (2017).

⁵⁰N. Iwamoto and B. G. Svensson, "Point defects in silicon carbide," in *Defects in Semiconductors, Semiconductors and Semimetals* Vol. 91, edited by L. Romano, V. Privitera, and C. Jagadish (Elsevier, 2015), Chap. 10, pp. 369–407.

- ⁵¹J. Philibert, in *Atom Movements: Diffusion and Mass Transport in Solids*, Monographies de physique (Editions de Physique, 1991).
- ⁵²S. Castelletto, A. F. M. Almutairi, K. Kumagai, T. Katkus, Y. Hayasaki, B. C. Johnson, and S. Juodkazis, "Photoluminescence in hexagonal silicon carbide by direct femtosecond laser writing," *Opt. Lett.* **43**, 6077–6080 (2018).
- ⁵³Y.-C. Chen, P. S. Salter, M. Niethammer, M. Widmann, F. Kaiser, R. Nagy, N. Morioka, C. Babin, J. Erlekampf, P. Berwian, M. J. Booth, and J. Wrachtrup, "Laser writing of scalable single color centers in silicon carbide," *Nano Lett.* **19**, 2377–2382 (2019).
- ⁵⁴W. J. Choyke and L. Patrick, "Photoluminescence of H- and D-implanted 4H SiC," *Phys. Rev. B* **9**, 3214 (1974).
- ⁵⁵D. Prezzi, T. A. G. Eberlein, R. Jones, B. Hourahine, P. R. Briddon, and S. Öberg, "Hydrogen-related photoluminescent centers in SiC," *Phys. Rev. B* **70**, 205207 (2004).
- ⁵⁶A. Gali, B. Aradi, P. Deák, W. J. Choyke, and N. T. Son, "Overcoordinated hydrogens in the carbon vacancy: Donor centers of SiC," *Phys. Rev. Lett.* **84**, 4926 (2000).
- ⁵⁷S. Z. Karazhanov, M. Ganchenkova, and E. S. Marstein, "Vibrational zero point energy for H-doped silicon," *Chem. Phys. Lett.* **601**, 49–53 (2014).

Paper VI

Conversion pathways of primary defects by annealing in proton-irradiated n -type 4H-SiC

R. Karsthof, M. E. Bathen, A. Galeckas, L. Vines

Accepted in *Physical Review B* (2020).

VI

Conversion pathways of primary defects by annealing in proton-irradiated n -type 4H-SiC

Robert Karsthof, Marianne Etzelmüller Bathen, Augustinas Galeckas, and Lasse Vines

Centre for Materials Science and Nanotechnology, Universitetet i Oslo, Gaustadalléen 23A, 0373 Oslo, Norway^{a)}

(Dated: 7 July 2020)

The development of defect populations after proton irradiation of n -type 4H-SiC and subsequent annealing experiments is studied by means of deep level transient (DLTS) and photoluminescence (PL) spectroscopy. A comprehensive model is suggested describing the evolution and interconversion of irradiation-induced point defects during annealing below 1000 °C. The model proposes the EH_4 and EH_5 traps frequently found by DLTS to originate from the $(+/-0)$ charge transition level belonging to different configurations of the carbon antisite-carbon vacancy (CAV) complex. Furthermore, we show that the transformation channel between the silicon vacancy (V_{Si}) and CAV is effectively blocked under n -type conditions, but becomes available in samples where the Fermi level has moved towards the center of the band gap due to irradiation-induced donor compensation. The annealing of V_{Si} and the carbon vacancy (V_{C}) is shown to be dominated by recombination with residual self-interstitials at temperatures of up to 400 °C. Going to higher temperatures, a decay of the CAV pair density is reported which is closely correlated to a renewed increase of V_{C} concentration. A conceivable explanation for this process is the dissociation of the CAV pair into separate carbon antisites and V_{C} defects. Lastly, the presented data supports the claim that the removal of free carriers in irradiated SiC is due to introduced compensating defects and not passivation of shallow nitrogen donors.

I. INTRODUCTION

Silicon carbide (SiC) possesses a variety of point defects and defect complexes that are promising for quantum communication and quantum computing applications, due to both the emission of single photons upon optical excitation and the existence of high-spin states for electrons being trapped at these defect sites. Among the most studied polytypes (3C, 4H, 6H), 4H-SiC possesses the largest band gap of 3.23 eV at room temperature. It can be grown with acceptably low residual impurity concentrations such that intrinsic defects play a dominant and controllable role in material properties. Moreover, many of its intrinsic defects that can be introduced by electron or ion irradiation, or implantation, have been shown to be excellent candidates for quantum building blocks¹.

Herein, we mainly consider six intrinsic defects in 4H-SiC that are electrically and/or optically detectable: the carbon and silicon vacancies (V_{C} , V_{Si}) and self-interstitials (C_i , Si_i), the carbon antisite-carbon vacancy pair ($\text{C}_{\text{Si}}\text{V}_{\text{C}}$), and the divacancy ($\text{V}_{\text{C}}\text{V}_{\text{Si}}$). The V_{C} has been shown to have formation energies below 5 eV^{2,3}, and therefore is expected to be present in as-grown SiC, in accordance with experimental observations^{4,5}. In 4H-SiC, V_{C} can occur in two crystallographically inequivalent lattice sites labeled h and k for pseudo-hexagonal and pseudo-cubic, respectively, and the formation energies of these two defects can differ by several 100 meV, depending on the charge state². V_{C} also exhibits strong negative- U effects and a pronounced Jahn-Teller distortion

of the singly-negative charge state^{6,7}, leading to the direct transition from the neutral to doubly-negative $(0/2-)$ acceptor state at around 0.7 eV below the conduction band edge E_{C} ⁸. V_{C} seems to be an efficient center for non-radiative recombination and is therefore considered a lifetime-limiting defect⁹ which has detrimental implications for bipolar devices.

The formation energy of the silicon monovacancy V_{Si} spans over a large range from around 7.5 eV under p -type and intrinsic conditions to as low as 4.5 eV in n -type SiC^{2,3}. V_{Si} is mainly acceptor-like, possessing charge states between neutral and threefold negative, although a shallow donor-like $(+/-0)$ transition close to the valence band is possible^{2,3}. Analogously to V_{C} , two configurations of $\text{V}_{\text{Si}}(h, k)$ exist. Charge transition levels (CTLs) for the V_{Si} occur at around $E_{\text{C}} - 0.7$ eV for the $(-2/-)$ and $E_{\text{C}} - 0.4$ eV for the $(2-/-3-)$ levels^{2,10}. V_{Si} , in contrast to V_{C} , does not exhibit negative- U character. The singly-negative charge state of V_{Si} is optically addressable with a spin of $S = 3/2$ that has been shown to have a long spin coherence time¹¹. This makes it an ideal candidate for both solid-state qubits as well as single-photon sources, given its favorable emission wavelengths in the near-infrared spectral range (V lines). V_{Si} defects can be controllably introduced into SiC by proton irradiation¹² and its charge state can be controlled using, e.g., Schottky barrier diodes¹⁰.

The carbon antisite-carbon vacancy pair (CAV pair) is considered the counterpart to V_{Si} ¹³, because it can be formed by a single carbon hop into a neighboring V_{Si} . In p -type material, the formation energies of the CAV pair are significantly lower than that of the V_{Si} ². At around 1 eV below the conduction band edge E_{C} , the situation is reversed, with V_{Si} becoming thermodynamically slightly more favorable. Because the CAV pair in-

^{a)}Electronic mail: r.m.karsthof@smn.uio.no

volves one site from the C and another from the Si sublattice, four inequivalent configurations of the CAV pair can be realized, termed hh , hk , kh and kk , adapting the notation for the monovacancies and referring to the Si site with the first and the C site with the second symbol, respectively. The CAV pair possesses three CTLs within the 4H-SiC band gap, two of which are donor-like ($(2+/+)$ and $(+/0)$ transitions at roughly mid-gap and 1.0-1.1 eV below E_C , respectively) and one is acceptor-like ($(0/-)$ CTL, around 0.5 eV below E_C). The CAV pair in its singly-positive charge state is known to be an ultra-bright single-photon source, emitting in the visible spectral range¹⁴ (AB lines).

It shall be noted that the silicon antisite-vacancy pair ($\text{Si}_\text{C}\text{V}_\text{Si}$) is excluded from the list of relevant defect complexes here because it has been shown to be unstable with regard to V_C ¹⁵.

Formation of the divacancy $\text{V}_\text{Si}\text{V}_\text{C}$ (VV)^{4,16} requires not only abundance of single Si and C vacancies, but also their adjacency which can be achieved at elevated temperatures via defect diffusion. Therefore, although its formation energy has been calculated to be in the same range as for V_Si and the CAV pair¹⁷, the equilibrium concentration of VV defects depends on the extent to which the single vacancies (mostly V_Si , due to their lower migration barriers as compared to V_C ¹⁸) are allowed to diffuse, for example through post-annealing or during high-temperature growth or irradiation. Thermodynamic CTLs for the VV defect have been calculated in the literature to be in the range of 0.7-0.9 eV and 1.2-1.4 eV below E_C for the $(-/2-)$ and $(0/-)$ CTLs, respectively¹⁹⁻²¹. Analogously to the CAV pair, being a complex comprising two lattice sites, there are four non-degenerate configurations of the VV as well, yielding an energetic spread of each of the CTLs. The VV defect in the neutral charge state is also a known single-photon source in 4H-SiC, emitting in the infrared range around 1.2 eV^{20,22}.

Even though many routes have been explored on how to introduce and control certain defects by irradiation and subsequent annealing, a complete picture of the conversion pathways through which defects can be interconverted, and under which conditions this occurs, is still missing. Such a general model can be expected to be indispensable when developing post-irradiation annealing strategies to achieve a specific population of defects. This paper aims at taking a step towards such a model by studying epilayers that are proton-irradiated to a wide range of fluences, and thereafter annealed in isochronal steps to increasingly higher temperatures. In each step, the defect population is monitored by means of deep level transient spectroscopy (DLTS) and photoluminescence (PL) spectroscopy in order to reveal defect interconversion and out-annealing processes.

II. EXPERIMENTAL METHODS

The investigated samples consisted of 10 μm thick, nitrogen-doped, (0001) oriented epitaxial 4H SiC layers, purchased from Cree Inc. The doping concentration was around $N_\text{D} \approx 1 \times 10^{15} \text{ cm}^{-3}$, as determined by capacitance-voltage (C - V) measurements. The n -doping of the SiC substrate amounted to about $8 \times 10^{18} \text{ cm}^{-3}$. Formation of intrinsic defects was achieved by room temperature irradiation with 1.8 MeV protons, having a projected range of 27 μm , well outside the epilayer, as simulated based on collision Monte Carlo models implemented in the SRIM package²³. In order to suppress channeling effects, the incident beam was tilted by 8° with respect to the surface normal. Irradiation fluences were chosen between $1 \times 10^{11} \text{ cm}^{-2}$ and $6 \times 10^{13} \text{ cm}^{-2}$. This lead to two subsets of samples: one in the fluence range of up to $4 \times 10^{12} \text{ cm}^{-2}$, with trap concentrations being low enough ($< 0.2N_\text{D}$) to perform DLTS measurements, and one being subjected to higher fluences that exhibited defect concentrations above the lower detectivity threshold for PL measurements. Moreover, the higher-fluence set showed full donor compensation and was therefore not suitable for DLTS initially.

After irradiation the samples were thermally annealed at 300 $^\circ\text{C}$ in a tube furnace in flowing N_2 ($30 \text{ cm}^3 \text{ min}^{-1}$) to alleviate the influence of irradiation-induced unstable defects. In order to perform defect spectroscopy measurements, Schottky barrier diodes (SBDs) were fabricated on the epilayer surface, using electron beam-evaporated nickel patterned by deposition through a shadow mask. Before SBD fabrication, the samples underwent RCA cleaning to remove contaminations, including any SiO_2 surface layers. The SBDs were of circular cross-sections and had an area of $7.85 \times 10^{-3} \text{ cm}^2$, with a Ni thickness of 150 nm. The samples intended for PL measurements were thoroughly cleaned in an ultrasonic bath in acetone and isopropyl alcohol for 5 minutes each, but were left untreated otherwise.

In order to study the influence of thermal treatment on defect conversion, isothermal annealing at increasingly higher temperatures and subsequent DLTS characterization was performed. This included the removal of SBDs before each annealing step to avoid in-diffusion and alloying of Ni into the SiC surface. For that purpose, the samples were placed in a 5:1:1 mixture of $\text{DI-H}_2\text{O:HCl:H}_2\text{O}_2$ at a temperature of 80 $^\circ\text{C}$ for ten minutes, which leaves the SiC free of metal residues. After annealing, the samples were quenched to room temperature using a cold plate, and the SBDs were re-applied. The annealing steps took place at 400 $^\circ\text{C}$, 600 $^\circ\text{C}$, 800 $^\circ\text{C}$ and 1000 $^\circ\text{C}$, otherwise analogously to the conditions described for the first step above.

DLTS measurements were carried out using a high-temperature setup operating between 77 K and 700 K. The measurement frequency was 1 MHz, the pulse length was 20 ms and the pulse height 10 V at a reverse bias of -10 V . Six rate windows between 20 ms and 640 ms were

chosen for evaluation of the transients, using a standard lock-in correlation function. The concentrations of the different levels found in the measured spectra were extracted by a numerical simulation of the transients and the resulting spectra, based on assumed (variable) values for trap energy, capture cross section and density of the traps. The lambda correction was included for increased accuracy of the thusly determined trap concentrations. Photoluminescence measurements were carried out using a closed-cycle He refrigerator system (Janis, CCS450) and a 405 nm wavelength cw-laser of 75 mW power as excitation source. The focused laser beam, impinging on the sample surface at a 27° angle, yielded an excitation intensity of $\leq 1 \text{ kW cm}^{-2}$ and polarization perpendicular to the optic c -axis of 4H-SiC. The PL signal was collected in a back-scattering geometry by a microscope objective (Mitutoyo, LWD 10X), spectrally filtered (long-pass LP 550 nm filter) and analyzed by an imaging spectrometer (Horiba, iHR320) coupled to an EMCCD camera (Andor, iXon Ultra 888) with a spectral resolution below 0.2 nm. A near-confocal configuration of the detection, ensured by a high numerical aperture objective and narrow slit of the imaging spectrometer, allowed for maximized collection of the PL signal from the uppermost 3–4 μm of the epilayer.

III. RESULTS AND DISCUSSION

A. Assessment of initial defect populations

Fig. 1 shows DLTS spectra of samples irradiated to three different fluences, and subsequently annealed at 300°C (pre-diffusion) for measurement temperatures between about 180 K and 570 K, where six frequently reported trap levels are visible. The activation energies of these levels are summarized in Table I, together with assignments to specific point defects made in the literature. The defect levels dominating the spectra, independent of irradiation fluence, are the so-called $Z_{1/2}$ level, which has been attributed to the $(0/2-)$ CTL of the carbon vacancy V_C ^{8,24}, and the S center possessing the levels S_1 and S_2 , which have been identified as the $(-/2-)$ and $(2-/3-)$ CTLs of the silicon vacancy V_{Si} ¹⁰. We consequently interpret their concentration as equivalent to the content of V_C and V_{Si} ²⁵. The feature labelled $EH_{6/7}$ at the high-temperature end of the spectra has been associated with the deeper lying $(2+/+/0)$ CTLs of V_C in different configurations²⁶. Two more peaks are noteworthy: EH_4 , a rather broad and asymmetric peak spreading between about 350 K and 450 K, and EH_5 , which in the 300°C annealed samples appears only as a weak shoulder on the low-temperature flank of $EH_{6/7}$. By using a high-resolution weighting function for the DLTS spectra, it becomes apparent that EH_4 possesses a substructure, and that three levels in total are needed to explain the considerable broadening in temperature this feature exhibits (inset of Fig. 1). The chemical identity of the de-

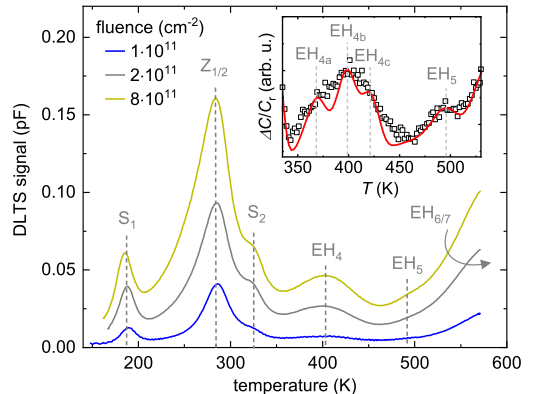


FIG. 1. DLTS spectra of 4H-SiC proton-irradiated to three different fluences after an initial annealing step to 300°C , with dominant defect levels indicated. The corresponding rate window was 1.56 s^{-1} . Inset: high-resolution DLTS spectrum (fluence $8 \times 10^{11} \text{ cm}^{-2}$) showing the temperature region of the EH_4 and EH_5 traps, revealing three contributions to EH_4 .

TABLE I. Properties of defect levels documented in Fig. 1 (trap energy with respect to conduction band edge, as well as assignments to specific point defects from the literature).

label	$E_C - E_t$ (eV)	assignment, reference
S_1	0.42	$V_{Si} (2-/3-)$ ¹⁰
$Z_{1/2}$	0.67	$V_C (0/2-)$ ^{8,24}
S_2	0.71	$V_{Si} (1-/2-)$ ¹⁰
EH_4	≈ 1.0	
EH_5	≈ 1.1	
$EH_{6/7}$	1.5-1.6	$V_C (2+/+/0)$ ^{8,26}

fects or defect complexes producing both EH_4 and EH_5 has not been clarified so far.

While the V_C acts mainly as a non-radiative recombination center and therefore does not emit light, V_{Si} , CAV and VV have well-documented PL lines in certain charge states. Fig. 2 demonstrates the light emission from these three defects in two irradiated (to different fluences) samples at pre-diffusion conditions. Due to its energetically inequivalent configurations, the positively charged CAV pair $(C_{Si}V_C)^+$ exhibits a set of multiple emission lines in the range 648 nm–677 nm (labeled AB lines, Fig. 2(a))¹³. As can be seen, AB emission becomes visible for increasing irradiation fluence, and is channeled mainly into the B1/B2 line pair associated with excited states of the kk configuration of CAV²⁷. Importantly, it can be stated that the CAV pair is present in our samples to detectable amounts after proton irradiation and pre-diffusion.

Figs. 2(b) and 2(c) display the emission windows from the silicon vacancy. The so-called V lines appear in two regions, one of which contains the double line $V1/V1'$ at 858.7 and 861.3 nm, and the other is the single V2 line at

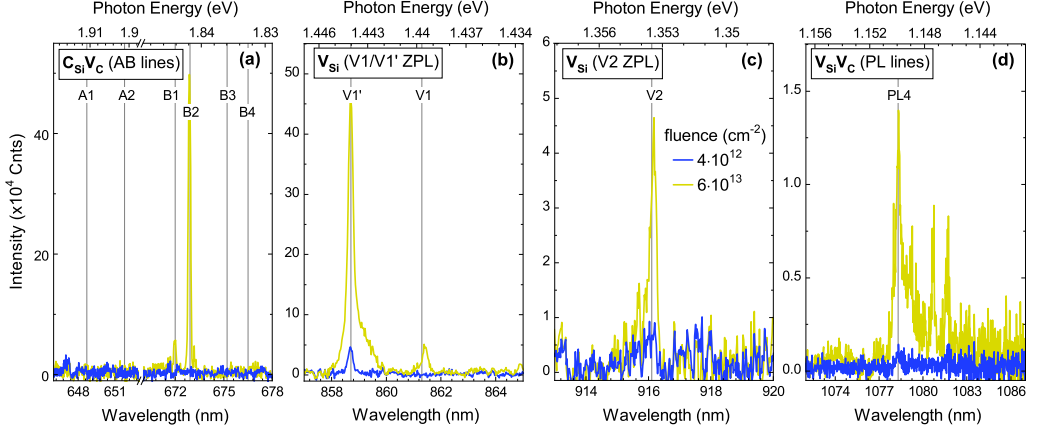


FIG. 2. PL spectra of SiC epilayers irradiated to two different fluences and post-annealed at 300 °C. Measurements were done at 10 K in four different spectral windows containing the emission of (a) the CAV defect (AB lines), V_{Si} with (b) its $V1/V1'$ doublet and (c) $V2$ lines, and (d) the divacancy (PL4 line). Excitation at 405 nm, 75 mW (cw). Vertical grey lines are reference values for the lines.

916.1 nm. These have been associated with emission from excited states of the single negative V_{Si} defect on the h and k site for the $V1/V1'$ and $V2$ lines, respectively²⁸. Under the experimental conditions used here, emission from V_{Si} is mainly channeled into the $V1'$ line. Emission from the divacancy $V_{Si}V_C$, in its neutral charge state, is shown in the fourth window in Fig. 2(d). Analogously to the CAV pair, the VV is a two-component complex possessing four inequivalent configurations as well, each emitting at a specific IR wavelength in a wide range between 1077 and 1132 nm^{20,29}. The lines are labeled PL1, PL2, PL3 and PL4, of which we only show the latter due to detection limitations for longer wavelengths. PL4 has been shown to belong to the hk configuration of the VV defect²⁰. Similar to CAV, the divacancy is present in irradiated and pre-diffused SiC in our experiments.

B. Identification of the $C_{Si}V_C$ defect by DLTS

Turning to the defect identity giving rise to the EH_4 and EH_5 traps in DLTS, we start with the observation that the occurrence of these traps is correlated, i.e. either both or none of them are detectable in the same experiment. Moreover, their concentrations are always seen to be very similar, which is shown for the present study in Fig. 3. We take this as an indication for a common origin of the traps. Moreover, the $EH_{4,5}$ traps occur in concentrations similar to, but slightly lower than, those of the isolated vacancies V_C , V_{Si} (Fig. 3). For these defects, dynamic annealing and the subsequent 300 °C anneal have been estimated to leave 3 % of the initially created vacancies remaining¹⁰. Based on their similar concentrations,

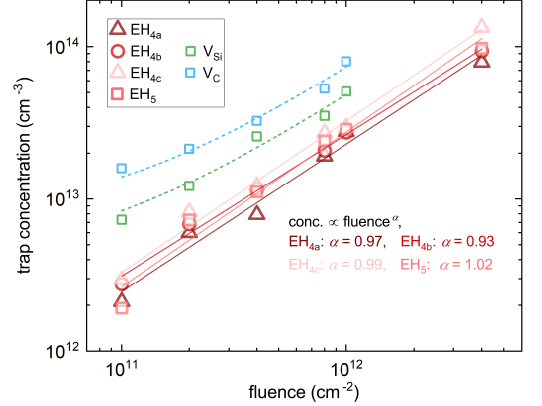


FIG. 3. Fluence dependence of the concentration of EH_4 and EH_5 traps, as well as V_C and V_{Si} , after pre-diffusion. Compact lines: fits demonstrating the linear fluence dependence of $EH_{4,5}$ traps. Dashed lines: fits to V_C and V_{Si} concentrations according to a shifted-linear model.

it can be stated that the rate of introduction of the defect causing the $EH_{4,5}$ traps to appear is comparable, although slightly lower, than that of the monovacancies. This rules out larger defect complexes as the origin, a claim that is also supported by the fluence dependence of the $EH_{4,5}$ level concentration in Fig. 3. For a primary defect like V_{Si} and V_C , above a certain background level, a linear relationship of concentration with fluence is expected. This is exemplified by the linear fits³⁰ to the

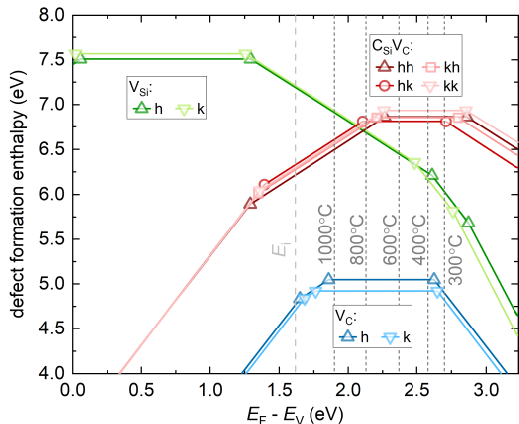


FIG. 4. Defect formation enthalpies in the carbon-rich limit for the V_{Si} , V_C and $C_{Si}V_C$ defects in different configurations, values adapted from Ref.². Position of Fermi energy for the temperatures used in our annealing experiment, and intrinsic Fermi level present after high-fluence irradiation, indicated as dashed lines.

monovacancy concentrations in Fig. 3. For higher-order defect complexes, the fluence dependence is expected to be superlinear, as multiple displacement events have to occur at adjacent lattice sites in order to create them. Fig. 3 shows that for all four traps $EH_{4,5}$, the fluence dependence is linear, which combined with the large introduction rate narrows down the list of candidates responsible for these levels to small complexes involving V_C , V_{Si} , Si_i and C_i , and possibly another impurity contained in the sample with significant concentrations. However, a participation of interstitials is unlikely due to their low thermal stability³¹ as compared to the $EH_{4,5}$ levels. This will be further supported by the thermal evolution of the defect population below. Moreover, electron irradiation experiments with energies below and above the Si displacement threshold^{32,33} have shown that $EH_{4,5}$ only appear when V_{Si} is created. Therefore, the Si vacancy is likely to be involved in their formation.

Since the nitrogen content in the samples is approximately 10^{15} cm^{-3} , an additional involvement of N is conceivable, for example in the form of $N_C V_{Si}$ (NV) centers. There are, however, arguments opposing this assignment. The formation of NV centers during room-temperature irradiation is possible when a V_{Si} is formed adjacent to a N_C donor. Because this process is much less likely than the formation of V_{Si} at any lattice site, the initial density of NV centers is lower than $[V_{Si}]$ (brackets [] denote concentration) by some orders of magnitude, so we do not expect NV to be detectable in DLTS in the pre-diffusion stage – in particular not in concentrations comparable to $[V_{Si}]$ itself, as seen in Fig. 3. Further, the $EH_{4,5}$ levels have been observed in a variety of SiC mate-

rial from different sources, including nominally undoped epilayers³⁴. Consequently, the candidates responsible for the $EH_{4,5}$ traps can be further narrowed down to simple and intrinsic defect complexes involving V_{Si} . This leaves mainly two possibilities: the CAV pair, and the divacancy.

The formation energy diagram for the V_C , V_{Si} and CAV defects as calculated in Ref.² is reproduced in Fig. 4. CTLs related to the divacancy have not been calculated in the referenced work, but are generally expected to be in the range 0.7 eV–0.9 eV and 1.2 eV–1.4 eV, as discussed in the introduction. It must be stated that no prominent traps with activation energies in that range have been found by DLTS in the present work. Moreover, even though VV could be detected by PL for the highest-fluence samples in the pre-diffusion stage, [VV] is expected to be low in the lowest-fluence sample set when compared to V_{Si} , for example, while $[S_2]$ and $[EH_{4,5}]$ are of the same magnitude in these samples. We therefore argue for discarding the divacancy as the origin of the $EH_{4,5}$ traps. For the CAV pair, the formation energy diagram predicts the (+/0) and the (0/−) transitions to be at around 1 eV and 0.5 eV below E_C , respectively. While the latter is energetically similar to the (−/2−) and (2−/3−) CTLs of the V_{Si} (the S_1 and S_2 centers) and the (0/2−) double acceptor transition of the V_C (the $Z_{1/2}$ level), the deeper-lying (+/0) CTL is energetically isolated and are therefore more suitable for the identification of the defect. An important observation of Fig. 4 is the splitting of the (+/0) CTL belonging to the different CAV configurations into a set of three (hk , hh , kk) at around 1.0 eV and a single one (kh) at 1.13 eV. Referring to Table I, it becomes evident that these agree well with the activation energies found for the EH_4 and EH_5 traps. As was discussed in the last section, the EH_4 peak consists of three sublevels ($EH_{4,a,b,c}$) with very similar activation energies of around 1 eV, which is consistent with the hypothesis that EH_4 is produced by the hk , hh and kk configurations of the CAV pair, while EH_5 is connected to the slightly deeper kh . Indeed, a recent EPR study³⁵ has found the ionization energies of the neutral CAV pair to be roughly 1.1 eV, with detectable energetic splitting between the configurations, which further supports our assignment.

We next turn to the more elusive (0/−) transition at lower activation energies. It is conspicuous that $Z_{1/2}$ possesses an extended low-temperature flank towards S_1 , rendering it asymmetric in shape. This flank, upon annealing at 1000 °C, developed a clearly resolvable substructure containing four trap levels with activation energies in the range between 0.45 and 0.58 eV (indicated by arrows in Fig. 5), having signal intensities comparable to those of the $EH_{4/5}$ centers which were also present in this sample. The same substructure can be seen in DLTS spectra published by Alfieri *et al.* (Fig. 5 in Ref.²⁴). These levels could therefore be the expected acceptor transitions of the CAV pair.

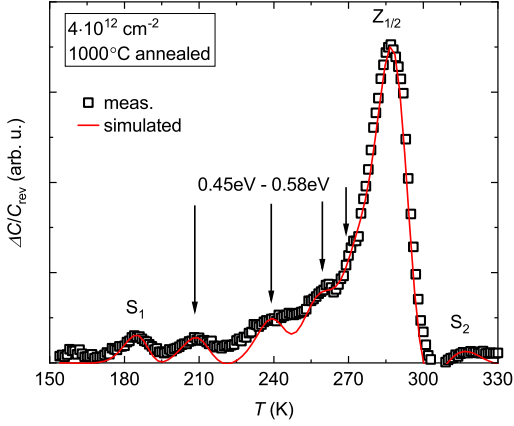


FIG. 5. High-resolution DLTS spectrum of a high-fluence irradiated and 1000 °C annealed sample, revealing a substructure of the low-temperature flank of $Z_{1/2}$ which is possibly related to the (0/-) CTL of the CAV pair.

C. Evolution of defect concentrations with annealing

In this section, the different pathways through which intrinsic defects in n -type 4H-SiC can anneal out will be explored. The development of the defect population after each annealing step was monitored using DLTS for the low-fluence and PL for the high-fluence irradiated samples. Irradiation introduces a large variety of defects, and the dominant defects in 4H-SiC, like V_C , V_{Si} and the complexes VV and CAV have acceptor-like states in the upper part of the band gap. Therefore it is not surprising that such experiments usually lead to the removal of free carriers with increasing irradiation fluence^{36–39}. This was also observed in the present work. In Fig. 6(a) the net doping of the low-fluence samples, as determined by means of capacitance-voltage measurements, is shown after each annealing step. It can be seen that starting from a proton fluence of $4 \times 10^{11} \text{ cm}^{-2}$ an initial reduction of net doping becomes noticeable. For the sample with the highest fluence in this sample set, room temperature C - V measurements were not possible in the initial state as the free carriers were entirely compensated. Interestingly, annealing can recover the free carriers almost entirely, with the temperature required to achieve recovery depending on the initial compensation. DLTS measurements on the highest-fluence sample across the full temperature range therefore became possible only after the 800 °C anneal. However, even for the partially compensated state, gradual charge carrier recovery was observed for elevated temperatures, e.g. approximately 400 °C for the initial (300 °C) stage, as is demonstrated in Fig. 6(b) where the temperature dependence of the reverse capacitance C_{rev} is shown. The temperature at which this capacitance recovery occurs decreased after each anneal-

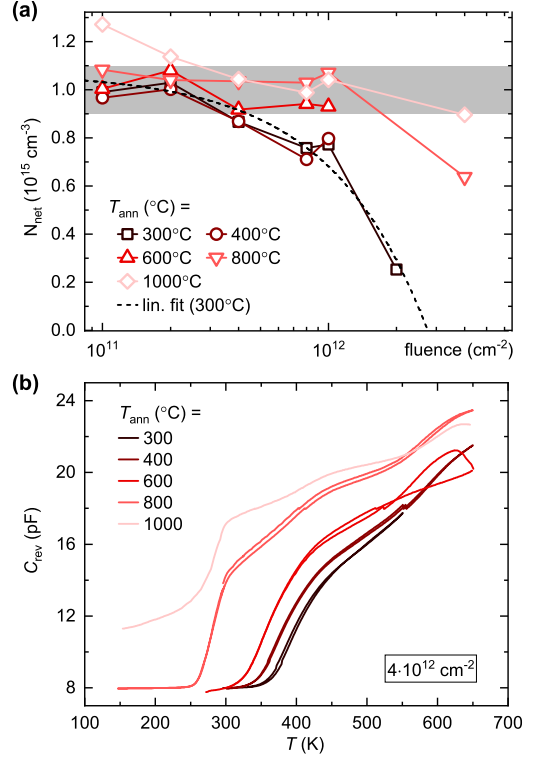


FIG. 6. (a) Net doping concentrations of low-fluence irradiated samples after annealing at different temperatures; data collected by means of C - V measurements at a reverse voltage of 10 V. Dashed line: linear fit, dashed-dotted line: exponential fit to initial (300 °C) doping data. Nominal doping range highlighted in grey. (b) C_{rev} - T curves of a sample exhibiting initial compensation and partial free carrier recovery upon heating (reversible; temperature sweeps in both directions are shown) and annealing (irreversible).

ing step. The recovery during measurements was shown to be reversible, in contrast to the effect induced by annealing. This behavior is indicative of the compensation being due to low-stability acceptors that form independently of the doping concentration, and in contradiction to a previously suggested model according to which carrier removal is due to the irradiation-induced passivation of shallow N_C donors³⁶. Introduction of compensating acceptors removes charge carriers in dependence on the Fermi level position which changes with temperature. Consequently, a partial recovery of free carriers at elevated temperatures is expected. The compensation hypothesis is also supported by the observation of the net doping density decreasing linearly with irradiation fluence, as is demonstrated by the fit (dashed line) in

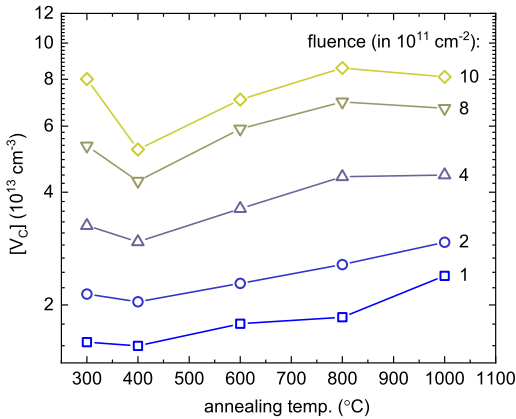


FIG. 7. C vacancy concentrations, as determined from the $Z_{1/2}$ level intensity, of SiC irradiated to various proton fluences after isochronal (30 min) annealing steps to the given temperatures.

Fig. 6(a). Importantly, the total concentration of the detectable acceptor-like defects with known concentrations (V_C , V_{Si} , CAV pair) in our experiments is close to the concentration of the observed carrier removal. Hence the removal effect can to a large extent be explained by the aforementioned defects, indicating that there are no other prominent defects that have to be taken into account. It is also noteworthy from Fig. 6 that for the lowest irradiation fluences, annealing increases the net doping to values significantly above the nominal doping of 10^{15} cm^{-3} . We have currently no definite explanation for this behavior, but it is possible that the as-received SiC either already contained thermally unstable compensating acceptors that anneal out at around 1000°C , or a population of inactive donors that became activated after the anneal.

1. Thermal evolution of the carbon vacancy

Fig. 7 shows the development of the V_C concentration, as determined from the DLTS signal of the $Z_{1/2}$ center, with annealing at increasingly higher temperatures for the different irradiation fluences. $[V_C]$ initially drops at 400°C and then increases with increasing annealing temperatures. The relative amount of the initial decrease is seen to be lowest for the lowest fluence, i.e. more V_C is annealed out at low temperatures when the initial defect concentration is higher. For the highest annealing temperature of 1000°C , there is a renewed drop of $[V_C]$ for higher fluences.

A comparable observation was made by Alfieri *et al.*²⁴ in a multi-stage annealing experiment on electron-irradiated 4H-SiC. Irradiation is known to produce self-

interstitials and vacancies in comparable concentrations. Dynamic annealing during the irradiation and the subsequent 300°C pre-diffusion step are believed to lead to a significant decrease in interstitial concentration, but our results, combined with those by Alfieri *et al.*, demonstrate that annealing at up to 400°C is necessary to produce a stable V_C concentration by inducing recombination with residual interstitials. In fact, based on a model for vacancy-interstitial recombination developed by Bockstedte, Mattausch and Pankratov³¹, the annihilation of these intrinsic defects is expected to occur in two stages in *n*-type SiC. Herein, the recombination of closely spaced vacancy-interstitial pairs happens at a comparatively low temperature of around 200°C , whereas pairs separated by more than the nearest-neighbor distance anneal out via an interstitial diffusion-limited process that requires slightly elevated temperatures of up to 500°C . Besides regular recombination which restore normally occupied lattice sites, formation of antisites through the same mechanism is also conceivable. However, SiC has been shown to only possess one CTL close to the valence band³ which is inaccessible in our experiments, such that it is not possible to distinguish antisite formation from C_i - V_C recombination. In any case, it can be stated that long-range interstitial diffusion is likely the reason for the continued annealing of V_C . The process is enhanced under *n*-type conditions which produce defects in more negative charge states, lowering interstitial diffusion barriers^{15,31,40}.

At the same time, considering the similarity of our experiments with those by Alfieri *et al.*, it can be stated that the renewed increase of V_C concentration above 400°C is a process that is induced under different experimental conditions (electron vs. proton irradiation). A conceivable explanation is thermal release of V_C from defect complexes. It was previously shown in Fig. 2(d) that the VV defect is actually present in the samples after the pre-diffusion step. The thermal dissociation of VV into the isolated vacancies would explain an increase of $[V_C]$. However, the VV center has been shown to be thermally stable and have a high binding energy^{16,41,42}, such that thermal dissociation below 1100°C is unlikely. Another possibility of V_C release is from the CAV pair via its dissociation, which is discussed in Subsection 3. Analogously to VV, CAV has formed in detectable amounts over the course of dynamic annealing during proton irradiation, as has already been shown in Fig. 2(a).

2. The silicon vacancy and the CAV pair

PL spectroscopy is a technique used for the identification and relative quantification of defect concentrations, but not their absolute values. However, because the signatures of V_{Si} and CAV in both the DLTS measurements (S center, $EH_{4,5}$ traps) and the PL spectra (V lines, AB lines) have been identified, and the DLTS and PL results overlap for one fluence ($4 \times 10^{12} \text{ cm}^{-2}$), we normal-

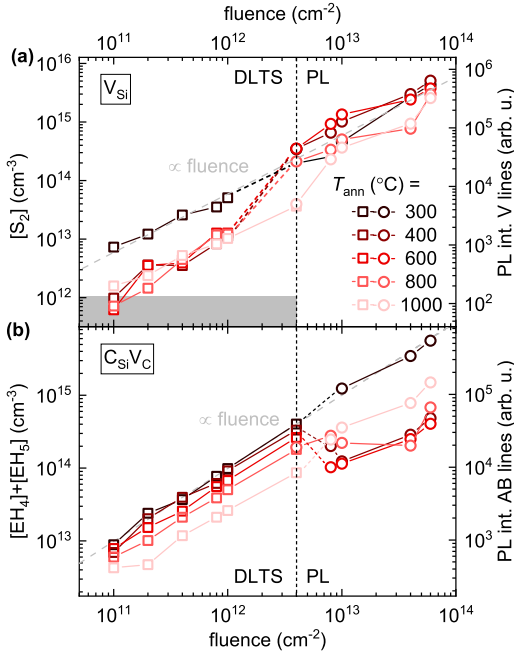


FIG. 8. Fluence dependence of the (a) V_{Si} and (b) CAV pair concentration, obtained from combined DLTS (S_2 and $EH_{4,5}$ traps) and PL results (V and AB lines) after annealing at increasingly high temperatures. The sample irradiated to a fluence of $4 \times 10^{12} \text{ cm}^{-2}$ (dashed black line) could be characterized by both methods in several annealing stages and was therefore used for calibration. Grey area marks onset of increased inaccuracy in DLTS measurement.

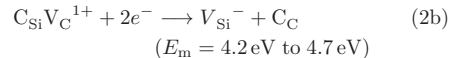
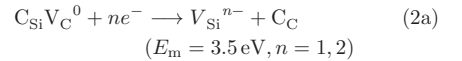
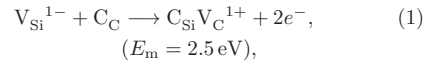
ized the PL data with regard to the DLTS concentrations in the overlapping region, and then used the established fixed multiplier to calibrate the rest of the PL data to obtain estimates for the absolute defect concentrations for both defects across the whole fluence range.

Fig. 8(a) shows that there is a distinct difference between the thermal evolution of the Si vacancy at low and at high irradiation fluences. For samples with fluences at and below $1 \times 10^{12} \text{ cm}^{-2}$, i.e. the dilute concentration regime, the evolution is dominated by an abrupt drop of $[V_{Si}]$ for anneals at 400 °C. While annealing to increasingly higher temperatures, the V_{Si} concentration remains almost constant. Analogously to the V_C defect, it can be stated that the stark drop is probably due to recombination of residual Si and C interstitials that initially lack an immediate V_{Si} neighbor (Si_i-V_{Si} recombination cannot be distinguished from C_{Si} antisite formation by DLTS, as this defect does not have any CTLs in the band gap³). This requires somewhat elevated temperatures due to longer diffusion ranges. The migration barrier for C_i and Si_i are below 1 eV for the electrically neutral charge state and

increase to around 2 eV as the Fermi level moves deeper into the band gap⁴⁰. This means that interstitial diffusion is facilitated in n -type and partially blocked for compensated material, which is a likely explanation for the absence of a decrease in concentration in the 400 °C samples for fluences larger than 10^{12} cm^{-2} . For these compensated samples, the V_{Si} concentration evolution is instead mainly characterized by a slow decrease above 400 °C.

To understand the evolution of V_{Si} , it is insightful to compare it with the simultaneous development of the CAV pair concentration (Fig. 8(b)). Here, a similar dichotomy of the annealing behavior can be stated. At fluences of up to $4 \times 10^{12} \text{ cm}^{-2}$, [CAV] decreases slowly with annealing temperature, by a factor of 3.75 between 300 °C and 1000 °C independent of fluence; the decrease appears to be somewhat accelerated at the highest temperatures. For the higher fluences, within the PL sample set, the 400 °C anneal induces a pronounced drop of [CAV] starting from a fluence of $8 \times 10^{12} \text{ cm}^{-2}$ which is completely alleviated in the 1000 °C step.

We conjecture that the evolution of both defects at fluences higher than $4 \times 10^{12} \text{ cm}^{-2}$ are partially related to the interconversion of V_{Si} and the CAV pair. The preferential direction of this process depends on the position of the Fermi level (see formation energy diagram, Fig. 4): in p -type and intrinsic SiC, the CAV pair possesses lower formation energies than V_{Si} and will therefore be the more favorable defect species, while the situation is reversed for n -type conditions when the Fermi energy is closer to the conduction band than approximately 1 eV. Additionally, the transformation between those defects is connected to a migration barrier E_m for the C atom which also depends on the position of the Fermi level. Further, since for a fixed E_F , both V_{Si} and CAV are never in the same charge state (see Fig. 4), there are electron capture or emission processes associated with the conversion. For the charge states most likely occupied in our experiments, and considering only those reactions that yield an overall energy gain upon transformation, those processes read



with n being the number of captured electrons, and the migration barriers E_m from Ref.¹⁸ given in parentheses. The conversion of V_{Si} to CAV (Eq. (1)) is hindered by a migration barrier of 2.5 eV, but also includes

double electron emission which requires an additional 1.6 eV (0.5 eV for ionization of the first and 1.1 eV for the second electron, based on the CAV pair CTLs), consequently increasing the transformation barrier to approximately 4.1 eV. The reverse process, CAV to V_{Si} , only requires free electrons available for capture, but the migration barriers are 3.5 eV and higher. Since both reactions described by the equations (1) and (2) contain a single atomic hop, the corresponding hopping rate for a specific C atom at any given temperature is given by $f_{hop} = \nu_0 \exp(-E_m/k_B T)$, with ν_0 the attempt frequency typically in the order of a typical phonon frequency, i.e. $\nu_{ph} \approx 10^{13} \text{ s}^{-1}$. Both V_{Si} and V_C are tetrahedrally coordinated, therefore the total fraction of V_{Si} converted to CAV during an annealing experiment of duration t can be approximated by

$$\frac{[C_{Si}V_C](t)}{[V_{Si}](t)} = 4t \cdot \nu_{ph} \exp\left(-\frac{E_m}{k_B T}\right), \quad (3)$$

and with inverted roles of V_{Si} and CAV for the reverse process. Based on the above migration barrier of at least 3.5 eV for the transformation of CAV to V_{Si} , a considerable fraction of converted defects, say $[CAV]/[V_{Si}] \approx 0.5$, can be achieved above 750 °C. However, the charge state of the CAV pair changes from neutral to 1+ just below 800 °C (compare Fig. 4). The associated CAV to V_{Si} transformation barrier then increases to at least 4.2 eV which shifts the required temperatures for conversion up even further. Given the fact that from 800 °C on, the CAV pair also becomes energetically more favorable than V_{Si} , we believe that the transformation CAV to V_{Si} plays an insignificant role in n -type 4H-SiC. Conversely, using a combined migration and emission barrier of 4.1 eV for the V_{Si} -to-CAV process, this should be observable for the highest temperatures used in this experiment. There is no corresponding trend visible in the low-fluence samples, likely because a large fraction of V_{Si} have recombined with interstitials until 400 °C, and the remaining V_{Si} concentration is an order of magnitude lower than that of the CAV pair. If the reaction described by Eq. (1) occurs, its effect can be considered negligible compared to the already existing CAV defect population. In the high-fluence (compensated) samples however, where interstitial diffusion is suppressed, it should be observable. Indeed, the partial recovery of [CAV] for the highest temperatures may be due to this process. It is also accompanied by a decrease of $[V_{Si}]$ of comparable magnitude, as expected.

3. Correlation between CAV and V_C concentrations

What remains to be explained is the decrease of [CAV] upon annealing, in particular the remarkable drop already at quite low temperatures for fluences of $4 \times 10^{12} \text{ cm}^{-2}$ and higher. In the low-fluence range, [CAV] decreases by a factor of 3.75 in the course of the

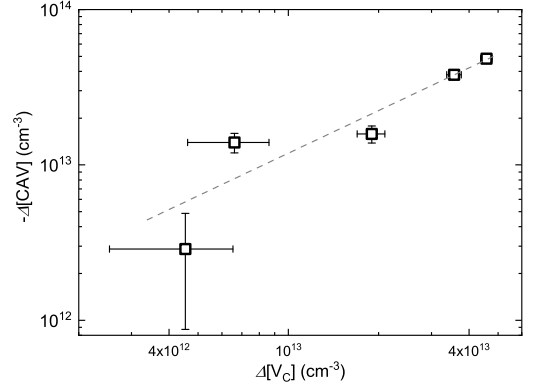


FIG. 9. Correlation of concentration differences between V_C and CAV defects. Grey dashed line indicates a linear 1:1 relation.

entire annealing experiment, independent of irradiation fluence. This indicates that the mechanism behind the decrease does not include other defect species. A mechanism which would conform to this restriction is the dissociation of CAV, as was already suggested earlier when the enhanced concentration of V_C defects was discussed. The reaction $C_{Si}V_C \rightarrow C_{Si} + V_C$ produces an isolated carbon vacancy and a carbon on silicon-antisite C_{Si} . It requires at least a single hop of a nearest-neighbor C atom into the vacancy in order to separate the two components. C_{Si} is a defect without CTLs inside the band gap of 4H-SiC^{3,43}, and is therefore electrically inactive. For that reason, the dissociation of CAV pairs exclusively leads to the increase of V_C concentration, as it was observed in our experiments (Fig. 7). Plotting the measured decrease of CAV pair concentration in the low-fluence samples with annealing temperature above 400 °C versus the simultaneous increase of V_C content from Fig. 7, it becomes apparent that these quantities agree well which each other, and share a linear 1:1 relation within experimental error (see Fig. 9). We interpret this as an indication that the decay of the concentration of CAV is closely related to the gain in V_C density, or even the dominant contributor to this process. Using an expression similar to Eq. (3) for the estimation of the dissociation fraction, and assuming that the temperature of 400 °C corresponding to the renewed increase of $[V_C]$ also marks the onset of CAV dissociation, the barrier associated with that process can be expected to be in the range of 2.4 eV. However, there are not many theoretical considerations of the energetics of this process for comparison; one of the available works has been published by Wang *et al.*¹⁷ who consider the dissociation as one possible conversion channel of the CAV pair. Based on a comparatively high dissociation barrier, which they estimate to be 5.9 eV and moreover identical to the migration barrier of V_C , their assessment

is that this process is not of significance compared to the inter-conversion between CAV and V_{Si} ; however, this assessment was made assuming p -type conditions. As was already stated, shifting the Fermi level towards n -type conditions can drastically change migration barriers for defects. In fact, for the neutral C vacancy, a migration barrier between 3.7 eV and 4.2 eV⁴⁴ has been calculated, which is considerably lower than the value given by Wang *et al.* However, this value would still be too large for the V_C migration to play a significant role below 1000 °C. It can be debated whether the migration barrier for the single vacancy is actually a good approximation for the dissociation energy of the CAV in general. Although the process resembles V_C migration, the energetics are different: both initial and final defect configuration of the dissociation ($C_{Si}V_C$ vs. $C_{Si} + V_C$) have higher formation energies compared to pure V_C diffusion. For most annealing temperatures in our experiments, the CAV pair is in the neutral state, which according to Fig. 4 has a formation energy of roughly 7 eV, about 2 eV higher than the neutral state of V_C . The final state consists of the separate V_C^0 and C_{Si}^0 defects, having formation energies of 5 eV and roughly 2 eV³. Therefore, both initial and final state are about 2 eV higher in energy than V_C . If, apart from these constant energy shifts, the hopping carbon atom experiences the same electrostatic forces during its migration, it is conceivable that the dissociation barrier for the CAV pair is considerably lower (by an estimated 1 to 2 eV) than the pure V_C migration barrier. Taking into account the result of Wang *et al.*¹⁷ claiming that the dissociation energy of the CAV pair is identical for the case in which both components are second-nearest neighbors as well as the case where they are located inside different unit cells, it can also be stated that a single carbon hop is probably enough to restore the electronic properties of the isolated V_C .

As for the compensated samples, it is presently unclear if the pronounced drop of [CAV] can be similarly attributed to the dissociation process. If it was, there would be a fundamental difference between the compensated and the n -type samples with regard to the annealing temperature that is necessary to induce the dissociation, with a considerably lower associated barrier for lower-lying E_F .

4. The divacancy

The divacancy can form during irradiation, or at elevated temperatures during post-irradiation annealing when the isolated vacancies become mobile – mostly due to V_{Si} diffusion, because the carbon vacancy has been shown to be immobile below 1200 °C⁴⁴. Fig. 10 displays the development of the PL4 line intensity with fluence and annealing temperature, which is taken as a qualitative measure for [VV] here. After irradiation and the 300 °C step, the divacancy is detectable in all high-fluence samples, following a linear relationship with fluence, as expected. Heating the samples to up to 600 °C only leads

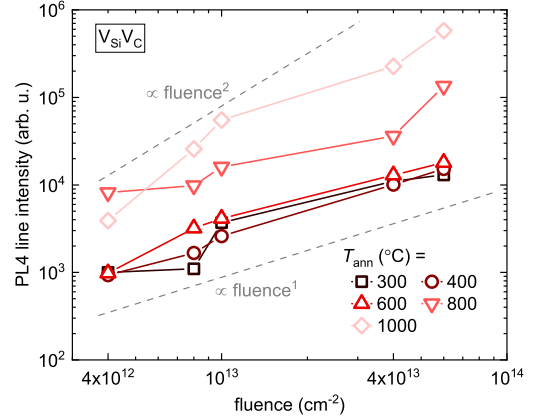


FIG. 10. Evolution of the intensity of the PL4 line (divacancy $V_{Si}V_C$) with annealing temperature.

to a minor change of [VV]; above that temperature, the divacancy concentration exhibits a steep increase, with the highest concentrations detected after 1000 °C. [VV] now also follows an approximately quadratic relation with fluence, which can be attributed to the fact that a large portion of the defects have been formed by diffusion of V_{Si} and their pairing with V_C , the concentration of both of which is roughly proportional to the fluence. Son *et al.*¹⁶ have reported on the formation of the EPR P6/7 center, which has likewise been attributed to the divacancy, in considerable amounts by annealing above 750 °C, which matches the critical VV formation temperature in this study.

The formation of VV reduces both the V_{Si} and V_C density to a certain extent. The resulting [VV] cannot be directly inferred from the PL measurements. However, it can be taken from Figs. 7 that the trend of a slow increase of V_C density with temperature reverses at the highest annealing temperatures for irradiation fluences above $2 \times 10^{11} \text{ cm}^{-2}$. In contrast to the lower-fluence samples, the V_C - V_C inter-defect distance for the higher fluences becomes low enough for the V_{Si} to migrate during annealing such that VV can form. A similar trend can be found for $[V_{Si}]$ (Fig. 8(a)): the $8 \times 10^{11} \text{ cm}^{-2}$ and $1 \times 10^{13} \text{ cm}^{-2}$ fluences exhibit a slight decrease of $[V_{Si}]$ at the highest annealing temperatures. For both defects, the change of concentrations when going from 800 °C to 1000 °C match well, and amount to approximately $2 \times 10^{12} \text{ cm}^{-3}$ which would then correspond to the final divacancy concentration in these samples after the 1000 °C anneal. This is an order of magnitude lower than the concentration of the CAV pair, for instance, which has CTLs in the same range as expected for the VV. It may therefore be that DLTS peaks corresponding to the VV defect are completely superimposed by the $EH_{4,5}$ traps, and hence are not resolvable in the spectra.

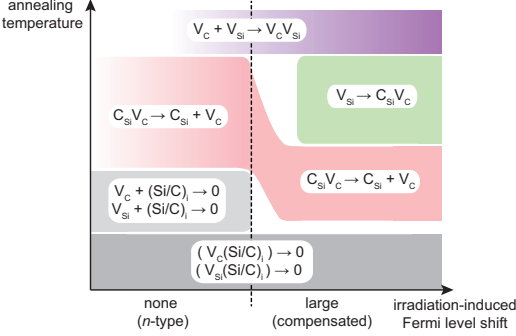


FIG. 11. Proposed model for the interconversion of defect species created in irradiated *n*-type 4H-SiC. Color gradients encode concentration of the defects produced by the reactions (darker = higher conc.).

D. Summary of defect evolution model

The model we propose for the annealing-induced conversion of intrinsic defects in irradiated *n*-type 4H-SiC is illustrated in Fig. 11 and will now be summarized. At annealing temperatures of 300 °C and below, closely spaced pairs of Si and C vacancies and interstitials ($V_C(\text{Si/C})_i$ and $V_{\text{Si}}(\text{Si/C})_i$) annihilate easily in both *n*-type and compensated material. Increasing the temperature leads to continued recombination of non-nearest neighbor interstitial-vacancy pairs. This can only occur in *n*-type material because interstitial diffusion is severely hampered with increasingly positive charge state. The next annealing stage is the dissociation of carbon antisite-vacancy pairs via formation of individual C_{Si} and V_C defects. This process seems to be triggered more abruptly and at lower temperatures for compensated as compared to *n*-type samples. At even higher annealing temperatures, conversion of V_{Si} to CAV pair occurs in the compensated samples. This process is visible because a large fraction of originally formed vacancies remained unannealed in the previous stage of blocked vacancy-interstitial recombination. For the highest temperatures in this experiment, the formation of divacancies via the diffusion of V_{Si} and binding to V_C defects is observed.

IV. CONCLUSION

The defect population in proton-irradiated, *n*-type 4H-SiC epilayers and its evolution during post-annealing have been studied through a combination of optical and electrical methods. We have shown that the dominant defect species are silicon and carbon vacancies and interstitials, the carbon antisite-carbon vacancy pair (CAV), and the divacancy (VV). All these are already present after irradiation and dynamic annealing. Irradiation is

also shown to lead to compensation of donors with increasing proton fluence, which can be partially reversed upon high-temperature annealing, supporting the notion of compensation by acceptor defects rather than by donor passivation. The presented data further support the assignment of the high-temperature EH₄ and EH₅ levels observed by deep level transient spectroscopy to the (+/0) CTL of the CAV pair in its four energetically inequivalent configurations. We show that a temperature-induced interconversion between the single Si vacancy (V_{Si}) and the CAV pair, as it has been reported in *p*-type material, is suppressed under *n*-type conditions. Instead, CAV defects appear to anneal out via a different route that, at the same time, leads to an equally large increase of carbon vacancy (V_C) concentration. We present a model describing this as a simple dissociation into isolated V_C and carbon antisite (C_{Si}) defects – a process which, according to our data and model, could be activated at a much lower temperature than previously expected. It also seems to occur more abruptly and at lower temperatures when the Fermi level is lower in the band gap (under compensation). We furthermore show that until 400 °C, the annealing behavior of irradiated *n*-type SiC is dominated by continued recombination of vacancies V_C , V_{Si} with self-interstitials, a process which is blocked in compensated SiC. Annealing at temperatures at 800 °C and above lead to the diffusion-mediated formation of divacancies $V_{\text{Si}}V_C$.

ACKNOWLEDGMENTS

The authors are obliged to C. Zimmermann for supplying the software for simulating DLTS spectra. Financial support was kindly provided by the Research Council of Norway and the University of Oslo through the frontier research project FUNDAMeNT (no. 251131, FriPro ToppForsk-program). The Research Council of Norway is acknowledged for the support to the Norwegian Micro- and Nano-Fabrication Facility, NorFab, project number 245963.

CONFLICTS OF INTEREST

There are no conflicts to declare.

REFERENCES

- ¹A. Lohrmann, B. C. Johnson, J. C. McCallum, and S. Castelletto, “A review on single photon sources in silicon carbide,” *Reports on Progress in Physics* **80**, 034502 (2017).
- ²K. Szász, V. Ivády, I. A. Abrikosov, E. Janzén, M. Bockstedte, and A. Gali, “Spin and photophysics of carbon-antisite vacancy defect in 4H silicon carbide: A potential quantum bit,” *Physical Review B* **91** (2015), 10.1103/physrevb.91.121201.
- ³T. Kobayashi, K. Harada, Y. Kumagai, F. Oba, and Y.-I. Matsushita, “Native point defects and carbon clusters in 4H-SiC: A

- hybrid functional study,” *Journal of Applied Physics* **125**, 125701 (2019).
- ⁴N. T. Son, P. Carlsson, J. Ul Hassan, B. Magnusson, and E. Janzén, “Defects and carrier compensation in semi-insulating 4H-SiC substrates,” *Physical Review B* **75** (2007), 10.1103/physrevb.75.155204.
 - ⁵B. Zippelius, J. Suda, and T. Kimoto, “High temperature annealing of n-type 4H-SiC: Impact on intrinsic defects and carrier lifetime,” *Journal of Applied Physics* **111**, 033515 (2012).
 - ⁶X. T. Trinh, K. Szász, T. Hornos, K. Kawahara, J. Suda, T. Kimoto, A. Gali, E. Janzén, and N. T. Son, “Negative-U carbon vacancy in 4H-SiC: Assessment of charge correction schemes and identification of the negative carbon vacancy at the quasicubic site,” *Physical Review B* **88** (2013), 10.1103/physrevb.88.235209.
 - ⁷J. Coutinho, V. J. B. Torres, K. Demmouche, and S. Öberg, “Theory of the carbon vacancy in 4H-SiC: Crystal field and pseudo-Jahn-Teller effects,” *Physical Review B* **96** (2017), 10.1103/physrevb.96.174105.
 - ⁸N. T. Son, X. T. Trinh, L. S. Løvlie, B. G. Svensson, K. Kawahara, J. Suda, T. Kimoto, T. Umeda, J. Isoya, T. Makino, T. Ohshima, and E. Janzén, “Negative-U system of carbon vacancy in 4H-SiC,” *Physical Review Letters* **109** (2012), 10.1103/physrevlett.109.187603.
 - ⁹H. M. Ayedh, R. Nipoti, A. Hallén, and B. G. Svensson, “Thermodynamic equilibration of the carbon vacancy in 4H-SiC: A lifetime limiting defect,” *Journal of Applied Physics* **122**, 025701 (2017).
 - ¹⁰M. E. Bathen, A. Galeckas, J. Müting, H. M. Ayedh, U. Grossner, J. Coutinho, Y. K. Frodason, and L. Vines, “Electrical charge state identification and control for the silicon vacancy in 4H-SiC,” *npj Quantum Information* **5** (2019), 10.1038/s41534-019-0227-y.
 - ¹¹R. Nagy, M. Niethammer, M. Widmann, Y.-C. Chen, P. Udvarhelyi, C. Bonato, J. Ul Hassan, R. Karhu, I. G. Ivanov, N. T. Son, J. R. Maze, T. Ohshima, O. O. Soykal, Á. Gali, S.-Y. Lee, F. Kaiser, and J. Wrachtrup, “High-fidelity spin and optical control of single silicon-vacancy centres in silicon carbide,” *Nature Communications* **10** (2019), 10.1038/s41467-019-09873-9.
 - ¹²H. Kraus, D. Simin, C. Kasper, Y. Suda, S. Kawabata, W. Kada, T. Honda, Y. Hijikata, T. Ohshima, V. Dyakonov, and G. V. Astakhov, “Three-dimensional proton beam writing of optically active coherent vacancy spins in silicon carbide,” *Nano Letters* **17**, 2865–2870 (2017).
 - ¹³J. W. Steeds, “Photoluminescence study of the carbon antisite-vacancy pair in 4H- and 6H-SiC,” *Physical Review B* **80** (2009), 10.1103/physrevb.80.245202.
 - ¹⁴S. Castelletto, B. C. Johnson, V. Ivády, N. Stavrias, T. Umeda, A. Gali, and T. Ohshima, “A silicon carbide room-temperature single-photon source,” *Nature Materials* **13**, 151–156 (2013).
 - ¹⁵M. Bockstedte, A. Mattausch, and O. Pankratov, “Ab initio study of the migration of intrinsic defects in 3C-SiC,” *Physical Review B* **68** (2003), 10.1103/physrevb.68.205201.
 - ¹⁶N. T. Son, P. Carlsson, J. Ul Hassan, E. Janzén, T. Umeda, J. Isoya, A. Gali, M. Bockstedte, N. Morishita, T. Ohshima, and H. Itoh, “Divacancy in 4H-SiC,” *Physical Review Letters* **96** (2006), 10.1103/physrevlett.96.055501.
 - ¹⁷X. Wang, M. Zhao, H. Bu, H. Zhang, X. He, and A. Wang, “Formation and annealing behaviors of qubit centers in 4H-SiC from first principles,” *Journal of Applied Physics* **114**, 194305 (2013).
 - ¹⁸R. K. Defo, X. Zhang, D. Bracher, G. Kim, E. Hu, and E. Kaxiras, “Energetics and kinetics of vacancy defects in 4H-SiC,” *Physical Review B* **98** (2018), 10.1103/physrevb.98.104103.
 - ¹⁹L. Gordon, A. Janotti, and C. G. V. de Walle, “Defects as qubits in 3C- and 4H-SiC,” *Physical Review B* **92** (2015), 10.1103/physrevb.92.045208.
 - ²⁰B. Magnusson, N. T. Son, A. Csóré, A. Gällström, T. Ohshima, A. Gali, and I. G. Ivanov, “Excitation properties of the divacancy in 4H-SiC,” *Physical Review B* **98** (2018), 10.1103/physrevb.98.195202.
 - ²¹A. Csóré, B. Magnusson, N. T. Son, A. Gällström, T. Ohshima, I. Ivanov, and Á. Gali, “First-principles study on photoluminescence quenching of divacancy in 4H-SiC,” *Materials Science Forum* **963**, 714–717 (2019).
 - ²²C. P. Anderson, A. Bourassa, K. C. Miao, G. Wolfowicz, P. J. Mintun, A. L. Crook, H. Abe, J. Ul Hassan, N. T. Son, T. Ohshima, and D. D. Awschalom, “Electrical and optical control of single spins integrated in scalable semiconductor devices,” *Science* **366**, 1225–1230 (2019).
 - ²³J. F. Ziegler, M. Ziegler, and J. Biersack, “SRIM – the stopping and range of ions in matter (2010),” *Nuclear Instruments and Methods in Physics Research Section B: Beam Interactions with Materials and Atoms* **268**, 1818–1823 (2010).
 - ²⁴G. Alfieri, E. V. Monakhov, B. G. Svensson, and M. K. Linnarsen, “Annealing behavior between room temperature and 2000 Celsius of deep level defects in electron-irradiated n-type 4H silicon carbide,” *Journal of Applied Physics* **98**, 043518 (2005).
 - ²⁵In the former case, since two electrons are emitted because of the negative-U property of the $Z_{1/2}$ center, $[V_C] = [Z_{1/2}]/2$ is assumed.
 - ²⁶I. D. Booker, E. Janzén, N. T. Son, J. Hassan, P. Stenberg, and E. O. Sveinbjörnsson, “Donor and double-donor transitions of the carbon vacancy related EH_{6/7} deep level in 4H-SiC,” *Journal of Applied Physics* **119**, 235703 (2016).
 - ²⁷V. Ivády, I. A. Abrikosov, E. Janzén, and Á. Gali, “Theoretical investigation of the single photon emitter carbon antisite-vacancy pair in 4H-SiC,” *Materials Science Forum* **778-780**, 495–498 (2014).
 - ²⁸V. Ivády, J. Davidsson, N. T. Son, T. Ohshima, I. A. Abrikosov, and A. Gali, “Identification of Si-vacancy related room-temperature qubits in 4H silicon carbide,” *Physical Review B* **96** (2017), 10.1103/physrevb.96.161114.
 - ²⁹W. F. Koehl, B. B. Buckley, F. J. Heremans, G. Calusine, and D. D. Awschalom, “Room temperature coherent control of defect spin qubits in silicon carbide,” *Nature* **479**, 84–87 (2011).
 - ³⁰Here, the simple linear model $[V_{C/Si}] = [V_{C/Si}]^0 + i_{C/Si} \cdot d$, was used where $[V_{C/Si}]^0$ are the background concentrations, $i_{C/Si}$ are the defect introduction rates by irradiation and d is the fluence.
 - ³¹M. Bockstedte, A. Mattausch, and O. Pankratov, “Ab initio study of the annealing of vacancies and interstitials in cubic SiC: Vacancy-interstitial recombination and aggregation of carbon interstitials,” *Physical Review B* **69** (2004), 10.1103/physrevb.69.235202.
 - ³²L. Storasta, J. P. Bergman, E. Janzén, A. Henry, and J. Lu, “Deep levels created by low energy electron irradiation in 4H-SiC,” *Journal of Applied Physics* **96**, 4909–4915 (2004).
 - ³³F. C. Beyer, C. G. Hemmingsson, H. Pedersen, A. Henry, J. Isoya, N. Morishita, T. Ohshima, and E. Janzén, “Capacitance transient study of a bistable deep level in e⁻-irradiated n-type 4H-SiC,” *Journal of Physics D: Applied Physics* **45**, 455301 (2012).
 - ³⁴C. Hemmingsson, N. T. Son, O. Kordina, J. P. Bergman, E. Janzén, J. L. Lindström, S. Savage, and N. Nordell, “Deep level defects in electron-irradiated 4H-SiC epitaxial layers,” *Journal of Applied Physics* **81**, 6155–6159 (1997).
 - ³⁵N. T. Son, P. Stenberg, V. Jokubavicius, H. Abe, T. Ohshima, J. Ul Hassan, and I. G. Ivanov, “Energy levels and charge state control of the carbon antisite-vacancy defect in 4H-SiC,” *Applied Physics Letters* **114**, 212105 (2019).
 - ³⁶D. Åberg, A. Hallén, P. Pellegrino, and B. G. Svensson, “Nitrogen deactivation by implantation-induced defects in 4H-SiC epitaxial layers,” *Applied Physics Letters* **78**, 2908–2910 (2001).
 - ³⁷A. Castaldini, A. Cavallini, and L. Rigutti, “Assessment of the intrinsic nature of deep level Z1/Z2 by compensation effects in proton-irradiated 4H-SiC,” *Semiconductor Science and Technology* **21**, 724–728 (2006).
 - ³⁸V. V. Kozlovskii, V. V. Emtsev, K. V. Emtsev, N. B. Stokran, A. M. Ivanov, V. N. Lomasov, G. A. Oganessian, and A. A. Lebedev, “Effect of electron irradiation on carrier removal rate in silicon and silicon carbide with 4H modification,” *Semiconductors* **42**, 242–247 (2008).

- ³⁹Ž. Pastuović, R. Siegle, I. Capan, T. Brodar, S.-I. Sato, and T. Ohshima, “Deep level defects in 4H-SiC introduced by ion implantation: the role of single ion regime,” *Journal of Physics: Condensed Matter* **29**, 475701 (2017).
- ⁴⁰X. Yan, P. Li, L. Kang, S.-H. Wei, and B. Huang, “First-principles study of electronic and diffusion properties of intrinsic defects in 4H-SiC,” *Journal of Applied Physics* **127**, 085702 (2020).
- ⁴¹L. Torpo, T. E. M. Staab, and R. M. Nieminen, “Divacancy in 3C- and 4H-SiC: An extremely stable defect,” *Physical Review B* **65** (2002), 10.1103/physrevb.65.085202.
- ⁴²Q. Xu, T. Yoshiie, and M. Okada, “Positron annihilation of vacancy-type defects in neutron-irradiated 4H-SiC,” *Journal of Nuclear Materials* **386-388**, 169–172 (2009).
- ⁴³L. Torpo, M. Marlo, T. E. M. Staab, and R. M. Nieminen, “Comprehensive ab initio study of properties of monovacancies and antisites in 4H-SiC,” *Journal of Physics: Condensed Matter* **13**, 6203–6231 (2001).
- ⁴⁴M. E. Bathen, J. Coutinho, H. M. Ayedh, J. Ul Hassan, I. Farkas, S. Öberg, Y. K. Frodason, B. G. Svensson, and L. Vines, “Anisotropic and plane-selective migration of the carbon vacancy in SiC: Theory and experiment,” *Physical Review B* **100** (2019), 10.1103/physrevb.100.014103.

Paper VII

Muon interaction with negative- U and high spin state defects: Differentiating the C and Si vacancy in 4H-SiC

J. Woerle, M. E. Bathen, T. Prokscha, A. Galeckas, H. M. Ayedh, L. Vines, U. Grossner

Accepted in *Physical Review Applied* (2020).

Muon interaction with negative- U and high spin state defects: Differentiating the C and Si vacancy in 4H-SiC

J. Woerle,^{1,*} M. E. Bathen,² T. Prokscha,³ A. Galeckas,² H. M. Ayyedh,² L. Vines,² and U. Grossner¹

¹*Advanced Power Semiconductor Laboratory, ETH Zurich, Physikstrasse 3, 8092 Zurich, Switzerland*

²*Department of Physics/ Centre for Materials Science and Nanotechnology, University of Oslo, N-0316 Oslo, Norway*

³*Laboratory for Muon Spin Spectroscopy, Paul Scherrer Institute, 5232 Villigen, Switzerland*

(Dated: September 4, 2020)

Low-energy muon spin rotation spectroscopy (LE- μ SR) is employed to study silicon and carbon vacancies in proton-irradiated 4H-SiC. We show that the implanted muon is quickly attracted to the negative Si vacancy (V_{Si}) where it forms a paramagnetic muonium (Mu^0) state, resulting in a reduction of the diamagnetic fraction. In samples with predominantly C vacancies (V_{C}), on the other hand, the formation of Mu^0 is very short-lived and the muon quickly captures a second electron to form a diamagnetic Mu^- state. The results are corroborated by density functional calculations, where significant differences in the relaxation mechanism of the vacancies' nearest-neighbor dangling bonds are discussed. We propose that the LE- μ SR technique is capable of differentiating between high-spin and negative- U behavior in semiconducting materials. Finally, our findings emphasize the large potential of LE- μ SR to probe surface-near semiconductor defects, a capability that is crucial for further development of many electronic and quantum technology applications.

I. INTRODUCTION

Vacancy defects are a fundamental aspect of solids, frequently altering the electronic and optical properties of materials. In silicon carbide (SiC), a semiconductor material showing promise for both power electronics and quantum technology applications, slight differences in electronegativity between the two atomic species have profound implications for the effect of a specific vacancy on the electronic properties of the material at large.

Silicon carbide is considered a covalent material, where Si and C form a strong bond. At the same time, there is also a distinct ionic contribution to the bonding where C is the negatively charged constituent. Consequently, SiC embodies two vacancy types, silicon and carbon vacancies (V_{Si} and V_{C} , respectively), with significantly different behavior. V_{C} is surrounded by Si atoms having extended dangling bonds that overlap, and the degenerate ground state makes V_{C} susceptible to a symmetry-lowering Jahn-Teller (JT) distortion [1–5]. In epitaxially grown 4H-SiC, V_{C} has been identified as a lifetime-killing defect, thereby lowering the performance of 4H-SiC power electronic devices [6]. Furthermore, V_{C} is associated with a negative- U behavior which manifests in the $(-2/-)$ charge-state transition of V_{C} taking place at higher energies than $V_{\text{C}}(0/-)$ [7]. V_{Si} , on the other hand, is surrounded by highly localized C orbitals with negligible overlap, similar to the vacancy in diamond. Without nearest-neighbor bonding, there is no driving force for a JT distortion in V_{Si} , and an inward displacement is only achieved at a high energetic cost. Instead, the Si-C bonds shorten, yielding a symmetry conserving outward-breathing relaxation. Moreover, V_{Si} exhibits a spin of $S = 3/2$, long spin coherence times and single-photon emission [8], in contrast to the low-spin ($S = 0$) and negative- U character of V_{C} [7,9]. Owing to these properties, the V_{Si}

has been identified as a promising candidate for a wide range of quantum applications, including quantum communication, computing and sensing [8,10,11].

There exists a range of techniques capable of detecting and identifying isolated point defects in SiC. In photoluminescence (PL) spectroscopy, the V_{Si} exhibits a well-known fingerprint [12,13], and using deep level transient spectroscopy (DLTS), the $(-2/-)$ and $(2/-3-)$ charge transition levels of V_{Si} [14] and the $(0/2-)$ transition of V_{C} [7] have been successfully identified. However, especially the top ~ 300 nm of a sample, i.e., wherein a qubit V_{Si} will likely reside, is difficult to analyze with the aforementioned methods. DLTS is most accurate starting from some hundred nanometers depending on the nature of the junction [15], and depth resolved PL spectroscopy is challenging due to the difficulty in localizing light emitters.

Recently, low-energy muon spin rotation (LE- μ SR), a depth-resolved and surface-sensitive local-probe technique, was demonstrated to detect carbon vacancies in irradiated n-type 4H-SiC [16]. Herein, we investigate the interaction of the muon with both V_{Si} and V_{C} in n-type 4H-SiC samples that are proton-irradiated to varying fluences, and compare experimental findings with density functional theory (DFT) calculations using hydrogen as a substitute for the muon. We find a distinct difference in the response of the muons to the silicon and carbon vacancies, both using LE- μ SR and DFT, and propose that the LE- μ SR technique is sensitive to the distinct relaxation mechanisms driven by the vacancy nearest-neighbor dangling bonds. Our results demonstrate that LE- μ SR is a promising technique for detecting and identifying point defects in semiconductors in a non-destructive fashion, with the added benefit of gaining detailed information on the defect's local magnetic environment.

*Electronic address: woerle@aps.ee.ethz.ch

II. METHODS

A. Sample preparation and characterization

In this study, proton-irradiated n-type 4H-SiC samples containing both V_{Si} and V_{C} defects were investigated. The samples studied were 10 μm thick (0001) 4H-SiC epitaxial layers, grown 4° off the c -axis on a 4H-SiC substrate (CREE). The net carrier concentration in the epi-layers was approximately $N_{\text{D}} = 10^{15} \text{ cm}^{-3}$ as determined from capacitance-voltage measurements, while the substrate n-type doping was reported to be $\sim 8 \times 10^{18} \text{ cm}^{-3}$. To generate the Si and C vacancies, the samples were irradiated at room temperature to different fluences with 1.8 MeV protons and at an angle 8° off the surface normal to reduce channeling effects. According to Monte Carlo simulations (as implemented in the Stopping and Range of Ions in Matter (SRIM) code [17]), the projected range of the protons was $\sim 27 \mu\text{m}$. A low-temperature annealing process ($T_{\text{Anneal}} = 300^\circ\text{C}$, 30 min, N_2 flow) was used to alleviate implantation damage and remove unstable defects, leaving predominantly V_{Si} and V_{C} with a ratio of ~ 0.6 [14] in the samples. Two additional samples, one with and one without a prior proton irradiation step, received a heat treatment at $T_{\text{Anneal}} = 1200^\circ\text{C}$ (30 min, Ar atmosphere). In the case of the irradiated sample, the high-temperature heat treatment was conducted to reduce the concentration of silicon vacancies, leaving mainly V_{C} present in the sample. The non-irradiated reference sample was included to gauge the effect of the annealing process on the defect population. Hydrogen from the proton irradiation itself is not expected to be present in the near-surface region probed during the muon experiments. Sample processing conditions and estimated V_{Si} and V_{C} concentrations in each sample, based on SRIM simulations and the DLTS/PL correlation methodology of Ref. [14], are summarized in Table I.

Deep level transient spectroscopy (DLTS) measurements were performed on the non-irradiated reference sample to monitor any defects present in the as-grown material, and to investigate whether additional defects were induced during the post-irradiation annealing step ($T_{\text{Anneal}} = 1200^\circ\text{C}$). For the DLTS analysis, Ni Schottky barrier diodes of 1 mm diameter

and 150 nm thickness were deposited on the sample surface using an electron-beam evaporator. DLTS was performed in the temperature range from 25 K to 300 K to encompass both the S1 (related to V_{Si}) and $Z_{1/2}$ (related to V_{C}) peaks, along with any impurities arising close to the conduction band edge. The reverse bias was kept at -10 V using a 10 V filling pulse, rate windows in the 20 ms to 640 ms range, and a standard lock-in weighting function to extract the DLTS signal.

To ascertain the presence and relative concentration of V_{Si} in the samples, additional photoluminescence (PL) measurements were conducted prior to the μSR analysis. Experiments were performed at 10 K, using a pulsed Ti:sapphire tunable laser at 740 nm excitation and a polarization perpendicular to the optical c -axis of 4H-SiC to monitor V_{Si} signatures. For investigating the presence of divacancy ($V_{\text{Si}}V_{\text{C}}$) defects, a 405 nm excitation was employed using a cw-laser of 75 mW power.

B. LE- μSR measurements

The μSR measurements were performed at the low-energy muon (LEM) beamline of the Swiss Muon Source ($\text{S}\mu\text{S}$) [18,19]. Samples were fixed on a Ni-coated aluminum plate and mounted onto a cryostat placed perpendicular to the muon beam. A magnetic field was applied parallel to the beam axis and the positrons from the muon decay were detected by a set of scintillator detectors placed around the beam axis. The final kinetic energy of the μ^+ implanted into the sample was varied between 2 keV and 18.5 keV, resulting in probing depths up to 120 nm. Consequently, only near-surface defects in the proton-irradiation tail were probed. During a LE- μSR experiment, $\sim 100\%$ polarized positive muons are implanted into the 4H-SiC sample. After a short lifetime of $\sim 2.2 \mu\text{s}$, the μ^+ decays and emits a positron preferentially in the direction of its polarization at the time of the decay. Using an appropriate detector geometry, the asymmetry of the muon decay along different directions as a function of time, $A(t)$, can be measured, which is proportional to the time evolution of the muon spin polarization. $A(t)$ depends on the local electronic environment of the muon and can be used to obtain information on the hyperfine interaction between the muon and the electrons in the system. For more details on the μSR technique, see also [20–23].

C. Density functional calculations

In addition to the experimental investigations, DFT calculations as implemented in the vasp code were performed [24–27]. The electronic ground state was obtained within the Kohn-Sham formalism, using the projector augmented-wave (PAW) method [28] to describe core electrons, 420 eV energy cutoff, and setting the stopping criterion for the electronic self-consistent loop to 10^{-6} eV . Muons are commonly not directly implemented in vasp, but are instead emulated using the hydrogen pseudopotential [29,30]. Herein, we study interactions between muons and vacancies in 4H-SiC as rep-

TABLE I: Sample processing conditions and estimated V_{Si} and V_{C} concentrations (based on Ref. [14]) in the near-surface region of the 4H-SiC samples. The V_{C} concentration of the non-irradiated sample was determined using DLTS.

Fluence (cm^{-2})	T_{Anneal} ($^\circ\text{C}$)	$[V_{\text{Si}}]$ (cm^{-3})	$[V_{\text{C}}]$ (cm^{-3})
1×10^{13}	300	3.0×10^{14}	5.0×10^{14}
4.5×10^{13}	300	1.4×10^{15}	2.3×10^{15}
1×10^{14}	300	3.1×10^{15}	5.2×10^{15}
3×10^{14}	300	9.3×10^{15}	1.5×10^{16}
None	1200	$\ll 5.0 \times 10^{12}$	5.0×10^{12}
4.5×10^{13}	1200	$\ll 3.0 \times 10^{14}$	$\sim 2 \times 10^{15}$

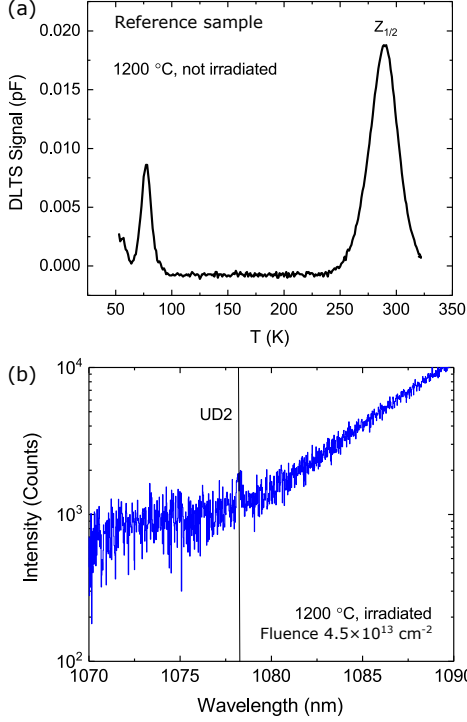


FIG. 1: (a) DLTS spectrum using the 640 ms rate window for the non-irradiated reference sample. (b) PL spectrum of a proton irradiated 4H-SiC samples annealed at 1200 °C (fluence $4.5 \times 10^{13} \text{ cm}^{-2}$) showing the UD2 signal related to the divacancy ($V_{\text{Si}}V_{\text{C}}$).

represented by hydrogen-vacancy complexes ($V_{\text{Si}}\text{-H}$ and $V_{\text{C}}\text{-H}$), from here on denoted as $V_{\text{Si}}\text{-Mu}$ and $V_{\text{C}}\text{-Mu}$. In this context, Mu (one μ^+ bound to one e^-) corresponds to H consisting of one proton and one electron. Formation energy diagrams for the defects were constructed according to Refs. [31,32] using the extended Freysoldt-Neugebauer-Van de Walle charge correction scheme [33–35].

For the vacancy-Mu complexes, 400-atom hexagonal supercells were employed. Defect relaxation was conducted using the HSE06 [36,37] hybrid functional and Γ -only \mathbf{k} -point sampling until the maximum force was below 0.05 eV/Å. Note that results for $V_{\text{Si}}\text{-H}$ are based on that of Ref. [38].

In the case of isolated monovacancies, orthorhombic 96-atom supercells and hybrid-derived lattice parameters (using HSE06) were employed. Here, one may discuss whether unintended defect overlap effects may influence the results for defects situated within smaller 96-atom supercells. However, the supercells in question were near-cubic with approximately 10 Å between defects in all three dimensions, and hybrid-level relaxations were performed using a $2 \times 2 \times 2$ Monkhorst-Pack type \mathbf{k} -mesh.

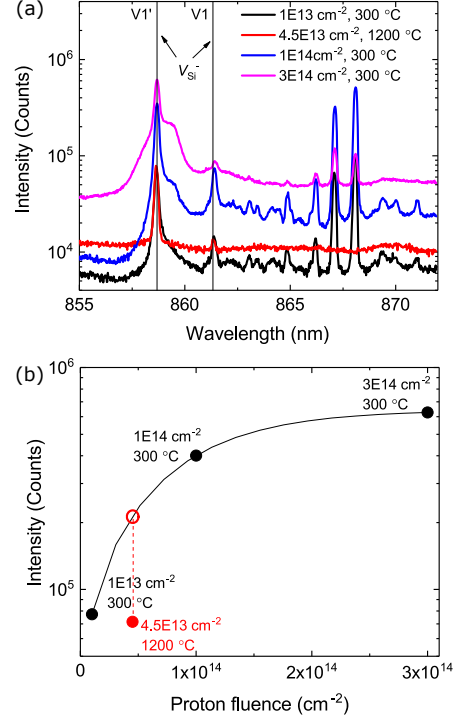


FIG. 2: PL spectra of 4H-SiC samples irradiated to different fluences and annealed at 300 °C or 1200 °C, with (a) showcasing the V1/V1' lines related to V_{Si} emission, and (b) showing the background-subtracted V_{Si} -related emission intensities ($V1+V1'+V2$) versus proton fluence. Annealing at 1200 °C results in a decrease of V_{Si} , indicated by the filled red circle.

III. RESULTS

A. Semiconductor bulk analysis

Before elaborating on the muon beam analysis, we discuss our results of DLTS and PL spectroscopy measurements used to estimate the defect populations in the 4H-SiC samples. In a first step, DLTS measurements were performed on the sample without proton irradiation to investigate the defect concentration already present in the epitaxial layer. As shown in Figure 1a, the $Z_{1/2}$ peak, related to the (0/2-) negative- U transition of the carbon vacancy [7] and commonly present in 4H-SiC epitaxial layers, is clearly observed. The measured peak intensity of $Z_{1/2}$ translates to a carbon vacancy concentration of $5 \times 10^{12} \text{ cm}^{-3}$. The second peak around 80 K is assigned to the cubic crystalline site of the nitrogen donor level [39] and is too small to play a significant role in the LE- μ SR experiment. V_{Si} , on the other hand, was not detected in the prior to irradiation, as is apparent from the absence of the S1 peak

near 200 K [14].

As the upper detection limit of DLTS is below $\sim 0.2N_D$, and $N_D = 1 \times 10^{15} \text{ cm}^{-3}$, the irradiated samples could not be studied using this technique. Instead, PL measurements were performed to investigate the presence of optically active defects such as V_{Si} , the divacancy ($V_{\text{Si}}V_{\text{C}}$), the carbon-antisite vacancy ($\text{C}_{\text{Si}}V_{\text{C}}$) pair and the nitrogen-vacancy ($\text{N}_{\text{C}}V_{\text{Si}}$) center. The V_{Si} is clearly visible in all cases after irradiation, while neither the $\text{C}_{\text{Si}}V_{\text{C}}$ nor $\text{N}_{\text{C}}V_{\text{Si}}$ centers could be identified in any of the studied samples. Interestingly, in the irradiated sample that was annealed at 1200°C , we observe a weak UD2 signal (Fig. 1b) that has previously been attributed to the divacancy [40]. Its appearance can be attributed to the increased annealing temperature at which V_{Si} becomes more mobile and hence facilitates the formation of the divacancy [41]. Annealing the samples at 300°C , on the other hand, is not sufficient to promote this mechanism.

For an estimation of the V_{Si} population we monitor the $V1/V1'$ (at 1.44 eV) and $V2$ (at 1.35 eV) emission lines that are associated with the negative charge state of hexagonal (h) and pseudo-cubic (k) V_{Si} , respectively [13,42,43]. Emission from the proton-irradiated samples is shown in Figure 2a for the wavelength range associated with $V1/V1'$. We find that the V_{Si} emission intensities increase with the proton fluence as expected for the 300°C -annealed samples (shown by the black line in Figure 2b). The V_{Si} is present also in the sample that was irradiated to a proton fluence of $4.5 \times 10^{13} \text{ cm}^{-2}$ and annealed at 1200°C , but at much lesser quantities (illustrated by the red dot and line in Fig. 2b). Annealing of the V_{Si} above 300°C happens by either out-diffusion or, as described before, by transformation into the divacancy.

Importantly, all the irradiated samples have defect concentrations close to or above N_D (see Table I) and hence are partly or fully compensated. For the lowest proton fluence (10^{13} cm^{-2}), the Fermi level likely resides somewhere between the $(+0)$ transition of V_{C} near mid-gap [9] and the (-2) transition of V_{Si} at 0.7 eV below the CBM [14,44], while for the higher fluence samples the Fermi level will be pinned close to mid-gap by $V_{\text{C}}(+0)$. Consequently, for the present sample set, the equilibrium vacancy states are V_{Si}^- and V_{C}^0 (see, e.g., Refs. [9,14,44]).

B. LE- μ SR Analysis

When a μ^+ is implanted into a semiconductor during a μ SR experiment, it stops at an interstitial site and forms the hydrogen-like bound state called muonium (Mu) that can occur in three different charge states: either as a neutral paramagnetic state Mu^0 (μ^+e^-), or as one of the two diamagnetic states Mu^- ($\mu^+e^-e^-$) or Mu^+ (μ^+). Having different precession frequencies in an external magnetic field, the paramagnetic and diamagnetic states can be spectroscopically distinguished, and from the amplitudes of the corresponding precession signal the decay asymmetries A_{Mu} and A_{D} can be determined. Knowing the total asymmetry $A_{\text{tot}} = A_{\text{D}} + 2A_{\text{Mu}}$, the diamagnetic fraction $F_{\text{D}} = A_{\text{D}}/A_{\text{tot}}$ and the paramagnetic fraction $F_{\text{Mu}} = 2A_{\text{Mu}}/A_{\text{tot}}$ can be extracted. The factor 2 in

$2A_{\text{Mu}}$ accounts for the fact, that in our experiments with low magnetic field (0.5 mT), only 50% of the Mu^0 polarization is visible in the Mu^0 precession signal.

The formation of paramagnetic Mu^0 inside the target material is closely connected to the deceleration process of the muon during the first ps after its implantation. Once the muon has slowed down sufficiently and reaches energies of a few keV to tens of eV, a cyclic charge exchange between a positive and a neutral charge state arises. The muon can leave this region either as positively charged Mu^+ , or as a neutral Mu^0 atom [45], which then thermalizes and stops at an interstitial site that is attributed to the tetrahedral silicon (T_{Si}) site [46,47]. In low-doped, non-irradiated 4H-SiC, more than half of the implanted μ^+ thermalize as Mu^0 [46,48], while typical values for the diamagnetic fraction F_{D} are below 0.1 [49]. The remaining missing fraction is the fraction of implanted μ^+ which does not contribute to the measured asymmetry due to fast depolarization effects.

In Fig. 3, F_{D} and F_{Mu} as a function of the muon implantation energy in a transverse magnetic field of 0.5 mT are shown. For low implantation energies ($< 10 \text{ keV}$), an increased diamagnetic fraction is observed for all samples (Fig. 3a), which can be explained by a partial suppression of the Mu^0 formation process, previously described in Refs. [50,51]: while slowing down, a fraction of the implanted μ^+ may capture an electron from its own ionization track and form - with some delay - Mu^0 at one of the antibonding AB_{C} and AB_{Si} sites [47]. This delayed Mu^0 fraction cannot be observed di-

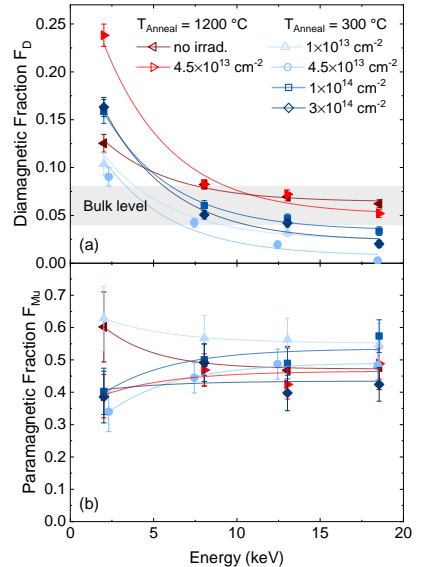


FIG. 3: (a) Diamagnetic and (b) paramagnetic fractions measured at 200 K and 0.5 mT. Lines are guides to the eyes.

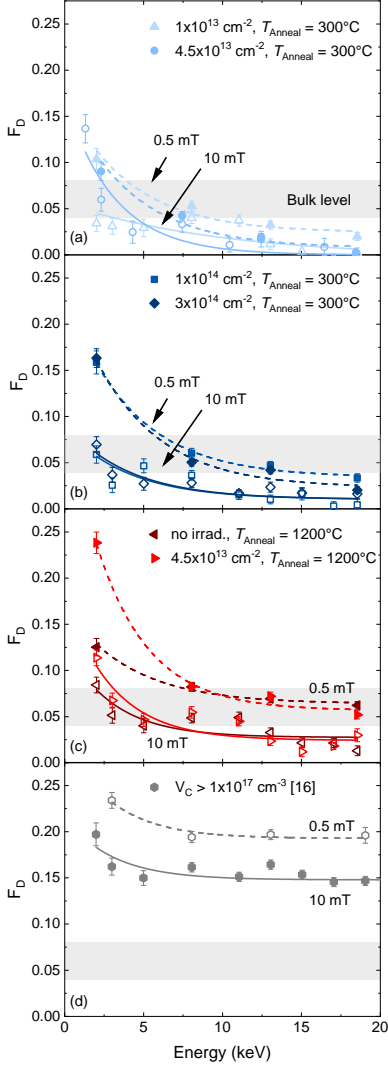


FIG. 4: Diamagnetic fraction measured at $B = 0.5$ mT (filled symbols) and $B = 10$ mT (empty symbols). (a,b) Samples annealed at 300°C with increasing amounts of V_{Si} and V_{C} . (c) Samples annealed at 1200°C and hence negligible V_{Si} densities. (d) Proton-irradiated sample with a very large V_{C} and again negligible V_{Si} concentration [16]. A field dependence, indicating a neutral precursor state, is most pronounced in the three samples in (c,d). Lines are guides to the eyes.

rectly but is only visible as an increase in F_{D} in the first few nanometers of the sample, where the number of electrons from the muon track is still insufficient for a transition from Mu^+ to Mu^0 . In contrast, F_{Mu} in Fig. 3b exhibits only a weak energy dependence, indicating that the measured Mu^0 fraction is formed promptly: this fraction is from muons leaving the charge cycles as Mu^0 , and thermalizing as Mu^0 , i.e. no track electrons are required for its formation. This fraction is relatively independent of the vacancy concentrations present in the samples.

At energies >10 keV, where most of the implanted μ^+ are expected to form either prompt or delayed Mu^0 , samples annealed at different temperatures show clear variations in F_{D} : for both samples with very small V_{Si} concentrations (annealing at 1200°C), F_{D} decreases to expected bulk values, while all four samples with larger V_{Si} concentrations exhibit significantly smaller diamagnetic fractions, indicating that nearly no Mu^+ (or Mu^-) is formed. Importantly, the two samples irradiated to the same fluence of $4.5 \times 10^{13} \text{ cm}^{-2}$, but annealed at different temperatures, exhibit a very different diamagnetic behavior, suggesting that their difference in V_{Si} concentration is the driving force behind the reduced F_{D} signal.

In Figure 4, the results of F_{D} at 0.5 mT from Fig. 3 are compared with additional measurements at 10 mT. At larger implantation depths, no or only a weak field dependence of F_{D} is observed in the samples annealed at 300°C containing larger V_{Si} concentrations (Figs. 4a,b) whereas it is much more pronounced in the 1200°C -annealed samples (Fig. 4c). Similar strong field dependencies have been reported in bulk- μSR studies of 4H-SiC [48,52], with clear indications for the presence of two diamagnetic species, (i.e. Mu^+ and Mu^-) and a fluctuation between the two via an intermediate Mu^0 state. Also in the process of reaching the final muon configuration after its implantation, such a behavior has been discussed: there, the muon comes first to rest in the unrelaxed host lattice and reaches its final configuration only via a paramagnetic transition state [45]. In the case of 4H-SiC with very small V_{Si} concentrations, the suggested fluctuation between Mu^+/Mu^- states might be a consequence of this transition sequence, involving the AB_{Si} and AB_{C} sites.

At larger V_{Si} concentrations (Figs. 4 and 4a,b), the decrease of F_{D} and the reduced field dependence suggests a different relaxation process: before reaching one of the AB sites, Mu^+ may be attracted to the negative V_{Si} center where it captures one electron and forms the paramagnetic Mu^0 state. As a consequence, the diamagnetic signal drops below expected 4H-SiC bulk values and the field dependence is reduced.

In addition to the two discussed scenarios, it is interesting to compare our results with measurements on 4H-SiC with very large ($> 10^{17} \text{ cm}^{-3}$) V_{C} and negligible V_{Si} concentrations [16], depicted in Fig. 4d. Here, an increase of F_{D} and a decrease of F_{Mu} (not shown here) almost independent of the implantation energy is observed. In this case, the suppression of Mu^0 may be explained by i) its trapping at V_{C} , where it captures an electron from the defect to form diamagnetic Mu^- or ii) the capture of a Mu^+ at V_{C} , where a two-electron capture process leads first to the formation of Mu^0 , and finally to Mu^- .

C. DFT Analysis

To better understand the muon dynamics in 4H-SiC, it is worthwhile to consider the different physical natures of V_{Si} and V_{C} , in terms of symmetry and local atomic displacement. Figures 5a and 5c demonstrate the contrast between the symmetry-conserving outward breathing relaxation of V_{Si}^- (Fig. 5a), as compared to symmetry reduction and Si-Si dimer formation for V_{C}^0 (Fig. 5c). Note the larger charge of V_{Si} compared to that of V_{C} for the same Fermi level, and the larger void left by Si than for the V_{C} case.

To investigate the likelihood of the muon bonding to a vacancy, and the stability of the resulting complex, we turn to formation energy diagrams. Here, we can gauge the relative stability of the vacancies (V_{Si} and V_{C}) and vacancy-muon complexes ($V_{\text{Si}}-\text{Mu}$ and $V_{\text{C}}-\text{Mu}$) for different Fermi levels. Formation energy diagrams for $V_{\text{Si}}-\text{Mu}$ and V_{Si} , and $V_{\text{C}}-\text{Mu}$ and V_{C} , are shown in Figures 5b and 5d, respectively. As previously reported in Ref. [38] for the $V_{\text{Si}}-\text{H}$ complex, $V_{\text{Si}}-\text{Mu}$ is energetically more favorable than isolated V_{Si} (see Fig. 5b). Consequently, if both constituents are available and in close proximity, the complex is likely to form. In contrast, we find that the formation energies for V_{C} and $V_{\text{C}}-\text{Mu}$ are not significantly different, as shown in Fig. 5d. This may imply that the trapping of the muon into V_{C} is less efficient than in the case of V_{Si} , as the energy gain from the muon binding to the V_{C} is lower than the gain from a $V_{\text{Si}}-\text{Mu}$ formation for all Fermi levels. Upon considering the V_{C} and $V_{\text{C}}-\text{Mu}$ formation energy diagrams, we conclude that V_{C} is more stable than $V_{\text{C}}-\text{Mu}$ for Fermi levels close to the conduction band, while the opposite is true for Fermi levels close to mid-gap. Hence, the rate of muon capture by V_{C} is significantly impacted by the Fermi levels in the samples and as discussed above, the compensation of donors in our samples likely pushes the Fermi level towards mid-gap. Accordingly, trapping of muons by the V_{C} should be possible, but less likely than muon trapping by the V_{Si} .

To verify the electron capture mechanisms predicted for μ^+ , with the direct formation of the paramagnetic Mu^0 state at V_{Si} involving one electron, and a delayed two-electron capture at V_{C} , a Bader charge analysis [53–56] was performed. Overall, the electron cloud was found to predominantly locate around the C atoms, avoiding Si altogether. Upon considering the charge density surrounding the $V_{\text{C}}-\text{Mu}$ and $V_{\text{Si}}-\text{Mu}$ complexes for Fermi levels located both near mid-gap and close to CBM, we find a consistent trend: for the $V_{\text{C}}-\text{Mu}$ complex, two electrons are located close to the muon, whereas a muon bound to V_{Si} will only attach to one electron, in accordance with the interpretation of the experimental data.

IV. DISCUSSION

An intriguing aspect of our findings that evolves when comparing the present results to a previous 4H-SiC study in Ref. [16] is the subject of sensitivity. Indeed, the muons appear to be far more sensitive to some defects than others, which highlights the need for a thorough understanding of the

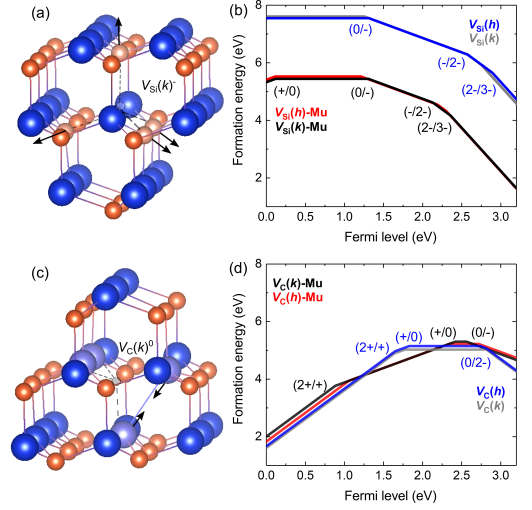


FIG. 5: Atomic structure and formation energy diagrams for h and k (a) V_{Si} and (b) V_{Si} & $V_{\text{Si}}-\text{Mu}$, and (c) V_{C} and (d) V_{C} & $V_{\text{C}}-\text{Mu}$. Si atoms are in blue or light blue (if distorted by the vacancy), and C atoms in orange or light orange. The total energies of V_{Si} are from Ref. [14], and those of $V_{\text{Si}}-\text{Mu}$ are from Ref. [38]. The valence band energy is offset to zero.

interplay between muons and different defect types. While a change in the μSR signal (i.e. a reduction of F_D) is already observed at V_{Si} concentrations around $3 \times 10^{14} \text{ cm}^{-3}$, this is not the case for comparable V_{C} densities, and the two samples annealed at 1200°C exhibit very similar behavior despite their different V_{C} concentrations (Fig. 3a). In short, we observe a much higher sensitivity of the muons towards V_{Si} than V_{C} . Based on the DFT calculations, this may be attributed to the greater charge of V_{Si} compared to V_{C} , providing a larger attractive Coulomb force for the positive muon, and a larger energy gain by $V_{\text{Si}}-\text{Mu}$ complex formation compared to that of $V_{\text{C}}-\text{Mu}$ (see Fig. 5). In addition, there are also structural differences between the two vacancies: as the void left by the Si atom is much larger than in the case of the V_{C} , the implanted muon may preferably stop at the more extended V_{Si} .

From our results, it is interesting to consider the close resemblance of the mechanisms for muon capture by V_{Si} and V_{C} , and their fundamental properties as either high-spin or negative- U defects. A μ^+ in the vicinity of V_{Si} is captured to form an isolated and stable Mu^0 , which does not interact further with the environment. This is similar to electron localization in V_{Si}^- , where weak interactions between V_{Si} and the surroundings result in long spin coherence times and a weak outward breathing motion of the neighboring carbon atoms. Conversely, the neighboring atoms surrounding V_{C} collapse inwards following a symmetry-lowering path, leaving a smaller lattice void for the muon to fill in V_{C} compared to V_{Si} . The capture of μ^+ at V_{C} may also result in the formation of Mu^0 , but interactions between V_{C} and the environment are strong,

prompting the capture of a second electron and the formation of delayed Mu^- . In other words, the strong electron-phonon coupling of V_C leads to a prominent Jahn-Teller distortion of the surrounding geometry, which may be indirectly probed via the Mu formation process of the implanted μ^+ . This interpretation is also supported by DFT calculations, where the geometric relaxation surrounding $(V_{\text{Si}}-\text{Mu})^-$ is almost identical to that of V_{Si}^- , while introducing a muon into V_C^0 and forming $(V_C-\text{Mu})^+$ yields significant interactions between μ^+ and the lattice. For Fermi levels approaching the CBM, the V_{Si} and V_C would take the charge states $3-$ and $2-$, respectively, while retaining their distinct relaxation characteristics. Thus, the different muon capture mechanisms by V_{Si} and V_C can be directly related to their proclivity towards either localized high-spin states or JT distortions.

V. CONCLUSION

In conclusion, the sensitivity of μ^+ to both V_{Si} and V_C with their distinct symmetry properties was successfully demonstrated. In the LE- μSR measurements performed on proton-irradiated 4H-SiC, it was revealed that V_{Si} concentrations as low as $3 \times 10^{14} \text{ cm}^{-3}$ already cause a reduction of F_D accompanied by a weakening of the field dependence. This is explained by the tendency of the Mu^+ to be trapped by V_{Si} and to capture one electron to form Mu^0 . An effect on the μSR signal in the case of V_C was only observed at considerably larger concentrations ($>10^{17} \text{ cm}^{-3}$) where a suppression of promptly formed Mu^0 causes a strong increase of F_D . There, a two-electron capture process at the V_C needs to be considered where a Mu^+ forms Mu^- via a short-lived Mu^0 state [16].

We propose that the LE- μSR technique is sensitive to the

distinct relaxation mechanisms driven by the vacancy nearest-neighbor dangling bonds, based on the muon experiments and supporting DFT calculations. Jahn-Teller distortions are often characteristics of negative- U defects [57] like V_C in SiC and the Si vacancy in silicon, while weak relaxations due to small electron-phonon interactions are commonly found for qubit candidates like V_{Si} in SiC and the NV center in diamond [58,59]. Consequently, the muon technique may be used to differentiate between high-spin and negative- U behavior also for systems besides SiC, e.g. in SiGe, where negative- U behavior and JT distortions are predicted for the Ge vacancy while the Si vacancy exhibits high-spin qubit capabilities [60]. Our results also emphasize the large potential of LE- μSR to identify and distinguish defects close to the semiconductor surface, which is a key aspect for many electronic and quantum technology applications.

Acknowledgments

The muon measurements have been performed at the Swiss Muon Source $\text{S}\mu\text{S}$, Paul Scherrer Institute, Villigen, Switzerland. Special thanks go to the HIPA team for providing a stable primary proton beam. Financial support was kindly provided by the Research Council of Norway and the University of Oslo through the frontier research project FUNDA-MeNT (no. 251131, FriPro ToppForsk-program). The Research Council of Norway is acknowledged for the support to the Norwegian Micro- and Nano-Fabrication Facility, NorFab, project number 245963. The computations were performed on resources provided by UNINETT Sigma2 - the National Infrastructure for High Performance Computing and Data Storage in Norway.

-
- [1] F. Bechstedt, A. Zywietz, and J. Furthmüller, *Europhysics Letters* **44**, 309 (1998).
 - [2] J. Furthmüller, A. Zywietz, and F. Bechstedt, *Materials Science and Engineering* **B61–62**, 244 (1999).
 - [3] A. Zywietz, J. Furthmüller, and F. Bechstedt, *Physical Review B* **59**, 15166 (1999).
 - [4] A. Zywietz, J. Furthmüller, and F. Bechstedt, *Physical Review B* **61**, 13655 (2000).
 - [5] A. Zywietz, J. Furthmüller, and F. Bechstedt, *Physical Review B* **62**, 6854 (2000).
 - [6] T. Kimoto, *physica status solidi (b)* **245**, 1327 (2008).
 - [7] N. T. Son, X. T. Trinh, L. S. Løvlie, B. G. Svensson, K. Kawahara, J. Suda, T. Kimoto, T. Umeda, J. Isoya, T. Makino, et al., *Physical Review Letters* **109**, 187603 (2012).
 - [8] M. Widmann, S.-Y. Lee, T. Rendler, N. T. Son, H. Fedder, S. Paik, L.-P. Yang, N. Zhao, S. Yang, I. Booker, et al., *Nature Materials* **14**, 164 (2014).
 - [9] J. Coutinho, V. J. B. Torres, K. Demmouche, and S. Öberg, *Physical Review B* **96**, 174105 (2017).
 - [10] S. Castelletto, L. Rosa, and B. C. Johnson, in *Advanced Silicon Carbide Devices and Processing* (InTech, 2015).
 - [11] H. Kraus, V. A. Soltamov, D. Riedel, S. Väh, F. Fuchs, A. Sperlich, P. G. Baranov, V. Dyakonov, and G. V. Astakhov, *Nature Physics* **10**, 157 (2014).
 - [12] E. Sörman, N. T. Son, W. M. Chen, O. Kordina, C. Hallin, and E. Janzén, *Physical Review B* **61**, 2613 (2000).
 - [13] M. Wagner, B. Magnusson, W. M. Chen, E. Janzén, E. Sörman, C. Hallin, and J. L. Lindström, *Physical Review B* **62**, 16555 (2000).
 - [14] M. E. Bathen, A. Galeckas, J. Mütting, H. M. Ayedh, U. Grossner, J. Coutinho, Y. K. Frodason, and L. Vines, *npj Quantum Information* **5**, 111 (2019).
 - [15] H. M. Ayedh, A. Hallén, and B. G. Svensson, *Journal of Applied Physics* **118**, 175701 (2015).
 - [16] J. Woerle, T. Prokscha, A. Hallén, and U. Grossner, *Physical Review B* **100**, 115202 (2019).
 - [17] J. F. Ziegler, M. Ziegler, and J. Biersack, *Nuclear Instruments and Methods in Physics Research Section B: Beam Interactions with Materials and Atoms* **268**, 1818 (2010).
 - [18] T. Prokscha, E. Morenzoni, K. Deiters, F. Foroughi, D. George, R. Kobler, A. Suter, and V. Vrankovic, *Nuclear Instruments and Methods in Physics Research Section A: Accelerators, Spectrometers, Detectors and Associated Equipment* **595**, 317 (2008).

- [19] E. Morenzoni, H. Glückler, T. Prokscha, H. P. Weber, E. M. Forgan, T. J. Jackson, H. Luetkens, C. Niedermayer, M. Pleines, M. Birke, et al., *Physica B: Condensed Matter* **289-290**, 653 (2000).
- [20] R. F. Kiefl and T. L. Estle, in *Semiconductor and Semimetals*, edited by J. I. Pankove and N. M. Johnson (Elsevier, 1991), vol. 34, URL <http://www.sciencedirect.com/science/article/pii/S0080878408628707>.
- [21] S. J. Blundell, *Contemporary Physics* **40**, 175 (1999).
- [22] K. Nagamine, *Introductory Muon Science* (Cambridge University Academic Press, 2003), URL <https://doi.org/10.1017/CBO9780511470776>.
- [23] P. Bakule and E. Morenzoni, *Contemporary Physics* **45**, 203 (2004), URL <https://doi.org/10.1080/00107510410001676803>.
- [24] G. Kresse and J. Hafner, *Physical Review B* **47**, 558 (1993).
- [25] G. Kresse and J. Hafner, *Physical Review B* **49**, 14251 (1994).
- [26] G. Kresse and J. Furthmüller, *Computational Materials Science* **6**, 15 (1996).
- [27] G. Kresse and J. Furthmüller, *Physical Review B* **54**, 11169 (1996).
- [28] P. E. Blöchl, *Physical Review B* **50**, 17953 (1994).
- [29] F. Bernardini, P. Bonfá, S. Massidda, and R. D. Renzi, *Physical Review B* **87**, 115148 (2013).
- [30] S. Sturniolo, L. Liborio, and S. Jackson, *The Journal of Chemical Physics* **150**, 154301 (2019).
- [31] S. B. Zhang and J. E. Northrup, *Physical Review Letters* **67**, 2339 (1991).
- [32] C. Freysoldt, B. Grabowski, T. Hickel, J. Neugebauer, G. Kresse, A. Janotti, and C. G. Van de Walle, *Reviews of Modern Physics* **86**, 253 (2014).
- [33] C. Freysoldt, J. Neugebauer, and C. G. Van de Walle, *Physical Review Letters* **102**, 016402 (2009).
- [34] H.-P. Komsa, T. T. Rantala, and A. Pasquarello, *Physical Review B* **86**, 045112 (2012).
- [35] Y. Kumagai and F. Oba, *Physical Review B* **89**, 195205 (2014).
- [36] J. P. Perdew, K. Burke, and M. Ernzerhof, *Physical Review Letters* **77**, 3865 (1996).
- [37] J. Heyd, G. E. Scuseria, and M. Ernzerhof, *The Journal of Chemical Physics* **118**, 8207 (2003).
- [38] M. E. Bathen, A. Galeckas, J. Coutinho, and L. Vines, *Journal of Applied Physics* **127**, 085701 (2020).
- [39] T. Kimoto, A. Itoh, H. Matsunami, S. Sridhara, L. L. Clemen, R. P. Devaty, W. J. Choyke, T. Dalibor, C. Pempmler, and G. Pensl, *Applied Physics Letters* **67**, 2833 (1995), <https://doi.org/10.1063/1.114800>, URL <https://doi.org/10.1063/1.114800>.
- [40] W. F. Koehl, B. B. Buckley, F. J. Heremans, G. Calusine, and D. D. Awschalom, *Nature* **479**, 84 (2011).
- [41] R. Karsthof, M. E. Bathen, A. Galeckas, and L. Vines, *Conversion pathways of primary defects by annealing in proton-irradiated n-type 4H-SiC* (2020), URL [arXiv:2007.03985](https://arxiv.org/abs/2007.03985).
- [42] E. Janzén, A. Gali, P. Carlsson, A. Gällström, B. Magnusson, and N. Son, *Physica B: Condensed Matter* **404**, 4354 (2009).
- [43] V. Ivády, J. Davidsson, N. T. Son, T. Ohshima, I. A. Abrikosov, and A. Gali, *Physical Review B* **96**, 161114(R) (2017).
- [44] T. Hornos, A. Gali, and B. G. Svensson, *Materials Science Forum* **679-680**, 261 (2011).
- [45] R. C. Vilão, R. B. L. Vieira, H. V. Alberto, J. M. Gil, and A. Weidinger, *Physical Review B* **96**, 195205 (2017).
- [46] R. L. Lichti, W. A. Nussbaum, and K. H. Chow, *Physical Review B* **70**, 165204 (2004).
- [47] H. Bani-Salameh, Y. Celebi, K. Chow, B. Coss, S. Cox, and R. Lichti, *Physica B: Condensed Matter* **374-375**, 368 (2006), ISSN 0921-4526, proceedings of the Tenth International Conference on Muon Spin Rotation, Relaxation and Resonance, URL <http://www.sciencedirect.com/science/article/pii/S0921452605013219>.
- [48] Y. G. Celebi, R. L. Lichti, B. R. Carroll, P. J. C. King, and S. F. J. Cox, *Physica B: Condensed Matter* **404**, 5117 (2009).
- [49] B. D. Patterson, *Rev. Mod. Phys.* **60**, 69 (1988).
- [50] D. G. Eshchenko, V. G. Storchak, J. H. Brewer, G. D. Morris, S. P. Cottrell, and S. F. J. Cox, *Physical Review B* **66**, 035105 (2002).
- [51] T. Prokscha, E. Morenzoni, D. G. Eshchenko, N. Garifanov, H. Glückler, R. Khasanov, H. Luetkens, and A. Suter, *Physical Review Letters* **98**, 227401 (2007).
- [52] Y. Celebi, R. Lichti, H. Bani-Salameh, A. Meyer, B. Carroll, J. Vernon, P. King, and S. Cox, *Physica B: Condensed Matter* **404**, 845 (2009), ISSN 0921-4526, URL <http://www.sciencedirect.com/science/article/pii/S0921452608006868>.
- [53] G. Henkelman, A. Arnaldsson, and H. Jónsson, *Computational Materials Science* **36**, 354 (2006).
- [54] E. Sanville, S. D. Kenny, R. Smith, and G. Henkelman, *Journal of Computational Chemistry* **28**, 899 (2007).
- [55] W. Tang, E. Sanville, and G. Henkelman, *J. Phys.: Condens. Matter* **21**, 084204 (2009).
- [56] M. Yu and D. R. Trinkle, *Journal of Chemical Physics* **134**, 064111 (2011).
- [57] G. D. Watkins, *Advances in Solids State Physics* (Springer, 1984), chap. Negative- U properties for defects in solids, pp. 163–189.
- [58] J. P. Goss, R. Jones, S. J. Breuer, P. R. Briddon, and S. Öberg, *Physical Review Letters* **77**, 3041 (1996).
- [59] A. Gali, M. Fyta, and E. Kaxiras, *Physical Review B* **77**, 155206 (2008).
- [60] J. Lento, M. Pesola, J.-L. Mozos, and R. M. Nieminen, *Applied Physics Letters* **77**, 232 (2000).

Paper VIII

Diffusion of the Carbon Vacancy in a-Cut and c-Cut n-Type 4H-SiC

M. E. Bathen, H. M. Ayedh, L. Vines, I. Farkas, E. Janzén, B. G. Svensson

Published in *Materials Science Forum*, June 2018, Volume 924, pp. 200-203.
DOI: 10.4028/www.scientific.net/MSF.924.200.

VIII

Paper IX

Anisotropic and plane-selective migration of the carbon vacancy in SiC: Theory and experiment

M. E. Bathen, J. Coutinho, H. M. Ayedh, J. Ul Hassan, I. Farkas, S. Öberg, Y. K. Frodason, B. G. Svensson, L. Vines

Published in *Physical Review B*, July 2019, Volume 100 (014103).
DOI: 10.1103/PhysRevB.100.014103.

Anisotropic and plane-selective migration of the carbon vacancy in SiC: Theory and experimentM. E. Bathen,^{1,*} J. Coutinho,² H. M. Ayedh,¹ J. Ul Hassan,³ I. Farkas,³ S. Öberg,⁴ Y. K. Frodason,¹ B. G. Svensson,¹ and L. Vines¹¹*Department of Physics/Centre for Materials Science and Nanotechnology, University of Oslo, N-0316 Oslo, Norway*²*Department of Physics and I3N, University of Aveiro, Campus Santiago, 3810-193 Aveiro, Portugal*³*Department of Physics, Chemistry and Biology, Linköping University, SE-58183 Linköping, Sweden*⁴*Department of Engineering Sciences and Mathematics, Luleå University of Technology, SE-97187 Luleå, Sweden*

(Received 25 February 2019; revised manuscript received 3 May 2019; published 8 July 2019)

We investigate the migration mechanism of the carbon vacancy (V_C) in silicon carbide (SiC) using a combination of theoretical and experimental methodologies. The V_C , commonly present even in state-of-the-art epitaxial SiC material, is known to be a carrier lifetime killer and therefore strongly detrimental to device performance. The desire for V_C removal has prompted extensive investigations involving its stability and reactivity. Despite suggestions from theory that V_C migrates exclusively on the C sublattice via vacancy-atom exchange, experimental support for such a picture is still unavailable. Moreover, the existence of two inequivalent locations for the vacancy in 4H-SiC [hexagonal, $V_C(h)$, and pseudocubic, $V_C(k)$] and their consequences for V_C migration have not been considered so far. The first part of the paper presents a theoretical study of V_C migration in 3C- and 4H-SiC. We employ a combination of nudged elastic band (NEB) and dimer methods to identify the migration mechanisms, transition state geometries, and respective energy barriers for V_C migration. In 3C-SiC, V_C is found to migrate with an activation energy of $E_A = 4.0$ eV. In 4H-SiC, on the other hand, we anticipate that V_C migration is both anisotropic and basal-plane selective. The consequence of these effects is a slower diffusivity along the axial direction, with a predicted activation energy of $E_A = 4.2$ eV, and a striking preference for basal migration within the h plane with a barrier of $E_A = 3.7$ eV, to the detriment of the k -basal plane. Both effects are rationalized in terms of coordination and bond angle changes near the transition state. In the second part, we provide experimental data that corroborates the above theoretical picture. Anisotropic migration of V_C in 4H-SiC is demonstrated by deep level transient spectroscopy (DLTS) depth profiling of the $Z_{1/2}$ electron trap in annealed samples that were subject to ion implantation. Activation energies of $E_A = (4.4 \pm 0.3)$ eV and $E_A = (3.6 \pm 0.3)$ eV were found for V_C migration along the c and a directions, respectively, in excellent agreement with the analogous theoretical values. The corresponding prefactors of $D_0 = 0.54$ cm²/s and 0.017 cm²/s are in line with a simple jump process, as expected for a primary vacancy point defect.

DOI: [10.1103/PhysRevB.100.014103](https://doi.org/10.1103/PhysRevB.100.014103)**I. INTRODUCTION**

The properties of silicon carbide (SiC), including a wide band gap, large breakdown field, and radiation hardness, are highly advantageous for conceiving novel quantum, optical, and electronic devices [1,2], such as power MOSFETs [3] and nuclear detectors operating under harsh conditions [4]. Recent breakthroughs have established SiC as a leading candidate host for solid-state single-photon emitters (SPEs) and spin centers that are highly desirable for quantum computing devices. Behind these findings are the silicon vacancy (V_{Si}) in 4H-SiC [5], as well as the nitrogen-vacancy (NCV_{Si}) [5,6] and divacancy ($V_C V_{Si}$) [6–8] centers in both 3C and 4H materials. On the other hand, for devices that essentially rely on the lifetime of charge carriers, defects remain a perennial threat. Unlike extended defects which have been largely eliminated from state-of-the-art epitaxial material, point defects and impurities still limit the minority carrier lifetime in SiC by acting as carrier traps and recombination centers.

The carbon vacancy (V_C), in particular, is a prominent trap with strong and detrimental impact on the carrier lifetime of 4H-SiC [9–11]. Being omnipresent even in state-of-the-art epitaxial material [12] (where V_C is typically found in concentrations in the range 10^{12} – 10^{13} cm⁻³), the V_C effectively limits the carrier lifetime to below $5 \sim \mu$ s, which is too low for devices operating with blocking voltages above 10 kV [13]. Understanding the behavior of this defect, especially during common device processing steps such as ion implantation and high temperature heat treatments, is therefore crucial for realizing the full potential of SiC.

In 4H-SiC, and disregarding any departure from the perfect vacancy structure due to pseudo-Jahn-Teller distortions [14], V_C may occur in two configurations, namely at pseudocubic and hexagonal sites [$V_C(k)$ and $V_C(h)$], essentially differing by some of their second neighbors and more remote ligands. The 3C-SiC cubic phase is isotropic, and only one V_C configuration can be found. Both V_C configurations in 4H-SiC are negative- U double acceptors, meaning that single-negative charge states are metastable and accessible only upon persistent illumination [15]. In n-type 4H-SiC, a twofold electron emission from V_C can be detected by deep level transient

*m.e.bathen@fys.uio.no

spectroscopy (DLTS), being manifested as a prominent peak at about 290 K (labeled $Z_{1/2}$). This peak was connected to the superposition of $(-2/0)$ charge-state transitions of both $V_C(k)$ and $V_C(h)$ defects. Measurements of the activation energy for electron emission placed the transition at 0.67 eV below the conduction band edge (E_C) [15]. As far as we are aware, no analogous DLTS peaks were detected in 3C-SiC. This could be explained if we consider that the valence band maxima of 3C- and 4H-SiC are essentially aligned (a small ~ 60 meV offset has been measured [16]), and that the Langer-Heinrich rule applies to defects in different SiC polytypes [17], i.e., V_C levels are approximately pinned to the vacuum level regardless of the polytype [18]. With this in mind, we estimate the $(-2/0)$ transition of V_C in 3C-SiC to be located at $\sim 0.3\text{--}0.4$ eV above E_C .

First-principles calculations show that the charge-neutral V_C in 4H-SiC has a low formation energy in the range 4.5–5 eV [14,19], partly explaining its prevalence in as-grown (nonirradiated) material, apparently showing a high thermal stability [12,20,21]. It has been shown that reaching the thermodynamic equilibrium of the V_C , at, e.g., $\sim 1500^\circ\text{C}$, requires less than 1 h and results in a V_C concentration of only $\sim 10^{11}\text{ cm}^{-3}$ [13]. On the other hand, electron paramagnetic resonance (EPR) studies reported that V_C anneals out already at 1100°C [22,23], with some traces remaining at 1600°C . These observations could however be explained by a reaction with an impurity or defect that becomes mobile above 1100°C , and not necessarily by the disappearance of V_C upon its motion. Thus, despite indications that V_C could be mobile over a wide temperature window ($\sim 1100\text{--}1600^\circ\text{C}$), both its diffusivity and underlying mechanism remain undetermined. At the above temperatures, intrinsic conditions apply to SiC, and most likely V_C adopts the neutral charge state in both 3C- and 4H-SiC. However, by noting that under these conditions the Fermi level is close to the donor transition of V_C , we cannot entirely rule out a possible contribution of a smaller population of positively charged vacancies to the diffusivity.

Previous theoretical studies suggest that the migration mechanism of V_C , in both 3C- and 4H-SiC, does not involve other defects. They indicate that V_C jumps are solely mediated by vacancy-atom exchange within the C sublattice [24,25]. For neutral V_C in 3C-SiC, the activation energy for migration via second-neighbor hopping was estimated at $E_A = 3.5$ eV using local density functional theory [24–26]. In order to mitigate the self-interaction error from the local functional, that figure was increased to 4.2 eV after post correcting the total energies by means of *ad-hoc* shifts to the one-electron energies [26]. Other studies, using larger supercells and an efficient but less accurate self-consistent density-functional-based tight-binding method, reported activation barriers as high as 4.8 eV [26,27]. Assuming that the diffusivity is thermally activated with an attempt frequency for jumping approximated by the Debye frequency of SiC, the above range of activation energies corresponds to an error bar in the annealing temperature of nearly 600°C .

The above discussion relates to V_C diffusivity in 3C-SiC. However, regarding 4H-SiC (the material of choice by the industry to fabricate power devices), we are dealing with a problem which is largely uncharted. Recently, activation barriers for the jumping of point defects in 4H-SiC (mostly

concerning the V_{Si} defect) were shown to depend substantially on the sublattice location of the starting and ending structures [28]. A subsequent study demonstrated a similar effect for neutral V_C [29]. Interestingly, and although not reported by the authors, from their results we can infer that V_C diffusivity could be anisotropic. Hence, the large scattering in the reported theoretical barriers, as well as a poor understanding of the connection between crystalline anisotropy and vacancy diffusivity, call for a close look at this problem.

A deep level transient spectroscopy (DLTS) study indicated that V_C could diffuse laterally in *c*-cut (0001) samples already at room temperature [30]. This was, however, put into question in a recent experimental study, where we found that temperatures above 1200°C [31] are required for significant V_C migration along both the *a* and the *c* directions ($\langle 11\bar{2}0 \rangle$ and $\langle 0001 \rangle$, respectively). In the same study, V_C diffusion in 4H-SiC was demonstrated to be anisotropic [31]. This was achieved by combining heat treatments up to 1400°C with subsequent DLTS depth profiling to resolve V_C depth distributions before and after diffusion [31]. The defect was found to diffuse much farther along the basal direction (in comparison to the axial direction), but unfortunately activation energies and diffusivities for V_C migration were not reported at the time due to lack of data. Still, the small ($\sim 0.02\%$) difference between basal and pseudoaxial jump lengths in 4H-SiC can hardly explain that observation. In Ref. [31] it was suggested that the anisotropy could be related to the fact that 4H-SiC holds two distinct carbon vacancies, namely $V_C(k)$ and $V_C(h)$, but the argument was not sufficiently developed as to substantiate such a statement.

Anisotropic diffusivity can lead to inhomogeneities in the V_C concentration across SiC-based devices, degrading carrier lifetime in certain areas which are then rendered useless. Such problems are likely to be extended to dopant activation and distribution, which depend on vacancy diffusion, thus prompting a search for the details behind anisotropy during thermally activated V_C migration. In the present study we aim at elucidating the atomistic aspects of V_C migration in 3C- and 4H-SiC by combining theory and experiments while taking the duality of lattice sites in 4H-SiC into account. To that end, we employ hybrid (nonlocal) and semilocal density functional calculations, combining the nudged elastic band and dimer methods to explore the potential energy surface along individual vacancy jumps. Moreover, we study thermally activated V_C migration experimentally (in 4H-SiC only), by combining heat treatments and DLTS depth profiling measurements, and quantify V_C diffusivities along two different crystallographic directions: the *c* direction and the *a* direction. In addition to yielding the energy barriers for V_C migration, the experimental data offers the possibility to determine the mechanism by which carbon vacancies migrate in 4H-SiC.

The paper is organized in the following way. Section II contains the relevant computational details, with a large portion of this section devoted to tests and benchmarking to support our results. The experimental methods used are also found in Sec. II. The main findings of this work are presented in Sec. III, divided into a theory section (which is separated according to the SiC polytype under scrutiny) and an experimental section. Section IV is devoted to a comparison of the theoretical and experimental results, a discussion of

key issues including the electronic and atomistic structure along migration paths, and consequences for self-diffusion in 4H-SiC. Finally, concluding remarks are provided in Sec. V.

II. METHODS

A. Theory

1. Computational details

All defect calculations were performed using the VASP density functional software [32–35], with which we found electronic ground states within the Kohn-Sham formalism, using the projector augmented-wave (PAW) method [36] and plane waves to describe core and valence electrons, respectively. Supercells of 3C-SiC (4H-SiC) with cubic (hexagonal) shape were constructed by replicating $3 \times 3 \times 3$ ($5 \times 5 \times 2$) conventional (primitive) cells along the main axes. Pristine supercells comprised a total of 216 (400) atoms, from which one carbon atom was removed to create a V_C defect. The lattice constants were $a_0 = 4.347$ Å for 3C-SiC, while for 4H-SiC we used $a = 3.071$ Å and $c = 10.152$ Å. These figures were obtained within screened hybrid density functional theory (HSE06 [37,38]), upon relaxation of primitive cells using fully converged $13 \times 13 \times 13$ - and $13 \times 13 \times 7$ - Γ -centered grids of \mathbf{k} points to sample the Brillouin zone (BZ), respectively. While differing by less than 0.6% from their experimental counterparts [39,40], such a discrepancy is not expected to induce significant effects to the calculated migration barriers.

All V_C ground state geometries were relaxed within the generalized gradient approximation to the exchange correlation potential as proposed by Perdew, Burke, and Ernzerhof (PBE) [41]. The plane-wave energy cutoff was set to 420 eV. Brillouin zones of 3C- and 4H-SiC supercells were sampled with $2 \times 2 \times 2$ Monkhorst-Pack and $2 \times 2 \times 2$ Γ -centered \mathbf{k} -point meshes, respectively. The electronic self-consistent energy was minimized to a numerical accuracy of 10^{-6} eV, while atomic coordinates of stable structures were relaxed by means of a conjugate-gradient algorithm until the largest force was lower than 0.01 eV/Å. The resulting defect structures matched recent semilocal and hybrid DFT calculations [14,19,42].

To investigate individual jumps between different lattice sites during V_C migration, a combination of the nudged elastic band (NEB) [43,44] and the dimer [45] methods was employed at the PBE level. When commencing a NEB calculation of each jump, initial and final geometries are fixed, and a chain of intermediate changeable *images* (like frames in a movie sequence) are created along the configurational space between the end points. The images are connected by spring interactions to avoid becoming either too close or too distant from each other. Finally, they are collectively optimized, resulting in a series of images that closely follow a minimum energy path (MEP) connecting the end structures.

In a first step, NEB calculations yielded a preliminary portrayal of the MEP for each vacancy-atom exchange step. They approximately describe the mechanism where a carbon atom neighboring the vacancy jumps into the vacant site, leaving a new V_C in its wake. For these *exploratory* inspections of the MEP, 11 intermediate images, a plane-wave energy

cutoff of $E_{\text{cut}} = 300$ eV, and the Γ point for BZ sampling were deemed sufficient. The end structures were still those obtained within the higher level of accuracy (concerning basis and BZ sampling) as employed during the relaxation of the ground state structures.

Due to the use of supercells and the concomitant BZ folding, the band gap of the Kohn-Sham electronic structure becomes direct and narrowest at $\mathbf{k} = \Gamma$. On top of that, the use of a semilocal functional, and the unavoidable underestimated gap width, affects structures and energies due to spurious over mixing of gap states (from the vacancy) with crystalline states, particularly at the Γ point [42].

Given the above, a refinement of the calculated transition-state structures was needed, most importantly to employ a set of BZ sampling points with lower mixing effects. For that purpose, the \mathbf{k} points for BZ sampling and E_{cut} were chosen to be identical to those used for the ground state relaxations. Hence, we either carried out (i) upgraded NEB calculations restricted to a narrower sequence of images enclosing the higher energy section obtained from the exploratory MEP or (ii) used a local search algorithm, namely the dimer method to find the saddle point. In both cases, the starting point was the result from the exploratory Γ -point NEB calculations. We found that either way, both methods yield approximately identical results. However, due to its lower computational cost, the dimer method was mostly used.

The dimer method requires two images comprising the actual *dimer*, which are displaced from each other by a small distance and should be close to the saddle point. The saddle point can then be identified by consecutive dimer rotations and changes in dimer separation within the potential energy surface [45]. Provided that we have a good starting structure, the dimer method was found to be a swift and dependable transition-state search algorithm [46].

Finally, after identification of the transition-state geometries, single-point energies of the initial, transition, and final states were determined self-consistently by using the screened hybrid density functional HSE06 [37,38], Γ only for BZ sampling and $E_{\text{cut}} = 420$ eV for the plane-wave energy cutoff. Activation energies for V_C jumps were obtained from the energy difference between transition and initial states.

The HSE06 functional is widely accepted as capable of accurately capturing the 3C- and 4H-SiC electronic structure, yielding calculated band gaps of 2.24 eV and 3.17 eV at $T = 0$ K, respectively, close to the experimental values of 2.4 eV [11] and 3.27 eV [47]. The use of screened hybrid DFT energies of PBE-relaxed structures was recently tested for solid-state problems, including defects in SiC [48]. This approach allows us (i) to employ large enough supercells to accommodate the strain fields produced by the vacancy and at the same time (ii) to avoid artificial hybridization between vacancy and crystalline states.

We may summarize the methodology employed as the following recipe (applied to both 3C- and 4H-SiC):

- (1) Relaxation at PBE level, with BZ $2 \times 2 \times 2$ -sampling and $E_{\text{cut}} = 420$ eV, to obtain initial and final V_C structures involved in the jumps.
- (2) Exploratory NEB calculation at PBE level, with BZ Γ sampling and $E_{\text{cut}} = 300$ eV, to identify an approximate MEP and transition state.

(3) Transition-state search using the dimer method at PBE level, BZ $2 \times 2 \times 2$ sampling and $E_{\text{cut}} = 420$ eV. The initial dimer was made from the two highest energy structures from the exploratory NEB run.

(4) Total energy calculations of PBE geometries at HSE06-level, with BZ Γ sampling and $E_{\text{cut}} = 420$ eV, to find the energy barriers for V_C jumps.

2. Workflow testing

While the method presented in the previous section was being developed, several tests were performed to ensure the accuracy and correctness of each calculation step by investigating whether the V_C migration barrier height was converged with respect to the BZ sampling at both the PBE and HSE06 levels. Moreover, several variations of the methodology were tested, to ensure that they yielded the same result. Due to the larger supercell size and greater complexity of 4H-SiC, tests were firstly performed in 3C-SiC. Final HSE06-level results for 4H-SiC will be presented in Sec. III. However, some benchmarking tests are also included herein for reference.

Prior to testing barrier height convergence with respect to \mathbf{k} -point sampling, the credibility of the method needed to be verified. Following an 11-image Γ -NEB calculation to obtain an exploratory MEP of V_C in 3C-SiC, we performed a second and more *focused* NEB calculation using a $2 \times 2 \times 2$ mesh of \mathbf{k} points and seven images distributed along a short configurational segment enclosing the saddle point region of the exploratory MEP. A comparison between the activation energy for migration, E_A , obtained according to the twofold NEB calculation described above and that obtained from the dimer approach, is shown in Table I. We conclude that both methods essentially lead to the same result, $E_A = 3.7$ eV. Table I also shows that the simpler exploratory NEB calculation (first data row) provides a barrier which is only ~ 0.2 eV below the best result, suggesting that the highest energy image is indeed a good starting point for the subsequent methods.

We also verified the BZ-sampling accuracy of a $2 \times 2 \times 2$ \mathbf{k} -point sampling mesh. The test was carried out using seven-image focused NEB runs as described above. An identical calculation with a $4 \times 4 \times 4$ \mathbf{k} -point mesh gave an energy

TABLE I. Test of the transition state optimization method in 3C-SiC. First row: Exploratory MEP search using a Γ -point 11-image NEB calculation. Second row: Focused 7-image NEB calculation over a short configurational segment of the exploratory MEP, near the saddle point, using $2 \times 2 \times 2$ BZ sampling. Third row: Dimer run for identifying the saddle point structure. Fourth row: Focused 7-image NEB calculation near the saddle point, using $4 \times 4 \times 4$ BZ sampling. All calculations were done at the PBE level with $E_{\text{cut}} = 300$ eV for the Γ -NEB and $E_{\text{cut}} = 420$ eV for the remaining calculations.

Method	Functional	\mathbf{k} -mesh	E_A (eV)
NEB (11-img)	PBE	Γ	3.52
NEB (7-img)	PBE	$2 \times 2 \times 2$	3.66
Dimer	PBE	$2 \times 2 \times 2$	3.69
NEB (7-img)	PBE	$4 \times 4 \times 4$	3.66

TABLE II. Convergence testing of V_C migration barrier heights in 3C- and 4H-SiC with respect to BZ sampling when using the two-step method Dimer+SCF@HSE06, namely a PBE-level dimer search (employing a MP- or Γ -centered $2 \times 2 \times 2$ \mathbf{k} mesh) followed by a SCF (self-consistent field) calculation at the HSE06 level. In 4H-SiC, one in-plane jump [namely hh , standing for $V_C(h) \rightarrow V_C(h)$] and two out-of-plane jumps (hk and kh) were investigated. Coordinates of \mathbf{k} points are in units of reciprocal lattice vectors. All values are in eV.

BZ sampling	3C-SiC	4H-SiC		
		hh	hk	kh
$\Gamma = (0, 0, 0)$	3.97	3.68	4.06	4.17
$R = (\frac{1}{2}, \frac{1}{2}, \frac{1}{2})$	4.03			
$A = (0, 0, \frac{1}{2})$		3.68	4.05	4.17
MP- $2 \times 2 \times 2$	4.07			
Γ - $2 \times 2 \times 2$			4.11	

barrier which differed by less than 2 meV from the analogous quantity obtained with a coarser $2 \times 2 \times 2$ mesh.

The energy barrier convergence with respect to BZ sampling was investigated in 3C-SiC when employing the dimer method followed by a final HSE06-level self-consistent field (SCF) calculation. The results of the test are summarized in Table II, including similar tests performed for the 4H-SiC case. In 3C-SiC, we find that the Γ -sampling result is already very close to that using a single \mathbf{k} -point at the corner of the BZ, namely $R = (\frac{1}{2}, \frac{1}{2}, \frac{1}{2})$, or even using the most accurate $2 \times 2 \times 2$ mesh. The difference between the Γ - and $2 \times 2 \times 2$ -sampled results is only 0.1 eV, the same as the expected error bar of the method.

In 4H-SiC, single-point sampling tests, namely Γ and $A = (0, 0, \frac{1}{2})$, were performed for in-plane (hh) and out-of-plane (hk and kh) vacancy jumps. The difference to the Γ -centered $2 \times 2 \times 2$ result was actually smaller, down to about 0.05 eV. Accordingly, the method of choice (Dimer+SCF@HSE06) with Γ -only sampling at the HSE06 level is deemed sufficient for capturing the energetics of V_C migration in 3C- and 4H-SiC.

B. Experiment

The experimental section of this work concerns 4H-SiC only as, to the best of our knowledge, no DLTS signal has been attributed to the carbon vacancy in 3C-SiC. Epitaxial layers (~ 10 μm) of n-doped (nitrogen) 4H-SiC with two different surface orientations were used: c -cut samples grown 4° off the c axis purchased from Cree Inc., and a -cut samples grown on-axis by chemical vapor deposition at 1650°C at the University of Linköping [49]. The samples were implanted with 4.0 MeV C ions to fluences of either 4×10^8 cm^{-2} or 6×10^8 cm^{-2} and having a projected range of ~ 2.5 μm according to collision Monte Carlo calculations as manifested in the SRIM (stopping and range of ions in matter) code [50]. All implantations were performed at room temperature with the samples tilted $\sim 8^\circ$ off with respect to the surface normal to reduce channeling. Carbon implantation was chosen to ensure selective formation of point defects while avoiding

non-native species, and the implantation energy was chosen for the projected range to be within the DLTS probing region. Following ion implantation, metastable peaks tend to appear near the $Z_{1/2}$ level in 4H-SiC DLTS spectra [51]. Hence, a post-implantation annealing at 200 °C was conducted to alleviate implantation damage and ensure that the V_C was primarily being addressed. Measurements after this initial annealing step are labeled *prediffusion*. Heat treatments were carried out at temperatures in the 200–1600 °C range, where the low temperature anneals between 200 °C and 600 °C were performed for 0.5 h in air using a conventional tube furnace, while at higher temperatures argon (Ar) atmosphere and a rf-heated furnace equipped with a graphite crucible were employed.

After the heat treatments, circular Ni Schottky contacts, having a diameter of ~ 1 mm and thickness ~ 150 nm, were deposited on top of the epilayers using an electron-beam evaporator, whereas silver paste was used as backside Ohmic contacts. The V_C concentration as a function of depth from the surface was investigated by monitoring the $Z_{1/2}$ peak at ~ 285 K using DLTS depth profiling employing a 640 ms⁻¹ rate window, while keeping the temperature within ± 0.1 K. The DLTS setup is described elsewhere [52]. The reverse bias was kept constant at -10 V, while gradually increasing the filling pulse voltage (50 ms duration) from 0 to 11 V. DLTS depth profiling yields a DLTS signal versus voltage, which can be converted into defect concentration versus depth according to [53]

$$N_t(x) = -\left(\frac{qW^2N_b}{\epsilon}\right)N_d(x)\frac{\partial(\Delta C/C)}{\partial V}, \quad (1)$$

where $N_t(x)$ is the defect (trap) concentration as a function of depth from the surface, q is the elementary charge, W the depletion width, N_b the concentration of ionized donors at the end of the depletion region, ϵ the semiconductor permittivity, $N_d(x)$ the concentration of ionized donors versus depth, and the last factor is the derivative of the DLTS signal versus voltage. The ionized donor concentrations, N_b and $N_d(x)$, were determined from capacitance-voltage measurements that were performed prior to each individual DLTS depth profiling procedure. For all measurements, $N_t < 0.1N_d$. Note that Eq. (1) is a commonly used approximation which neglects

the λ -correction term [54–56]. We will return to this issue in Sec. III B.

III. RESULTS

A. Theory

First of all, let us identify the number of possible ways a V_C defect can jump into a neighboring carbon site. Due to (pseudo-)Jahn-Teller effects, neutral V_C adopts tetragonal (D_{2d}) and monoclinic (C_{1h}) ground state structures in 3C- and 4H-SiC, respectively [14,24,42,57,58]. In the cubic phase, each carbon site has one shell of 12 carbon second neighbors, shown as black haloed spheres in Fig. 1(a). Due to symmetry lowering, a tetragonal V_C in 3C-SiC has two distinct shells of C neighbors (respectively populated with $4 + 8 = 12$ atoms). After each jump the vacancy can *land* with up to three symmetry-equivalent orientations, meaning that in principle we would have to consider 2 (shells) $\times 3$ (orientations) = 6 different ways of jumping. For the case of monoclinic V_C in 4H-SiC, there are two inequivalent lattice sites, each having seven inequivalent shells of carbon neighbors (respectively populated with $1 + 2 + 2 + 2 + 2 + 1 = 12$ atoms). Given that there are three symmetry-equivalent orientations of V_C for each lattice site, we end up with a total of 42 different jumps.

Fortunately, we know that the height of the energy barriers for conversion between equivalent (pseudo-)Jahn-Teller induced alignments, are about 0.3–0.4 eV [14]. Consequently, during vacancy migration, the temperatures are high enough to allow the defect to freely roam around all orientations and effectively show tetrahedral or trigonal symmetry in 3C- and 4H-SiC, respectively. From the NEB runs, we actually found that during the very early stages of each jump, the V_C defect nearly gains the full symmetry, and from there, proceeds with the actual jump. Hence, we assume that the saddle point structure does not depend on the choice of initial/final orientation of the defect. This reduces the number of jumps to one in 3C-SiC and to three for each vacancy [$V_C(k)$ and $V_C(h)$] in 4H-SiC.

The possible jumps are depicted in Fig. 1, where curved arrows illustrate approximate paths of the carbon vacancy. In

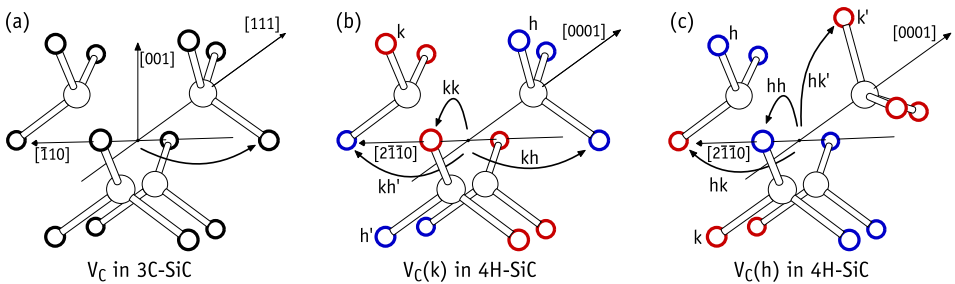


FIG. 1. Illustration of the possible jumps of (a) V_C in 3C-SiC, (b) $V_C(k)$ in 4H-SiC, and (c) $V_C(h)$ in 4H-SiC, into nearest neighbor C sites. Si and C atoms are represented in white, with thin and thick halos, respectively. Red- and blue-circled atoms in 4H-SiC differentiate C atoms occupying k and h planes. Curved arrows illustrate approximate paths of the carbon vacancy and point to the C_x atom of that particular jump (see text). Individual jumps are labeled by letter pairs indicating initial and final lattice sites of V_C . In 4H-SiC, kh and kh' are symmetrically related to hk and hk' , respectively (see text).

3C-SiC all V_C jumps are symmetrically equivalent, leaving a single jump (among 12 possibilities) to be explored. It is convenient at this point to single out the shell of twelve carbon atoms directly bound to the Si atoms that are edging the vacancy. During a vacancy jump, any of these C atoms can exchange their position with the vacancy. Hereafter, the jumping C atom is labeled C_x , standing for *exchanging C atom*. Analogously, the shell of twelve carbon atoms is referred to as C_x shell.

In Figs. 1(b) and 1(c), individual jumps in 4H-SiC are labeled by letter pairs indicating initial and final lattice sites of V_C . Pseudocubic and hexagonal carbon sites are highlighted with red and blue halos, respectively. For each lattice site we have one basal jump (kk' and hh') and two pseudoaxial jumps,¹ namely $\{kh, kh'\}$ for $V_C(k)$ and $\{hk, hk'\}$ for $V_C(h)$, respectively. We also note that, if $h'-k-h-k'$ stands for the sequence of four carbon atoms in the 4H-SiC primitive cell along the axial direction, kh is related to hk by reversal symmetry, and in the same way, kh' is a reversed hk' jump. So, the irreducible number of jumps to consider in 4H-SiC is four. Two of them span a basal lattice vector ($\{kk, hh\}$), while the other two, for instance $\{kh', kh\}$ span the axial vector along a $-h'-k-h-k'$ chain of sites.

1. 3C-SiC

As reported previously in Ref. [24], V_C in 3C-SiC migrates on the C sublattice over a calculated barrier of 3.5 eV. This figure was obtained using a local functional and Γ sampling [59,60], and reproduced by us (see first data row in Table I). A subsequent NEB calculation with $2 \times 2 \times 2$ BZ sampling mesh, followed by a dimer saddle-point search, raised the barrier to 3.7 eV. Despite the difference, the mechanism for the vacancy hop, as well as the transition state geometry, are essentially the same and confirm what was previously found.

Figure 2(a) shows a C_x atom (highlighted in black) initiating its jump in NEB image number 1. We note that NEB image numbers in the figure refer to the location of the vacancy (black dot). Both the C_x atom and V_C meet at the transition state near NEB image number 5 and finally exchange their locations at the final (ground) state in NEB image number 13. The calculated exploratory MEP along the configurational space (using Γ sampling and $E_{\text{cut}} = 300$ eV) is shown in Fig. 2(b) using a dashed line and black dots. In Ref. [24], the transition state was rationalized as the configuration at which the C_x atom crosses through a *gate* defined by the rectangle drawn in Fig. 2(a). Although this picture is well suited for 3C-SiC, it is not general enough to be applied in 4H-SiC. We prefer to describe the transition state (close to NEB image number 5) as a Si-C split-interstitial (nearly aligned along $\langle 001 \rangle$) shouldered by two carbon vacancies. Below we argue that the height of the barrier depends mostly on the coordination of the atoms in the Si-C unit at the saddle-point configuration, including bond lengths and angles with their ligands.

¹The term *pseudoaxial* is employed here to emphasize that this is not a purely axial jump of V_C along a $\langle 0001 \rangle$ crystallographic direction. This contrasts with basal jumps, where vacancy motion proceeds strictly within a basal plane.

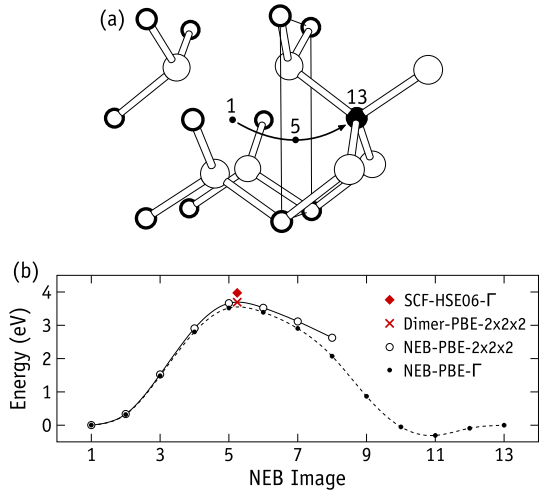


FIG. 2. V_C migration in 3C-SiC as illustrated by (a) the atomistic structure surrounding a V_C defect (Si and C shown with thin and thick halos, respectively) and the approximate path a C_x atom (shown in black) will follow when jumping into the vacant site, in the opposite direction of the curved arrow. Dots and numbers indicate the position of the V_C and respective NEB images along the MEP. In (b) we show the energies of intermediate structures along the MEP, as obtained using the NEB method with different BZ sampling meshes (dots and open symbols), using the dimer method (red cross), and performing a SCF calculation within hybrid-DFT using the structure identified by the dimer search (red diamond).

The below-zero dip towards the end of the MEP curve of Fig. 2(b) (close to NEB image number 11) is an artifact. It arises because the end structures (which are not changed during the NEB relaxation) were obtained using a denser BZ sampling mesh and a higher plane-wave cutoff energy than the NEB calculation. Structures from NEB images number 11 and 13 are rather close in configurational space. However, the former is closer to the ground state when using Γ sampling and $E_{\text{cut}} = 300$ eV.

Figure 2(b) also shows transition state energies calculated (i) using a more accurate NEB run focused on a shorter path near the saddle point (NEB-PBE- $2 \times 2 \times 2$, solid line and open symbols), (ii) using the dimer method (Dimer-PBE- $2 \times 2 \times 2$, red cross), and (iii) using the structure from the dimer search to perform a SCF calculation at the HSE06-level (SCF-HSE06- Γ , red diamond). While both PBE-level calculations give $E_A = 3.7$ eV, the hybrid-DFT result is $E_A = 4.0$ eV, significantly increasing the calculated barrier with respect to the 3.5 eV previously found [24].

As referred by Rauls *et al.* [26], the total energy of a defect (and consequently its migration barrier) is sensitive to the energetic position of the occupied defect levels within the band gap. Our results indicate that improving the level of theory from local or semilocal DFT to hybrid density functional theory with a converged Brillouin-zone sampling grid, opens up the calculated gap of SiC, decreases the coupling between defect-levels and crystalline states, and for the case of V_C the

TABLE III. Activation energies, E_A , for all four inequivalent jumps of V_C in 4H-SiC via exchange with carbon neighbors, see Figs. 1(b) and 1(c). The three data columns refer to the three steps of the calculation, namely (1) the exploratory NEB run, (2) the dimer run with stringent BZ sampling mesh and E_{cut} , and (3) the SCF calculation of the transition state within HSE06. All activation energies for individual jumps are calculated with respect to the energy of the initial state. The overall barriers for axial and basal migration are also reported. Relevant computational details are listed in the bottom part of the table.

Jump	Activation energy, E_A (eV)		
kh'	3.5	3.9	4.2
kh	3.3	3.8	4.1
kk	3.3	3.7	4.0
hh	3.0	3.4	3.7
Axial barrier	3.5	3.9	4.2
Basal barrier	3.0	3.4	3.7
Calculation	NEB	Dimer	SCF
Functional	PBE	PBE	HSE06
E_{cut} (eV)	300	420	420
BZ-sampling	Γ	$2 \times 2 \times 2$	Γ

barrier suffers an enhancement of about 0.5 eV. This energy cannot be interpreted as a source of error and is not negligible.

2. 4H-SiC

The agreement between our calculations for V_C migration in 3C-SiC and previous works [24] provides a reassuring benchmark for the following and more involved calculations in 4H-SiC. Table III summarizes the calculated activation energies for single V_C jumps in 4H-SiC after each of the three calculation steps (exploratory NEB, dimer, and HSE06-SCF, respectively), clearly demonstrating an influence of the initial/final lattice sites on the barrier height. According to our previous analysis, four jumps were considered: two pseudoaxial (kh' and kh) and two basal (hh and kk). The notation found in Table III is the same as that of Fig. 1, describing how a vacancy moves from a particular site into neighboring sites. We also note that for the pseudoaxial jumps (first two data rows) the barrier for the reversed jump is readily obtained by subtracting $E(h) = 0.1$ eV, which is the energy of $V_C(h)$ with respect to $V_C(k)$, to the reported barriers.

Comparing basal to axial activation barriers we conclude that V_C migration in 4H-SiC exhibits substantial anisotropy. Furthermore, we find that there are considerable differences when we compare the barriers for basal migration within k and h planes. The difference between activation energies of pseudoaxial and basal jumps persists across all three computational steps (NEB, dimer, hybrid-DFT SCF calculations). However, as we improve the calculation specifications and the calculated band gap width opens up, the barriers are progressively raised.

For axial migration, the relevant barrier is the highest with respect to the ground state $V_C(k)$, namely $E_A(kh') = 4.2$ eV. For basal migration, we have to consider that for irradiation-induced V_C populations at 1400 °C, the populations of $V_C(k)$ and $V_C(h)$ are comparable, and in this case the faster species

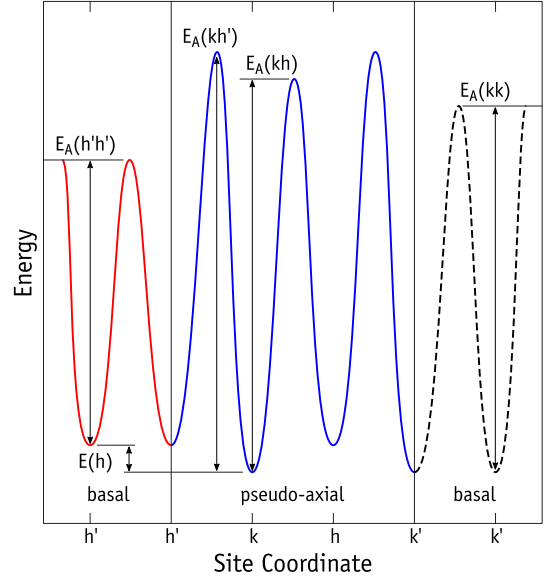


FIG. 3. Schematic potential energy profile along axial (h' - k - h - k') and basal (h' - h' and k' - k') migration paths of V_C in 4H-SiC. The diagram was constructed based on the results of Table III, combined with the calculated energy of $V_C(h)$ with respect to $V_C(k)$, $E(h) = 0.1$ eV. The qualitative character of the profiles is not affected by the level of theory employed (NEB, dimer or HSE06-SCF).

will set the pace. Hence, the barrier to consider is the lowest, $E_A(hh) = 3.7$ eV. The migration along the k plane is limited by a barrier of $E_A(kk) = 4.0$ eV, which is essentially identical to that found for the cubic phase. An overall picture of the migration of V_C in 4H-SiC is provided in Fig. 3. The figure shows a schematic potential energy profile along axial (h' - k - h - k') and basal (h' - h' and k' - k') migration paths of V_C in 4H-SiC. The blue and red lines rationalize the potential energy surface for effective axial and basal migration, whereas the dashed black line indicates that migration along the k -plane should be inactive. These results explain what has been previously observed in Ref. [31] but not accounted for by a physical model at the time.

Axial migration of V_C in 4H-SiC was experimentally found to be substantially slower than basal migration [31]. At 1400 °C they differ by about one order of magnitude [31], corresponding to a difference in activation energy of ~ 0.3 eV. Here we are assuming identical exponential prefactors (which account for the jump attempt frequencies). This figure is in excellent agreement with the calculated $E(kh') - E(hh) = 0.5$ eV as reported in Table III. Further details regarding more recent and comprehensive experimental observations will be provided in the next section.

Interestingly, the calculated anisotropy is pronounced for h -basal and not so much for k -basal migration (compared to axial migration). As pointed out already, the activation barrier for k -basal migration, $E_A(kk) = 4.0$ eV, is identical to the barrier for V_C migration in 3C-SiC, suggesting that the

resulting anisotropy could be explained based on differences between the hexagonal and cubic crystal fields or bond coordination at the respective transition states within the k and h planes of carbon atoms. We will come back to this issue in Sec. IV. From a practical point of view, knowledge of how basal migration is activated and proceeds preferentially along h planes could shape device processing techniques. For instance, deployment of impurities or dopants at a preferential site could be leveraged by interactions with either $V_C(k)$ or $V_C(h)$ defects, eventually biased by selective diffusion.

In a recent report by Kuate Defo *et al.* [29], although the diffusivity of V_C was not addressed, the energy barrier for a kh' jump of V_C in 4H-SiC was found to be as high as $E_A \approx 4.7$ –4.8 eV using a semilocal approximation to DFT. This result is actually ~ 0.5 eV above our hybrid-DFT result, in opposition to the trend displayed by the semilocal results for V_C migration in 3C-SiC. For the same barrier, our semilocal calculation using the nudged elastic band + dimer method gives $E_A = 3.9$ eV (cf. kh' jump in Table III), which in turn agrees with the referred trend. We are unable to explain this inconsistency and can only suggest that the transition-state geometries from Ref. [29] were away from the true saddle point for being obtained by classical molecular dynamics.

Until now we have not mentioned the impact of entropy on the diffusivity of V_C . An account on this problem was previously reported in Ref. [26]. Based on the vibrational spectrum of V_C in 3C-SiC at the ground and transition states, vibrational entropy was found to lower the barrier by about $1.9 k_B$ eV/K, where k_B stands for the Boltzmann constant. From a practical point of view, this translates into a decrease of the barriers by 0.1–0.3 eV at 1100–1600 °C. While it is important to bear in mind that these values and the experimental/theoretical error bars are close in magnitude, it is equally important to note that to some extent entropy effects will affect all barriers, irrespective of the polytype or jump type.

All four relevant MEPs for V_C migration in 4H-SiC are shown in Fig. 4. Each chain of points on each plot (including solid and open symbols) refer to image energies from a NEB run using exploratory conditions (Γ sampling of the BZ and $E_{\text{cut}} = 300$ eV). The solid symbols at the ends are distinguished because they refer to single-point energy calculations employing ground state structures previously obtained using production conditions ($2 \times 2 \times 2$ sampling and $E_{\text{cut}} = 420$ eV). Hence, likewise Fig. 2, during the NEB runs the structures edging the fixed ends relaxed towards the lowest energy configurations under exploratory conditions, which differ slightly from the true ground states (end points).

Figures 4(a) and 4(b) refer to jumps of $V_C(k)$ into neighboring h sites. Note that kh' and kh plots should be read from right to left and from left to right, respectively. Both jumps (or their symmetric reversals) are performed during axial migration. They are depicted by curved arrows in Fig. 1(b). Clearly, kh' and kh jumps have distinct energy profiles and expectingly different mechanisms. Conversely, kk and hh jumps show energy profiles close to that of kh , foreshadowing similar mechanisms for all three. It is also interesting that from the exploratory NEB calculations we can already infer that kh' is the highest barrier and therefore the limiting jump for axial migration. Conversely, hh has the lowest barrier and should be

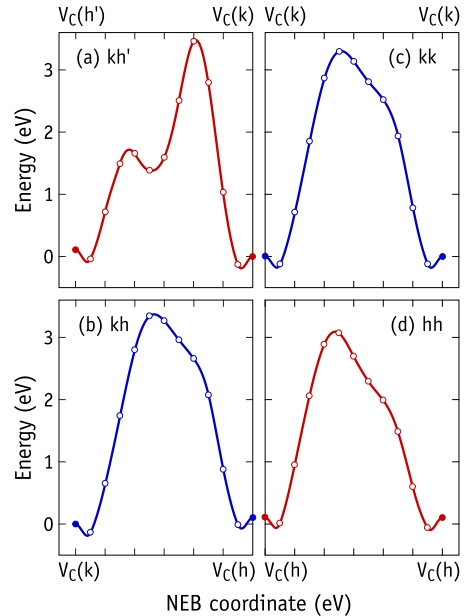


FIG. 4. Minimum energy paths (MEPs) for single jumps of V_C in 4H-SiC. (a) kh' -jump, (b) kh -jump, (c) kk -jump, and (d) hh -jump. Calculations represented as open symbols were carried out using exploratory conditions, namely Γ sampling of the BZ and $E_{\text{cut}} = 300$ eV. Solid symbols at the ends represent ground state structures obtained using $2 \times 2 \times 2$ sampling and $E_{\text{cut}} = 420$ eV. Red curves indicate the MEPs which limit the diffusivity of V_C along axial and basal directions.

the limiting step regarding the diffusivity along basal planes. Below we discuss the origin of these differences.

B. Experiment

Experimentally, V_C diffusion was studied using a combination of heat treatments and deep level transient spectroscopy on C implanted 4H-SiC samples. Figure 5(a) shows DLTS spectra of c - and a -cut samples implanted with $4 \times 10^8 \text{ cm}^{-2}$ C ions, both under prediffusion conditions and after annealing the samples at 1400 °C. Several DLTS signatures are observable in Fig. 5(a), including the previously reported peaks normally labeled S_1 , S_2 , and $Z_{1/2}$, with activation energies of 0.4, 0.71, and ~ 0.7 eV, respectively [61]. The latter defect is associated with the V_C and corresponds to a twofold electron emission due to a $(-2/0)$ transition [15]. Vacancies at hexagonal and pseudocubic lattice sites have similar energy level positions and are only distinguishable by Laplace-DLTS [62]. The S_1 and S_2 centers arise in implanted samples but are less stable than the $Z_{1/2}$ level, and disappear at high temperatures [61] as seen in Fig. 5(a). Similar arguments can be presented for most of the primary defects expected to arise in the samples; the Si vacancy (V_{Si}) is expected to transform into the carbon antisite-vacancy (CAV) pair above 400–600 °C [63,64], which again anneals out at 900–1200 °C

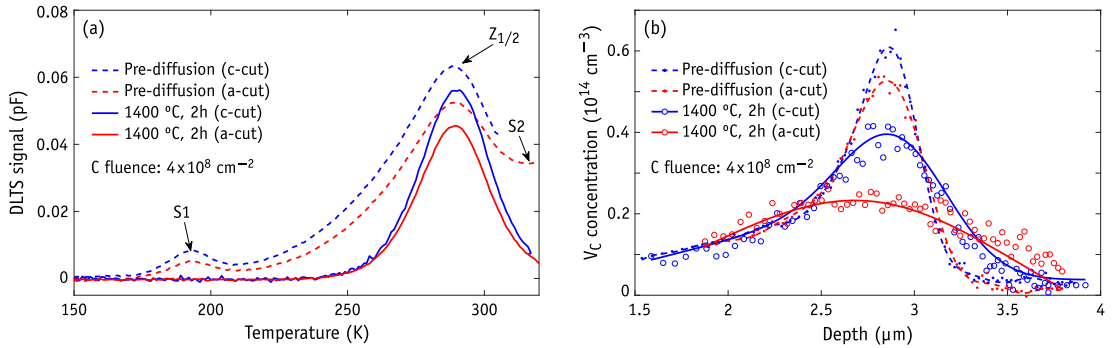


FIG. 5. (a) DLTS spectra of *c*-cut (blue) and *a*-cut (red) *n*-type 4H-SiC in the vicinity of the $Z_{1/2}$ level under pre- and post-diffusion conditions. The spectra have been scaled for the $Z_{1/2}$ peak size to represent the V_C concentration of the relevant sample. (b) V_C concentration vs depth profiles along the *c* (blue) and *a* (red) directions in prediffusion samples and after annealing at 1400 °C for 2 h, with dots representing experimental data, dashed lines the prediffusion fits and solid lines being the diffused profiles calculated by solving the diffusion equation.

[64,65]. Carbon and silicon self-interstitials have even lower thermal stabilities than V_{Si} and CAV, with migration energies close to ~ 1 eV [11]. Hence, the interstitials generated both from ion collisions and implantation of C are expected to rapidly disappear above 200 °C, and therefore their interaction with V_C is neglected herein.

Ion implantation may also create more complex defects such as antisites, divacancies, and antisite-vacancy pairs. However, the implantation fluence ensures the selective formation of point defects to concentrations well within the dilute limit. Hence, complex defects are likely to be much less abundant than V_C , and with only $\sim 10^{14}$ cm $^{-3}$ V_C 's in the samples implanted to the highest fluence, there should be at least ~ 100 nm between defects of any kind. Therefore, and in the absence of long-range Coulomb attraction, neutral V_C 's will encounter potential sinks only rarely, and any ensuing lowering of V_C concentration (caused by reactions between V_C and complexes) should be negligible. Thus, to summarize, a target temperature range exists (~ 1200 – 1600 °C), where V_C becomes mobile, standing as the main prevalent point defect, thus enabling experimental observation of its diffusion.

A quantitative conversion of the DLTS peak amplitude to concentration is strictly valid for uniform defect profiles only. Thus, depth profiling measurements are highly appropriate for the present study, and the results for the prediffused and 1400 °C annealed samples are shown in Fig. 5(b). A striking feature of the profiles in Fig. 5(b) is the significantly lower and broader concentration profile along the basal *a* direction (in red) compared to that of the axial *c* direction (in blue) for the same annealing treatment. This confirms that thermally activated V_C diffusion shows considerable anisotropy as previously proposed [31].

Figure 6 displays V_C concentration versus depth profiles for (a) *c*-cut and (b) *a*-cut samples implanted with 6×10^8 cm $^{-2}$ C ions, before and after annealing at temperatures between 1200 °C and 1500 °C. The profiles in Figs. 6(a) and 6(b) demonstrate the temperature evolution of the V_C concentration along axial and basal crystallographic directions, respectively, and confirm the anisotropic V_C migration in 4H-SiC. For instance, after annealing at 1500 °C the V_C

has clearly moved further along the *a* direction than the *c* direction, despite the shorter annealing time (at 1500 °C) for the *a*-cut samples as compared to the *c*-cut ones. As seen from the figure, higher temperatures and/or longer diffusion times are required to obtain similar diffusion profiles for the *c*-cut [Fig. 6(a)] and the *a*-cut [Fig. 6(b)] samples, demonstrating the anisotropy in V_C diffusion. The intermediate temperature V_C profiles, i.e., between 1300 °C and 1500 °C, become gradually lower and broader as expected from Fig. 6 for both the *c*- and *a*-cut samples, and are therefore not shown for the sake of clearness. Annealing *c*-cut and *a*-cut samples at 1600 °C resulted in uniform V_C concentration profiles and revealed out-diffusion of the V_C , most likely to the surface and possibly to other defect sinks.

Assuming that the Si and C sublattices are independent and a single diffusion mechanism prevails with no external driving force, V_C migration is equivalent to migration in a chemically homogeneous system where isolated V_C 's migrate exclusively on the C sublattice. This allows V_C diffusion to be described by a diffusion equation in the form of Fick's second law [66],

$$\frac{\partial c}{\partial t} = D \frac{\partial^2 c}{\partial x^2}, \quad (2)$$

where c denotes the concentration and D is the diffusivity. Using the prediffusion fit to the experimental data as the initial V_C concentration, we deduced the V_C diffusivity (D) at each temperature by solving the diffusion equation numerically and selecting the diffusivity which resulted in the lowest least mean square error between the calculated V_C concentration profile (for a given D) and the fit to the experimental diffused V_C concentration profile. The resulting diffusivities were estimated to have accuracies in the range 20–30%, which we will return to below.

Importantly, we note that high temperature heat treatments induce surface degradation and may influence the capacitance measured by the Schottky barrier diodes, as reflected in the relatively large error bars for the diffusivity of 20–30%. Indeed, protective surface layers such as carbon caps exist but are known to introduce carbon interstitials that may interfere with the irradiation induced vacancies [67]. Therefore, the

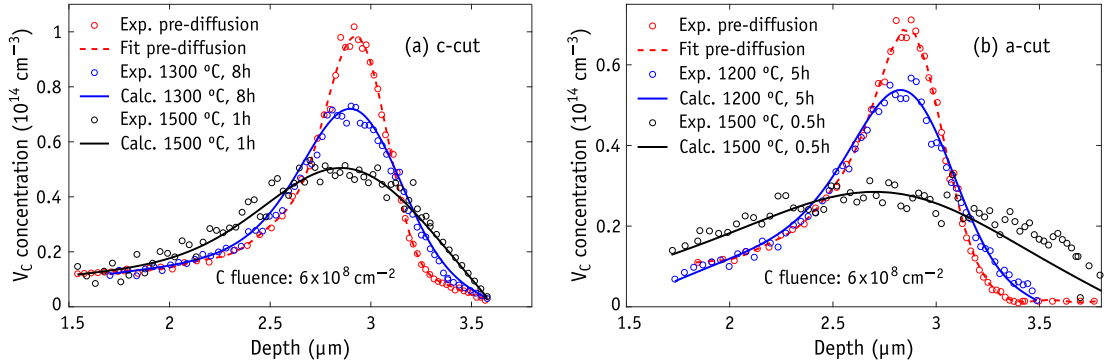


FIG. 6. V_C concentration vs depth profiles along the (a) c and (b) a direction before (red) and after (blue and black) annealing at temperatures between 1200 °C and 1500 °C. Circular marks represent experimental data, red dashed lines are fits to the initial profiles, and solid lines are the diffused profiles calculated by solving the diffusion equation.

following assumptions and appropriate corrections were made when processing the data: (i) the ionized donor concentration does not change during diffusion, (ii) the V_C peak position does not shift during diffusion, and (iii) the amount of V_C defects contained within the depletion region remains constant during diffusion.

The calculated V_C concentrations are shown as solid lines and experimental data as circular dots in Fig. 6, while the dashed red lines represent numerical fits to the initial experimental profiles. Evidently, solving the diffusion equation for the V_C concentration [Eq. (2)] results in an excellent agreement between the experimental and calculated V_C concentration profiles, hence, adequately describes the thermally activated V_C migration. Note that the V_C concentration profiles have been shifted slightly in depth (0.1–0.2 μm) and corrected to remedy the loss of accuracy caused by surface degradation at high temperatures. The correction was performed to preserve the number of carbon vacancies within the depletion region before and after the diffusion process. Note that we assume negligible out-diffusion of V_C 's below 1600 °C — Fick's second law relies on mass conservation. The choice of Fick's second law and conservation of V_C concentration during diffusion for modeling of the diffusion process is validated by observation of essentially identical shapes for the measured and calculated concentration profiles in Fig. 6. We note that isothermal annealing of c -cut samples at 1400 °C for two and four hours, revealed identical V_C diffusivities of $D = (4 \pm 1.2) \times 10^{-14} \text{ cm}^2/\text{s}$. This is the expected observation should V_C motion in 4H-SiC be governed by independent vacancy jumps. Furthermore, the samples annealed at 1400 °C for 2 and 4 h were implanted to different C fluences ($4 \times 10^8 \text{ cm}^{-2}$ and $6 \times 10^8 \text{ cm}^{-2}$, respectively). The lack of temporal dependence in the V_C diffusivity indicates no transient effects with time and confirms the elementary diffusion process.

Figure 6 demonstrates that V_C diffusion is adequately described by Fick's diffusion equation. Assuming that the underlying mechanism involves a thermally activated jump, the temperature dependence of the V_C diffusivity should follow an

Arrhenius behavior according to

$$D = D_0 \exp(-E_A/k_B T). \quad (3)$$

Here, T is the absolute temperature, k_B is the Boltzmann constant, E_A is the activation energy for migration, and D_0 is the exponential prefactor encompassing the jump frequency. Indeed, Fig. 7 reveals a pronounced Arrhenius behavior for V_C diffusivity in the 1300–1500 °C range along the c direction and in the 1200–1500 °C range along the a direction, where circles represent deduced D values as described above. In the same figure, solid lines represent linear fits to the data. Error bars ranging from 20 to 30% are included. The error in each D value was estimated from the deviation between the diffusivity and the linear fit to the experimental data in Fig. 7, combined with the observed effect of choosing different differentiation methods (smoothed vs nonsmoothed) when converting the

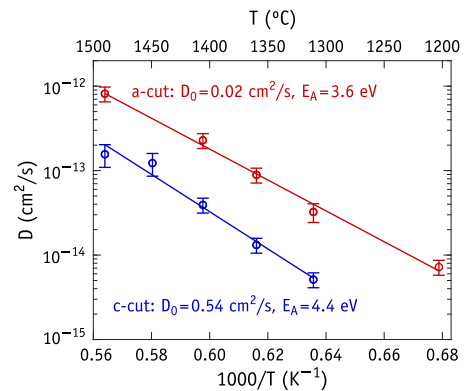


FIG. 7. Temperature dependence of V_C diffusivity (D) along the c direction (blue) and a direction (red), with D clearly obeying Arrhenius behavior. Circular marks represent D and solid lines are linear fits to the data. The extracted fitting parameters (D_0 and E_A) are included in the figure.

DLTS data into concentration vs depth profiles as described by Eq. (1). From the Arrhenius plot, fitting parameters of $D_0 = 0.54 \text{ cm}^2/\text{s}$ and $E_A = (4.4 \pm 0.3) \text{ eV}$ were deduced for migration along the c direction, and $D_0 = 0.02 \text{ cm}^2/\text{s}$ and $E_A = (3.6 \pm 0.3) \text{ eV}$ along the a direction. The absolute accuracy for the exponential prefactors is estimated to be approximately an order of magnitude, but the calculated activation energies are much more accurate with error bars of $\pm 0.3 \text{ eV}$ along both axial directions.

As previously mentioned, Eq. (1) does not account for the transition region, or λ effect, arising during fast DLTS pulsing [53]. The effect has been omitted in the present data due to the surface degradation mentioned above. Tests were performed to verify our approach, e.g., for the a -cut sample annealed at 1500°C for 0.5 h, where the high temperature is potentially associated with large surface degradation. Diffusivities deduced with and without the λ correction differed by less than 10%, which is well below the estimated error bars.

We finally note that if single negatively or double negatively charged vacancies had any influence in V_C motion, eventually for being so fast diffusing as to compensate for their low concentration under intrinsic conditions, that would be reflected in the Arrhenius plot of Fig. 7. On the contrary, it is clear that V_C motion is thermally activated with rather high barriers.

IV. DISCUSSION

Comparing the Arrhenius profiles in Fig. 7 to the theoretical calculations reported above, we can explain the experimentally observed V_C diffusion along the c and a directions as the result of pseudoaxial jumps between [0001] planes and basal jumps within the h plane, respectively. The measured activation energies for diffusion along the c and a directions, respectively, 4.4 eV and 3.6 eV, match well with the pseudoaxial and basal barriers $E(kh') = 4.2 \text{ eV}$ and $E(hh) = 3.7 \text{ eV}$, respectively. Furthermore, and although exponential prefactors were not calculated in this work, we expect D_0 to be in the 10^{-2} – $10^{-3} \text{ cm}^2/\text{s}$ range for fundamental vacancy migration [66]. This interval overlaps the prefactor found for V_C migration along the a direction. Along the c direction the prefactor falls off the high limit of the expected range, possibly due to limitations in the experimental accuracy. It is conceivable that configurational entropy could favor axial diffusivity due to the existence of more equivalent paths joining an axial lattice vector than a basal lattice vector. For instance, the shortest path between two vacancy configurations separated by one basal vector is unique, while up to 15 equivalent shortest paths are available for a displacement along the axial lattice vector. Another effect that would be worth exploring is correlation effects taking place during the consecutive jumps needed for axial migration. To that end, kinetic Monte Carlo simulations could be helpful.

The strong correlation between experimental and theoretical values for V_C migration demonstrates that the defect travels faster along basal directions (than along the main axial direction). Combining the experimentally observed V_C diffusion characteristics with the theoretically predicted atomistic aspects of V_C migration, we arrive at the conceptual migration diagram shown in Fig. 8, which provides an interpretation of

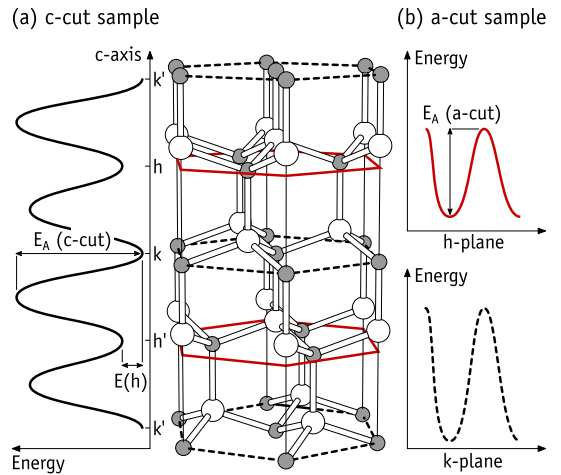


FIG. 8. 4H-SiC atomic structure (middle) and schematic potential energy profiles along axial (right) and basal (left) migration paths of V_C in 4H-SiC. Axial V_C migration ($h'k'k'$) along the c direction is shown to the left (a), and basal V_C migration (hh and kk) along the a direction is pictured to the right (b). The diagram was constructed based on the results of Table III, combined with the calculated energy of $V_C(h)$ with respect to $V_C(k)$, $E(h) = 0.1 \text{ eV}$.

the experimental observables based on the theoretical model presented herein. Schematic potential energy profiles for V_C migration along the axial direction and within the h -basal plane [Figs. 8(a) and 8(b), respectively] are related to experimentally observed diffusivities measured in c -cut and a -cut samples, respectively. Relevant basal planes are also represented in the middle panel of Fig. 8. The shape of the potential energy profiles in Figs. 8(a) and 8(b) are representative of their relative barrier heights as reported in Table III.

Finally, we expect ion implantation to generate approximately equal amounts of $V_C(k)$ and $V_C(h)$ defects, overwriting whatever population ratio existed prior to implantation. Despite $V_C(k)$ being the ground state and $V_C(h)$ being $E(h) = 0.1 \text{ eV}$ higher in energy, the annealing temperatures employed herein ($\sim 1500^\circ\text{C}$) are too low to drive a significant population difference by generating new carbon vacancies. Hence, lateral migration along the h plane is expected to be dominant, as supported by the strong overlap between experimentally and theoretically deduced activation energies for V_C migration (3.6 eV and 3.7 eV, respectively) along the a direction.

To better understand the anisotropy in V_C migration, let us have a closer look at the migration path. The carbon vacancy in 3C-SiC migrates according to the mechanism depicted in Fig. 2 [24]. The transition state is located close to midway between two neighboring ground state structures. Near NEB images number 5 and 6, the C_x atom becomes overcoordinated (connected to five Si atoms), while its Si nearest neighbor becomes undercoordinated (connected to three C atoms). This departure from the stable fourfold coordination is responsible for most of the potential energy to be surmounted during the jump.

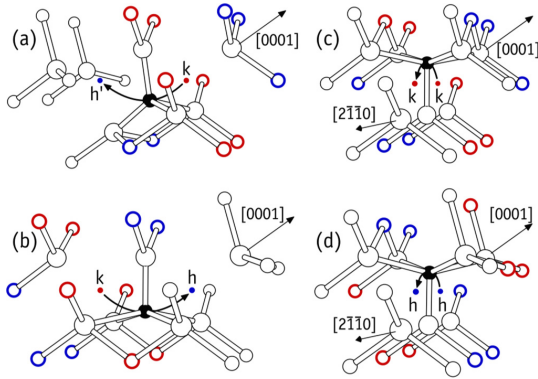


FIG. 9. Atomistic structures of V_C in 4H-SiC near midway between two neighboring lattice sites. Respective exploratory MEP energies are shown in Fig. 4. Si atoms are shown as large white spheres, while C_x -shell atoms are highlighted with red and blue halos when located in k and h planes, respectively. The jump of the vacancy is represented by an arrow. The C_x atom is shown in black.

Figure 9 represents structures of V_C defects near midway along their MEPs according to the four different jump types that were investigated in 4H-SiC. The curved arrows indicate approximate paths of the vacancy during the jump. The C_x atom (shown in the middle) moves in the opposite direction, i.e., departs from the site pointed by the arrow head.

In 4H-SiC, axial migration involves a sequence of kh - and kh' -like jumps. While the kh MEP of Fig. 4(b) is similar both in height and shape to the MEP of V_C in 3C-SiC shown in Fig. 2, the kh' MEP displays an asymmetric *camel back* shape with a local minimum close to halfway. We can follow the C_x atom during the kh' jump with the help of Figs. 4(a) and 9(a). Accordingly, C_x departs from the h' site when V_C departs from the k site. The structure quickly arrives at the saddle point, where C_x passes between two Si atoms, becoming twofold coordinated. This is a highly unfavorable coordination for carbon and leads to the highest energy configuration along the MEP for axial migration. Then, at midway towards the k site, the moving C_x atom becomes fourfold coordinated as depicted in Fig. 9(a), leading to the prominent local minimum in the middle of Fig. 4(a). From here, C_x has to overcome a small (~ 0.3 eV barrier) to reach the k site, annihilating the original $V_C(k)$ defect but creating a new $V_C(h')$ defect. We note that the structure of Fig. 9(a) is a true local minimum. A free relaxation of that structure (without the spring constraints of the NEB method) did not significantly alter the geometry, and the energy of the metastable configuration was 2.11 eV (HSE06-level) above that of the $V_C(k)$ ground state.

The local minimum structure depicted in Fig. 9(a) (with C_x showing fourfold coordination), is not visited during other vacancy jumps in 4H-SiC, namely kh , kk , and hh . There, the picture was found to be analogous to that of 3C-SiC. The transition-state structures are close to halfway between initial and final structures as depicted in Figs. 9(b)–9(d). Similarly to the transition state in 3C-SiC, the C_x atom at the saddle point of kh , kk , and hh jumps is overcoordinated.

A more careful inspection of Figs. 9(b) and 9(c) allows us to conclude that, for the saddle-point structures of kh and kk jumps, besides C_x having identical Si first neighbors, the whole C_x shell is similar to that found at kh and kk saddle points [Figs. 9(b) and 9(c), respectively], it is clear that some carbon atoms within the C_x shell, namely those in the $Si-C_3(k)$ structures near the arrow pointing along the $\langle 0001 \rangle$ direction in Fig. 9(d), differ from the analogous $Si-C_3(h)$ structures of Fig. 9(c). Importantly, for the hh jump, the C_x -Si-C(k) bond angles (with apex at Si) near the transition state structure deviate less from the perfect sp^3 bond angle of 109.5° . The kk transition state shows two particularly acute C_x -Si-C angles of 70° , while the lowest angle for the hh transition state is 82° . The lower departure from perfect sp^3 bonding of the Si atoms neighboring C_x during hh jumps is invoked to explain its lower activation barrier.

Figure 9(d) shows the atomistic structure of V_C in 4H-SiC near the saddle point along the hh jump. Although the coordination of C_x is similar to that found at kh and kk saddle points [Figs. 9(b) and 9(c), respectively], it is clear that some carbon atoms within the C_x shell, namely those in the $Si-C_3(k)$ structures near the arrow pointing along the $\langle 0001 \rangle$ direction in Fig. 9(d), differ from the analogous $Si-C_3(h)$ structures of Fig. 9(c). Importantly, for the hh jump, the C_x -Si-C(k) bond angles (with apex at Si) near the transition state structure deviate less from the perfect sp^3 bond angle of 109.5° . The kk transition state shows two particularly acute C_x -Si-C angles of 70° , while the lowest angle for the hh transition state is 82° . The lower departure from perfect sp^3 bonding of the Si atoms neighboring C_x during hh jumps is invoked to explain its lower activation barrier.

The investigation of migration barriers for intrinsic defects such as vacancies is crucial for understanding one of the most fundamental mechanisms of mass transport in materials, namely self-diffusion. The mechanisms for Si and C self-diffusion in SiC have previously been attributed to their corresponding intrinsic defects [68,69], and the energy barrier for C self-diffusion in 4H-SiC along the c axis has been experimentally estimated at 7.6 eV [70] and 8.5 eV [71]. However, whether C self-diffusion is primarily mediated by C interstitials (as proposed in Refs. [24,70] and [72]) or by vacancies (as inferred in Ref. [71]) has not been resolved experimentally. It is therefore interesting to verify the compliance of our results within the above views.

One can estimate the activation energy for self-diffusion (a process which occurs only at very high temperatures, where intrinsic conditions apply) as the sum of the formation energy and the migration barrier of the mediating defect. Under C-rich conditions (which are usually imposed during SiC growth to reduce the concentration of V_C defects) the calculated formation energy of neutral $V_C(k)$ is $E_f = 5.0$ eV. For this calculation, the carbon chemical potential was considered as the energy per atom in bulk diamond (within hybrid-DFT). Hence, we anticipate activation energies for basal and axial V_C -mediated carbon self-diffusion of 8.7 eV and 9.2 eV, respectively. The latter figure is the one to be compared to the experiments referred above, where C-rich conditions are also expected, overestimating the observations by 1.6 eV (Ref. [70]) and 0.7 eV (Ref. [71]).

Although a detailed account of interstitial carbon (C_i) in SiC is beyond the scope of the present work, for the sake of completeness we leave the reader with a brief analysis of carbon self-diffusion in 4H-SiC, eventually mediated by C_i defects. The ground state of neutral C_i has spin-1 and consists of a C-C dimer replacing a C(k) site [73]. In 3C-SiC the structure consists on a $\langle 001 \rangle$ -aligned split interstitial [73]. In C-rich material, the formation energy of a neutral C_i defect (which is the stable state under intrinsic conditions) is $E_f = 6.6$ eV (using HSE06). According to local density functional

calculations, the estimated migration barrier of neutral C_i in 3C-SiC is estimated at $E_A = 0.5\text{--}0.6$ eV [24,72], suggesting that it could migrate already at room temperature. We note however, that the above figure is probably underestimated. If we consider that analogous calculations for the V_C migration yielded a barrier ~ 0.5 eV below the hybrid-DFT value [24], we arrive at $E_A \sim 1$ eV for the estimated migration barrier of C_i , matching the estimated barrier for C_i migration in Ref. [11]. Hence, combining this figure with the formation energy, we arrive at ~ 7.6 eV for the activation energy for C_i -mediated carbon self-diffusion in 4H-SiC. This matches the activation enthalpy measured for self-diffusion reported by Rüschemschmidt *et al.* [70], and it is substantially lower than the analogous quantity for V_C -mediated self-diffusion, supporting a model where carbon self-diffusion in 4H-SiC is not promoted by vacancies but rather probably by carbon interstitials [24,70,72].

V. CONCLUDING REMARKS

We presented a detailed investigation of the mechanisms behind V_C migration in 3C- and 4H-SiC based on first-principles calculations within hybrid DFT, combined with experimental studies using heat treatments and subsequent deep level transient depth profiling. We started by reproducing previous local-DFT results for 3C-SiC (where a migration barrier of $E_A = 3.5$ eV was previously found [24]), followed by calculations with higher \mathbf{k} sampling, using the dimer method and a hybrid functional. The latter method yielded $E_A = 4.0$ eV. The main reasons for the previous underestimation were (i) insufficient BZ sampling and (ii) over-resonance between vacancy levels and crystalline states within the narrow gap as obtained using a (semi)local treatment to the exchange-correlation potential.

We showed that in 4H-SiC, neutral V_C migrates anisotropically and faster along basal directions. V_C migration is also found to be plane selective, meaning that the defect travels substantially faster within the h plane (avoiding transiting through the k plane). A total of four inequivalent jumps, labeled by pairs of sublattice sites, were identified: Two of them (kh' and kh) contribute to axial migration, while the other two (kk and hh) are involved in basal migration. Whereas kh and kk jumps are very similar to that occurring in 3C-SiC, including their respective barrier heights, kh' and hh are singled out by showing the highest and lowest barriers, namely $E_A = 4.2$ eV and 3.7 eV, and are therefore identified as critical mechanisms governing axial and basal diffusivity of V_C , respectively. While kh' hinders V_C migration due to the

involvement of a high-energy twofold coordinated C atom at the transition state, hh jumps are favored against others due to a lower departure of Si-C bond angles from those in perfect sp^3 bonded structures.

Experimentally, the activation energy for V_C diffusion in n-type 4H-SiC was determined, and from the adherence of the experimental data to Fick's second law we firmly establish the mechanism governing V_C motion as that of fundamental vacancy migration, namely vacancy-atom exchange on the C sublattice. The predicted anisotropy in V_C diffusion was experimentally determined, with activation energies of $E_A = (4.4 \pm 0.3)$ eV and $E_A = (3.6 \pm 0.3)$ eV for V_C migration along the c and a directions, respectively, and corresponding prefactors of 0.54 cm²/s and 0.017 cm²/s. The magnitude of the prefactors support a simple jump process as expected for fundamental vacancy migration, and the experimentally obtained activation energies provide an excellent match with theoretical predictions of 4.2 eV for axial and 3.7 eV for basal h sublattice V_C migration.

Finally, we examined our results within the current view of self-diffusion and whether carbon self-diffusion in 4H-SiC is mediated by vacancies or interstitials. Although the formation energy of V_C is about 1.5 eV lower than that of C_i , we support the argument that the large migration barrier of V_C makes C_i the most likely mediator for carbon self-diffusion in 4H-SiC [24,70,72].

ACKNOWLEDGMENTS

Financial support was kindly provided by the Research Council of Norway and the University of Oslo through the frontier research project FUNDAMeNT (No. 251131, FriPro ToppForsk-program), and the Norwegian Micro- and Nanofabrication Facility (NorFAB 245963). Some of the computations were performed on resources provided by UNINETT Sigma2 - the National Infrastructure for High Performance Computing and Data Storage in Norway. J.C. thanks the Fundação para a Ciência e a Tecnologia (FCT) for support under project UID/CTM/50025/2019, co-funded by FEDER funds through the COMPETE 2020 Program. J.C. also acknowledges support by the NATO SPS programme (Project No. 985215). J.U.H. would like to acknowledge support from the Swedish Energy Agency Energimyndigheten project number 43611-1 and the Swedish Government Strategic Research Area in Materials Science (AFM). Some computational resources were provided by the Swedish National Infrastructure for Computing (SNIC) at HPC2N and PDC.

- [1] W. Choyke and G. Pensl, *MRS Bull.* **22**, 25 (1997).
- [2] W. Bolse, *Nucl. Instrum. Methods Phys. Res., Sect. B* **148**, 83 (1999).
- [3] M. Bhatnagar and B. Baliga, *IEEE Trans. Electron Devices* **40**, 645 (1993).

- [4] T. R. Garcia, A. Kumar, B. Reinke, T. E. Blue, and W. Windl, *Appl. Phys. Lett.* **103**, 152108 (2013).
- [5] J. R. Weber, W. F. Koehl, J. B. Varley, A. Janotti, B. B. Buckley, C. G. V. de Walle, and D. D. Awschalom, *Proc. Natl. Acad. Sci.* **107**, 8513 (2010).

- [6] L. Gordon, A. Janotti, and C. G. Van de Walle, *Phys. Rev. B* **92**, 045208 (2015).
- [7] S. Castelletto, L. Rosa, and B. C. Johnson, in *Advanced Silicon Carbide Devices and Processing* (InTech, Rijeka, 2015).
- [8] M. Bockstedte, F. Schütz, T. Garratt, V. Ivády, and A. Gali, *npj Quantum Materials* **3**, 31 (2018).
- [9] P. B. Klein, B. V. Shanabrook, S. W. Huh, A. Y. Polyakov, M. Skowronski, J. J. Sumakeris, and M. J. O'Loughlin, *Appl. Phys. Lett.* **88**, 052110 (2006).
- [10] K. Danno, D. Nakamura, and T. Kimoto, *Appl. Phys. Lett.* **90**, 202109 (2007).
- [11] N. Iwamoto and B. G. Svensson, in *Defects in Semiconductors*, edited by L. Romano, V. Privitera, and C. Jagadish (Elsevier, San Diego, 2015), Vol. 91 of *Semiconductors and Semimetals*, pp. 369–407.
- [12] B. Zippelius, J. Suda, and T. Kimoto, *J. Appl. Phys.* **111**, 033515 (2012).
- [13] H. M. Ayedh, A. Hallén, and B. G. Svensson, *J. Appl. Phys.* **118**, 175701 (2015).
- [14] J. Coutinho, V. J. B. Torres, K. Demmouche, and S. Öberg, *Phys. Rev. B* **96**, 174105 (2017).
- [15] N. T. Son, X. T. Trinh, L. S. Løvlie, B. G. Svensson, K. Kawahara, J. Suda, T. Kimoto, T. Umeda, J. Isoya, T. Makino *et al.*, *Phys. Rev. Lett.* **109**, 187603 (2012).
- [16] K.-B. Park, Y. Ding, J. P. Pelz, P. G. Neudeck, and A. J. Trunek, *Appl. Phys. Lett.* **89**, 042103 (2006).
- [17] J. M. Langer and H. Heinrich, *Phys. Rev. Lett.* **55**, 1414 (1985).
- [18] S. Sasaki, K. Kawahara, G. Feng, G. Alfieri, and T. Kimoto, *J. Appl. Phys.* **109**, 013705 (2011).
- [19] T. Hornos, A. Gali, and B. G. Svensson, *Mater. Sci. Forum* **679–680**, 261 (2011).
- [20] H. M. Ayedh, V. Bobal, R. Nipoti, A. Hallén, and B. G. Svensson, *J. Appl. Phys.* **115**, 012005 (2014).
- [21] A. Kawasuso, F. Redmann, R. Krause-Rehberg, M. Weidner, T. Frank, G. Pensl, P. Sperr, W. Triftshäuser, and H. Itoh, *Appl. Phys. Lett.* **79**, 3950 (2001).
- [22] T. Umeda, J. Isoya, N. Morishita, T. Ohshima, and T. Kamiya, *Phys. Rev. B* **69**, 121201(R) (2004).
- [23] Z. Zolnai, N. T. Son, C. Hallin, and E. Janzén, *J. Appl. Phys.* **96**, 2406 (2004).
- [24] M. Bockstedte, A. Mattausch, and O. Pankratov, *Phys. Rev. B* **68**, 205201 (2003).
- [25] M. Bockstedte, A. Mattausch, and O. Pankratov, *Phys. Rev. B* **69**, 235202 (2004).
- [26] E. Rauls, T. Frauenheim, A. Gali, and P. Deák, *Phys. Rev. B* **68**, 155208 (2003).
- [27] F. Gao, W. J. Weber, M. Posselt, and V. Belko, *Phys. Rev. B* **69**, 245205 (2004).
- [28] X. Wang, M. Zhao, H. Bu, H. Zhang, X. He, and A. Wang, *J. Appl. Phys.* **114**, 194305 (2013).
- [29] R. Kuate Defo, X. Zhang, D. Bracher, G. Kim, E. Hu, and E. Kaxiras, *Phys. Rev. B* **98**, 104103 (2018).
- [30] L. S. Løvlie, L. Vines, and B. G. Svensson, *J. Appl. Phys.* **111**, 103719 (2012).
- [31] M. E. Batten, H. M. Ayedh, L. Vines, I. Farkas, E. Janzén, and B. G. Svensson, *Mater. Sci. Forum* **924**, 200 (2018).
- [32] G. Kresse and J. Hafner, *Phys. Rev. B* **47**, 558 (1993).
- [33] G. Kresse and J. Hafner, *Phys. Rev. B* **49**, 14251 (1994).
- [34] G. Kresse and J. Furthmüller, *Comput. Mater. Sci.* **6**, 15 (1996).
- [35] G. Kresse and J. Furthmüller, *Phys. Rev. B* **54**, 11169 (1996).
- [36] P. E. Blöchl, *Phys. Rev. B* **50**, 17953 (1994).
- [37] J. Heyd, G. E. Scuseria, and M. Ernzerhof, *J. Chem. Phys.* **118**, 8207 (2003).
- [38] A. V. Krukau, O. A. Vydrov, A. F. Izmaylov, and G. E. Scuseria, *J. Chem. Phys.* **125**, 224106 (2006).
- [39] Z. Li and R. C. Bradt, *J. Appl. Phys.* **60**, 612 (1986).
- [40] J. Kräußlich, A. J. Bauer, B. Wunderlich, and K. Goetz, *Mater. Sci. Forum* **353–356**, 319 (2001).
- [41] J. P. Perdew, K. Burke, and M. Ernzerhof, *Phys. Rev. Lett.* **77**, 3865 (1996).
- [42] X. T. Trinh, K. Szász, T. Hornos, K. Kawahara, J. Suda, T. Kimoto, A. Gali, E. Janzén, and N. T. Son, *Phys. Rev. B* **88**, 235209 (2013).
- [43] G. Mills and H. Jónsson, *Phys. Rev. Lett.* **72**, 1124 (1994).
- [44] G. Mills, H. Jónsson, and G. K. Schenter, *Surf. Sci.* **324**, 305 (1995).
- [45] G. Henkelman and H. Jónsson, *J. Chem. Phys.* **111**, 7010 (1999).
- [46] A. Heyden, A. T. Bell, and F. J. Keil, *J. Chem. Phys.* **123**, 224101 (2005).
- [47] P. Grivickas, V. Grivickas, J. Linnros, and A. Galeckas, *J. Appl. Phys.* **101**, 123521 (2007).
- [48] J. D. Gouveia and J. Coutinho, *Electron. Struct.* **1**, 015008 (2019).
- [49] I. D. Booker, I. Farkas, I. G. Ivanov, J. Hassan, and E. Janzén, *Physica B, Condens. Matter* **480**, 23 (2016).
- [50] J. F. Ziegler, M. Ziegler, and J. Biersack, *Nucl. Instrum. Methods Phys. Res., Sect. B* **268**, 1818 (2010).
- [51] G. Alfieri, E. V. Monakhov, B. G. Svensson, and M. K. Linnarsson, *J. Appl. Phys.* **98**, 043518 (2005).
- [52] B. G. Svensson, K.-H. Rydén, and B. M. S. Lewerentz, *J. Appl. Phys.* **66**, 1699 (1989).
- [53] P. Blood and J. W. Orton, *The Electrical characterization of Semiconductors: Majority Carriers and Electron States* (Academic Press Limited, London, 1992).
- [54] S. D. Brotherton, *Solid-State Electron.* **26**, 987 (1983).
- [55] B. G. Svensson, C. Jagadish, A. Hallén, and J. Lalita, *Phys. Rev. B* **55**, 10498 (1997).
- [56] E. V. Monakhov, J. Wong-Leung, A. Y. Kuznetsov, C. Jagadish, and B. G. Svensson, *Phys. Rev. B* **65**, 245201 (2002).
- [57] L. Torpo, M. Marlo, T. E. M. Staab, and R. M. Nieminen, *J. Phys.: Condens. Matter* **13**, 6203 (2001).
- [58] A. Zywiets, J. Furthmüller, and F. Bechstedt, *Phys. Rev. B* **59**, 15166 (1999).
- [59] W. Kohn and L. J. Sham, *Phys. Rev.* **140**, A1133 (1965).
- [60] J. P. Perdew and A. Zunger, *Phys. Rev. B* **23**, 5048 (1981).
- [61] M. L. David, G. Alfieri, E. M. Monakhov, A. Hallén, C. Blanchard, B. G. Svensson, and J. F. Barbot, *J. Appl. Phys.* **95**, 4728 (2004).
- [62] I. Capan, T. Brodar, J. Coutinho, T. Ohshima, V. P. Markevich, and A. R. Peaker, *J. Appl. Phys.* **124**, 245701 (2018).
- [63] A. Kawasuso, H. Itoh, S. Okada, and H. Okumura, *J. Appl. Phys.* **80**, 5639 (1996).
- [64] J. W. Steeds, W. Sullivan, A. Wotherspoon, and J. M. Hayes, *J. Phys.: Condens. Matter* **21**, 364219 (2009).
- [65] T. Umeda, N. T. Son, J. Isoya, E. Janzén, T. Ohshima, N. Morishita, H. Itoh, A. Gali, and M. Bockstedte, *Phys. Rev. Lett.* **96**, 145501 (2006).

- [66] J. Philibert, *Atom movements: Diffusion and mass transport in solids*, Monographies de physique (Editions de Physique, Les Ulis, 1991).
- [67] H. M. Ayedh, R. Nipoti, A. Hallén, and B. G. Svensson, *Appl. Phys. Lett.* **107**, 252102 (2015).
- [68] J. Hong, M. Hon, and R. Davis, *Ceramurgia Int.* **5**, 155 (1979).
- [69] J. D. Hong and R. F. Davis, *J. Am. Ceram. Soc.* **63**, 546 (1980).
- [70] K. Rüschemschmidt, H. Bracht, N. A. Stolwijk, M. Laube, G. Pensl, and G. R. Brandes, *J. Appl. Phys.* **96**, 1458 (2004).
- [71] M. K. Linnarsson, M. S. Janson, J. Zhang, E. Janzén, and B. G. Svensson, *J. Appl. Phys.* **95**, 8469 (2004).
- [72] O. N. Bedoya-Martínez and G. Roma, *Phys. Rev. B* **82**, 134115 (2010).
- [73] A. Gali, P. Deák, P. Ordejón, N. T. Son, E. Janzén, and W. J. Choyke, *Phys. Rev. B* **68**, 125201 (2003).

Paper X



Influence of Carbon Cap on Self-Diffusion in Silicon Carbide

**M. E. Bathen, M. K. Linnarson, M. Ghezellou, J. Ul Hassan, L.
Vines**

Published in *Crystals*, August 2020, Volume 10 (752).
DOI: 10.3390/cryst10090752.

Article

Influence of Carbon Cap on Self-Diffusion in Silicon Carbide

Marianne Etzelmüller Bathen ^{1,*}, Margareta Linnarsson ², Misagh Ghezellou ³ ,
Jawad Ul Hassan ³ and Lasse Vines ¹

¹ Department of Physics, Centre for Materials Science and Nanotechnology, University of Oslo, N-0316 Oslo, Norway; lasse.vines@fys.uio.no

² Materials and Nanophysics, Department of Applied Physics, SCI, KTH Royal Institute of Technology, SE-106 91 Stockholm, Sweden; marga@kth.se

³ Department of Physics, Chemistry and Biology, Linköping University, SE-58183 Linköping, Sweden; misagh.ghezellou@liu.se (M.G.); jawad.ul-hassan@liu.se (J.U.H.)

* Correspondence: m.e.bathen@fys.uio.no

Received: 23 June 2020; Accepted: 24 August 2020; Published: 26 August 2020



Abstract: Self-diffusion of carbon (^{12}C and ^{13}C) and silicon (^{28}Si and ^{30}Si) in 4H silicon carbide has been investigated by utilizing a structure containing an isotope purified 4H- $^{28}\text{Si}^{12}\text{C}$ epitaxial layer grown on an n-type (0001) 4H-SiC substrate, and finally covered by a carbon capping layer (C-cap). The ^{13}C and ^{30}Si isotope profiles were monitored using secondary ion mass spectrometry (SIMS) following successive heat treatments performed at 2300–2450 °C in Ar atmosphere using an inductively heated furnace. The ^{30}Si profiles show little redistribution within the studied temperature range, with the extracted diffusion lengths for Si being within the error bar for surface roughening during annealing, as determined by profilometer measurements. On the other hand, a significant diffusion of ^{13}C was observed into the isotope purified layer from both the substrate and the C-cap. A diffusivity of $D = 8.3 \times 10^6 e^{-10.4/k_B T} \text{ cm}^2/\text{s}$ for ^{13}C was extracted, in contrast to previous findings that yielded lower both pre-factors and activation energies for C self-diffusion in SiC. The discrepancy between the present measurements and previous theoretical and experimental works is ascribed to the presence of the C-cap, which is responsible for continuous injection of C interstitials during annealing, and thereby suppressing the vacancy mediated diffusion.

Keywords: self-diffusion; silicon carbide; Carbon cap

1. Introduction

Self-diffusion of atomic species is a fundamental process in semiconductors, and vital for understanding both the thermally induced melting process and diffusion of impurities which are introduced during growth and doping. In silicon carbide, self-diffusion has been investigated extensively using both experimental [1–6] and theoretical [7,8] methods, but with conflicting results. Initially, carbon self-diffusion was predicted to have an energy barrier of $E_A = 7.4 \text{ eV}$ in intrinsic 6H-SiC [2] using ^{14}C radio-tracer techniques, with silicon diffusivities being more than 2 orders of magnitude lower than those for carbon [2,3]. Later, secondary ion mass spectrometry (SIMS) experiments on the 4H polytype yielded activation energies for ^{13}C self-diffusion of 8.5 eV [5] and 7.6 eV [6]. Interestingly, the findings of Ref. [6] suggested that Si and C diffusivities are of comparable magnitudes, in contrast to that of Hong et al. [2] and Hon et al. [3]. Although the experiments provide hints as to the mediating species for C and Si self-diffusion in SiC, they are not conclusive, with Ref. [5] predicting vacancy-mediated C self-diffusion and Ref. [6] proposing an interstitial-mediated mechanism, both on the C sub-lattice. Moreover, reported diffusivity values

for Si differ by several orders of magnitude. Note, however, that for high temperature annealing of SiC material and devices, a carbon cap is typically utilized in order to suppress the loss of surface atoms (in particular Si) and prevent surface roughening [9–11]. This may influence the migration mechanisms, further complicating the interpretation and understanding of self-diffusion in SiC.

The main intrinsic defects relevant for self-diffusion processes in SiC are the Si and C vacancies (V_{Si} and V_C), interstitials (Si_i and C_i), and antisites (Si_C and C_{Si}). The antisite defects have proven challenging to detect experimentally in 4H-SiC, potentially due to their predicted lack of charge state transition levels in the upper portion of the band-gap [12]. The vacancies and interstitials, on the other hand, are all electrically active in 4H-SiC, and behave as deep electron or hole traps in n-type or p-type material, respectively [12–14]. Hence, their presence is strongly detrimental to power electronics applications, and V_C is in fact known to be a prominent minority lifetime killer in 4H-SiC [15]. Conversely, V_{Si} is a high-spin single-photon emitter, showing considerable promise for quantum technology applications [16].

Density functional theory (DFT) has been used to investigate the mechanism for Si and C self-diffusion in SiC. When assessing the predicted activation energy for self-diffusion using DFT, we proceed by considering each defect species individually. First, a Fermi level range relevant for the annealing temperature being used is chosen, then the relevant defect charge state is identified, and finally the corresponding formation energy and energy barrier for migration are combined to form the activation energy for self-diffusion. This was done for several candidate defects in SiC in, e.g., Ref. [7]. Note that defect migration is anisotropic in 4H-SiC, often with higher barriers for migration between than within lattice planes. For the mid-gap Fermi levels (E_F) which manifest during the high-temperature heat treatments needed to induce migration in n-type 4H-SiC, V_C is expected to occupy the neutral or positive charge state [12,13], while V_{Si} will be negatively charged [14]. Both antisites are likely neutral, which is the case for the carbon interstitial as well, while Si_i defects reside in either the $q = 2+$ or $q = 4+$ charge state depending on whether they occupy a hexagonal (h) or pseudo-cubic (k) lattice plane in 4H-SiC, respectively [12].

Carbon vacancy migration was studied in-depth and for different migration paths using density functional theory in Ref. [17] in combination with the Heyd–Scuseria–Ernzerhof (HSE06) screened hybrid functional [18], the nudged elastic band [19,20] and dimer [21] methods, and comparing to experimental data, resulting in energy barriers for V_C^0 migration of 3.7–4.2 eV. In Ref. [22] Monte Carlo methods were instead employed, yielding migration barriers of 4.2–4.4 eV for the neutral charge state, while studies using the Perdew–Burke–Ernzerhof (PBE) functional [23] yield lower values of 3.3–3.5 eV for the same charge state of V_C [7,24]. Using the PBE functional is known to produce lower energies than, e.g., HSE06 as a result of underestimating the SiC band gap, which likely explains the lower values found in Refs. [7,24] as compared to Refs. [17,22]. Moreover, the calculations of Ref. [24] were not able to capture the full energetics of V_C , as no negative- U characteristics were shown for the $V_C(0/2-)$ transition [25], and Ref. [7] focused on the 3C polytype only. The HSE06-level values of Ref. [17] are therefore quoted for V_C^0 migration herein, using the axial barriers for V_C diffusion along the c -direction.

Migration of V_{Si} is an emerging popular focus [22,24,26] due to the qubit potential of the Si vacancy [16]. Under intrinsic conditions, V_{Si} inhabits the negative charge state, with predicted inter-planar migration barriers of 3.2–4.2 eV [22,24,26]. Interstitial defects are somewhat less studied than vacancies in 4H-SiC, perhaps on account of their greater complexity compared to the vacancies with more fixed lattice positioning. Migration barriers (E_A for migration) for both Si and C interstitials were estimated at ~ 1 eV in Ref. [27], but lattice configuration and Fermi level dependence were not discussed. Refs. [7,24] incorporated the charge state dependence of E_A for migration of Si_i and C_i , yielding barriers between 0.1–2 eV for both defect species and different migration paths. Using PBE and combining the formation and migration energies, Ref. [7] estimated activation energies for C self-diffusion in 3C-SiC (for $q = 0$) at around 7 eV via both C vacancies and interstitials, while that for Si was accompanied by higher barriers in the 8–12 eV range. An even more complete picture was

painted in Ref. [8], where self-diffusion of C and Si via their respective self-interstitials was studied while incorporating both temperature and entropy effects, although for 3C-SiC only. Here, activation energies for self-diffusion of carbon via C_i in 3C-SiC were estimated at 7.1 eV and 7.8 eV under C rich conditions for the neutral and doubly positive charge state, respectively. Si self-diffusion via Si_i was accompanied by much higher barriers, in the 10–11 eV range [8].

The available defect species for mediating self-diffusion in 4H-SiC, their charge state(s) when E_F resides at mid-gap, and the corresponding formation energy and migration barrier as collected from the literature are summarized in Table 1. C self-diffusion via C interstitials and vacancies appears to be separated by an energy difference of up to 1.5 eV, while E_A for Si self-diffusion is predicted in the 10–11 eV range regardless of whether Si_i or V_{Si} is responsible for mediation. Notice also that antisite defects are accompanied by large activation energies for self-diffusion around 13–15 eV, which translates into the interstitial and vacancy defects being more likely candidates for mediating thermally induced Si and C redistribution from their lattice sites in SiC.

Table 1. Calculated activation energies (E_A) for self-diffusion collected from the literature, defined as the sum of the formation energy and energy barrier for migration, via the various defect species available in 4H-SiC. During high-temperature annealing, the Fermi level (E_F) is located near mid-gap in the 4H-SiC samples, and the formation energy is quoted for this value of E_F . All formation energies are, wherever possible, quoted for Si poor and C rich conditions. Formation energies are quoted for HSE06 calculations, while the migration barriers are mostly deduced at PBE-level.

Defect Type	q When E_F = Mid-Gap	Formation Energy (eV)	Migration Barrier (eV)	E_A For Self-Diffusion
V_C	+ or 0	4.8 eV [13,17]	4.2 eV [17]	9.0 eV, 7.9 eV [7] (3C)
C_i	0	6.3 eV [12], 6.5 eV [24]	~1 eV [27], 0.9 eV [24]	7.5 eV, 7.1 eV [8] (3C), 6.6 eV [7] (3C)
C_{Si}	0	3 eV [24]	~10 eV [24]	13 eV
V_{Si}	–	7.0 eV [14]	4.2 eV [26], 3 eV [22]	10–11 eV
$Si_i(h)$	2+	8.5 eV [12]	~1 eV [27]	~9.5 eV, 10.2 eV (3C) [8]
$Si_i(k)$	4+	9.5 eV [12]	~1 eV [27], 1.8 eV [24]	~10.5 eV, ~11 eV (3C) [8]
Si_C	0	5 eV [24]	~10 eV [24]	15 eV

In the present work, we revisit the concept of self-diffusion in the 4H SiC polytype. By studying the motion of both C and Si within the same sample, we attempt to establish whether Si self-diffusion enthalpies are comparable to those of C or not, as the literature is not conclusive in this regard. An important feature of the present study is the use of a carbon cap (C-cap) covering the 4H-SiC surface during annealing to reduce the loss of Si from the surface and thereby suppressing surface roughening. However, the C-cap also presents a continuous injection channel for C interstitials from the C-cap/4H-SiC interface towards the 4H-SiC bulk. By comparing the present and previous experiments, we find that the mechanism for self-diffusion is significantly affected by the presence of the C-cap. In fact, the pre-factors for diffusion are several orders of magnitude higher when the C-cap is present as compared to the cap-free case, indicating a mechanism involving Frenkel pair formation in the sample bulk for self-diffusion.

2. Methods

An epitaxial layer (epi-layer) of 4H- $^{28}Si^{12}C$ silicon carbide was grown by chemical vapor deposition (CVD) on a n-type (0001) 4H-SiC substrate at the University of Linköping. The CVD-grown layer is ~7 μm thick, and the isotope purity is estimated to be $^{28}Si > 99.85\%$ and $^{12}C > 99.98\%$. A C-cap was applied to all samples prior to annealing by graphitizing a photoresist film at 900 °C on the sample surface, in order to avoid surface roughening during the elevated heat treatments. The samples were subjected to high temperature treatments employing an inductively heated furnace (RFA) holding Ar atmosphere in the temperature range 2300–2450 °C. A Cameca IMS7f Secondary Ion Mass Spectrometer (SIMS) equipped with an O_2 primary ion beam source was used to measure the concentration versus depth profiles of Si and C. Absolute concentration values were obtained by

assuming natural abundance in the substrate. For depth calibration, the sputtered crater depths were measured by a Dektak 8 stylus profilometer and a constant erosion rate was assumed.

The diffusion profiles were fitted according to the error function

$$c = c_2 + \frac{c_1 - c_2}{2} \operatorname{erfc} \left\{ \frac{x - d}{2\sqrt{Dt}} \right\} \quad (1)$$

to extract the ^{13}C diffusivities (D) at each temperature, where c is the concentration, t the annealing time, x denotes the depth and d the interface position. Moreover, c_1 and c_2 define the boundary conditions at $t = 0$ for $x - d \leq 0$ and $x - d > 0$, respectively. Finally, the diffusion parameters for the migrating species were determined according to an Arrhenius model

$$D = D_0 e^{-E_A/k_B T}, \quad (2)$$

with D_0 being the exponential pre-factor for diffusion, E_A the activation energy for self-diffusion, k_B the Boltzmann constant, and T the annealing temperature.

Surface roughness will broaden the measured SIMS profiles. To account for this extra broadening, the surface irregularities have been included as root mean square (rms) values and the measured diffusion coefficients have been corrected according to

$$\sigma_D = \sqrt{\sigma_M^2 - \text{rms}^2}, \quad (3)$$

where $\sigma = \sqrt{2Dt}$. M and D stand for measured and corrected, respectively. Note that extraction of diffusivity values was performed for the samples annealed for the longest times only, in order to ensure steady-state conditions.

3. Results

An illustration of the sample geometry prior to heat treatments, by means of ^{13}C concentration profiles as detected by SIMS, is depicted in Figure 1. The figure reveals a ^{13}C -lean epi-layer with both the C-cap and substrate acting as ^{13}C sources. Please note that the SIMS signal in the C-cap layer has not been normalized, and that no correction was performed for the lower carbon ionization yield in the pure carbon (C-cap) matrix relative to the 4H-SiC matrix. The lower ionization yield in the graphitized layer compared to 4H-SiC explains the differences in carbon concentration between the C-cap and 4H-SiC layers in Figure 1. Moreover, one should expect slightly different sputtering rates in the SIMS measurements for the C-cap and 4H-SiC material layers.

Figure 2 displays the temperature-dependent ^{13}C profiles as deduced from SIMS measurements after sequential annealing steps. The ^{13}C profiles are shown after isothermal annealing at 2300 °C for 15–230 min at the interface between the 4H-SiC substrate, which has a natural abundance of ^{13}C , and the ^{12}C isotope purified epitaxial layer in Figure 2a, at approximately 7 μm from the 4H-SiC epi-layer surface. The same interface is studied in Figure 2b, but for 15 min annealing steps in the temperature range 2300–2450 °C. Figure 2c showcases the ^{13}C profiles at the C-cap/4H-SiC interface for isochronal annealing at temperatures between 2300–2450 °C for 15 min. Indeed, Figure 2 demonstrates that C diffuses readily at both the internal 7 μm interface (4H-SiC epi-layer/substrate) and at the C-cap/4H-SiC interface above a temperature of ~ 2300 °C. The profiles are fitted reliably by Equation (1), as indicated by the dotted data points and the solid fit lines in Figure 2. Due to the different ionization levels in the C-cap and 4H-SiC layers and accompanying challenges with normalization, the fitted concentration profiles for ^{13}C are only shown on the 4H-SiC epi-layer side of the interface depicted in Figure 2c. Note that the placing of the C-cap/4H-SiC interface adds some additional uncertainty to the extracted diffusivities for C moving from the C-cap layer to the isotope purified 4H-SiC material.

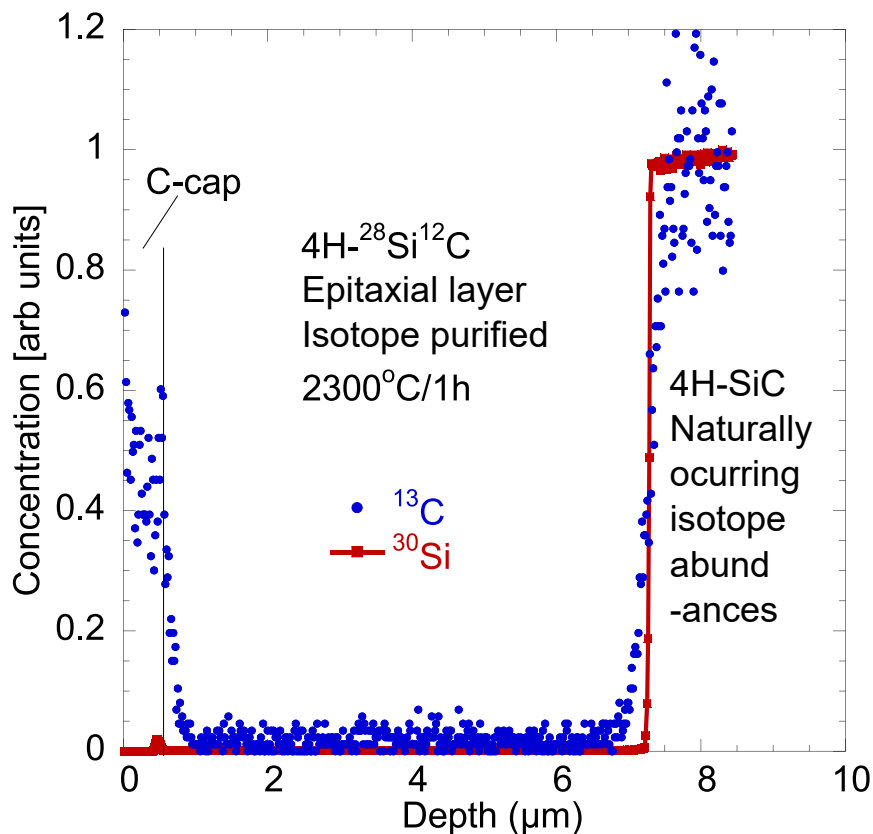


Figure 1. Overview of the sample geometry as detected by secondary ion mass spectrometry (SIMS), with ^{13}C concentration values normalized to 1 in the 4H-SiC substrate. Note that the sample was heated to 2300 °C for 1 h.

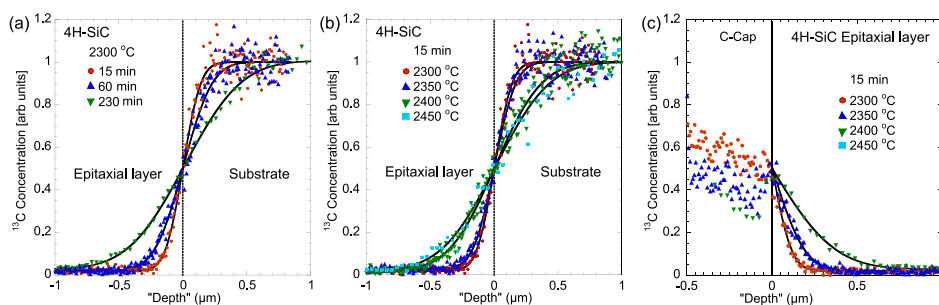


Figure 2. ^{13}C profiles as deduced by SIMS and fitted according to Equation (1), at (a) the interface between the isotope purified epi-layer and the substrate for 2300 °C annealing for 15–230 min, (b) the interface between the isotope purified epi-layer and the substrate for 2300–2450 °C annealing for 15 min, and (c) at the C-cap/epi-layer interface for 2300–2450 °C annealing for 15 min.

The corresponding ^{30}Si depth profiles are shown in Figure 3 at the 4H-SiC substrate/isotope purified epi-layer interface. The time dependence of Si motion at 2300 °C is highlighted in Figure 3a, and temperature dependence in Figure 3b for 15 min isochronal annealing between 2300–2450 °C.

In contrast to the ^{13}C case, the ^{30}Si profiles exhibit a small redistribution only, i.e., any self-diffusion observed for Si within the studied temperature range is significantly smaller than that found for C. Indeed, the redistribution of ^{30}Si observed for, e.g., the 2300 °C sample is similar to that measured at a reference sample (not annealed) with a C-cap (not shown in Figure 3). Note that the shoulder in the ^{30}Si profiles extending from the interface towards the surface, e.g., exhibiting a ^{30}Si concentration of 0.3 at $-0.2\text{ }\mu\text{m}$ for the 230 min sample in Figure 3a, likely arises due to pinholes manifesting in the C-cap at longer annealing times and high temperatures. The pinholes were unavoidable in our SIMS experiment, but are not considered with respect to the diffusion behavior. An alternative explanation for the Si shoulder in Figure 3a related to transient diffusion is discarded, as the same profile shapes are obtained for a reference sample with a C-cap and samples annealed during 15 and 60 min. Most likely, the observed ^{30}Si profile broadening is caused by variations in the thickness and surface structure of the C-cap film. Unfortunately, for long annealing times (230 min), the C-cap starts to degrade.

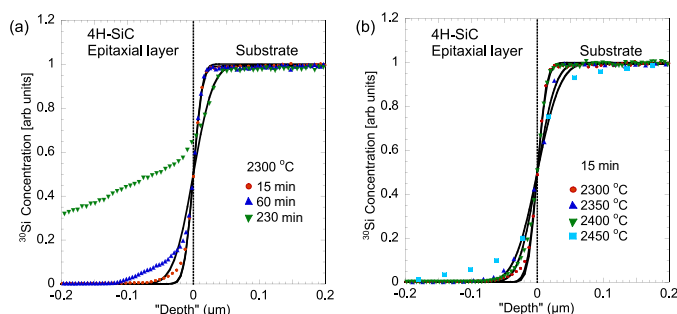


Figure 3. ^{30}Si profiles as detected by SIMS and fitted according to Equation (1), at (a) 2300 °C for 15, 60, and 230 min annealing, and (b) for annealing at various temperatures between 2300–2450 °C for 15 min. The profiles were collected at the interface between the isotope purified epi-layer and the 4H-SiC substrate, at approximately 7 μm from the epi-layer surface.

Estimated diffusivities (D) for ^{13}C (at the two interfaces) and ^{30}Si (at the internal 4H-SiC interface) are collected in Table 2. The D -values are extracted from fits to the experimental data presented in Figures 2 and 3 using Equation (1). Indeed, if one assumes that Si migration is observed in Figure 3, the Si diffusivities are at least a factor 100–1000 times lower than those for C, which agrees reasonably well with previous studies [2,5,6,28,29]. However, the high-temperature heat treatments induce surface roughening effects that complicate measurements of the Si and C depth distributions. For the 2300 °C samples, the peak-to-peak roughness is about 20 nm, which is further increasing to around 30 nm for the 2400 °C samples. From the estimated diffusivities extracted for Si from Figure 3 (see Table 2), we infer diffusion lengths for Si in the 20–30 nm range. Hence, the surface roughness is in the same range as the observed ^{30}Si diffusion lengths, meaning that the estimated ^{30}Si diffusivities must necessarily be of the same order as the uncertainty arising from the surface roughening. Therefore, the ^{30}Si D -values and redistribution depicted in Table 2 and Figure 3 must be considered as an upper bound. Moreover, due to the overlap between ^{30}Si diffusion lengths and surface roughening, the estimates for D_0 and E_A for Si self-diffusion are highly uncertain and will therefore not be quoted herein. The redistribution of ^{13}C , on the other hand, is above the surface roughness and therefore adequately represents the carbon migration. From Figures 2 and 3 combined with the above discussion, we thus infer that carbon migrates readily in 4H-SiC within a 2300–2450 °C temperature interval while silicon does not.

Table 2. Estimated diffusivities for ^{13}C and ^{30}Si migration in 4H-SiC samples under intrinsic conditions and at various temperatures. ^{13}C profiles are collected both at the interface $7\text{ }\mu\text{m}$ into the epi-layer, and at the C/4H-SiC surface, while ^{30}Si diffusivities are from the internal 4H-SiC interface only.

<i>T</i> (°C)	<i>t</i> (min)	<i>D</i> (cm ² /s)		
		^{13}C	^{13}C	^{30}Si
		7 μm into epi	SiC/C Interface	7 μm into epi
2300	15	6.63×10^{-14}	4.45×10^{-14}	6.3×10^{-16}
2300	60	4.45×10^{-14}	3.15×10^{-14}	1.6×10^{-16}
2300	230	4.45×10^{-14}	3.02×10^{-14}	2.0×10^{-16}
2350	15	9.68×10^{-14}	8.90×10^{-14}	2.6×10^{-15}
2400	15	4.59×10^{-13}	3.94×10^{-13}	7.9×10^{-16}
2400	101	1.97×10^{-13}	1.30×10^{-13}	4.2×10^{-15}
2450	15	6.18×10^{-13}	3.80×10^{-13}	4.2×10^{-15}

Figure 4 displays the Arrhenius behavior of the carbon and silicon diffusivity values as summarized in Table 2. The diffusivities extracted for SiC samples employed both herein (No. 5 and 11, brown data points and fit) and in other works [2,5,6,28,29] are included in Figure 4, with the corresponding temperature range, migrating species, D_0 , E_A value and reference collected in Table 3. Note that the data points used for the fit for No. 10 (data and fit collected from Ref. [28]) were chosen based on an upper limit for surface roughening of 15 nm.

Table 3. Collection of Arrhenius data for C and Si self-diffusion from the literature and the present work (No. 5 and 11), see also Figure 4.

No.	<i>T</i> Interval (°C)	Conditions	Isotope	D_0 (cm ² B)	E_A (eV)	Reference
1	1850–2180	Si-rich, 6H	^{14}C	8.6×10^5	7.41	[2]
2	1850–2180	Si-rich, 6H	^{14}C	3.3×10^7	8.20	[2]
3	2000–2290	Si-rich, 6H	^{30}Si	1.5×10^5	8.18	[2]
4	2000–2290	Si-rich, 6H	^{30}Si	5.0×10^2	7.22	[2]
5	2300–2450	4H	^{13}C	8.3×10^6	10.4	Present work
6	2100–2350	4H	^{13}C	8.4×10^2	8.50	[5]
7	2000–2450	4H	^{13}C	4.8×10^{-2}	6.7	[28]
8	2000–2200	4H	^{13}C and ^{30}Si	4.8	7.6	[6] Deduced in combination with B-diffusion
9	1950–2200	Probably 6H	Si	7.3×10^{-5}	5.4	[29] Deduced from B-diffusion
10	2000–2450	4H	^{30}Si	3.8×10^4	10.6	[28]
11	2300–2450	4H	^{30}Si	Uncertain	Uncertain	Present work

Importantly, our results (Table 3 and Figure 4) exhibit a significantly higher activation energy ($E_A^C = 10.4\text{ eV}$) and larger pre-exponential factor ($D_0^C = 8.3 \times 10^6\text{ cm}^2/\text{s}$) for self-diffusion of C compared to that reported in the literature. In addition, from the extracted diffusivities collected in Table 2, we observe that the diffusivity of C decreases with time for the 2300 °C annealing, and that D is lower at the C/4H-SiC surface than at the internal interface between the CVD-grown epi-layer and the substrate at $7\text{ }\mu\text{m}$ depth. It should be noted that the data points used for representing the ^{13}C diffusivities deduced in the present work, and presented as dark brown data points (No. 5) in Figure 4, were collected at the interface located $7\text{ }\mu\text{m}$ into the 4H-SiC epi-layer (third column of Table 2), and not at the C-cap/4H-SiC surface.

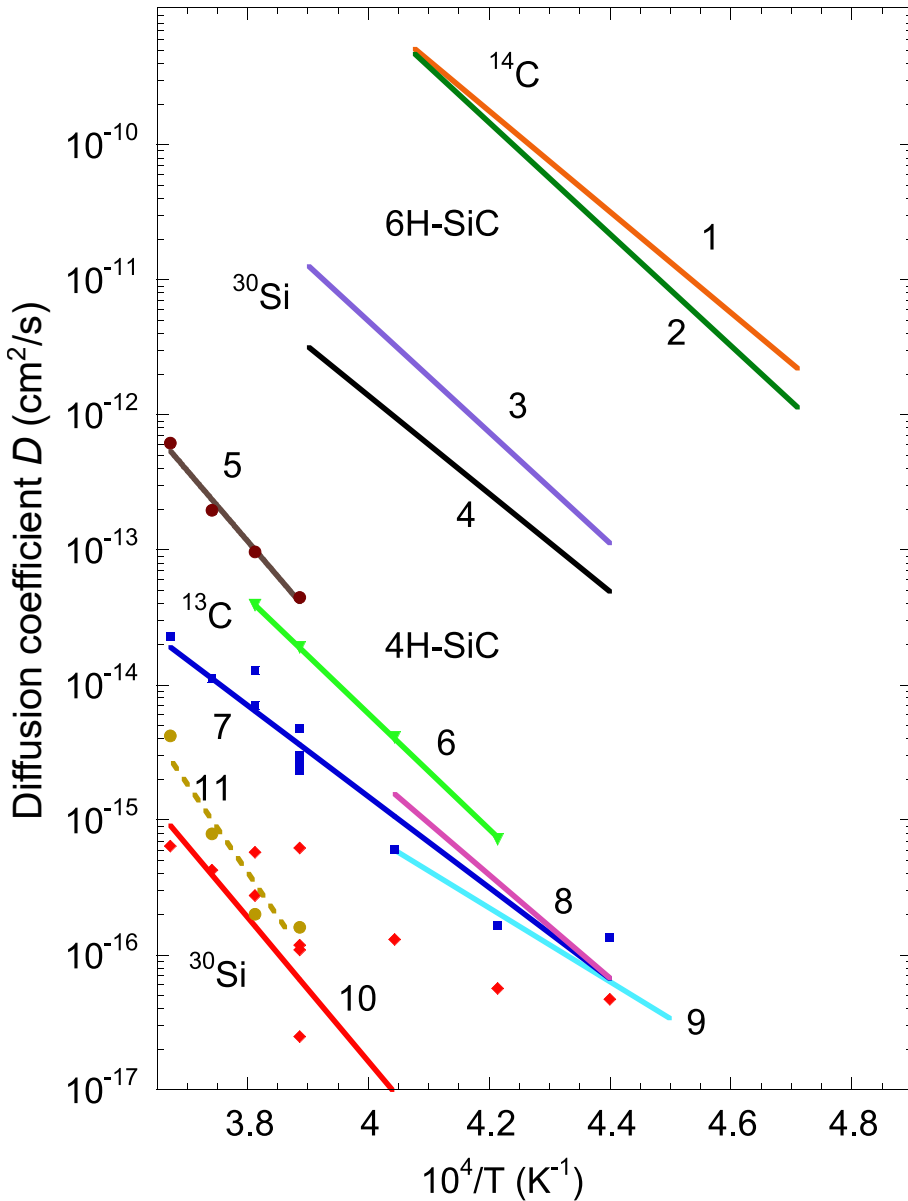


Figure 4. Arrhenius behavior of Si and C diffusivities fitted according to Equation (2), from both this work and the literature. Numbers refer to the present work (No. 5 for ^{13}C and No. 11 for ^{30}Si) and Refs. [2,5,6,28,29] (No. 1–4 and No. 6–10), with additional specifiers for the numbering collected in Table 3. Note that results in the same color are related. For example, the dark brown data points and fit refer to ^{13}C , while the light brown ones refer to ^{30}Si , both from the present work.

4. Discussion

First, let us consider the mechanisms for self-diffusion of Si and C in SiC, that is, the sub-lattice on which migration occurs and the mediating species for migration. Diffusion via antisites (Si_C and

C_{Si}) is expected to be negligible due to the high activation energies for self-diffusion via antisites, as highlighted in Table 1. Thus, we anticipate that both Si and C self-diffuse strictly on their individual sub-lattice. Importantly, self-diffusion via interstitials would first necessitate the formation of Frenkel pairs, which has not been directly calculated in any of the cited works. Self-diffusion via vacancies, on the other hand, does not have to involve Frenkel pairs, as vacancies can be injected from the surface and thereby present a means of travel for the lattice atoms. We thus conjecture that injection of vacancies from the surface, followed by Si or C atoms from the lattice propagating via the vacancies throughout the lattice, is likely associated with a lower total activation energy than Frenkel pair formation in the semiconductor bulk.

The experimental findings of the present work show a strong discrepancy when comparing to previous reports, and provide an important hint towards illuminating the process of self-diffusion in SiC. Indeed, the barrier for C self-diffusion found herein ($E_A^C = 10.4$ eV) shows agreement with neither previous experimental data (see Figure 4) nor theoretical predictions for migration via vacancies, interstitials and antisites on the C sublattice (see Table 1). Note that the high estimated pre-factor for C self-diffusion ($D_0^C = 8.3 \times 10^6$ cm²/s) evidences that we are not, in fact, monitoring diffusion solely via fundamental nearest-neighbor atomic hops [30]. However, an intriguing difference between previous experiments and the present ones is the presence of a C-cap combined with a lower as-grown vacancy concentration, as the epitaxial growth process has improved over the years. Importantly, using a C-cap is at present a standard processing step in device fabrication, with obvious implications for the C diffusivity as carbon interstitials are injected into the material.

In Ref. [31] (on GaAs), it was proposed that self-diffusion processes with pre-factors in the 10^8 – 10^9 cm²/s range indicate a self-diffusion mechanism related to Frenkel pair formation in the semiconductor bulk, which is expected to be dominant when vacancy formation is suppressed at the surface. Thus, with D_0 for C far above the 10^{-3} – 10^{-2} cm²/s expected for fundamental hops [30], it appears evident that the present findings are not representative of undisturbed self-diffusion in SiC. Instead, our results illuminate the competition between Frenkel pair formation in the bulk, and vacancy injection from the surface, as mechanisms for self-diffusion. Previous works have shown that the C-cap is responsible for continuous injection of C interstitials during high-temperature annealing [32], creating a continuous route for recombination of C vacancies that might be generated at the 4H-SiC surface under the high-temperature conditions. Moreover, the idea that C interstitials are being injected from the surface is further supported by the difference in measured C diffusivity at the surface (C-cap/4H-SiC interface) and in the bulk (isotope-pure epi-layer/substrate interface). Therefore, when there is a C-cap covering the sample surface during annealing, self-diffusion via injected vacancies is suppressed, instead pointing towards Frenkel pair formation in the bulk as the dominant route for mediating atomic redistribution. Si self-diffusion may also be impacted by the C-cap, e.g., via formation of immobile antisites.

The present experimental approach is distinctly different from that of, e.g., studying diffusion using self-implantation. For example, in Ref. [17] we tentatively attributed the mediating species for C self-diffusion in SiC to C_i . However, in samples without the C-cap, there is no permanent supply of C_i recombining with vacancy defects at the surface. Therefore, we can briefly consider both V_C and C_i as the responsible party for C self-diffusion, with E_A for self-diffusion via V_C being predicted at 9.0 eV and E_A via C_i at 7.5 eV (see Table 1). Interestingly, both values resonate well with experiment, albeit different ones; Ref. [5] predicted an E_A for ¹³C motion of 8.5 eV, while Ref. [6] deduced that $E_A = 7.4$ eV. Indeed, the lower pre-factors for diffusion in Refs. [5,6] as compared to the present work indicate that Frenkel pair formation does not dominate in the un-capped samples, and instead we attribute C and Si self-diffusion to the formation and injection of Si and C vacancies at the surface. In fact, injection of C_i from the C-cap would delay C self-diffusion if it occurred via C vacancies, and one would expect a significant delay in C migration upon the recombination between the injected C_i and the thermally generated V_C , which would thus prevent further motion of ¹³C atoms. A similar mechanism can be proposed for Si self-diffusion via V_{Si} , if the injected C_i form nearly immobile C_{Si}

antisites. The injection of C_i from the C-cap therefore explains both the higher activation energies and the higher pre-factors for self-diffusion deduced for C (and Si) in the present work.

5. Concluding Remarks

We investigate the effect of C injection from a carbon cap during high-temperature annealing on self-diffusion of C and Si in 4H-SiC. The continuous excess of C interstitials results in recombination of the injected C interstitials with Si and C vacancies generated in the near-surface region. Hence, the presence of the C-cap promotes the formation of Frenkel pairs in the SiC bulk as opposed to the injection of vacancies from the semiconductor surface, as evidenced by the elevated exponential pre-factors for C self-diffusion found herein as compared to previous works. In conclusion, we tentatively attribute C self-diffusion in un-capped samples to the injection of carbon vacancies from the SiC surface. The case for Si, however, is less straightforward, with predicted activation energies for Si self-diffusion overlapping regardless of whether Si vacancies or interstitials act as the mediating species. Thus, resolving Si self-diffusion on the Si sub-lattice is challenging, but following the argument for the C case, injection of Si vacancies from the surface likely outcompetes Si Frenkel pair formation when a C-cap is not present.

Author Contributions: Conceptualization, M.E.B., M.L. and L.V.; methodology, M.L., L.V., M.G. and J.U.H.; validation, M.L.; formal analysis, M.L. and M.E.B.; investigation, M.L. and L.V.; resources, M.G. and J.U.H.; writing—original draft preparation, M.E.B.; writing—review and editing, M.E.B., M.L., L.V. and J.U.H.; visualization, M.E.B. and M.L. All authors have read and agreed to the published version of the manuscript.

Funding: Financial support was kindly provided by the Research Council of Norway and the University of Oslo through the frontier research project FUNDAMeNT (no. 251131, FriPro ToppForsk-program). The Research Council of Norway is acknowledged for the support to the Norwegian Micro- and Nano-Fabrication Facility, NorFab, project number 245963. J.U.H. would like to acknowledge support from the Swedish Energy Agency Energimyndigheten project number 43611-1.

Acknowledgments: The authors would like to thank the late B.G. Svensson for contributing to the idea for this study.

Conflicts of Interest: The authors declare no conflicts of interest.

References

- Hon, M.H.; Davis, R.F. Self-diffusion of ^{14}C in polycrystalline β -SiC. *J. Mater. Sci.* **1979**, *14*, 2411, ISSN 1573-4803. [\[CrossRef\]](#)
- Hong, J.D.; Hon, M.H.; Davis, R.F. Self-diffusion in alpha and beta silicon carbide. *Ceramurg. Int.* **1979**, *5*, 155. [\[CrossRef\]](#)
- Hon, M.H.; Davis, R.F.; Newbury, D.E. Self-diffusion of ^{30}Si in polycrystalline β -SiC. *J. Mater. Sci.* **1980**, *15*, 2073, ISSN 1573-4803. [\[CrossRef\]](#)
- Hong, J.D.; Davis, R.F. Self-Diffusion of Carbon-14 in High-Purity and N-Doped α -SiC Single Crystals. *J. Am. Ceram. Soc.* **1980**, *63*, 546. [\[CrossRef\]](#)
- Linnarsson, M.K.; Janson, M.S.; Zhang, J.; Janzén, E.; Svensson, B.G. Self-diffusion of ^{12}C and ^{13}C in intrinsic 4H-SiC. *J. Appl. Phys.* **2004**, *95*, 8469. [\[CrossRef\]](#)
- Rüschenschmidt, K.; Bracht, H.; Stolwijk, N.A.; Laube, M.; Pensl, G.; Brandes, G.R. Self-diffusion in isotopically enriched silicon carbide and its correlation with dopant diffusion. *J. Appl. Phys.* **2004**, *96*, 1458. [\[CrossRef\]](#)
- Bockstedte, M.; Mattausch, A.; Pankratov, O. Ab initio study of the migration of intrinsic defects in 3C-SiC. *Phys. Rev. B* **2003**, *68*, 205201. [\[CrossRef\]](#)
- Bedoya-Martínez, O.N.; Roma, G. Activation entropies for diffusion in cubic silicon carbide from first principles. *Phys. Rev. B* **2010**, *82*, 134115. [\[CrossRef\]](#)
- Negoro, Y.; Katsumoto, K.; Kimoto, T.; Matsunami, H. Electronic behaviors of high-dose phosphorus-ion implanted 4H-SiC (0001). *J. Appl. Phys.* **2004**, *96*, 224. [\[CrossRef\]](#)

10. Sundaresan, S.G.; Mahadik, N.A.; Qadri, S.B.; Schreifels, J.A.; Tian, Y.-L.; Zhang, Q.; Gomar-Nadal, E.; Rao, M.V. Ultra-low resistivity Al⁺ implanted 4H-SiC obtained by microwave annealing and a protective graphite cap. *Solid-State Electron.* **2008**, *52*, 140. [[CrossRef](#)]
11. Nipoti, R.; Mancarella, F.; Moscatelli, F.; Rizzoli, R.; Zampolli, S.; Ferri, M. Carbon-Cap for Ohmic Contacts on Ion-Implanted 4H-SiC. *Electrochem. Solid-State Lett.* **2010**, *13*, H432. [[CrossRef](#)]
12. Kobayashi, T.; Harada, K.; Kumagai, Y.; Oba, F.; Matsushita, Y. Native point defects and carbon clusters in 4H-SiC: A hybrid functional study. *J. Appl. Phys.* **2019**, *125*, 125701. [[CrossRef](#)]
13. Coutinho, J.; Torres, V.J.B.; Demmouche, K.; Öberg, S. Theory of the carbon vacancy in 4H-SiC: Crystal field and pseudo-Jahn-Teller effects. *Phys. Rev. B* **2017**, *96*, 174105. [[CrossRef](#)]
14. Bathen, M.E.; Galeckas, A.; Müting, J.; Ayedh, H.M.; Grossner, U.; Coutinho, J.; Frodason, Y.K.; Vines, L. Electrical charge state identification and control for the silicon vacancy in 4H-SiC. *NPJ Quantum Inf.* **2019**, *5*, 111. [[CrossRef](#)]
15. Klein, P.B.; Shanabrook, B.V.; Huh, S.W.; Polyakov, A.Y.; Skowronski, M.; Sumakeris, J.J.; O'Loughlin, M.J. Lifetime-limiting defects in n- 4H-SiC epilayers. *Appl. Phys. Lett.* **2006**, *88*, 052110. [[CrossRef](#)]
16. Weber, J.R.; Koehl, W.F.; Varley, J.B.; Janotti, A.; Buckley, B.B.; Van de Walle, C.G.; Awschalom, D.D. Quantum computing with defects. *Proc. Natl. Acad. Sci. USA* **2010**, *107*, 8513. [[CrossRef](#)]
17. Bathen, M.E.; Coutinho, J.; Ayedh, H.M.; Ul Hassan, J.; Farkas, I.; Öberg, S.; Frodason, Y.K.; Svensson, B.G.; Vines, L. Anisotropic and plane-selective migration of the carbon vacancy in SiC: Theory and experiment. *Phys. Rev. B* **2019**, *100*, 014103. [[CrossRef](#)]
18. Heyd, J.; Scuseria, G.E.; Ernzerhof, M. Hybrid functionals based on a screened Coulomb potential. *J. Chem. Phys.* **2003**, *118*, 8207. [[CrossRef](#)]
19. Mills, G.; Jónsson, H. Quantum and thermal effects in H₂ dissociative adsorption: Evaluation of free energy barriers in multidimensional quantum systems. *Phys. Rev. Lett.* **1994**, *72*, 1124. [[CrossRef](#)]
20. Mills, G.; Jónsson, H.; Schenter, G.K. Reversible work transition state theory: application to dissociative adsorption of hydrogen. *Surf. Sci.* **1995**, *324*, 305. [[CrossRef](#)]
21. Henkelman, G.; Jónsson, H. A dimer method for finding saddle points on high dimensional potential surfaces using only first derivatives. *J. Chem. Phys.* **1999**, *111*, 7010. [[CrossRef](#)]
22. Kuate Defo, R.; Zhang, X.; Bracher, D.; Kim, G.; Hu, E.; Kaxiras, E. Energetics and kinetics of vacancy defects in 4H-SiC. *Phys. Rev. B* **2018**, *98*, 104103. [[CrossRef](#)]
23. Perdew, J.P.; Burke, K.; Ernzerhof, M. Generalized Gradient Approximation Made Simple. *Phys. Rev. Lett.* **1996**, *77*, 3865. [[CrossRef](#)] [[PubMed](#)]
24. Yan, X.; Li, P.; Kang, L.; We, S.-H.; Huang, B. First-principles study of electronic and diffusion properties of intrinsic defects in 4H-SiC. *J. Appl. Phys.* **2020**, *127*, 085702. [[CrossRef](#)]
25. Son, N.T.; Trinh, X.T.; Løvlie, L.S.; Svensson, B.G.; Kawahara, K.; Suda, J.; Kimoto, T.; Umeda, T.; Isoya, J.; Makino, T.; et al. Negative-*U* System of Carbon Vacancy in 4H-SiC. *Phys. Rev. Lett.* **2012**, *109*, 187603. [[CrossRef](#)] [[PubMed](#)]
26. Wang, X.; Zhao, M.; Bu, H.; Zhang, H.; He, X.; Wang, A. Formation and annealing behaviors of qubit centers in 4H-SiC from first principles. *J. Appl. Phys.* **2013**, *114*, 194305. [[CrossRef](#)]
27. Iwamoto, N.; Svensson, B.G. Chapter Ten—Point Defects in Silicon Carbide. In *Defects in Semiconductors*; Romano, L., Privitera, V., Jagadish, C., Eds.; Volume 91 of Semiconductors and Semimetals; Elsevier: Amsterdam, The Netherlands, 2015; pp. 369–407.
28. Rüschemschmidt, K. Selbst- und Fremddiffusion in Siliziumkarbid zur Charakterisierung der atomaren Eigenpunktdefekte. Ph.D. Thesis, Westfälischen Wilhelms-Universität Münster, Münster, Germany, 2006.
29. Konstantinov, A.O. Nature of point defects generated during diffusion of acceptor impurities in silicon carbide. *Sov. Phys. Semicond.* **1992**, *26*, 151.
30. Philibert, J. *Atom Movements: Diffusion and Mass Transport in Solids*; Editions de Physique: Les Ulis, France, 1991; ISBN 9782868831613.

31. Wager, J.F. Energetics of self-diffusion in GaAs. *J. App. Phys.* **1991**, *69*, 3022. [[CrossRef](#)]
32. Ayedh, H.M.; Nipoti, R.; Hallén, A.; Svensson, B.G. Elimination of carbon vacancies in 4H-SiC employing thermodynamic equilibrium conditions at moderate temperatures. *Appl. Phys. Lett.* **2015**, *107*, 252102. [[CrossRef](#)]



© 2020 by the authors. Licensee MDPI, Basel, Switzerland. This article is an open access article distributed under the terms and conditions of the Creative Commons Attribution (CC BY) license (<http://creativecommons.org/licenses/by/4.0/>).